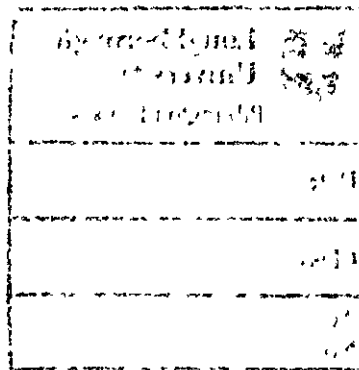# DIRECT POLYMERIC ENCAPSULATION OF ELECTRONIC SYSTEMS FOR AUTOMOTIVE APPLICATIONS

By

Nee Joo Teh

A doctoral thesis

submitted in partial fulfilment of the requirements for the award of

Doctor of Philosophy of Loughborough University

By Nee Joo Teh, December 2004

ABSTRACT

Over the past forty years, compelling demands for safer, cleaner and more efficient vehicles have given rise to a drastic increase in the replacement of many traditional mechanical and electrical mechanisms by more advanced electronic systems. Due to their harsh operating environments, automotive electronic systems are subject to failures from thermomechanical stresses and corrosive breakdown, adversely affecting their reliability and lifespan. Furthermore, the development of bus communication protocols for improved control capabilities has prompted wider systems distribution within the restricted space of a vehicle and inadvertently led to higher assembly complexity, increased vehicle weight and manufacturing costs. Despite advancements in the industry, no commercially viable process exists that is capable of providing electronic systems with sufficient robustness for their operating environments while also offering assembly consolidation to enable cost reduction.

The primary focus of this thesis is the engineering of a low-cost, single-cycle process for the direct encapsulation of electronic systems within thermoplastic structures, leading to the production of robust, geometrically flexible and ready-to-assemble plastic automotive components with integrated electronics and requisite power distribution. An injection overmoulding technique, developed from conventional processes, is presented as a cost effective and technically feasible solution.

The contributions of this research are in four areas. Firstly, an in-depth investigation is presented, which has achieved a balanced pressure distributions of melt flow and reductions in deformation of the overmoulded electronic assembly. This has led to the engineering of a novel topographically contoured moulding tool with internal subassembly support mechanism. Secondly, systematic experimental studies of the interdependent process parameters in injection overmoulding were implemented through design of experiment (DOE) approaches and statistical analysis techniques to formulate optimised process conditions. Thirdly, knowledge of the stresses on the embedded subassembly has been gained through novel measurement of mechanical and electrical properties at board and chip-levels, providing an understanding of design requirements and process boundary conditions. Finally, by offering superior geometrical flexibility, a fast and efficient process cycle, and better consolidation with the existing plastic components, this technology has demonstrated improvements in the robustness of automotive electronic systems.

ACKNOWLEDGEMENT

In memory of my father, my thoughts are always with you.

To my family, your unconditional love and support all these years mean the world to me.

To my wife Jude, your incredible love, continuous encouragement and unrelenting support have been my inspiration.

To our daughter Isabelle, you have brought us endless joy and happiness.

TABLE OF CONTENTS

LIST OF FIGURES

LIST OF TABLES

GLOSSARY OF ACRONYMS

ABS	Acrylonitrile Butadiene Styrene
AEC	Automotive Electronics Council
ANOM	Analysis of means
ANOVA	Analysis of variance
ASTM	American Society for Testing and Materials
BGA	Ball grid array
BT	Bismaleimide Triazine
CBA	Chemical blowing agent
CFD	Computational fluid dynamics
COB	Chip-on-board
CTE	Coefficient of thermal expansion [ppm/°C]
DOE	Design of experiment
d_{SO}	Injection switch-over distance [mm]
d_{stroke}	Injection cylinder stroke distance [mm]
FEA	Finite element analysis
FFC	Flat flexible cable
FR4	Fire-retardant grade 4
GR	Glass-reinforced
HDI	High density interconnection
IC	Integrated circuit
IML	In-mould labelling
IPC	The Institute for Interconnecting and Packaging Electronics Circuits
IR	Infrared
JEDEC	Joint Electron Device Engineering Council
MCM	Multi-chip module
MID	Moulded interconnected devices
Mil. Std.	Military Standard
MPa	mega-Pascal
NTC	Negative temperature coefficient

Pa	Pascal
PBT	Polybutylene Terephthalate
PCB	Printed circuit board
PE	Polyester
PEN	Polyethylene Naphthalate
P_{hold}	Holding pressure [MPa or bar]
P_{inj}	Hydraulic injection melt pressure [MPa or bar]
P_{noz}	Nozzle melt pressure [MPa or bar]
PP	Polypropylene
PUR	Polyurethane
RSM	Response surface methodology
Si	Silicone
t_{cool}	Cooling time [s]
T_g	Glass transition temperature [°C]
t_{hold}	Holding time [s]
t_{inj}	Melt injection time [s]
T_{melt}	Melt temperature [°C]
T_{mould}	Moulding tool temperature [°C]
TP	Thermoplastic
TS	Thermoset or thermosetting
v_{inj}	Melt injection speed [m/s]

CHAPTER 1.   INTRODUCTION

1.1.   Background

Since its introduction in the 1960s, automotive electronics have experienced a dramatic growth in the replacement of many traditional mechanical and electrical systems. This development has largely been driven by legislative requirements, market competition and customer demands for safer, cleaner and more efficient automobiles. The ensuing push for more intelligent systems and telematics[†] has resulted in the distribution of electronic systems to various locations within the structure of vehicles and has prompted the development of bus communication protocols. Presently, electronic applications may be found from in-cabin to under-bonnet areas of most new vehicles. However, as in aeronautical and aerospace industries, safety and reliability requirements are of the utmost importance for automotive electronics, making it one of the most technologically-aware and yet safety-driven manufacturing sectors.

Many modern electronic systems offer the means for sensing, control and/or actuation capacities in arduous locations of a vehicle and are persistently subject to severe mechanical stresses, thermal cycles and environmental contaminants. Such strenuous operating conditions, typified by systems in the wheel arch and engine compartment, can lead to failures from detrimental thermomechanical stresses and corrosive breakdown. Moreover, there are strong industrial initiatives for the migration of electronics to on-engine mounting points, hence significantly increasing the temperature and vibrational exertions. Consequently, the survivability of automotive electronics under elevated mechanical and thermal conditions has a significant influence on its systems reliability. Providing the circuitry with sufficient robustness against such failure mechanisms is a critical design criterion for engineers in attaining reliability. Metal or plastic housings sealed with high-strength adhesives or ultrasonic bonding are generally used, many with their electronics shielded by polymeric conformal coating.

The recent development of different bus communication protocols as means of providing better data exchange and control capabilities have successfully enabled further

---

[†] The combined application of *tele*communications and in*formatics* technologies and services within the automotive and aeronautical industries [Information Society Technologies, 2003]

implementations of electronic and electromechanical systems in vehicles. However, this has inadvertently prompted a wider systems distribution within the restricted envelope of a vehicle. Due to inaccessibility or design considerations, many of the processing electronics have to be remotely wired to respective sensing or actuation mechanisms, thus necessitating the use of more harness looms, which in turn increases the overall vehicle weight. The assembly of heavy harnesses and mounting of electronic systems in inaccessible locations considerably increases shop-floor complexity and incurs extra assembly costs. Integrating electronics and some degree of power distribution within the existing structural plastic trim of a vehicle offers an opportunity to overcome these problems. As today's complex multi-chip control systems are predominantly limited to low-volume high-value cars, the eventual cost saving in the production and assembly processes will also allow the high-volume small and medium car markets to fully capitalise upon the benefits of increasing telematics.

The automotive industry is currently moving towards high-density interconnected electronic technologies with higher capabilities and size reduction. While the benefits from improved functionality may be apparent, packages such as wirebonded chip-on-board, flip-chips and ball-grid-arrays (BGAs) will require more stringent and robust structural buffering from thermomechanical forces for their long-term reliability.

The research reported in this thesis was motivated by the ever-increasing demands for robust and reliable electronic systems capable of withstanding severe automotive environments. The primary objective of this work has been to develop and implement an economically efficient technology for the encapsulation of electronics systems within thermoplastic structures in a single overmoulding process. The results achieved in this research provide a design platform for engineers in the manufacture of geometrically flexible, ready-to-assemble automotive plastic components, with the integration of robust electronics and the required power distribution.

1.2. Areas of Investigation and Research Approach

This research focused on the development of a single-cycle overmoulding process for the direct embedment of electronic systems in thermoplastic components. While the engineering platform established from the technology may bring benefits to many manufacturing industries, the current research has investigated applications from automotive electronics as

the springboard in the feasibility evaluation of the proposed technology as well as the technical demonstrators in its subsequent implementations.

This thesis begins from the baseline of reviewing the current state of technologies related to the research, to be followed by exploring how conventional technologies may be reengineered using innovative process designs to produce thermoplastic components in which electronics and structural features are fully integrated. It goes on to highlight the challenges to be addressed in order to improve upon traditional packaging approaches in automotive electronics to gain technical and economic advantages. The results from a preliminary process screening trial and modelling validation formed the basis of a feasibility study. Empirical investigations using systematic experimental design, comprehensive statistical analyses and innovative engineering were subsequently undertaken to optimise the process parameters. Finally, real-time measurements were implemented to gain insight and deeper understanding of the functional behaviour of the embedded electronics during the proposed process. The findings obtained in this research formulated a methodology for the implementation of direct injection overmoulding of electronic systems into thermoplastic modules.

1.3. Aims and Objectives

This research aimed to implement a technology that meets demands for robust and reliable electronic systems, capable of withstanding severe automotive environments. Based on the knowledge gained in this research, a design platform would be generated for the manufacture of geometrically flexible, ready-to-assemble automotive plastic components, with integration of electronics and power distribution. Finally, the technology would further enhance the application of electronics in automotive industry.

In order to fulfil the aims outlined above, studies were undertaken in this research to achieve the following objectives:

a) To understand and develop an economically viable technology for the encapsulation of electronics systems within thermoplastic structures, and

b) To use conventional electronics and polymer processing to achieve leaner assembly through parts consolidation

To achieve this advancement for the automotive electronic engineers, key elements of the injection overmoulding process have been identified and developed. These are:

1) **Electronic assembly** – Emphasis has to be placed on the selection of component packages, circuit substrates and interconnections in order to ensure their integrity during overmoulding. Extra stress buffering layers such as "glob-top", may have to be used for more sensitive components and solder joints.

2) **Selection of materials** – CTE matching, content and type of filler reinforcement, geometrical stability, rheological characteristics as well as processing and service specifications of polymers should be taken into consideration during the design stage.

3) **Process parameters** – The understanding of individual and any combinational influences from process factors is critical for the reduction of thermomechanical stresses and product defects through optimisation of the temperature, pressure and time variables.

4) **Tooling design** – The geometry and position of injection gate, overall part thickness and distribution of dynamic melt flow resistance are important factors in affecting the overmoulding. Engineers must also address the in-mould positioning apparatus for the electronic assembly.

5) **Qualification protocol** – Potential failure mechanisms must be identified and appropriate analysis techniques conducted to evaluate the significance of process factors in contributing to defects.

The main body of this thesis describes the design, development, experimental trials and results examination performed to address these process elements, and their interrelated integration to form the core of a novel electronic injection overmoulding technology.

1.4. Contributions of the Research

This research makes a number of contributions to the development of a polymeric encapsulation process of electronic systems and its implementation into the automotive electronic manufacturing industry. They are the following:

1) A novel moulding tool reengineering approach has been designed and implemented into the injection overmoulding of an electronic system. By maintaining the thermodynamic flow resistance for the molten polymer around the electronic assembly, the topographically contoured tool produced a balanced in-mould pressure distribution. Additionally, different methods of positioning mechanisms for the insert assembly were investigated and an in-mould supporting apparatus was designed and implemented.

2) Systematic design of experiment (DOE) of factorial and RSM paradigms have been comprehensively implemented into the experimental analysis to enable in-depth study of the interdependent process variables. ANOVA and ANOM were used jointly with parametric optimisation to isolate the prominent process variables and finally to identify the states of these variables to arrive at the most optimal yield for the overmoulded components.

3) Novel functional electronic test vehicles have been developed to allow real-time instrumentation and measurement of mechanical and electrical properties during the overmoulding process. The outputs from such board-level and chip-level monitoring systems provided an insight into the effects of thermomechanical stresses on the embedded components and formed a useful aid for system design and component selection. Furthermore, wirebonded silicon chips with glob-top coating have been investigated with favourable results and is a current subject of production planning for industrial partners. This is hoped to become a stepping stone for the use of advanced HDI electronic packages.

4) Finally, a novel overmoulding process which adapted and improved upon conventional injection moulding and electronic assembly has been successfully developed in collaboration with industry. The advent of such thermoplastic overmoulded electronic systems has helped to move forward the manufacturing industry from the use of non-recyclable thermoset materials as well as standard mounting practices. Moreover, the technology offers a fast and efficient process cycle to produce electronic-embedded plastic components with superior geometrical flexibility and improved consolidation with existing parts. Therefore, it has been recognised to improve the robustness of the automotive electronic systems, while maintaining its manufacturability through its ease of incorporation into existing moulding machinery setup, higher cost efficiency and better component handleability for leaner assembly procedures.

1.5.   Structure of the Thesis

This introductory Chapter is followed by a further seven chapters.

Chapter Two begins by discussing the current board-level packaging technologies, with comparisons drawn against thermosetting materials and the MID approach. It goes on to present a brief overview of the automotive electronic industry. The definition of this research is presented through a discussion of the adaptation of injection moulding for direct

encapsulation of electronics and its associated advantages. Finally, the technical challenges and potential failure mechanisms of overmoulded electronics are examined.

Chapter Three describes the preliminary experiments in this research. The initial trials and the subsequent process screening experiments are discussed. This is followed by an exploratory experiment in which a systematic experimental scheme was designed to further analyse the encapsulation process.

Chapter Four presents an in-depth discussion on the design of subassembly supports in the mould tool. It focuses on an experiment to study the adhesion between the interfacial polymers with a list of materials identified for overmoulding and pre-moulded support cradles.

Chapter Five concentrates on the re-engineering work of the mould tool in order to minimise structural distortions to the embedded electronic assembly.

Chapter Six reports on the study undertaken to achieve real-time monitoring of the overmoulding process at the board and component levels of the assembly. Component temperature excursion, substrate lateral strains and electronic integrity were among the measured entities. The results obtained are elaborated in detail to provide a deeper insight into the overmoulding process.

Chapter Seven discusses the chip-level real-time monitoring experiments, in which a wirebonded chip-on-board test vehicle with multiple capabilities was employed. The experimental setup is discussed and the measurements of temperature and strain are presented in order to establish the potential for such electronic interconnection in the proposed encapsulation process.

Chapter Eight provides an overall discussion, summarising all the significant results reached in the preceding chapters and conclusions are drawn from all observations. The technology demonstrators selected to illustrate implementation of the overmoulding process into industrial applications are also presented. The chapter ends with an assessment of the contributions and limitations of this study. A number of suggestions for further work and exploitations are also presented.

CHAPTER 2.   TECHNOLOGY REVIEW AND RESEARCH DEFINITION

2.1.   Introduction

This chapter sets out to give an outline of the different elements involved in the process suggested by this research. Firstly, an overview of electronic packaging processes related to the research is presented and evaluations are made against comparable technologies. As applications from the automotive electronic industry were used as technology demonstrators in this research, the background of automotive electronic industry is briefly presented to formulate the objectives and focus of this research. The discussion will also demonstrate that automotive electronics provide a good application platform for the feasibility study of plastic overmoulded electronics as they are exposed to extreme and arduous operating environments. This chapter then concentrates on the adaptation of the thermoplastic injection moulding to enable a single-cycle electronics encapsulation process technology. This is coupled with discussions on the inherent challenges and benefits associated with its development.

2.2.   Electronic Packaging and Interconnection

2.2.1.   Packaging Hierarchy and Current Technologies

The revolution of modern semiconductor electronics took place with the invention of the transistor at Bell Labs in 1947 and it has since become one of the most important industries for the advancement of science, technology and manufacturing economies. The innovation in packaging technologies for various electronic components and systems has formed an integral part of this development. Today, electronic packaging involves anything from passive components (resistors, capacitors, etc.), integrated circuits (ICs) to entire electronic subsystems (handheld devices, mobile phones, personal computers, etc.), and encompasses the following four key functions of [Tummala et al, 1997] [Wong, 2000]:

1) power distribution,
2) signal distribution,
3) thermal management, and
4) protection (mechanical, chemical, environmental, electromagnetic).

The levels of packaging process involved in electronic systems are defined in Figure 2-1, which begins with the lithography fabrication of polycrystalline silicon wafer using VLSI (very large scale integration) or ULSI (ultra large scale integration) to produce semiconductor chips integrated with tens of millions of transistors, resistors, capacitors and thin-film interconnections. The chip level interconnection is arguably the most critical stage, where the integrated chip (IC) is assembled into a housing or lead-frame and connected using wire bonding (WB), tape automated bonding (TAB), flip chip (FC) or beam lead (BL). At the next level, the interconnected ICs are packaged using plastic transfer moulding into different types of packages such as quad flatpack (QFP), plastic leadless components (PLCC), ball grid array (BGA), dual in-line package (DIP) and small outline package (SOP).

These packaged ICs are then populated to a laminate or ceramic PCB using surface mount (SM), plated through hole (PTH) and BGA with soldering materials or conductive adhesives. Alternatively, the bare ICs may also be populated directly onto PCB using direct chip attach (DCA) methods such as wire-bonded chip-on-board (COB) and FC, and protected by a layer of polymeric glob-top[†]. I/O interconnects in the forms of metal pins, wires and/or flexible cables are attached to the assembled circuit. System level packaging then takes place where one or multiple electronic circuitries are assembled into its host equipment (such as a handheld calculator, mobile phone, PC, etc.) or into an external housing which may be plugged or mounted into the final hosting equipment (such as a vehicle, industrial machinery, etc.).

The continual development of new and better polymers for use as moulding compounds, adhesives, underfills and heat transfer materials is at the heart of developments of next-generation electronic packaging including high-density PCBs, embedded passives and alternative high-density chip- and component-level interconnections. It has also been identified [Wong, 2000] that the advancement in VLSI semiconductor technology is also largely attributed to the advances in polymeric materials, such as photoresists for microelectronic lithography, dielectrics for interlayer and device passivation, encapsulants for coatings and mouldings. Table 2-1 projects the packaging trend and demands in consumer, automotive and high-performance systems over the last decade.

---

† The application of an encapsulant to protect vulnerable electronic components from environmental, mechanical or electrical damages [TWI, 1999]

In order to meet the technological requirements in these industries, ICs have gone through a very substantial miniaturisation process to increase its functionality per unit area [Brathwaite et al, 1997], as reflected in Figure 2-2, while the manufacturing process has evolved to produce packaging technologies with smaller geometry, higher interconnection density, functionality and reliability (as illustrated in Table 2-2).
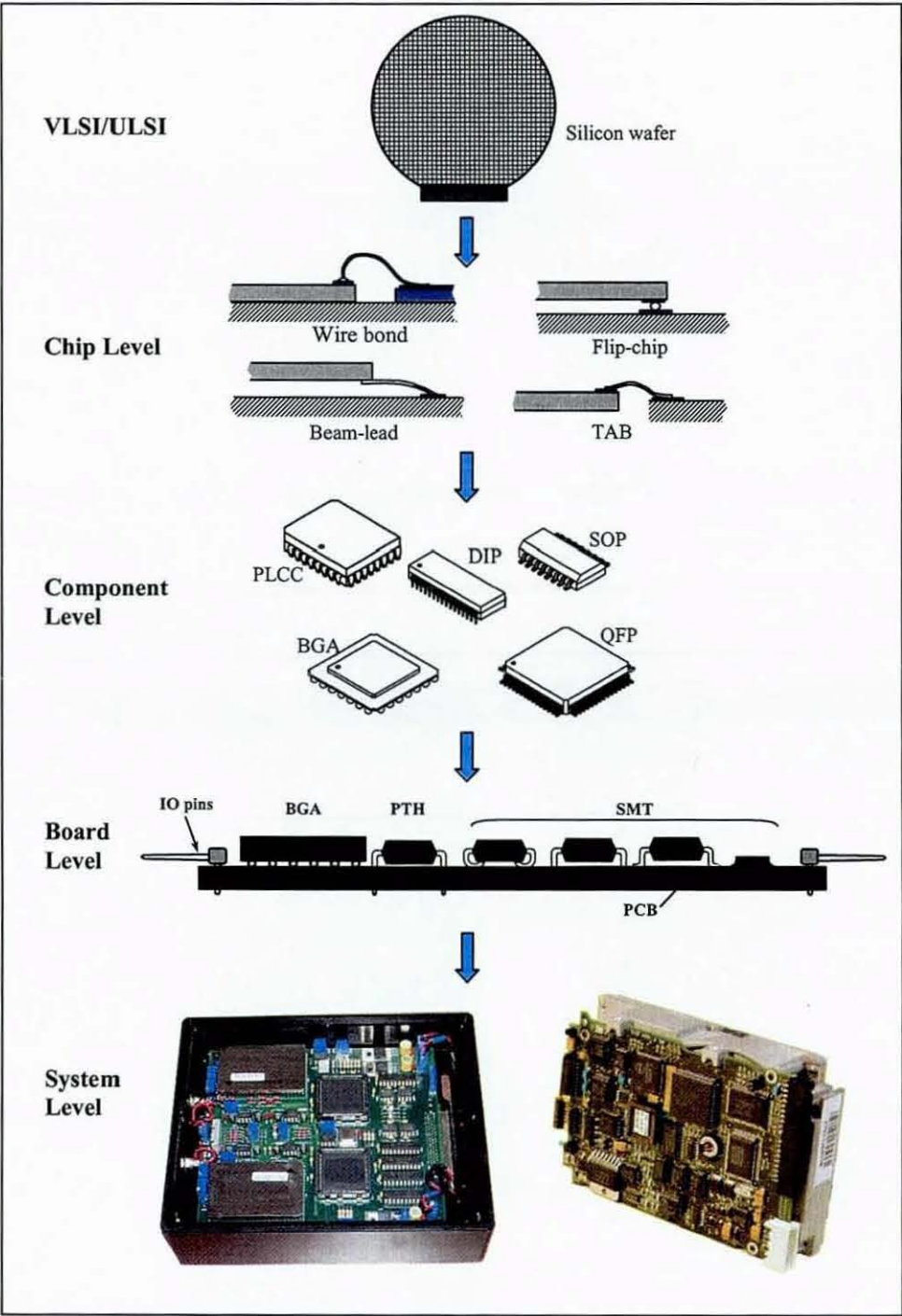
Figure 2-1 Conventional electronic packaging hierarchy

	Consumer Products			Automotive Electronics			High-Performance Systems		
	1996	2000	2004	1996	2000	2004	1996	2000	2004
I/O per chip	100	200	375	150	200	500	600	1,500	3,000
I/O density/in^2	100	200	375	30	100	150	150	300	400
Area array pitch (mm)	0.4	0.25	0.2	0.4	0.25	0.2	-	-	-
Board lines/spaces (mil)	5	4	2	6	3	2	3	2	1
Power/chip (W/chip)	1	1	1	6	12	15	40	60	80
				1.0	0.7	0.4	10.0	5.0	2.5
Board cost ($/in^2)	1	0.6	0.4	(6 layers)	(6 layers)	(6 layers)	(30 layers)	(30 layers)	(30 layers)
Max. board temp. (°C)	-	-	-	125	155	170	-	-	-
I/O per MCM	-	-	-	-	-	-	3,000	6,000	10,000

Table 2-1 Electronic packaging requirements in consumer products, automotive electronics and high-performance systems (MCM – multi chip module) [Tummala et al, 1997]
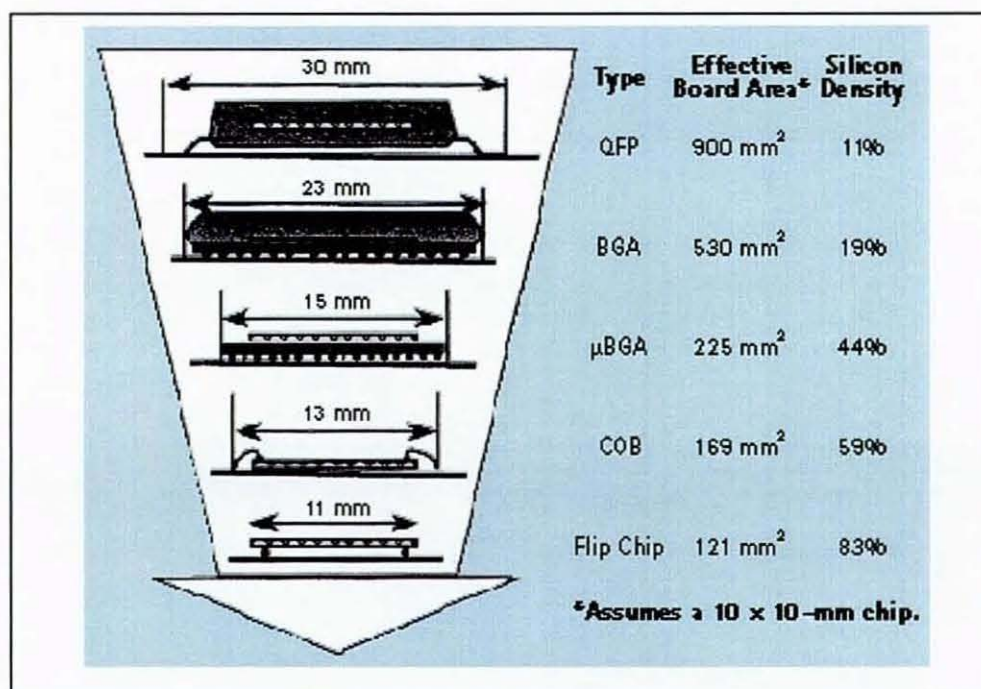
Figure 2-2 Packaging miniaturisation provides increased functionality per unit area [Brathwaite et al, 1997]

Chip interconnection
Wire bond (WB) → TAB → FC

Packaging interconnection
PTH → SMT → Fine-pitch SMT → BGA SMT → CSP SMT

Single-chip
DIP → QFP → Thin QFP (TQFP) → BGA → CSP

Multi-chip
Ceramic → Thin-film → Think-film on PCB/ceramic → Single-level integrated module (SLIM)

Table 2-2 Packaging technology evolution [Tummala et al, 1997]

2.2.2.   *Thermoplastic vs. Thermosetting Polymeric Packaging*

In the production of electronic components, such as ICs, active and passive components, the current, conventional approaches mostly employ potting or transfer moulding. Thermosetting (TS) compounds, such polyester, polyimide and epoxy resins are commonly used in these packaging processes. Further down the packaging scales at board-level packaging, current methods in the industry are based on potting, glob-topping, dam-and-fill, and sprayed or dipped conformal coating.

The advantages of thermoplastic (TP) injection moulding over TS potting packaging are briefly listed below:

- Injection moulding is suitable for mass production because the raw material can be converted to a finished part in one operation without the need for premixing of material components, i.e. continuous path from moulding compound to finished part.

- TP resins are supplied in the form of dust-free pellets and, unlike many liquid and solid TS materials, TP resins release only negligible amounts of volatile organic compounds during processing due to lesser extent of chemical reactions. This protects the product against the ionic contamination risks.

- Cost-efficiency, such as profitability, is heavily influenced by the output of parts per unit time. In injection moulding, this output rate depends heavily on the length of time required for the moulded part to cool within the mould and, as the cooling time increases/decreases as a square of the wall thickness, the wall thickness of the part plays the vital role. TP usually have cooling time of less than 1 minute, in comparison to TS which may take up to 30 minutes. However, it is rarely economical to produce injection moulded parts with thicknesses greater than 8mm.

- Short cycle time (elapsed time between discharges of two consecutive finished parts) on the production floor as plasticising time, curing time of TP are greatly reduced with greater machine efficiency as compared to TS. The moulded parts produced are also of higher reproducibility.

- TP injection moulding offers waste reduction – epoxy resins used in transfer moulding are not reusable after being moulded. It is said that the material utilisation ratio for epoxy resins is usually 30-50 wt-% due to the large amount of unrecyclable runner and sprue parts during transfer moulding process. On the other hand, TP may be re-melted for any product rework and eventually recycled at the end of operating life.

- The use of TP also allows the elimination of volatile organic compounds (VOCs) that are generated during potting or encapsulation of thermosetting materials.

On the other hand, whereas TP injection moulding may have the advantages over TS applications, the technology proposed in this research aims to develop a hybrid polymeric packaging process in order to produce larger plastic components/modules with electronic assemblies fully encapsulated within the structural bodies.

2.2.3.   Moulded Interconnect Devices (MID)

A polymeric packaging technology that may be closely related to injection moulding is moulded interconnect devices (MID), which was first introduced in the mid1980s and can be defined as a selective metal plating process of injection moulded parts to form 3-dimensional circuit patterns [Zippman, 1999]. In general, the production of MIDs employs four main methods [Housden et al, 2002]:

a) Single-shot injection moulding

This comprises of: injection moulding of plateable TP substrate – electroless plating of conductive copper layer – coating of photosensitive resist – exposure to UV through a photomask – metal electroplating with tin/lead or nickel/gold – resist removal and metal etching – population and soldering/bonding of components.

b) Two-shot moulding

Involves the following procedures: injection moulding of non-catalysed TP base – injection moulding of a plateable catalysed resin – chemical adhesion promotion – plating processes as in single-shot technique (above).

c) In-mould lamination

This uses a thermoformed flexible circuit which is inserted into an injection mould and the polymer injected behind the flexible carrier, forcing it against the outer surfaces of the mould and becomes an integral part of the plastic upon solidification. Electronic components are then populated.

d) Hotstamping

A flexible copper foil coated with adhesive is embossed onto a pre-moulded plastic substrate using a heated die and followed by population with electronic components.

Due to their 3-dimensional surfaces, placement of electronic components on MIDs is a complicated task, such that programmable automatic machines and robotic arms with an

extensive range of motions are required [Feldmann et al, 1996][Zussman, 1999]. Because components attachment using solders or conductive adhesives are performed at high temperatures on polymeric surfaces, higher temperature plastic resins, which are normally more expensive, must be used. Also, thermal expansion of most polymers is significantly greater than most metals, which may cause detachment of electroplated conductors if excessive heat input occurs during soldering [Housden et al, 2002]. In terms of manufacturability, the cost for the processes involved in production of MIDs is considerably higher than for standard circuitry, and therefore they are only selectively used in high-end products such as mobile telephones, portable computers and light fitting holders in automotives [Mapleston, 2000].

Another major limitation of MID is low circuit density because the technology is not capable of replicating layered circuitry or using embedded components [Yee, 2000]. A MID circuit has maximum two layers (top and bottom surfaces) of available populating areas, compared to standard rigid circuitry which can offer multi-layer interconnections (as many as 32 layers) and embedded passives. Currently, MIDs are mostly limited to applications with surface mounting components because the integration of higher density devices, such as wirebonding of chip-on-board or bonding of flip-chips (FCs), on the 3D polymeric surface is extremely difficult.

The encapsulation approach in this research seeks to establish a comparable, if not improved, alternative to MID, especially in comparison with the in-mould lamination technique. A brief comparison of the two packaging methods can be summarised in Table 2-3 below. It must, however, be recognised that the 2-shot moulding used in MID has the advantage of a higher degree of 3-dimensional density potential than plastic overmoulding, as the flexibility of the latter is limited to where substrate can be located. Figure 2-3 shows a number of sample MID components found today.

Plastic Overmoulding	MIDs
Standard substrate-based assembly followed by conventional polymer injection moulding. Moulding tool uncomplicated.	Complicated manufacture: special plateable resin and 2-component moulding tool needed for 2-shot moulding, thermoformed polymer thick film and metallisation for in-mould lamination.
Electronic component placement easily done.	Special equipment required for solder printing and SM component placing (e.g. Cartesian robotic arm [Krimi, 1998]).
Altering of product or circuit designs require only changes to mould tool.	Any design changes affect more complex reconfigurations to mould tool, 3D metallisation equipment and component placement machines.
Lower production cost – uses conventional technologies	High production cost due to design and manufacturing complexities.
Offers good protection from environmental hazards	Less protection for the electronics

Table 2-3. Comparisons between plastic overmoulding and MIDs
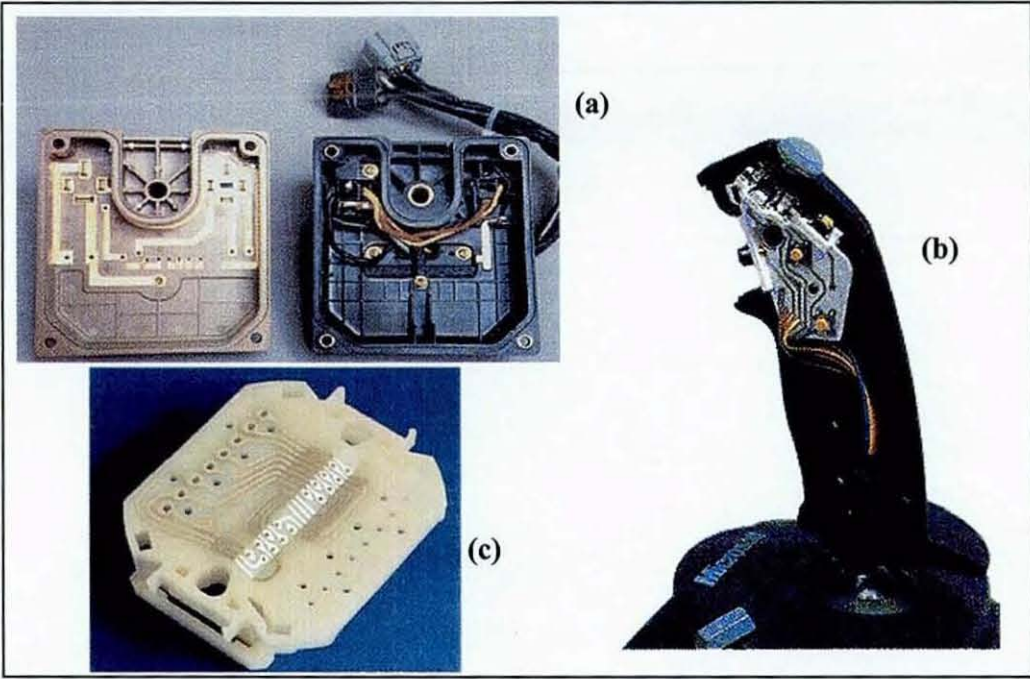
Figure 2-3 Examples of MID products: (a) automotive brake light holder [Yee, 2000], (b) circuit inside a joystick handle [Yee, 2000], (c) an ISDN plug produced from heat-embossing [Bayer Plastics, 2004]

2.3.   Thermoplastic Injection Overmoulding

Injection overmoulding can be conventionally defined as "a technique in which a preform produced in the initial injection phase is transferred to a second cavity in the same mould into which a second material is moulded onto or around the preform." [Stevenson, 1996]. While the term "overmoulding" is also widely used to describe complete embodiment of preforms or inserts in transfer moulding or potting processes using TS materials such as epoxy and polyurethane, it is important to emphasise that this research focuses on the development with injection overmoulding of TP polymers. This technology is categorised as one of the multi-material moulding techniques which now accounts for a growing array of plastic components worldwide and has expanded the capabilities of injection moulding to incorporate multiple materials in a single part and afford the design freedom to integrate application specific performance in multifunctional components. In addition to the design flexibility, the selective use of materials and processes to provide differential performance in localised areas of a plastic component provides significant enhancement in component performance, quality and cost control.

Currently, the TP overmoulding process has a broad usage in the manufacture of many mechanical and a number of electrical components. Among its most popular mechanical applications are in fusible-core technology which enables hollow core (usually cast in a low-melting point alloy) to be moulded as unified components in plastics, composites and rubbers. The core is melted out when the overmould has cured. Aircraft ducting, control cabinets and honeycomb structures are made in composites using this process [Morgan, 1997]. Elastomers are often overmoulded over handheld devices and appliances in order to provide non-slip elastic grip, mechanical shielding, product propriety protection or added cosmetic features. Among these products are included kitchen utensil handles, mobile phones, portable computer peripherals, handheld medical equipment, automotive structural parts and weaponry. One such example can be found in Figure 2-4(c), which is an overmoulded brake system for vehicles [Creative Storage Systems, 2001].

In the production of electrical parts, applications in which TP overmoulding has been developed may include solenoid and coil encapsulation to improve physical and electrical insulation [Patterson, 1992]. Figure 2-4(a) shows a cross-section through a transformer encapsulated with two layers of insulating polymer [DuPont, 1996], while Figure 2-4(b) shows an example of the overmoulded coil [DKC Corporation, 2004] [Hanrahan et al, 2002].

Figure 2-4(d) shows examples of overmoulded connectors [[Burk, 2000]. This approach has given the industry advantages such as reduced cost and tooling time, improved strain relief for cable exit, increased durability and resistance to shock, as well as cosmetic alternatives [Burk, 2001].
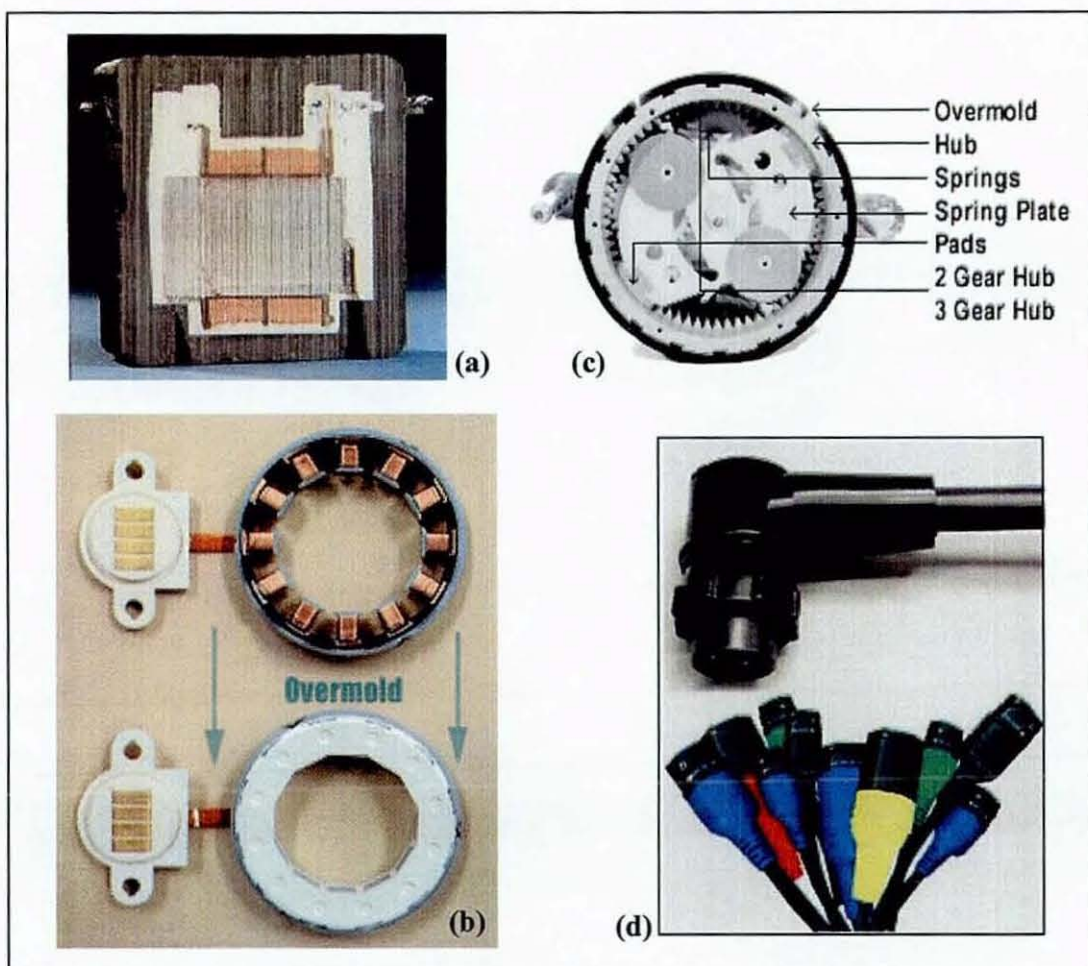
Figure 2-4 Example of applications of TP overmoulding: (a) overmoulded transformer [DuPont, 1996]; (b) coil [DKC Corporation, 2004] (c) brake system [Creative Storage Systems, 2001]; (d) electrical connectors [Burk, 2000]

It is therefore the primary objective of current research to further exploit and advance the TP injection overmoulding process to develop a cost-efficient manufacturing platform for a single-cycle direct-encapsulation of an electronic assembly within thermoplastic structures. Suffice to note that amongst the biggest underlying issues which must be addressed are the minimisation of thermomechanical stresses during overmoulding and the compatibility of material properties during overmoulding as well as in-service conditions. While combining

several materials in a single part, these materials must be optimised to somehow display the least thermomechanical disparity with each other. The differences in rheological and physical properties of adjoining materials are critical elements in this process, and serious mismatch may exacerbate adverse results. Section 2.7 identifies some of the potential problems which may be associated with direct overmoulding of electronics.

2.4. Overview of Automotive Electronics

Automotive electronic systems started to appear in significant volumes to replace electrical systems during the 1960s, with voltage regulators and ignition controls among the first popular applications. However, over the past two decades, legislative requirements, market-driven competition and customer demands have brought an even more dramatic increase in the incorporation of electronics within vehicles to replace many traditional mechanical or electrical systems. The growth in the electronic content of a vehicle has seen an explosive rise from an average of US$78 in 1980 to US$861 in 1990 and increasing to US$1,495 by 1998 [Yanik, 1998][Harkness, 1995]. This corresponds to an increase in the average electronic cost per vehicle from 13% (1980s) to 17% (1990s) and is forecast to break into the +20% range in the current decade with the addition of more software. In top-of-the-range cars, the electronic content can amount to 35% of the total vehicle cost [Frank et al, 1998]. Latest analysis projects a 13.4% growth for automotive electronics to reach US$25.4b by 2003 [Brancato, 2000] with primary adoptions to improve safety, emission, engine management, navigation, manoeuvrability and comfort. Table 2-4 provides an overview on the value and annual growth of electronics in the broad functional categories of the industry over the 1994-98 periods [Harkness, 1995]. Many of these features, such as fuel injection, ABS, airbag, electronic gearbox, and a security system have now become standard in many cars.

As discussed in Chapter 1, microprocessors are widely used to control an increasing number of electronic subsystems linked by bus protocols within a vehicle. This has led to the development of multiplexing concepts such as Controller Area Network (CAN), Vehicle Area Network (VAN) and the American SAE J1850 bus protocols [Kiencke et al, 1996] as a means of providing better data exchange and systems control with reduced harness costs. The J1850 and CAN bus architectures are illustrated by simplified block diagrams in Figure 2-5 [Bannatyne et al, 1997] and Figure 2-6, respectively. However, multiplexed controls have led to increases in system integration, advanced capabilities and complexities in electronics. Such

systems have therefore placed high demands on the automotive manufacturing sector to meet growing requirements, cost and complexity [Bannatyne, 2000].

Application	Million US$		Annual growth (%)
	1994	1998	
Engine management systems	2,936.1	4,194.4	9.33
ABS and traction control	779.0	1,401.8	15.82
Vehicle dynamics control	30.0	87.8	30.82
Airbag systems	395.5	919.8	23.49
Active suspension systems	119.8	351.0	30.82
Electronic gearbox	179.8	403.4	22.39
Electronic display	299.6	511.2	14.29
Navigational systems	659.1	1,930.5	30.82
Security systems	305.6	448.0	10.04
Servicing systems	239.7	464.7	18.00
Multiplexing	329.6	576.4	15.00
Total	*6,273.6*	*11,288.9*	*15.82*

Table 2-4 Growth of automotive electronics between 1994-98 [Harkness, 1995] [Yanik, 1998]
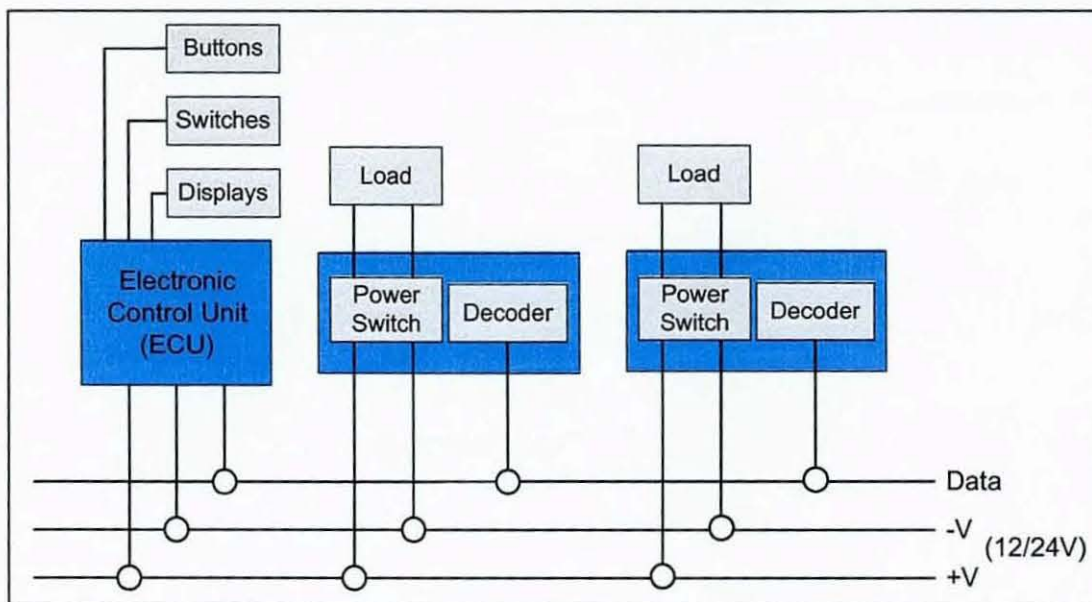
Figure 2-5 Simplified block diagram of the SAE-J1850 bus system [Bannatyne et al, 1997]
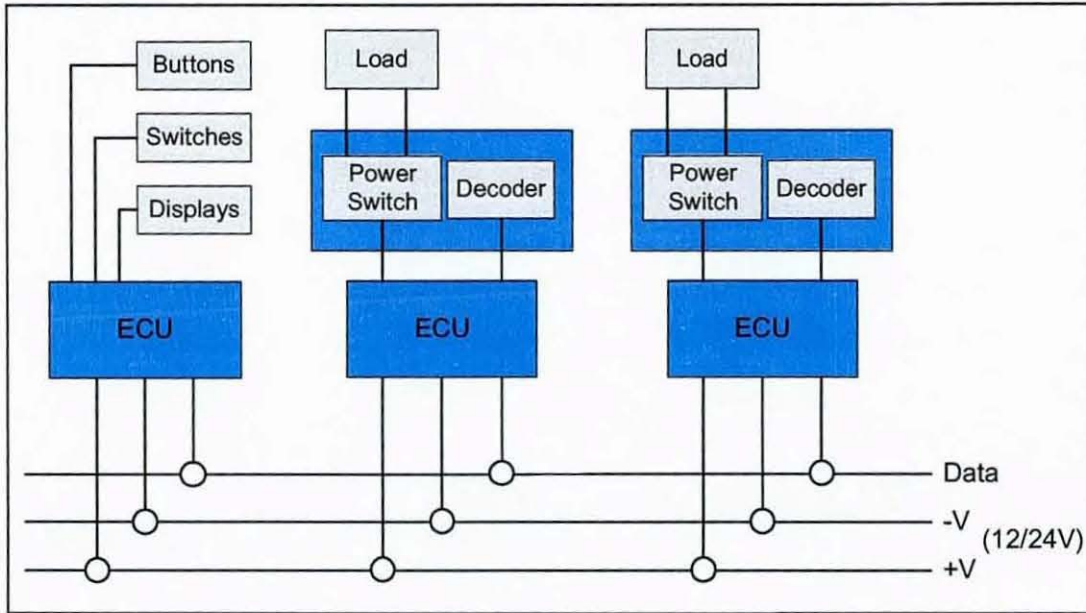
Figure 2-6 Simplified block diagram of a CAN bus system

Over their lifetime, failures in automotive electronics may be caused by different mechanisms. Table 2-5 gives an outline of the primary stress factors which may lead to failures on various sites of an electronic system [Wondrak et al, 1999]. These stress factors have significant effects on reliability issues and they can be distinguished into operating requirements (voltage, current density, power losses, operating temperature) and environmental conditions (ambient temperature, shock, vibration, humidity). In order to assure a certain level of reliability and quality, qualification testing for electrical, mechanical and environmental conditions of these devices has been initiated by the AEC and JEDEC. These tests may comprise of thermal cycling, power cycling, temperature-humidity bias, vibration and mechanical shock.

Failure Site	Stress Factor
Device Level	
Oxide	Voltage
Passivation system	Current density
Metallisation	Operating temperature
	Temperature
Package Level	
Moulding material	Humidity
Die attach	Current
Bonds	Temperature
	Chip size
	Operating temperature
	Vibration
Board Level	
Substrate	Humidity
Solder joints	Vibration
Bond	Temperature
Connector	Operating temperature
	Vibration

Table 2-5 Stress factors for related failure sites in automotive electronics [Wondrak et al, 1999]

2.5.   Injection Overmoulding for Direct Electronic Encapsulation

The proposed technology adapted conventional technologies of injection moulding and rigid printed circuit boards (PCBs) assembly in order to achieve cost efficiency. Figure 2-7 illustrates a PCB populated with SM components and I/O connectors positioned on the fixed-half of a mould. The moving-half of the mould closes and molten plastic injected into the mould cavity, thus completely encapsulating the assembly.

An illustration of this process can be seen in Figure 2-8. A rigid circuit, with a prospective of using a standard PCB material such as FR4, and populated with components of a variety of sizes and interconnections, is demonstrated in Figure 2-8(a). Figure 2-8(b) shows the resulting plastic module encapsulating the circuitry, which may be moulded with external structures that enables it to be readily fitted into larger or existing parts. On the other hand, Figure 2-9 shows an example of a circuit mounted in a conventional plastic housing

commonly found in automotive applications today. More importantly, with the automotive electronic industry gearing towards higher complexity subsystems with more sophisticated functions and envisaging the use of HDI components (through direct chip bonding such as flip-chips and BGAs) [Ward et al, 2000] in the foreseeable future, the use of rigid PCB-based circuitry will offer the flexibility to accommodate such capabilities. Such developments will also require more stringent test schemes to meet the JEDEC and AEC qualification standards. This would be considerably more difficult to implement using the MID platforms.
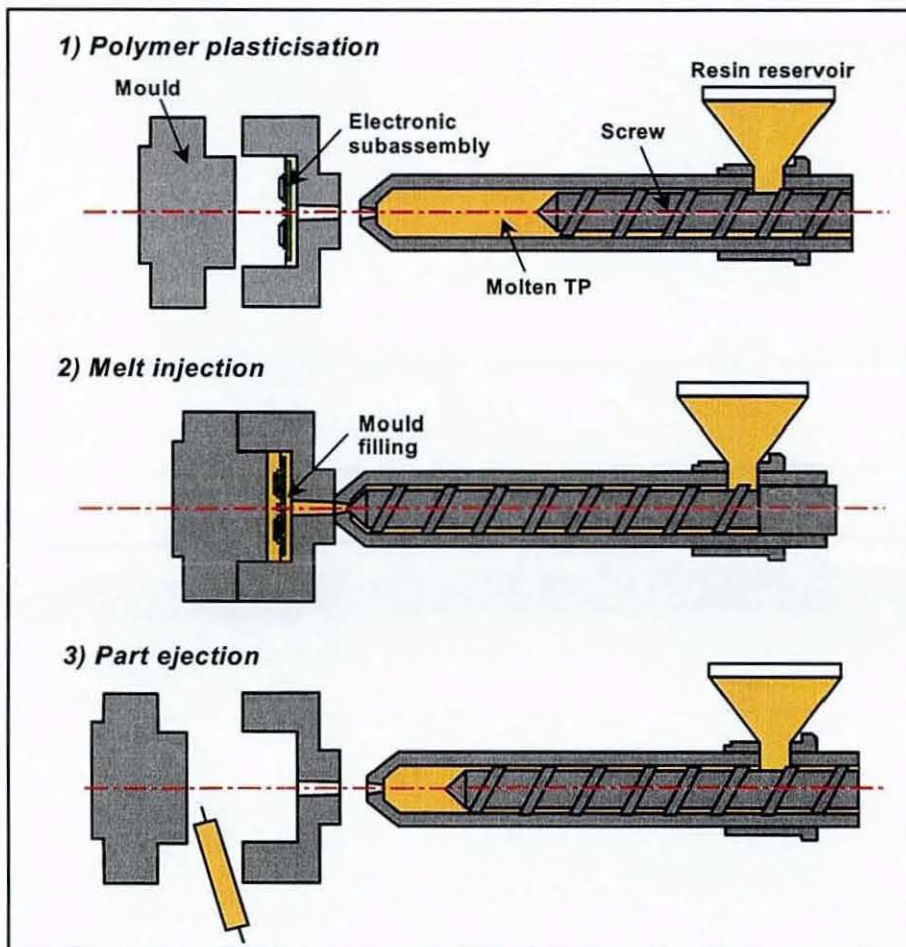
Figure 2-7 Schematic of electronic overmoulding using a conventional injection moulding machine
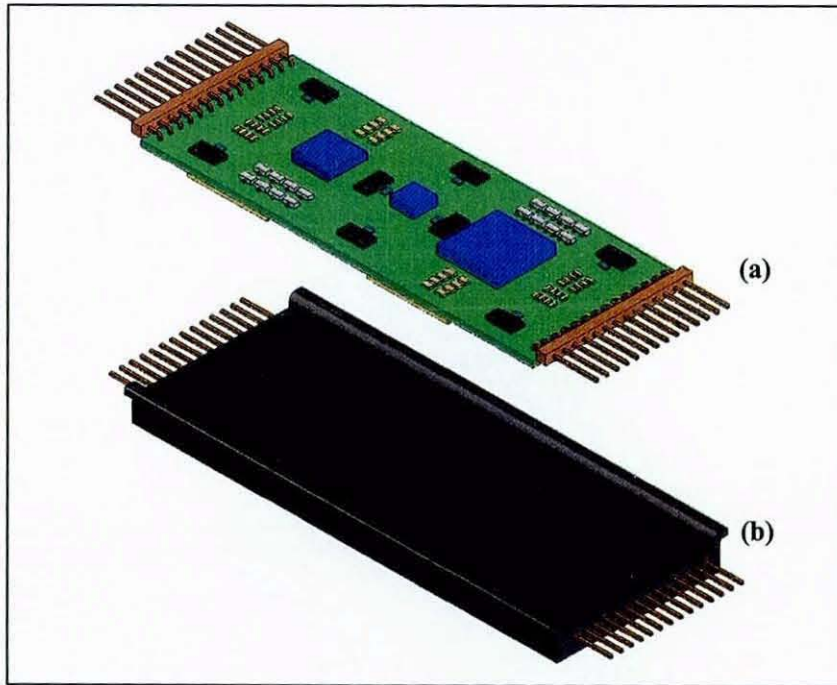
Figure 2-8 An overmoulded electronic module: (a) standard rigid circuitry (b) resultant overmoulded module, with configurable external geometry
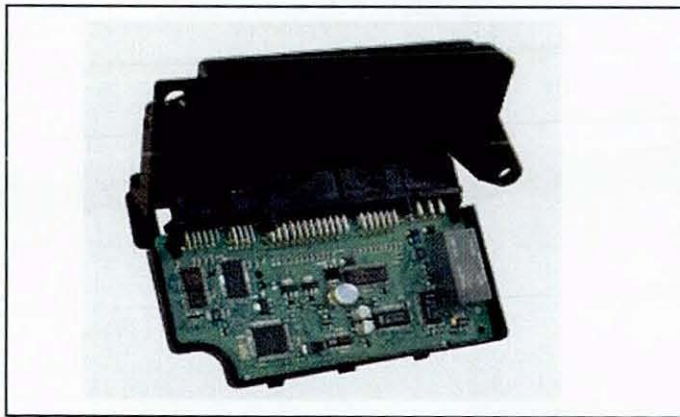
Figure 2-9 Conventional circuit mounted in a plastic housing

In terms of the electronic packaging hierarchy, the direct embedding of an electronic assembly into a polymeric structure can be identified as an alternative route to achieve combinational board-system level packaging. As illustrated in Figure 2-10, the single-cycle overmoulding process enables an electronic subsystem to be directly integrated into a plastic structure, hence simplifying the conventional system-level packaging with improved robustness. Also, due to its ability to accommodate standard PCB technologies (as compared to MID), the process allows the use of double-sided, multi-layer substrates with embedded

passives for increased functionality. Because the overmoulding polymer is capable of packaging the silicon chips to provide the additional ruggedness against adverse factors (e.g. thermal delamination, mechanical vibration and chemical contamination), it allows the incorporation of direct-chip-attach (DCA) interconnections such as COB and FC with glob-top coating.

Engineering thermoplastics have experienced accelerated progress in mechanical, chemical and fabrication processes over the last few decades and feature strongly in today's industries because they offer geometrical design flexibility, weight reduction, lower cost and the ability to survive in exigent automotive environments. Injection moulding is a cyclic process of forming plastic into a pre-determined shape by forcing the plasticized or molten polymer resin under pressure (injection pressure) into a specially shaped cavity (mould). The melt solidifies within the mould, which is then opened to remove/eject the part after a fixed cooling period (time). The quality and repeatability of moulded parts are principally governed by a set of key process parameters: temperature (melt, mould), time (injection, holding), pressure (injection, holding), speed (injection), moulding tool design, injection gate position and geometry. The interrelationship of these factors have significant influences on both in- and post-mould reactions of the plastic module and as such any design flaw may result in undesirable distortions such as thermal shrinkage, warpage, under-strength weld lines, sinks or voids in the final product.

For the success of direct electronic encapsulation, a number of critical factors must be addressed. Firstly, the technology must produce a single-cycle embedding process which can be controlled in order to avoid thermomechanical damage to the embedded electronics. The injection parameters play the most vital role in determining the rheology of the non-Newtonian molten polymer entering the mould cavity, subsequently wrapping around the electronics. The melt's temperature, viscosity and velocity develop thermal and mechanical (thermomechanical) stresses that may weaken the structural integrity of the circuit board, components and interconnectivity, as well as adversely affect the functionality and reliability of the assembly. This may be minimised through careful control and optimisation of the main processing temperatures, pressures and times. The design of moulding tool layout may also have a significant role in this process.

The interaction between the polymer and embedded subassembly at adjoining interfaces is another critical area of great importance. This must be investigated, particularly from the perspective of any consequent effects of the polymer on the PCB. The mismatch of material properties may produce disproportionate thermal shrinkages between the overmould and embedded elements, leading to undesired mechanical distortion and electrical breakdown to the embedded assembly.

In order to realise the manufacturability of the proposed encapsulation technique, it is therefore critical that *both* the optimum moulding parameters and materials matching criteria are achieved. In terms of the material selection, this must address the choice for both thermal processing on assembly and the function of the assembly; whereas the development of process and tooling layout must endeavour to overcome the material rheology causing unacceptable thermomechanical forces imparting on the embedded electronics.
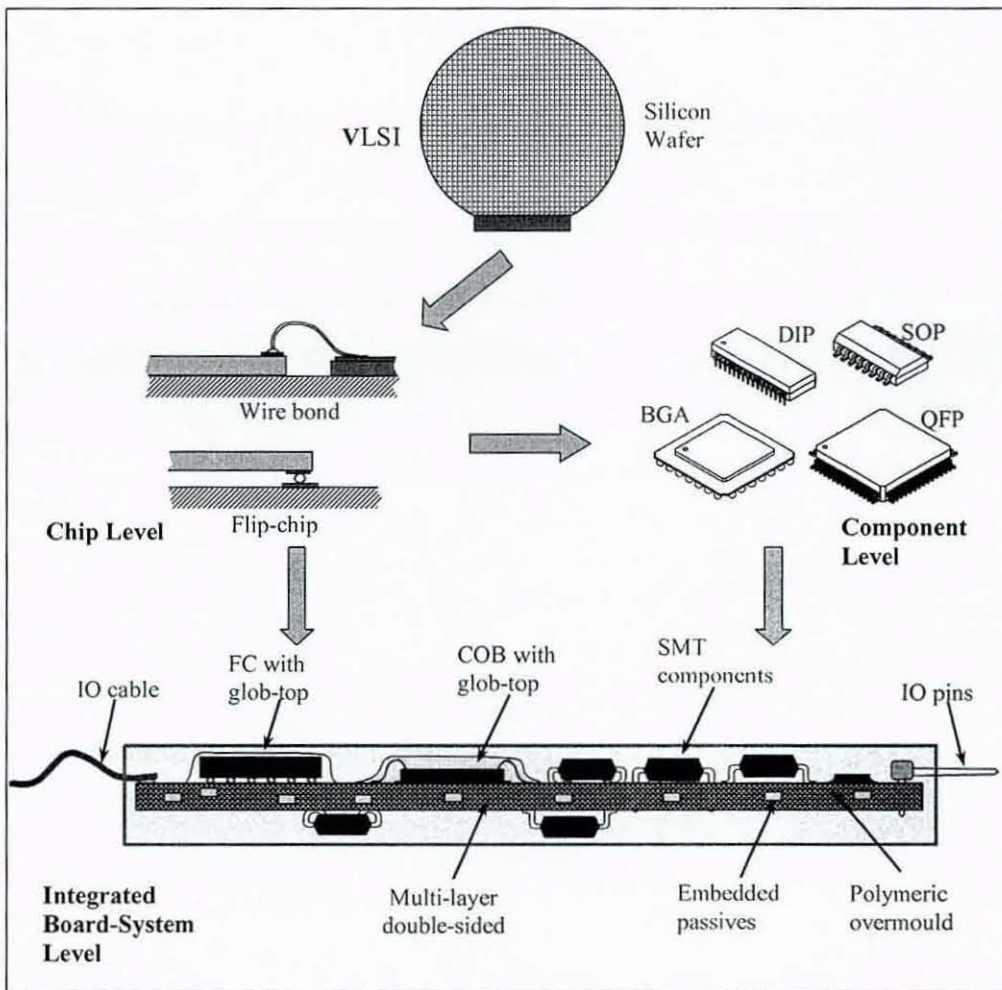
Figure 2-10 Implementation of hybrid board-system in electronic packaging hierarchy through direct polymeric overmoulding

2.6. Advantages of Thermoplastic-Overmoulded Electronics

The previous sections have focused on the objectives and technological challenges in the automotive sector. Such technology can also be integrated into other industries with applications that necessitate operation of electronics in hazardous conditions. The following sections outline the advantages anticipated from the resulting technology essentially that may be pertinent to other fields.

2.6.1. Improved Mechanical Ruggedness

Provided complete adhesion is achieved at the plastic-to-interconnect interfaces and halides are not present in the moulding compound (since moisture in the absence of a reactive contaminant will not cause corrosion), embedding the electronics within plastic will also minimise/eliminate moisture ingress that causes ionic contamination to electrical interconnections. This will reduce operating failure rates and thus enable a prolonged lifecycle to electronic systems.

2.6.2. Lower Manufacturing/Assembly Costs

The reduction of electronic component count and wiring loom achieved through the intelligent integration of several subsystems within a single structural moulding will reduce overall product complexity, thus enabling the manufacture of ready-to-assemble, reconfigurable electronic modules at more economical costs. Also, the overmoulding is implemented in the standard injection moulding machines, which means that manufacturers will not have to replace existing shop floor setup. The single-cycle process will eliminate the extra workload involved in mounting the electronic system into its housing as well as the sealant curing time. Also, by embedding the electronics inside a polymer part, it will increase its handleability and reduce defects on the assembly line. This will in turn reduce time and costs to enable a leaner and more efficient assembly.

2.6.3. Reduced Package Size

The overall functionality of the structural mouldings may be increased through further mechatronic integrations of circuitry, sensors and actuators. Within larger plastic trims, multiple units of circuits may be embedded, linked with each other through flexible or flat cables. Additional packaging is therefore eliminated, ensuring minimum space is utilised. Also, further reduction in the module dimensions may be achieved with the adaptation of

flexible PCB substrates that can be mechanically or thermally folded to reduce its effective cross-sectional area within the plastic module.

2.6.4. Improved Systems Robustness/Reliability

The subsystems integrated within a single structural moulding will reduce the number of interconnections compared with long conventional wiring or flexible strips and this reduction will increase reliability and robustness. Additional mechanical strength provided by the overmoulding plastic will also increase the lifespan of the electronics.

2.6.5. Platform for Emerging Electronic Technologies

Improvements in system robustness, reliability, life and size provided by the technology, will enable the use of electronics in other potential applications, such as in the more hazardous and exposed spaces of a car (wheel arch, engine bay etc.). The extra buffering and structural integrity can also enable the use of new technologies such as chip-on-board (COBs), ball grid arrays (BGAs), flip-chip and multi-chip modules (MCMs) in the automotive industry.

2.6.6. Increased Recyclability Potential

Unlike thermosetting compounds, such as epoxy resin used in the transfer moulding of packaged electronics, the thermoplastic (TP) materials used in this process can be recycled at the end of the product life. Figure 2-11 demonstrates a feasible recycling scheme for overmoulded electronic products. The recycling of populated PCBs has been established successfully [Yokoyama et al, 1995] [Yokoyama et al, 1998] where the resultant produce of copper-rich and glass-fibre resin powders can be used as re-material compounds and polymer fillers respectively. The recycled thermoplastic can be proportionally blended with virgin resin and used for domestic and commercially lower-grade plastic products.
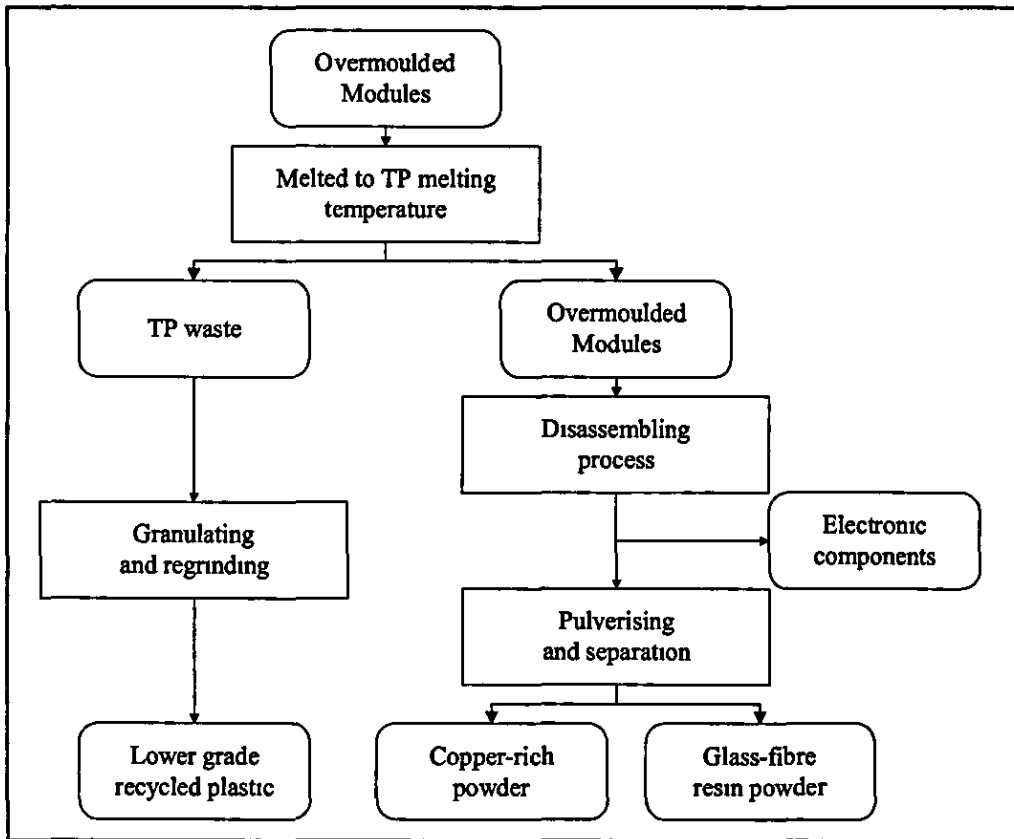
Figure 2-11 Recycling process for the over-moulded electronic module

2.7.   Problem Statement

The manufacture of the suggested plastic packaged electronic product requires not just in-depth knowledge in the fields of electronics, material and process, but also good understanding of the interrelated physical and chemical reactions. Because standard injection moulding occurs in elevated conditions at high temperatures (200-320 °C), pressures (30-120 MPa), viscosity (an attribute of TP) and velocity (over 50 mm/s), it imparts extreme thermal and mechanical stresses on the embedded assembly. Process design, including tooling layout and injection parameters, have to be optimised without compromising the resultant product reliability.

As the injected plastic experiences shrinkage cooling in the mould and post-ejection residual shrinkage, the encapsulated assembly can be subjected to localised strains leading to implacable distortions, joint fatigue, wire sweep, component cracking and substrate warpage (see Section 2.8). This problem may be minimised by reducing the disparity in the linear CTEs between the overmoulding polymer and the embedded subassembly through an

optimised injection process. The compatibility of materials is also vital to obtaining good interface adhesion to prevent delamination-induced moisture ingress. The following sections discuss some of the physical mechanisms which must be taken into consideration in overmoulding electronics.

2.7.1. Thermal Expansion and Resulting Stresses

2.7.1.1. Coefficient of Thermal Expansions

Almost all polymers expand when their temperature is raised and contract when cooled. The expansion or contraction of a material due to a temperature change in the absence of mechanical loads is called thermal strain (ϵ). Although the thermal strain is not exactly linear with temperature change, for first-order approximation over a temperature change, it is usually proportionate to the temperature change. This approximation is expressed in the coefficient of thermal expansion (CTE) of the material, which is defined as the change in length (ΔL) that a material sample of original length L_o undergoes over a certain temperature range (ΔT), i.e.:

$$\frac{\Delta L}{L_o} \approx \alpha.\Delta T \qquad \text{(Eqn. 2-1)}$$

where α is the defined linear CTE of the material in ppm/°C. It is important to ensure that the maximum tensile strength of the material is not exceeded by the temperature excursions. The CTE value in most polymers is a function of temperature, i.e. it may expand slightly with an increase in its temperature. The CTE is a critical parameter when dimensional stability of a material over different temperature ranges is important. This can be particularly crucial at the interface between two different materials.

2.7.1.2. Formulation of Shrinkage Stresses

Shrinkage stresses in moulded plastic packages result from polymerisation and the disparities in the CTE among the various materials which are in intimate contact. The following relationships can be used to calculate the magnitude of the thermal shrinkage stresses, σ, as the package goes through a thermal excursion from T_1 to T_2 [Pecht et al, 1995]:

$$\sigma = c_5 \int_{T_1}^{T_2} \frac{\left| \alpha_p(T) - \alpha_i \right|}{\dfrac{1}{E_p(T)} - \dfrac{1}{E_i}} dT \qquad \text{(Eqn. 2-2)}$$

where α is the temperature-dependent CTE, E is the Young's modulus of elasticity, c_5 is a design dependent geometric constant, the subscript *p* refers to the moulding polymer and the subscript *i* refers to the electronic insert. Since $1/E_i \ll 1/E_p$, α_p and E_p can be replaced with single values for the glassy region denoted by subscript *g* (up to T_g). Also, since the encapsulant is compliant above the T_g, the above integral can be approximated by:

$$\sigma^* \approx \left(\alpha_{pg} - \alpha_i\right) E_{pg}\left(T_g - T_l\right)$$
(Eqn. 2-3)

to provide the stress parameter σ^*.

The stress, σ, or the stress parameter, σ^*, is only a crude approximation of the stress level in the material and does not account for the stress concentration points or other geometric and interfacial features that influence delamination, bending or cracking. The thermo-mechanical property values needed for σ or σ^* calculation are normally provided by suppliers. The more commonly used simple equation for the calculation of thermal stresses is known as Hooke's Law:

$$\sigma \approx E\left(\alpha_1 - \alpha_2\right)\Delta T$$
(Eqn. 2-4)

where $\Delta T = T_1 - T_2$

2.7.1.3. *Residual Thermal Stress*

During the overmoulding process, when the polymer cool from glass transition temperature (T_g) to room temperature, a thermal mismatch can cause residual stress to be moulded into the structure. Due to a larger CTE in the PCB substrate, the polymer will be in a compressive stress state upon cooling to its ambient temperature (T_a) and this residual thermal stress (σ_{res}) may be derived from Eqn 2.2 above and be given by [Muraki et al, 2002]:

$$\sigma_{res} = E_p \int_{T_g}^{T_a} \left[\alpha_p(T) - \alpha_m(T)\right] dT$$
(Eqn. 2-5)

where $\alpha_p(T)$ = temperature function of CTE for the overmoulding plastic (ppm/°C)

        $\alpha_m(T)$ = temperature function of CTE for the embedded element (ppm/°C)

Therefore, σ_{res} in the polymer at the interface with the substrate induced during the cooling time, is a function of its Young's modulus, the disparity of CTEs and the CTE difference between at T_g and T_a [Muraki et al, 2002].

Reinforced polymers may display differing degrees of thermal expansion in the flow and cross-flow directions [Stevenson, 1996]. For example, when a glass-reinforced material is processed, the glass fibre will align in the direction of material flow. When this occurs, the material will display a lower CTE in the flow direction than the transverse direction because of the reinforcing effect of the glass fibre. To achieve uniform thermal expansion in both the directions, mineral fillers are often used. Even when this is done, the expansion in the third axis (Z-axis expansion) can vary significantly from that in the other two axes.

2.7.1.4. *Thermal Stress from Temperature Excursion*

When the temperature varies during operation for an overmoulded component, materials with different CTE values will experience different degrees of dimensional changes. These non-uniform variations will induce internal tensile and/or compressive stress within the structures and, if unrestricted, may even lead to failures. Therefore, when forming a rigid attachment interface with more than one material, the materials selected should have CTE values as close as possible. The thermal stress (σ_{th}) caused by differences in CTEs experienced by an element overmoulded inside a plastic material can be derived from Eqn. 2.4 to give [Rubin, 1972]:

$$\sigma_{th} = E_p (\alpha_p - \alpha_m) \Delta T \qquad \text{(Eqn. 2-6)}$$

where α_p = linear CTE of the overmoulding plastic (ppm/°C)

       α_m = linear CTE of the moulded element (ppm/°C)

Subsequently, the thermal strain (ε_{th}) from the corresponding stress may be found from the relationship of [Lin et al, 1997]:

$$\varepsilon_{th} = (\alpha_p - \alpha_m) \Delta T \qquad \text{(Eqn. 2-7)}$$

2.7.2. *Geometrical Differential Shrinkage*

Differential shrinkage is another issue that must be addressed in the design stage of multi-material moulding processes. In general, such shrinkage is the difference between the dimensions of a fabricated part at mould release and the cooled part. The degree of shrinkage largely depends on the types of polymer, the filler materials and part geometries. The type and amount of filler, such as reinforcement, can significantly reduce shrinkage and tolerances. Climatic conditions such as temperature and humidity, which the product will experience in

service, as well as conditions of storage, can also affect the shrinkage of a material [Rosato, 1995].

In an overmoulded component, dissimilar materials and different section thickness will have different amounts of shrinkage, resulting in warping deformation to the part. Complex part designs typically have sections of different thickness. The thinner sections cool rapidly in the mould during moulding and are close to their final dimensions upon ejection. Thick sections of the same component, however, will be significantly hotter at ejection and continue to cool and contract after the adjacent thinner sections have reached thermal and dimensional equilibrium. As a result of this differential shrinkage, the part distorts to accommodate for its non-uniform physical construction. The behaviour also occurs when adjacent sections are of materials with substantial difference in CTE values, as discussed above.

2.7.3. Materials Adhesion

Another important issue in multi-material injection moulding is the adhesion between the adjoining materials of the components. Whilst the deformations resulting from CTE or shrinkage differences may be theoretically predicted, we actually have to assume a perfect bonding between the materials at their interface. Therefore, before these issues can be predicted and managed, the formation of adhesion between two co-processed materials must be understood. Generally, adhesion between polymers may be expected to result from the mechanisms of [Stevenson, 1996]:

- *Chemical compatibility* of the polymers that results in adhesion due to the inter-diffusion of polymers and molecular attractions, and,
- *Mechanical bonding* between the materials as the results from glass entanglement, material entanglement due to mixing of polymer melts, or intentional interlocking design of different materials.

2.7.4. Heat Transfer, Moisture Diffusion and Hygrothermal Stresses

With the electronics fully packaged within the polymer body, due consideration must be given to its heat distribution capability. *Heat conduction* within the polymeric package is governed by the following equation [Lin et al, 1997]:

$$\frac{\partial T}{\partial t} = k\frac{\partial^2 T}{\partial x^2} + k\frac{\partial^2 T}{\partial y^2} \qquad\qquad \textbf{(Eqn. 2-8)}$$

where k is the thermal conductivity (in W/m-°C), t is the time (in seconds) and x, y the Cartesian coordinates. As a rule of thumb, k for the overmoulding material must be as high as possible to provide a good heat dissipation path for the electronics.

The *transient diffusion of moisture* within the package encapsulant is assumed to obey Fick's Law and be governed by the following equation:

$$\frac{\partial C}{\partial \tau} = D \frac{\partial^2 C}{\partial x^2} + D \frac{\partial^2 C}{\partial y^2}$$
(Eqn. 2-9)

where D is the coefficient of moisture diffusion and C the moisture concentration. As D is a function of the temperature T, the computations of the moisture diffusion and heat transfer should be carried out simultaneously.

The encapsulating polymer is assumed to be in a zero-stress state upon solidification at the curing temperature. When the temperature changes from this state, thermal stresses will be induced owing to different values of the CTEs of the constituent materials. The thermal strain is defined in Eqn. 2.7 above. As for the hygrostresses, these are developed when the plastic moulding compound swells due to the absorbed moisture. The relationship between hygrostrain (ε_{hy}), the moisture concentration (C) and the hygro-swelling coefficient (β) (unit ppm-wt.%) is:

$$\varepsilon_{hy} = \beta C$$
(Eqn. 2-10)

2.8.   Potential Electronic Failure Mechanisms

While the polymeric encapsulation will allow the operating of electronics in more severe applications and prolong the lifespan, the overmoulding process may incur high temperature and stresses on the embedded electronic assembly. The potential failure mechanisms for a standard PCB-based circuitry (with soldered, adhesive-bonded and/or wire-bonded components) are identified in this section. Consecutive overmoulding experiments have been undertaken in this research with the aim of avoiding or eliminating occurrences of such failures.

The direct contact of the high temperature, high viscosity of polymer melt during the overmoulding may produce a thermomechanical shock that has negative impacts on the

integrity of the embedded electronics, leading to failure problems. Firstly, for a circuit with solder and/or adhesive joints, the thermal stress and shear force can operate in tandem to cause shearing of these joints, manifesting solder cracking, joint deformation and subsequently displacement the components from their original pads. For circuits with wire-bonded COB (which is usually coated with a glob-top layer), the thermomechanical stresses can produce heat and/or compression stresses sufficient to deform the glop-top and cause undesirable movements and lift-off of the wirebonds. More serious forces may lead to misalignment of the silicon chip, cracking of its passivation layer or even complete fracture of the chip.

Popcorning is a phenomenon in which moisture trapped or absorbed with a packaged IC expands at high temperature and produces an internal hygrothermal pressure which leads to propagation of cracks [Gannamani, 1996]. The thermal shock from the molten polymer may induce this failure mechanism for surface mounted IC packages. It is also possible that the rigid PCB substrate may yield to the combined effect of heat and shear stress, resulting in physical distortion, particularly along the flow path of the melt. Such deformation will in turn transfer the physical stresses to the components and interconnection joints

The design of moulding tool must regulate the flow resistance around the embedded assembly; otherwise an uneven residual pressure distribution in the mould cavity may be produced during the uneven flow of molten plastic. Also, any severe CTE mismatch between the overmoulding polymer and substrate may contribute to the formation of differential pressure distribution. Warpage to the substrate may again set in as a result of these two problems and transfer thermomechanical fatigues to the electronics.

Because of the differential expansion or shrinkage between the polymer and the assembly, adhesion at the contacting interface may be weakened through cycling of temperature during its operation. The interfacial de-adhesion will allow permeation of water to occur in the presence of humidity and result in microcracking [Pecht et al, 1995] of the polymer body from swelling in high temperature. Moisture ingress into the electronics through hygrothermal diffusion will subsequently occur, promoting corrosion to the circuit conductor tracks and bond pad metallisation. With an applied DC field, moisture will set off ionic electromigration which forms dendritic growth between adjacent conductor tracks [Viswanadham et al, 1998], resulting in dielectric breakdown of the overmoulded electronics.

CHAPTER 3 . PRELIMINARY PROCESS SCREENING EXPERIMENTS

3.1. Introduction

This chapter introduces the process of electronic encapsulation with engineering thermoplastics. Through multi-phase empirical investigations, the customisation of conventional injection moulding in the overmoulding of electronic subassembly is demonstrated.

Whilst the first of these experiments was a *dummy trial* designed to investigate and identify a variety of process elements, it also demonstrated the strenuous demands placed upon the embedded subassembly by conventional plastic injection moulding. The findings from this trial were further examined in the following *exploration experiment* with various non-functional electronic combinations. Design of Experiment (DOE) was used in the latter experiment protocol, with statistical analysis of the results. The conclusions from these preliminary experiments produced the groundwork for the more focused studies.

3.2. Experimental Procedure

3.2.1. Preliminary Screening Experiment

At the outset, it was decided that a series of experimental investigations were required to identify technical challenges and establish optimum process conditions and techniques. To this end, dummy electronic assemblies were designed to explore a set of assembly variables that included the substrates, interconnection technologies and injection moulding parameters. The dummy specimens were then encapsulated in transparent ABS plastic (chosen for ease of investigation) under a range of moulding conditions.

The substrates included two grades of epoxy glass FR4, flexible polyester (PE) thick films and alumina ceramic. Conventional surface mount components were used to represent typical electronic subassemblies. The selection of substrates was based on their relevant material properties and application suitability to represent different substrate-based circuit technologies, while maintaining appropriate assembly cost and manufacturability. For

instance, a higher thermal specification class of FR4 and flexible circuits (flexes) could be investigated in addition to conventional grade materials.

The moulding tool had an aperture of approximately 60mm × 40mm × 10mm with the facility to allow wire pins to protrude from the final article. This configuration was chosen as representative of potential applications identified in automotive products. The complete tool is illustrated Figure 3-1. It also shows the open mould cavity with a dummy assembly comprising of a single gull-wing flat pack and eight external pins. The pins would also be able to serve the dual function of location and support during the moulding process and provide electrical connectivity in the final product.
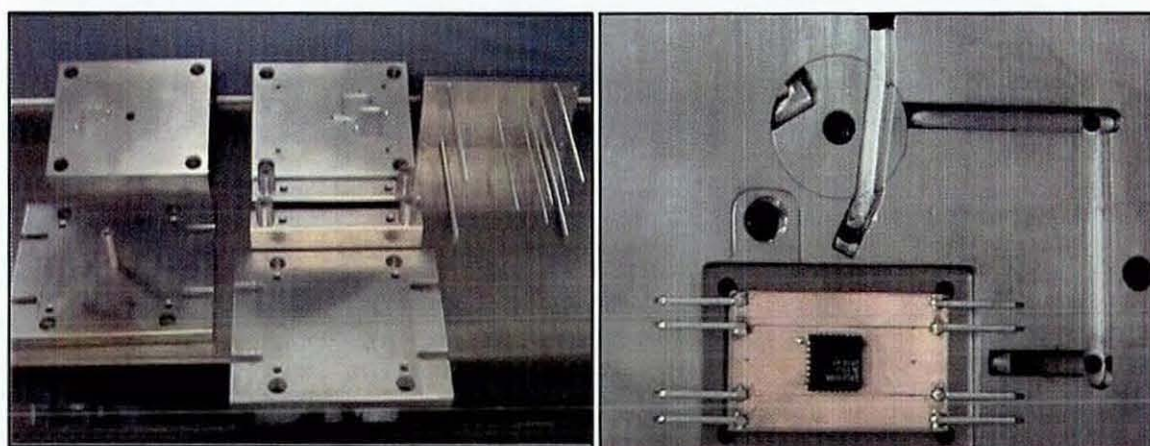
Figure 3-1 Moulding tool and placement of dummy assemblies in the moulding cavity

3.2.2. Observations and Results

The dummy assemblies were subjected to injection pressures in excess of 100bar, melt temperatures of up to 260°C and a range of injection speeds. The PE flexes were found to fare very badly under these extreme conditions and were completely destroyed. In each case, the substrate was torn from the pins as the polymer flowed into the mould, leaving the flex electrically disconnected and in a small folded mass opposite the polymer entry gate (refer to Figure 3-2). This shows that the selected flexes lacked the strength to survive the moulding settings used for the ABS injection. Further study will be required to find a more constructive moulding environment for this substrate, employing a more suitable polymer, possibly of lower melt temperature, injection pressure and material viscosity. Initial work on the alumina substrates resulted in cracking either during loading into the tool or during moulding process

(Figure 3-3). However, in the later stages of the experiment, this problem was overcome and the material has since shown potential for injection overmoulding.

Of all the candidates, FR4 substrates showed the most promise, although initial samples showed distortion due to the pressures involved (see Figure 3-4). There was further evidence that the pressures exerted by the polymer as it flowed into the mould represented a particular technical obstacle. Evidence of warping was seen in all samples as well as sufficient lateral bending to distort the pins supporting the substrate (see Figure 3-5). Weakly attached components were also found 'swept' aside by the force of the polymer flow, as shown in Figure 3-6 below.

These initial experiments highlighted both technical and design obstacles to successfully embed electronics using polymeric injection moulding. The results obtained were not very encouraging but provided a set of critical benchmarking process guidelines and materials selection criteria. The failure of the flexible PE film at this stage was perceived as representing a particular challenge since embedded flexible circuitry potentially offered a distinct advantage for achieving high-density encapsulation of complex, 3-dimensional, electronic assemblies within geometrically constricted polymer modules.
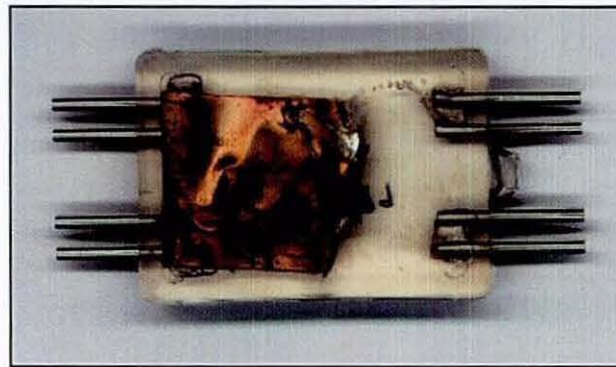
Figure 3-2 Flexible PE substrate showing detachment and distortion
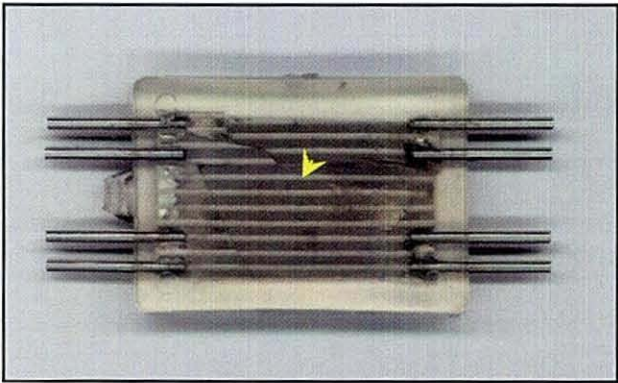
Figure 3-3 Alumina substrate cracking during moulding
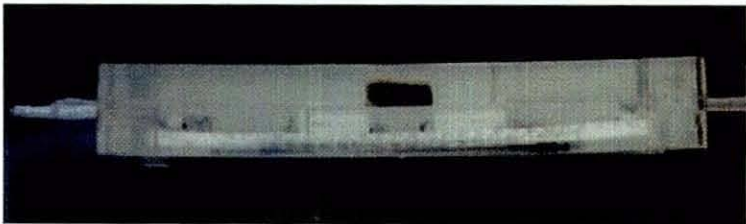
Figure 3-4 FR4 board showing warping
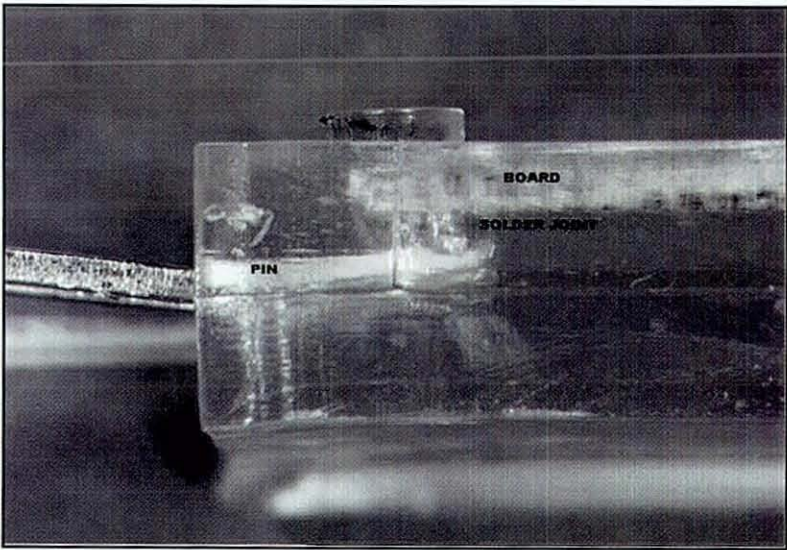
Figure 3-5 Effect of the injection force on the supporting pins
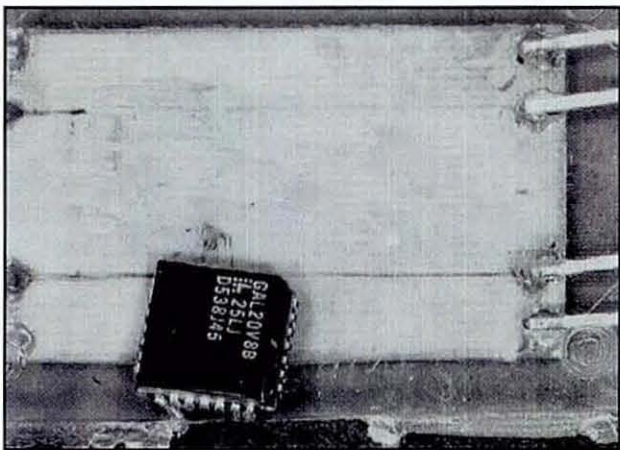
Figure 3-6 Component detachment during moulding

3.3. Structural and Flow Modelling

Structural modelling elsewhere using the NISA simulation package [De Cooper Jones, 1999] illustrated that the pressure distribution in the mould cavity from the advancing flow front produced a differential pressure of approximately 0.34MPa (34 bar) between the top and the bottom surfaces of the subassembly. The resultant net force caused deflection to the substrate in the direction of this pressure gradient, shown in Figure 3-7 below.
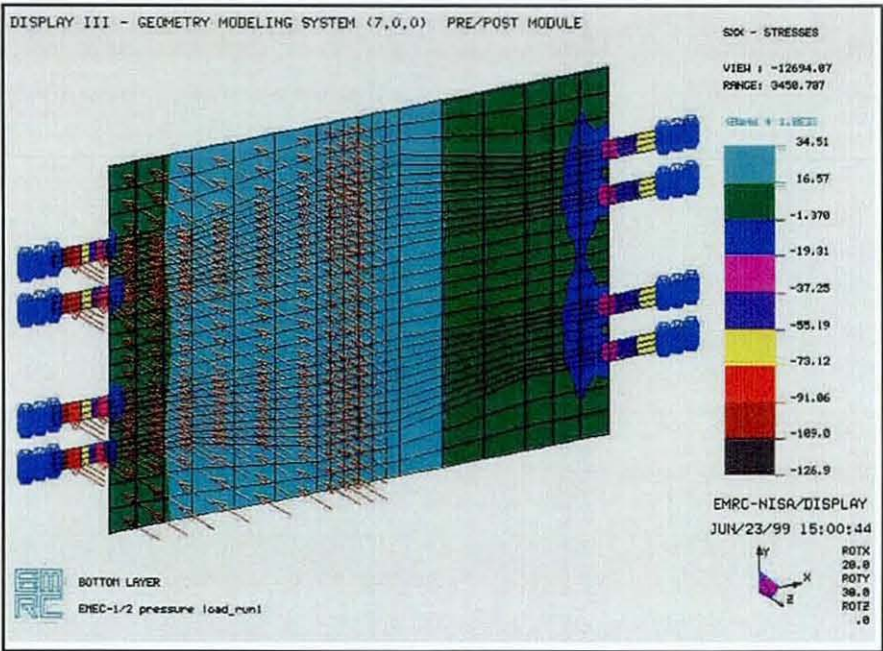
Figure 3-7 Pressure difference acting on the bottom surface of substrate [courtesy of De Cooper Jones, 1999]

Finite Element Analysis (FEA) models were built using the C-Mold package [De Cooper Jones, 1999] to study the advance of the flow front within the moulding cavity. Figure 3-8(a) and (b) show the advancement of the flow front as proportional to the total filling cycle time and clearly indicates the lack of uniform progress of the melt in the cavity. The top half of the substrate was filled completely within 50% of the cycle time, whilst the bottom half, populated with the electronic components restricting the flow, required nearly 70% of the cycle time. Figure 3-8(c) shows that the bulk temperature of the module was not homogenous at the end of filling because sections with varying thickness cooled at different rates. Figure 3-8(d) shows that, at 75% filling, the pressure within the cavity was nearly 0.25MPa. This is similar to the 0.34MPa cross-thickness stress obtained from the fully encapsulated thermo-mechanical model above.

As this result supported the empirical findings of the experiments, it suggested measures of support normal to the substrate to minimise or eliminate the warping deformation caused by the injection pressure on the substrate. Preliminary injection trials were therefore conducted to assess this requirement and indicated that supporting the circuit boards during moulding gave a reduction in the distortions, and therefore an improvement to the mould filling on both sides of the board. A suitable method of supporting the boards was developed. A support moulding was subsequently designed, a tool made and parts moulded in polypropylene (PP). The details of this method discussed further in Chapter 4.
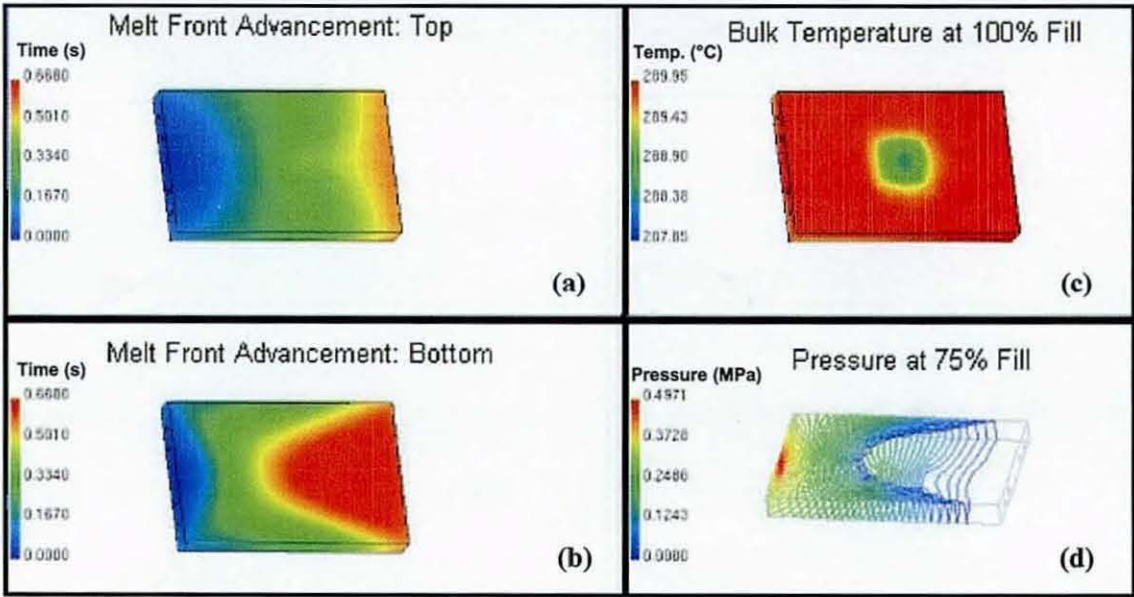
Figure 3-8 Flow models for the melt filling cycle [courtesy of De Cooper Jones, 1999]

3.4. Further Exploration Experiment

The effects and influences of polymeric science, injection parameters and geometrical mould design on qualities of injection moulded parts have been extensively investigated for plastic moulding over recent years [van der Sanden, 1992] [Rosato et al, 2000] [Kansala et al, 2001] [Lu et al, 2001] [Huang et al, 2001]. These well-found reports on conventional injection moulding processes have become an invaluable source of knowledge for the current research. The encapsulation technique investigated in this research, which embeds an electronic subassembly within the plastic, nevertheless carries significant deviations from conventional moulding practices and has therefore prompted the design of experimental screening at the outset.

The main focus of this experiment was to identify and explore the most dominant process variables for this technology. It was also hoped that through the elimination of trivial variables, other process uncertainties may be reduced. The variables selected as subjects of this investigation are discussed in the following sections.

3.4.1. Experimental Procedure

3.4.1.1. Polymers

Five commercial semi-crystalline resins widely used in automotive and consumer electronic applications were selected for the trials:

- Valox® Polybutylene Terephthalate (PBT) is an unreinforced polyester grades with a nominal melt temperature of 245°C. Its good processibility enables more efficient flow in thin sections.
- Crastin® is a 30% glass-reinforced grade PBT polymer with improved dimensional stability and surface finish, giving lower warpage and high stiffness. Its lowest processing melt temperature is 240°C.
- Zytel® is a Nylon-66 polymer with good electrical properties, abrasion and chemical resistance. Its high temperature properties mean that its melt temperature is relatively high for the proposed process, at approximately 280°C.
- Minlon® is a 40% mineral-filled grade of Nylon-66 that has higher tensile and flexural moduli and heat deflection temperature. Its most important characteristic is the substantially lower warpage than the unfilled Zytel.

- Delrin® is an Acetal virgin homopolymer that has a relatively lower melt temperature of 205°C. Its highly crystalline character suggests good dimensional stability with load and time.

Also included in the experiment are 2 levels of polymer encapsulating thickness of 7.4mm and 10.9mm.

3.4.1.2. Injection Parameters

Because of the substantial effects of the individual injection parameters on part shrinkage and electronic integrity, two levels of each injection setting specific for the respective material were chosen according to the manufacturer's guidelines. The moulding variables, together with the respective setting investigated in the experiment are listed in Table 3-1.

3.4.1.3. Tooling Design

In addition to the two different moulding cavity depths, the side-gate and end-gate design configuration (see Figure 3-1) was retained from previous dummy trials to study effects of melt injecting direction. This provided consideration of injection-induced shear force effects on the longitudinal deformation of the embedded assembly, particularly substrate warpage.

3.4.1.4. Electronic Subassembly

Specimen circuits, with the combinations of following components were constructed for this experiment and as shown in Figure 3-9:

- Substrate:
  - a) FR4 which is a conventional glass-fibre laminate (thickness: 0.8 and 1.6 mm)
  - b) BT-Epoxy (Bismaleimide Triazine) is a higher grade of laminate, with improved thermal properties, such as a higher glass transition temperature Tg of about 180°C (thickness: 0.8mm and 1.6 mm)
  - c) Rubalit® 96% alumina ceramic (thickness: 1.0mm)
- Electronics:
  - a) Surface-mounted components consisting of a 20-pin gull-wing IC, ceramic and tantalum capacitors, resistors
  - b) A wire bonded bare silicon die (COB)

	Melt Temp. (°C)		Inj. Press. (bar)		Mould Temp. (°C)		Holding Press. (bar)	
	Low	High	Low	High	Low	High	Low	High
Valox PBT	245	260	43	93	50	75	30	90
Grastin GR-PBT	240	260	64	107	30	130	30	100
Zytel Nylon	280	300	21	43	50	90	50	100
Minlon GR-Nylon	285	305	43	75	80	120	40	100
Delrin Acetal	210	220	27	48	80	100	75	100

Table 3-1 Injection parameters as variables in Stage 1 overmoulding experiment

3.4.1.5.   Glob-top Materials

With the knowledge of those hazards experienced by the subassemblies, a decision was taken to apply to the various component joints a layer of glob top coating to act as a stress buffer from the high temperature, high pressure injected melt. The inclusion of this barrier layer also provides protection for the components against ionic contaminants and moisture ingress. Figure 3-10 depicts the glob-top protected electronic components. To this end, a number of potentially suitable materials were also investigated and are listed in Table 3-2 below. For each material, the applications of the glob-top with single and double layers were used as an additional variable. Figure 3-11 shows a complete electronic subassembly constructed for this experiment. The specifications and characteristics of all the elements and chemicals used to create this Stage 1 specimen assembly are listed in Appendix 2.
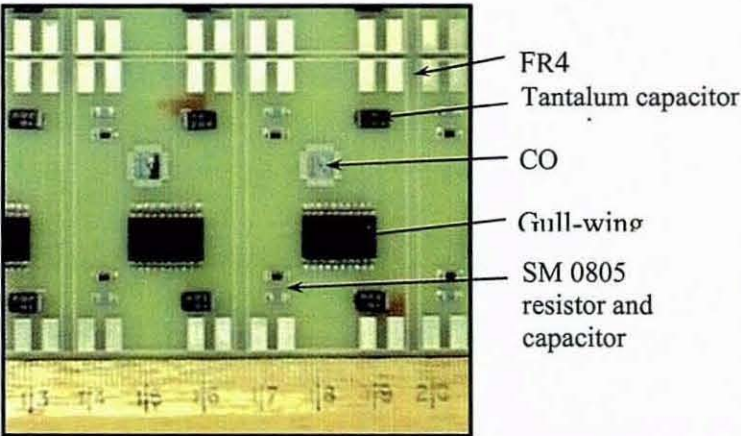
Figure 3-9 Specimen electronic assembly
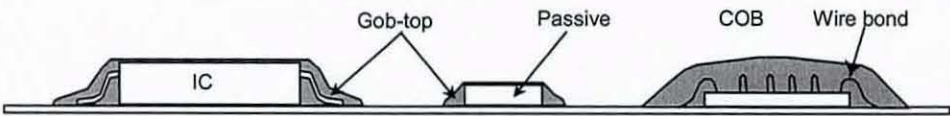
Figure 3-10 Glob-topping of electronic components
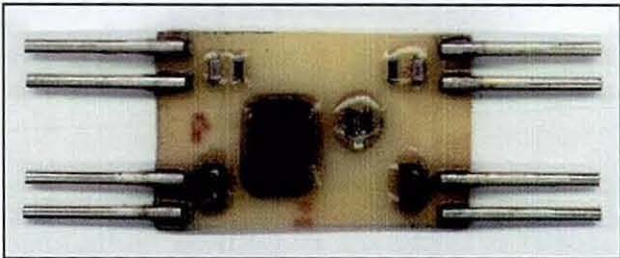
Figure 3-11 A complete Stage 1 electronic subassembly

Material	Properties	Comments
Epoxy	• Excellent chemical resistance • Excellent mechanical properties • Excellent wetting for application • Good adhesion to a wide variety of substrates under many environmental conditions • Acceptable moisture barrier • Thermal stability from 25 to 200°C	• Needs compliant buffer coating for low stress • Rework is difficult • Short shelf-life (1-component) • High stress • Moisture sensitive
Silicone	• Excellent electrical properties: dielectric constant & loss factor • Mechanically tough and flexible • Resistant to high temperature • Lower moisture absorption than epoxy • Low stress after cure • Good UV resistance • Thermal stability up to 260-315°C	• High CTE compared to epoxy and acrylic resins • Low tensile tear strength • Poor adhesion • Low resistance to hydro-carbons, attacked by halogenated solvents • High cost
Polyurethane	• Good mechanical properties (toughness, flexibility, resistance to abrasion) • Good adhesion to die and substrates • Low viscosity • Low moisture absorption • Ambient temperature curing possible • Thermal stability up to 150°C	• Most widely used • Flammable • Poor thermal stability • Poor weatherability • Difficult to rework • Unsuitable for high frequency circuits

Table 3-2 Glop top materials investigated in Stage 1

3.4.2. Design of Experiment (DOE)

With the results obtained from the previous trials and computational models, a series of experiments was devised using the DOE and an analysis software package known as RS-Discover [De Cooper Jones, 1999]. The complete DOE matrix is shown in Table 3-3. Three trial repetitions were allocated for each experiment combination listed in the plan, i.e. there were in total 3x27=81 specimens produced. It should be noted that the injection parameters for individual resins were specifically chosen to reflect extreme injection conditions, though remaining within the manufacturers' specifications.

3.4.3. Experimental Result Analyses

As this exercise was to investigate mostly mechanical failure mechanisms, in addition to visual inspection of surface and dimensional distortion, the overmoulded specimens were subjected to the following evaluation processes:

1. *X-ray radiography* (Mil. Std. 883 Test method 2012 1034 [U.S. Department of Defense, 2003])

   X-ray imaging is used to inspect for any damage to wire bonds (of the COB and inside the IC) and solder joints, component displacement, board deformation and cracking of the ceramic substrate.

2. *Longitudinal moulding warpage measurement*

   This length-wise measurement accounted for physical deformation as a result of polymeric thermal shrinkage and process design.

3. *Dye penetrant test* (Mil. Std. 883 Test method 1034 [U.S. Department of Defense, 2003])

   The specimens were impregnated by a dye penetrant resin in vacuum, followed by cross-sectioning to detect any ingress of the dye into the module. Through inspection of sectioned specimens, the distortion to the solder joints and laminate substrates was also examined. The inspection of the integrity of adhesion at the various interfacing layers was also performed.

Figure 3-12 shows the process flow of the experiments for Stage 1. The cross-section specimens revealed not only significant information on the degree of dye penetration as an indication to the interface integrity, but also clearly showed the conditions of the various components, quality of interconnection and dimensional distortion of the substrate.

TRIAL NO.	SUBSTRATE TYPE	SUBSTRATE THICKNESS	GLOB-TOP TYPE	GLOB-TOP THICKNESS	MOULDING MATERIAL	MELT TEMP.	INJECTION PRESSURE	MOULD TEMP.	HOLDING PRESSURE	WALL THICKNESS	GATE POSITION
		mm				deg-C	bar	deg-C	bar	mm	
1	Ceramic	1.00	PUR	1	GR PBT	260	64	30	30	10.9	End
2	FR4	1.60	PUR	2	Nylon 66	300	43	90	50	10.9	Centre
3	BT	0.80	Silicone	2	Acetal	210	48	100	75	10.9	End
4	Ceramic	1.00	Epoxy	1	PBT	245	43	50	30	7.4	End
5	FR4	1.60	Silicone	1	GR Nylon 66	285	75	80	100	10.9	Centre
6	BT	0.80	Epoxy	1	Acetal	220	48	80	100	7.4	Centre
7	BT	0.80	Epoxy	2	GR Nylon 66	305	75	80	100	10.9	End
8	FR4	1.60	PUR	1	GR Nylon 66	285	75	80	40	7.4	End
9	FR4	0.80	Silicone	2	Nylon 66	300	21	50	100	7.4	End
10	Ceramic	1.00	Silicone	2	GR Nylon 66	305	75	120	40	7.4	End
11	BT	0.80	PUR	1	Nylon 66	280	21	50	50	10.9	Centre
12	BT	0.80	Silicone	1	GR Nylon 66	285	43	120	40	7.4	End
13	BT	1.60	Silicone	1	PBT	260	96	50	90	7.4	End
14	BT	1.60	Silicone	2	GR PBT	240	64	30	30	7.4	Centre
15	Ceramic	1.00	Epoxy	1	GR PBT	240	107	130	90	10.9	Centre
16	FR4	1.60	Epoxy	1	Acetal	220	27	100	75	7.4	Centre
17	FR4	0.80	Epoxy	2	GR Nylon 66	285	43	120	40	10.9	Centre
18	FR4	0.80	Silicone	1	Acetal	220	48	100	75	10.9	End
19	BT	0.80	PUR	2	GR PBT	260	107	130	90	7.4	Centre
20	FR4	1.60	Silicone	2	Acetal	210	27	80	100	10.9	End
21	BT	1.60	Epoxy	2	Acetal	220	27	100	75	10.9	End
22	FR4	0.80	Epoxy	2	Nylon 66	280	43	90	100	7.4	End
23	Ceramic	1.00	PUR	2	Acetal	210	27	80	100	7.4	Centre
24	BT	0.80	Silicone	2	Acetal	210	48	100	75	7.4	Centre
25	BT	1.60	Silicone	1	Nylon 66	300	21	90	100	10.9	Centre
26	FR4	0.80	PUR	1	PBT	260	43	75	90	7.4	End
27	FR4	0.80	Silicone	2	PBT	260	43	50	30	10.9	Centre

Table 3-3 Stage 1 D.O.E. test plan

Specimen
electronic assembly

Injection Moulding

Overmoulded module

X-ray Radiography

X-ray image of the
assembly components

Dye Penetrant Test and Cross-
sectioning

(a)

(b)

Cross-sectional view of an
impregnated specimen under:
(a) normal lighting
(b) UV light
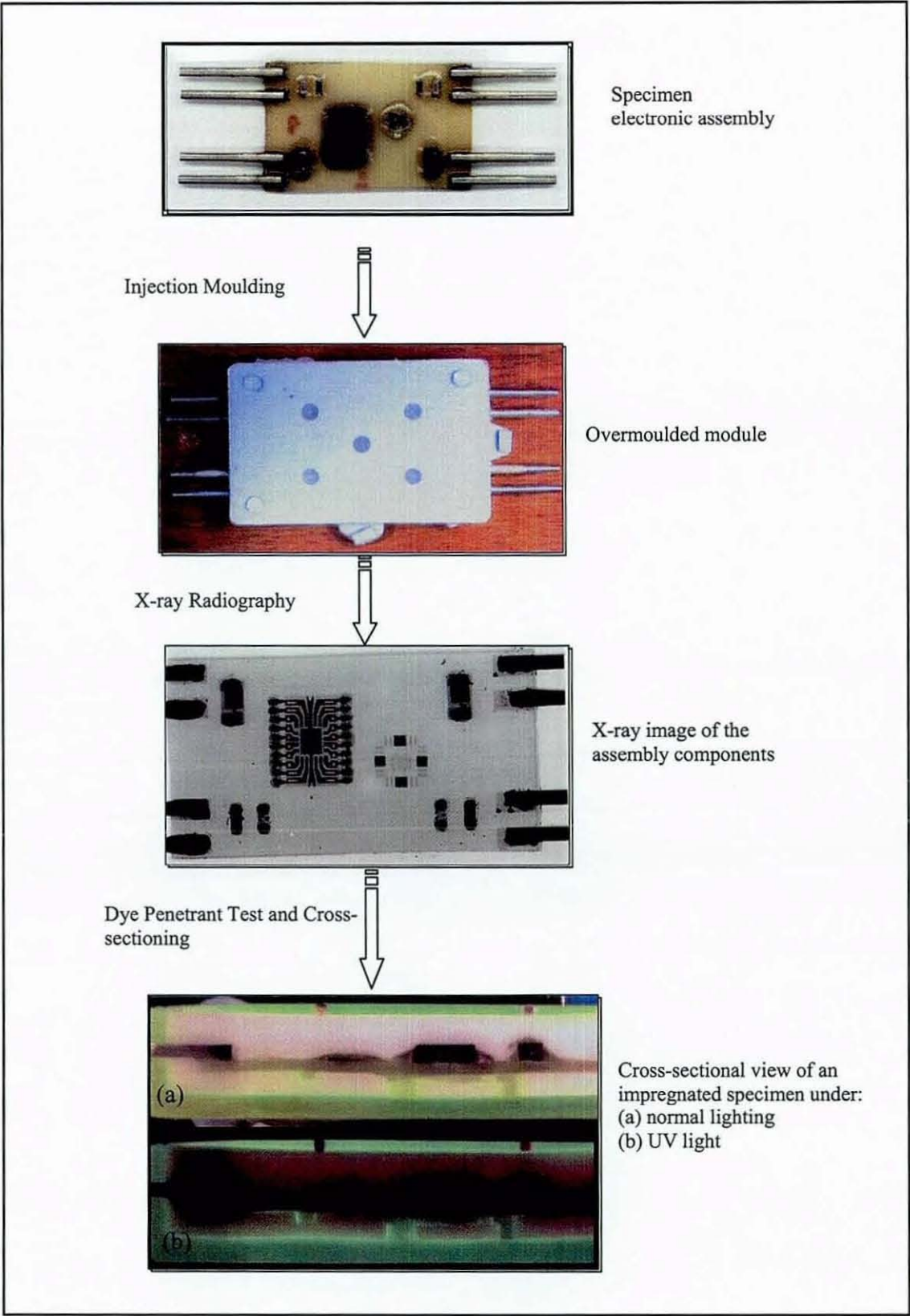
Figure 3-12 Flow diagram of the Stage 1 exploration experiment

The sample of a sectioned specimen (in this case, trial no. 3) in Figure 3-13 shows the glob-top protected wire bonds of the COB and solder joint of the IC. The image shows the longitudinal bowing of the distorted BT circuit board as well as traces of capillary dye ingress into the module. In almost all cases, this was via the support peg-polymer interface layers. The study also found that good adhesion was formed between the polymer and the metallic I/O pins, with no evidence of dye ingress through this interface. Despite the dye penetration, exacerbated by the CTE disparity between the PP material of the support and most of the overmoulding resins (as evidenced in Figure 3-14), the electronic components and interconnections have survived the severe mechanical conditions of the injection moulding process. Practicality apart, it is clear at this stage that the inclusion of the supporting pegs allowed the dye ingress into the subassembly. Unless complete adhesion can be attained at this interface, these artificial supports would contribute to failures in thermal-cycling tests.

The combination of the x-ray and cross-sectioning inspection have shown that all the glob-top compounds at both thicknesses investigated, have undergone the injection moulding encapsulation successfully, without sign of serious wire sweep/shearing and solder fatigue. Figure 3-15 shows specimen no. 12 from the DOE, with the PUR glob-top, which has not experienced mechanical damage to the wire bonds during the moulding. However, it must be stressed that the components and interconnections were only evaluated on the merits of their microscopic mechanical integrity at this point. The functionality of electronics will be critically appraised in the subsequent staged experiment.

Investigation of the ceramic substrate showed some degree of cracking under the injection-induced stresses. Figure 3-16 shows images of a specimen from trial no. 4 in the DOE, where a ceramic substrate was injected with virgin PBT. The side view across the length of the module in image (a) shows severe longitudinal warpage in the direction of injection flow, which was measured as 1400 microns. Image (b) is the cross-sectioned specimen, clearly revealing the bowing of the ceramic board that caused the cracks about the centre portion of the board. These cracks are further magnified in image (d). Image 20(c) shows a sectioned I/O pin with its solder joint, indicating that there was no dye penetration at this interface.
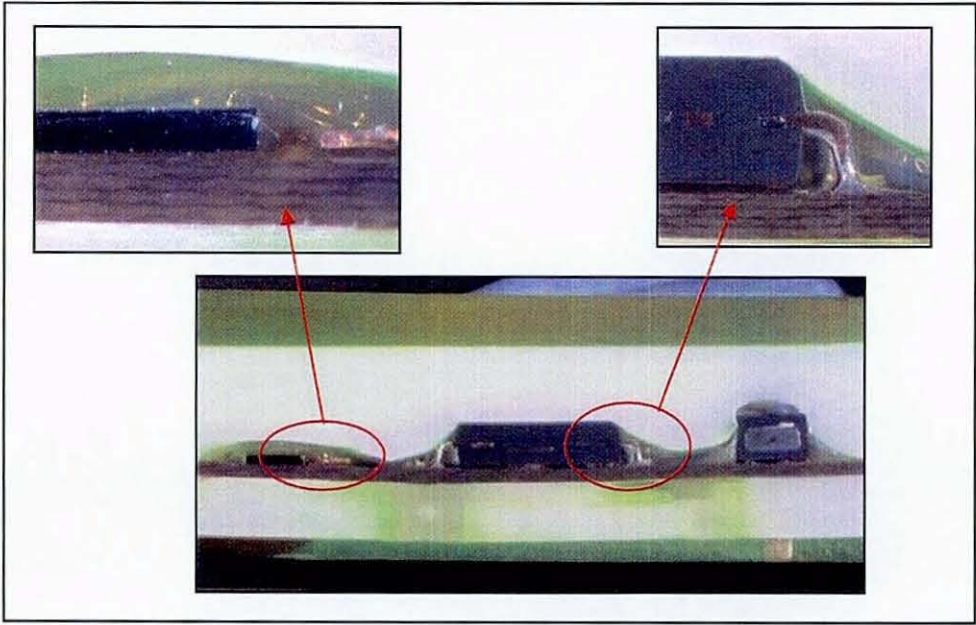
Figure 3-13 Cross-section specimen of Trial no. 3
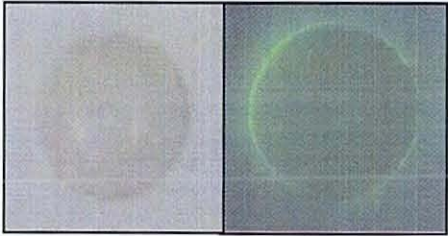
Figure 3-14 Dye penetration along the supporting peg peripheral (the eclipse effect)

Figure 3-15 Wire bonds within the PUR glob-top of specimen no. 12
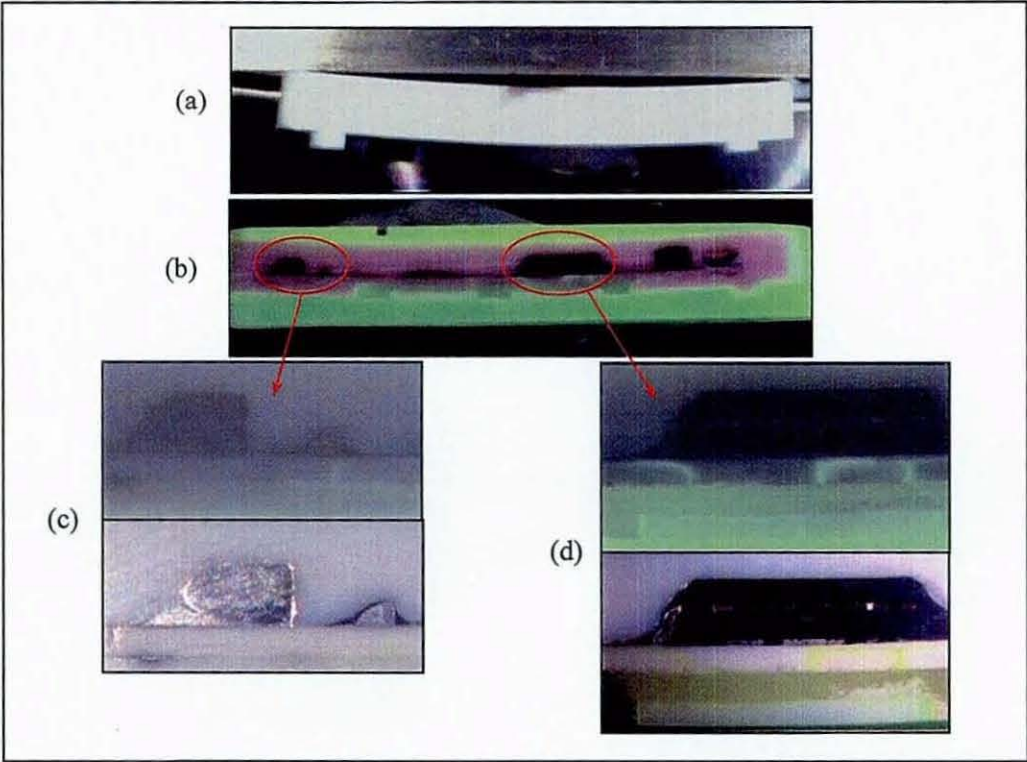
Figure 3-16 Assessment of specimen Trial no. 4 from stage 1 DOE

Amongst the different injection parameters, the linear CTE difference between polymer and substrate has a significant impact on the board warpage. For example, comparing the CTE values in Table 3-4 between the ceramic substrate and that of the encapsulating polymers shows that the mean deflection measured are proportional to this CTE difference, as illustrated by the graph in Figure 3-17 below.

	FR4	BT	Ceramic	PBT	GR-PBT	Nylon 66	GR-Nylon 66	Acetal
CTE (ppm/°C)	13-18 (x-y)	13-15 (x-y)	7.3 (x-y)	130(flow) 130 (xflow)	30(flow) 100 (xflow)	100(flow) 110 (xflow)	67(flow) 88 (xflow)	130 (flow) 150 (xflow)

Table 3-4 Linear CTE of the substrates and polymers
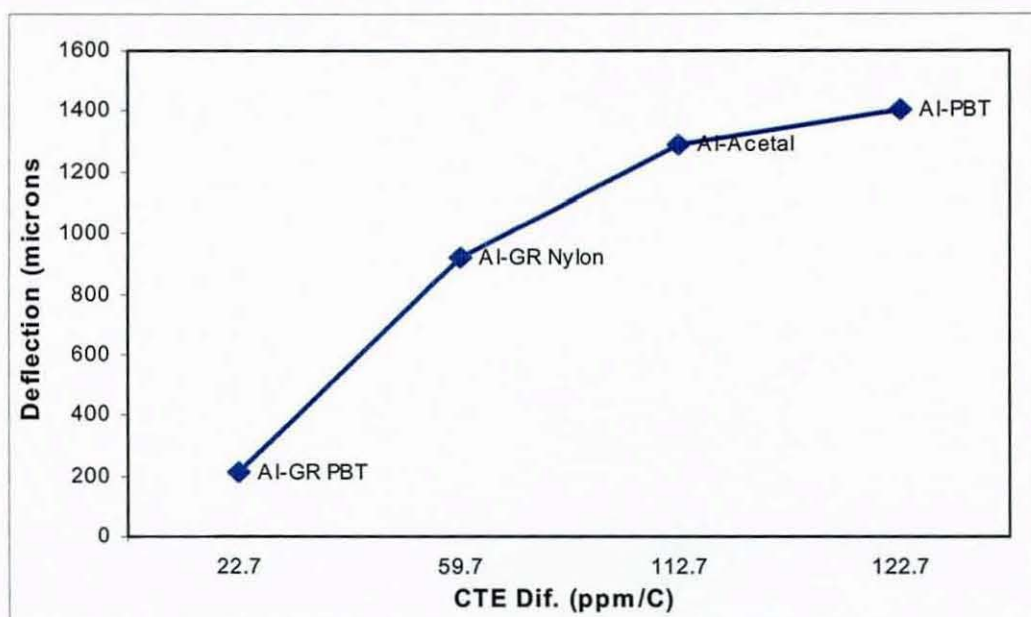
Figure 3-17 Module deflection Vs. ceramic-polymer CTE differences

A more detailed graph separating the different aspects of the experiments is shown in Figure 3-18. In this case, the CTE differences are calculated in accordance with the injection direction (gate location) relative to the module warpage, i.e. for end-gate trials, the CTE difference is in the flow direction; while in the transverse to the flow direction in the centre gate trials. The cases with dissimilar injection gate position and polymer wall thickness were filtered from the graph to enable further analysis.

A comparison between the trials with end-gate/7.4mm thickness (12 and 13) to that with end-gate/10.9mm thickness (3, 7 and 21) explored the significance of wall thickness in contributing to the module deflections. It is obvious that the trials with thicker moulded polymer showed a lower degree of module bowing due to the polymer mass/volume relative to the substrate, minimising the effect of the CTE disparity induced shrinkage. The flexural strength of the polymer also increases with the increase in cross-sectional surface area to resist the bending moments exerted by the strained substrate.

Another comparison shows that the injection gate positioned at the mid-point across the length of the mould cavity produced lower module warpage, as observed through sample trials end-gate/7.4mm and trials centre gate/7.4mm (4, 6, 19 and 24). However, no conclusive result can be drawn for this aspect from the sample trials with centre gate/10.4mm as there was no provision in the DOE for any CTE difference to be obtained.
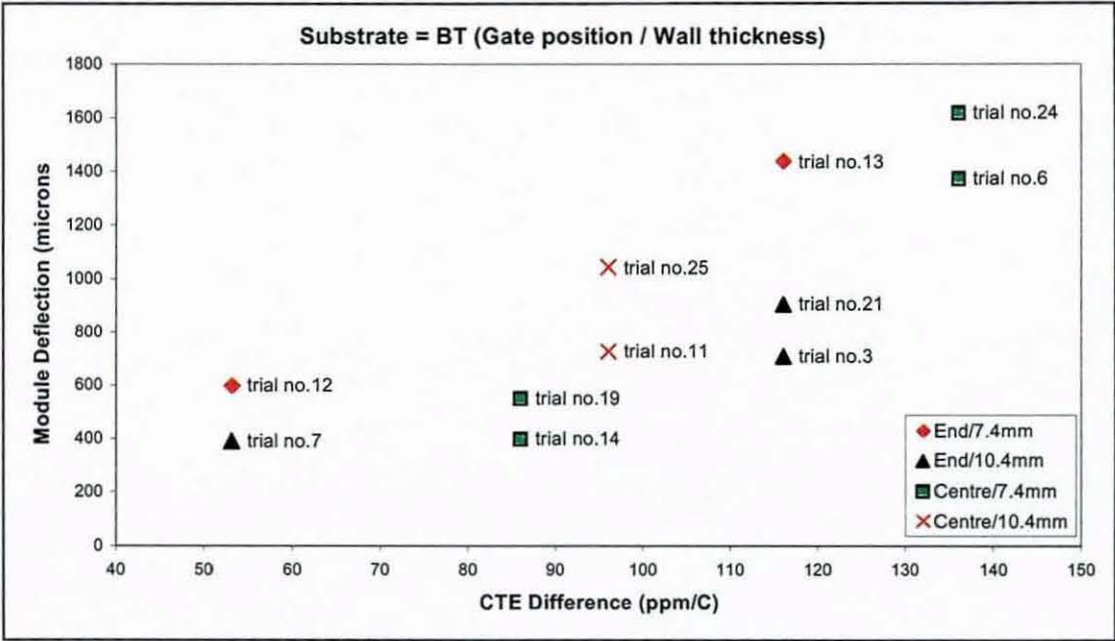
Figure 3-18 Longitudinal module deflections Vs. CTE difference for BT-substrate samples

3.4.4. Statistical Results Analysis

In order to complement the observations from the empirical evaluation, the test results were appraised by statistical failure mode analyses. The analysis of variance (ANOVA) for each defect was utilised to interpret the results from the DOE. An ANOVA breaks down the process complexity and identifies the percent contribution of the individual sources of variance to the total variance, i.e. identifies which factors are statistically significant in their contribution to piece-to-piece variation.

An analysis of means (ANOM) was performed to analyse the defect mode weighting for each of the major parameters nominated by ANOVA, which identified the optimum process level to obtain minimum moulding defects. In other words, ANOVA indicated which control parameters had the largest effect on the process responses, whilst ANOM identified where the potentially best setting for these parameters lay. The combination provided an effective statistical approach to optimise the moulding environment.

The defect mechanisms included in the failure mode analysis of the experiment were:

   a) *Substrate board distortions*: physical deformation and warpage

   b) *Dye penetration severity*: degree of dye ingress into the plastic module

   c) *Solder joint defects*: solder melting, migration, component displacement, popcorning

d) *Wirebond defects*: wire sweep, shearing, die fracture

e) *Module longitudinal deflections*: physical deformation and warpage

The results of the ANOVA carried out for each of the defect mechanisms evaluated in this exercise are presented in Table 3-5. The mean square of each effect is calculated by dividing the sum of squares by its degrees of freedom. From the ANOVA results, the variance contributions demonstrated by individual process variables on each of the failure mechanisms were broken down.

Defect Mode	Source of Variation	Type III Sum of Squares	D.O.F.	Mean Square	F-test Statistic	Sig. Level	Percentage Contribution
	Moulding Polymer	1366 3148	4	341 5787	2 37	0 21	12.12
	Melt Temperature	63 4296	1	63 4296	0 44	0 54	0 56
	Injection Pressure	192 6661	1	192 6661	1.34	0 31	1 71
	Mould Temperature	368 8499	1	368 8499	2 56	0.18	3 27
	Holding Pressure	1098 7600	1	1098 7600	7 64	0 05	9 75
	Part Thickness	84.2760	1	84.2760	0 59	0 49	0.75
Substrate	Substrate Laminate	175 4532	1	175 4532	1 22	0 33	1 56
Distortion	Substrate Thickness	2399 4656	1	2399 4656	16 68	0 02	21.28
	Glob-top Material	1622 1036	2	811 0518	5 64	0 07	14 39
	Glob-top Thickness	60 5465	1	60 5465	0 42	0 55	0 54
(Adjusted R^2 =	Injection Gate Position	7 6814	1	7 6814	0 05	0 83	0 07
0 940)	Melt Temp*Inj Pressure	71.7648	1	71 7648	0 50	0 52	0 64
	Melt Temp*Mould Temp	1654 5644	1	1654 5644	11 50	0 03	14 68
	Melt Temp*Holding Pressure	397 5883	1	397 5883	2.76	0 17	3 53
	Inj Pressure*Mould Temp	882 7534	1	882.7534	6 14	0 07	7 83
	Inj Pressure*Holding Pressure	248 7031	1	248 7031	1 73	0.26	2 21
	Mould Temp*Holding Pressure	3 5127	1	3 5127	0 02	0 88	0 03
	Error	575 4964	4	143 8741			5 10
	Total	11273.9300	25				100 00
	Moulding Polymer	4847 1239	4	1211 7810	2 21	0 23	40 12
	Melt Temperature	153 5770	1	153 5770	0 28	0 62	1 27
	Injection Pressure	680 7465	1	680.7465	1 24	0 33	5 64
	Mould Temperature	282 1440	1	282.1440	0 51	0 51	2 34
	Holding Pressure	2040 5104	1	2040.5104	3 71	0 13	16 89
	Part Thickness	298 4403	1	298 4403	0 54	0 50	2 47
Dye Penetration	Substrate Laminate	41.8004	1	41.8004	0 08	0 80	0 35
Severity	Substrate Thickness	20 5612	1	20 5612	0 04	0 86	0 17
	Glob-top Material	132 3034	2	66 1517	0.12	0 89	1.10
(Adjusted R^2 =	Glob-top Thickness	58 9677	1	58 9677	0.11	0 76	0 49
0 731)	Injection Gate Position	132 0350	1	132 0350	0 24	0 65	1 09
	Melt Temp*Inj Pressure	933 0060	1	933 0060	1.70	0 26	7 72
	Melt Temp*Mould Temp	98 3706	1	98 3706	0 18	0 69	0 81
	Melt Temp*Holding Pressure	5 9550	1	5 9550	0 01	0 92	0 05
	Inj Pressure*Mould Temp	0 2097	1	0 2097	0 00	0 99	0 00
	Inj Pressure*Holding Pressure	5 4680	1	5 4680	0 01	0 93	0 05
	Mould Temp*Holding Pressure	151 6286	1	151 6286	0.28	0 63	1 26
	Error	2197 3234	4	549 3308			18 19
	Total	12080 1711	25				100 00

Table continues next page...

Defect Mode	Source of Variation	Type III Sum of Squares	D.O.F.	Mean Square	F-test Statistic	Sig. Level	Percentage Contribution
Solder Joint Defect (Adjusted R^2 = 0 928)	Moulding Polymer	977 5552	4	244 3888	2 03	0 25	27 88
	Melt Temperature	3 7557	1	3 7557	0 03	0 87	0 11
	Injection Pressure	7.1410	1	7 1410	0 06	0 82	0 20
	Mould Temperature	841 9631	1	841 9631	6 99	0 06	24 02
	Holding Pressure	5 0654	1	5 0654	0 04	0 85	0 14
	Part Thickness	239 2454	1	239.2454	1.99	0 23	6 82
	Substrate Laminate	69 3272	1	69 3272	0 58	0 49	1 98
	Substrate Thickness	0 1889	1	0 1889	0 00	0 97	0 01
	Glob-top Material	412 7309	2	206 3654	1.71	0 29	11 77
	Glob-top Thickness	9 9733	1	9 9733	0 08	0 79	0 28
	Injection Gate Position	119 8523	1	119 8523	1 00	0 37	3 42
	Melt Temp*Inj Pressure	99 0860	1	99 0860	0 82	0 42	2 83
	Melt Temp*Mould Temp	2 4762	1	2 4762	0 02	0 89	0 07
	Melt Temp*Holding Pressure	49 5188	1	49 5188	0 41	0 56	1 41
	Inj Pressure*Mould Temp	85 8433	1	85 8433	0 71	0 45	2 45
	Inj Pressure*Holding Pressure	0 1928	1	0.1928	0 00	0 97	0 01
	Mould Temp*Holding Pressure	100 1783	1	100 1783	0 83	0 41	2 86
	Error	481 6564	4	120 4141			13 74
	Total	3505.7502	25				100.00
Wirebond Defect (Adjusted R^2 = 0 863)	Moulding Polymer	1493 6087	4	373 4022	1 50	0 35	18 97
	Melt Temperature	2 1566	1	2 1566	0 01	0 93	0 03
	Injection Pressure	534 1618	1	534.1618	2 14	0 22	6 79
	Mould Temperature	87 8104	1	87 8104	0 35	0 58	1 12
	Holding Pressure	274 8937	1	274 8937	1.10	0 35	3 49
	Part Thickness	34 6242	1	34 6242	0.14	0 73	0 44
	Substrate Laminate	1530 8786	1	1530 8786	6 15	0 07	19 45
	Substrate Thickness	10 3036	1	10 3036	0 04	0 85	0 13
	Glob-top Material	995 0456	2	497 5228	2 00	0.25	12 64
	Glob-top Thickness	344 6387	1	344 6387	1.38	0 30	4 38
	Injection Gate Position	508 4306	1	508 4306	2 04	0 23	6 46
	Melt Temp*Inj Pressure	75 4067	1	75 4067	0 30	0 61	0 96
	Melt Temp*Mould Temp	3 5267	1	3 5267	0 01	0 91	0 04
	Melt Temp*Holding Pressure	461 3532	1	461 3532	1 85	0 25	5 86
	Inj Pressure*Mould Temp	216 9216	1	216 9216	0 87	0 40	2 76
	Inj Pressure*Holding Pressure	233 2134	1	233 2134	0 94	0 39	2 96
	Mould Temp*Holding Pressure	69 1101	1	69 1101	0 28	0 63	0 88
	Error	996 2837	4	249 0709			12 66
	Total	7872 3679	25				100 00
Plastic Module Deflection (Adjusted R^2 = 0 929)	Moulding Polymer	2977 6216	4	744 4054	4 01	0 10	32 82
	Melt Temperature	202 2953	1	202 2953	1 09	0 36	2.23
	Injection Pressure	0 9179	1	0 9179	0 00	0 95	0 01
	Mould Temperature	120 1852	1	120 1852	0 65	0 47	1 32
	Holding Pressure	53 2745	1	53 2745	0 29	0 62	0 59
	Part Thickness	2587 0216	1	2587 0216	13 93	0 02	28 52
	Substrate Laminate	19 0649	1	19 0649	0 10	0 76	0 21
	Substrate Thickness	596 4812	1	596.4812	3 21	0 15	6 58
	Glob-top Material	105 1946	2	52 5973	0 28	0 77	1 16
	Glob-top Thickness	103 7377	1	103 7377	0 56	0 50	1 14
	Injection Gate Position	586 0179	1	586 0179	3 16	0.15	6 46
	Melt Temp*Inj Pressure	377 6351	1	377 6351	2 03	0.23	4 16
	Melt Temp*Mould Temp	62 2532	1	62.2532	0 34	0 59	0 69
	Melt Temp*Holding Pressure	209 7478	1	209 7478	1 13	0 35	2 31
	Inj Pressure*Mould Temp	220 9666	1	220 9666	1 19	0 34	2 44
	Inj Pressure*Holding Pressure	64 4002	1	64 4002	0 35	0 59	0 71
	Mould Temp*Holding Pressure	41 8504	1	41 8504	0 23	0 66	0 46
	Error	742 6334	4	185 6583			8 19
	Total	9071 2988	25				100 00

Table 3-5 Results from the ANOVA analysis

3.4.4.1.   *Solder Joint Deformation Analysis*

The polymeric variable provided nearly 28% of variance contribution from the solder joint defect ANOVA. The corresponding ANOM found that reinforced grades were marginally less hostile than the virgin resin. GR-PBT and GR-Nylon produced about 8% and 4% less defects respectively than their unfilled counterpart. The presence of filler has shown improvement, but is less significant as the melt temperature increases, as evident in the case of Nylon. At higher temperatures, the heat transferred to the solder joints becomes more significant than the viscosity-induced shearing forces that cause the occurrence of the breakdown mechanisms.

Amongst the unfilled resins, Acetal (nominal melt temp = 210°C) was found to be almost 6% and 26% better than PBT (245°C) and Nylon (280°C) respectively. With the lowest melt temperature of all candidate materials, it produced a 2% higher defect than the best candidate of GR-PBT. The second most important contributing factor was the mould temperature. From the ANOM, the overall reduction of solder defect rate achieved using lower mould temperatures was found to be nearly 10.4%, with the biggest impact seen in the reduction of almost 27% with the GR-Nylon samples.

As the solder joints of the encapsulated circuit assembly were protected by one of the three glob-top coatings, this variable predictably contributed about 12% to the solder joint defect analysis. The thermoset epoxy glob-top was found to be the most effective against the high temperatures. In the trials with Acetal encapsulant, all three glob-top materials produced similar defect rates. This effect increased as the melt temperature increased, such that the ANOM with the PBT polymer samples showed reductions of almost 12% and 30% by epoxy over Si and PUR respectively. A similar trend was found with Nylon samples where the improvements were nearly 27% and 30% respectively. The overall decrease in solder defects exhibited by epoxy over Si and PUR were about 8% and 12% respectively.

Another variable significantly affecting solder defects was the moulding wall thickness. It was observed from ANOMs that in trials using unfilled materials, the thinner mouldings produced less deformation of the solder joints. This lower moulding thickness, however, showed the opposite results with reinforced materials, i.e. a lower defect rate with thicker encapsulation. With Acetal, the 7.4mm-wall thickness sample defects were about 5% lower than the corresponding 10.9mm parts. Nylon samples showed a further reduction of nearly 30% with

the thinner moulding. In the case of PBT samples, nearly the same defect levels for both thicknesses were found. GR-PBT and GR-nylon produced about 10% and 6% less defects respectively with the 10.9mm wall thickness.

3.4.4.2.   Wirebond Deformations Analysis

The specimens designed for this experiment consisted of a bare silicon die attached to the substrate and manually interconnected to its neighbouring silver-plated pads with 25-micron gold wire using a thermosonic wirebonder. This chip-on-board (COB) device was then covered with a glob-top layer, which is a widely used approach in the industry to protect the wirebonds as well as the glass passivation on the silicone die. The failure modes explored here were mechanical integrity, such as wire sweep/shearing and breakage, by means of visual inspection of the x-ray images and cross-sectioned samples.

The ANOVA showed that the most significant factors to the wirebond defects were substrate laminate (19.5%), moulding polymer (19.0%) and glob-top material (12.6%). Injection pressure, injection gate position and second-order melt temperature*holding pressure were the other influential variables.

The ANOM showed that FR4 samples sustained the lowest amount of wirebond damage – nearly 5% and 16% less than ceramic and BT, respectively. In terms of the polymers, PBT was found to be the less hostile to the wirebonds. It produced nearly 3%, 10%, 25% and 30% lower defect rate than GR-PBT, GR-Nylon, Acetal and Nylon respectively. Amongst the glob-top materials used, ANOM indicated that silicone was more suitable to shield the wirebonds from the injection forces than epoxy and PUR.

In the subsequent interpretation of the significant injection variables, lower injection pressure and end injection gate position was individually found to be less detrimental to the COB. Being in direct contact with the substrate and glob-top, the COB experiences immediate effects from the deformations sustained by its two interfacing neighbours. The thermal stresses and forces generated by the melt flow would transport significant effects to the delicate wirebonds through the glob-top layer and the silicone die through the substrate. Therefore, the three factors found most influential from the data analysis above, together with the injection parameters, are closely interrelated and would be expected to have dynamic and complementary effects on the wirebond defects. It is therefore important to establish an

optimum materials and injection condition if direct-attached chips are to be embedded using the proposed technology.

3.4.4.3.   *Substrate Distortions Analysis*

a)   FR4 and BT laminates

The earlier work on the FEA modelling of the encapsulation process [De Cooper Jones, 1999] discovered that the pressure distribution in the mould cavity resulting from the advancing flow front produced a pressure difference of approximately 1MPa (10 bar) between the top (with components) and the bottom surfaces of the subassembly. The resultant net force, if not controlled, would cause deflection to the substrate in the direction of this pressure difference shown in Figure 3-19. The extent of this deflection can be seen in the x-ray image of a sample in Figure 3-20(a) and, by comparison, Figure 3-20(b) shows a sample with almost negligible deformation.

For the boards of the lower thickness, local deformation is observed when examining the sectioned modules. This was in the form of local buckling of the board at, or close to a support and could be explained as follows:

- At the high melt temperature, the glass transition temperature of the board had been exceeded
- The board was held rigidly at each end by the attached pins and partially by the pressure of the support pillar acting on it
- Expansion of the board caused buckling, the site of which was determined by the partial restraint imposed by the support pillars.

An image showing this feature is shown in Figure 3-21 below.

b)   Ceramic substrate

Investigation of the ceramic substrate showed some degree of cracking/snapping under the injection-induced stresses. Figure 3-22 shows the cross-sectioned and dye penetrant images of a specimen from trial no. 4 in the DOE. The side view of across the length of the module shows the severe longitudinal warpage in the direction of injection flow, which was measured as 1400μm. The magnified images clearly revealed the bowing of the ceramic board, resulting in the cracks about the centre portion of the board.

From the ANOVA results, the main contributing factors to substrate deformation in the moulded parts were the laminate thickness (21.3%), melt temperature* mould temperature

(14.7%), glob-top (14.4%) and moulding polymer (12.1%). Also, the other injection parameters were found to be quite significant.

The corresponding ANOMs showed that the higher-T_g BT laminates suffered slightly less distortion than the conventional FR4. However, the improvement became less significant as the substrate thickness increased. The 0.8m-BT deformed nearly 27% less than 0.8mm-FR4, but this difference decreased to just only 0.3% for the 1.6mm-laminates. In this respect, a within-grade comparison showed the 1.6mm-FR4 was nearly 28% better than its thinner counterpart, and this again decreased to just 0.6% for the BT laminates.

Overall, the following observations were obtained:

a) The BT substrate showed a consistent distortion rate, regardless of thickness

b) The 1.6mm-thick candidates out-performed their respective thinner counterpart

c) At 1.6mm thickness, both FR4 and BT showed an almost equal rate of substrate distortion.

The same ANOM showed that the distortion for the ceramic alumina substrate was the most serious at 70% of the overall sample investigated. The result indicated this material as the least suitable for the proposed encapsulation technique.

For minimum substrate distortions, the conditions with low melt temperature (nearly 8% lower defect rate), low mould temperature (nearly 2%) and high holding pressure (nearly 10%) were found from the ANOM to be the most favourable injection settings.

Although the glob-top factor was observed to be significant from the ANOVA, the results from ANOM, however, showed an almost constant merit of substrate distortion amongst the three investigated materials: epoxy – 40.6%, silicone – 43.3% and PUR – 44.3%. It was not anticipated that this variable would have any significant bearing on the failure modes explored in this analysis. Nevertheless, the samples with a double-layer of epoxy glob-top were found to have the lowest distortions.

These current analyses indicated that unfilled polymers of Nylon and Acetal were the two most optimum grades and this apparent contradiction to previous work will be investigated further.
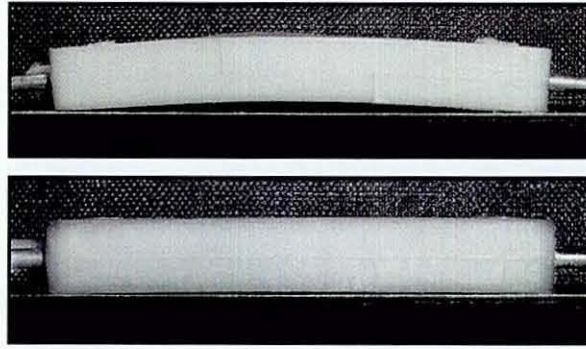
Figure 3-19 Warpage phenomena of plastic moulded module

(a)

(b)
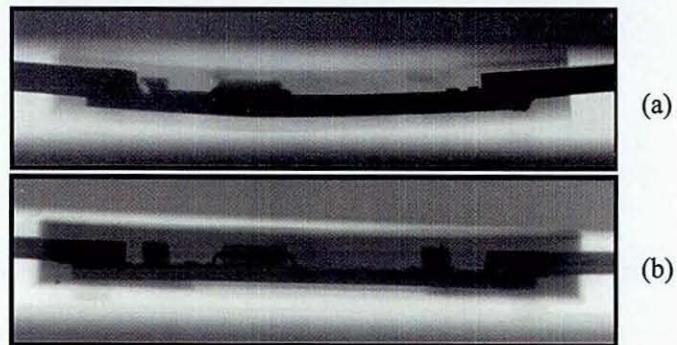
Figure 3-20 Distortion of the embedded substrate

Local buckling
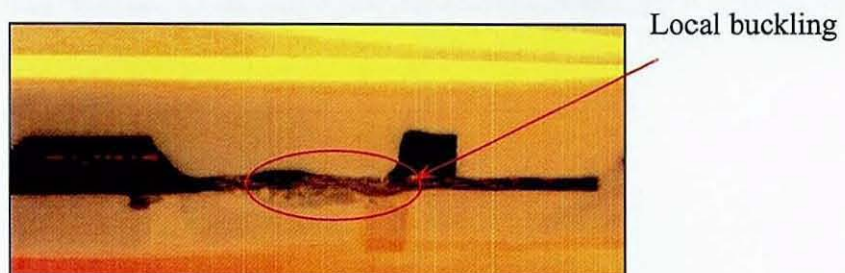
Figure 3-21 Local deformation of thinner substrate
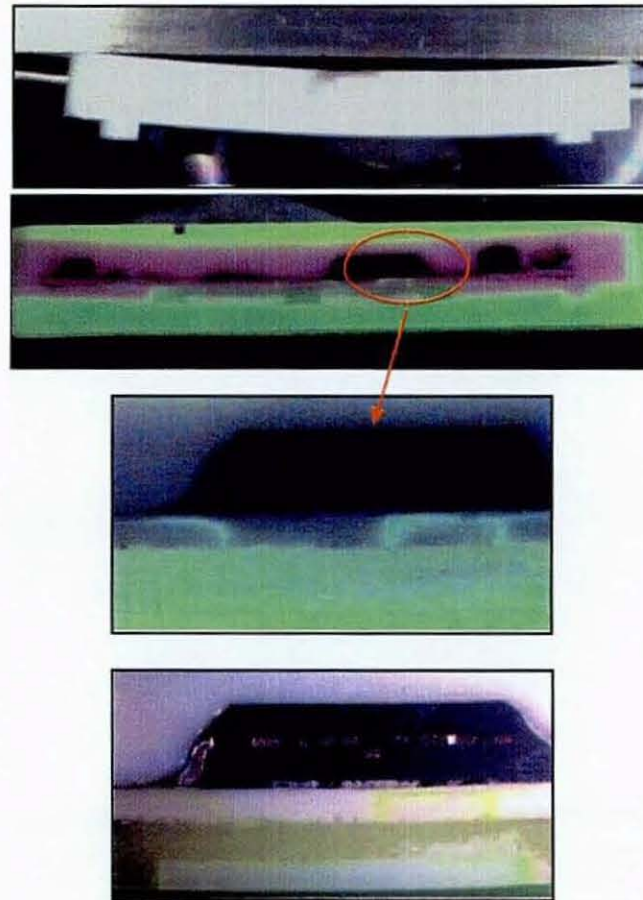
Figure 3-22 Cracking of ceramic substrate under injection stresses

3.4.4.4.   Dye Penetration Severity Analysis

The essence of the dye penetrant investigation mainly related to the interfacing layers'
integrity in the moulded module and it was designated to discover whether damage would
arise from the thermal and mechanical stresses of the injection moulding process. The quality
of adhesion or cohesion at the following interfaces was inspected:

    d) holding pin - moulding polymer

    e) supporting peg - moulding polymer

    f) substrate - moulding polymer

    g) glob-top - moulding polymer

    h) glob-top - substrate

Leakage along any point of the above interfaces will permit the penetration of the micro-scale fluorescent dye into the body of the plastic module, analogous to moisture ingress in the operating environments. Figure 3-23 shows an image of one such observation in the experiment. The severity of dye penetration into the overmoulded part was found from the ANOVA to be largely dominated by the moulding material factor (almost 40%), and to lesser extents, the injection parameters of holding pressure, melt temperature and injection pressure.

From the actual experimental results, the adhesion between the moulding materials and polypropylene supporting cradles was found to be the weakest. Although the degree of dye penetration was anticipated to correlate to the difference in the coefficients of thermal expansion (CTE) between the interfacing polymers, it was found to be non-linear. This resulted in inspection discrepancies, where the sources of leakage for dye traces were not easily and clearly identifiable. This occurred in the sample shown in Figure 3-23.
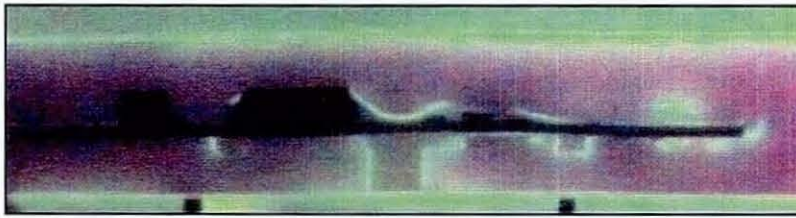
Figure 3-23 Dye penetration into the plastic module

The traces of dye along the bottom surface of the substrate originated from the supporting peg–polymer interface. However, the same conclusion could not be made with the dye along the top of the glob-top layer. Based on this argument, the ANOVA results for this failure mode were perceived to have skewed towards the moulding polymer factor. Nevertheless, the dye penetrant inspection had reliably validated the solidarity of the adhesion integrity between the glob-top materials and the substrates, which was found to have formed sufficient adhesion to withstand the thermal stresses during the injection moulding process. Through the sectioning across the normal surface of the metallic holding pins embedded within the polymer, it was verified that no significant dye penetration had occurred. The trace dye also enabled the detection of microscopic cracks in ceramic substrates.

3.4.4.5.   Module Deflection Analysis

Warpage of intrinsic polymer moulding is a well-established and widely reported issue with polymer properties, injection parameters and tooling geometry amongst the commonly known causes. In the process investigated here, however, the parity of the CTE between the moulding polymer and substrate laminate becomes another major factor. The ANOVA has shown that the polymer (32.8%), part thickness (28.5%) and substrate thickness (6.6%) were the most dominant variables for part deflection.

From the mean analysis, the glass-reinforced semi-crystalline plastics GR-Nylon and GR-PBT showed mean deflection reductions of approximately 37% and 48% over their respective unfilled polymer. This can be attributed to lower linear CTE difference, increased dimensional stability, homogenous crystallised nucleation and shorter crystallisation time with the presence of fillers. Acetal, with higher crystallinity, undergoes a much higher density increase upon solidification and hence more shrinkage. Overall Acetal produced 16% and 18% higher longitudinal deflection than the unfilled polymers Nylon and PBT, respectively. GR-PBT was found to be the most promising resin in this respect.

The ANOM results showed that thinner moulding produced a mean reduction of 41% in longitudinal warpage. This is due to the shorter solidification cycle required for the lower wall thickness. Also, with higher flexural modulus, BT laminates showed lower warpage over FR4.

CHAPTER 4. MATERIALS ADHESION TO SUBSTRATE SUPPORTS

4.1. Introduction

A known way to support a circuit board within the moulding cavity is by the use of retractable-pin tooling, in which steel pins hold the part at suitable positions (e.g. diagonally at corners), retracting just after mould fill, but before packing occurs, so that no voids would appear in the final product. However, for the electronic assembly process investigated here, it would have been prohibitively expensive to use this type of tooling. Also, it was thought best to decouple part retention issues from those concerning the basic performance of the circuits during the overmoulding process and reliability development stages. Therefore, a technique to support the electronic subassembly in the moulding tool by using a plastic "cradle" on both sides of the substrate was investigated. These cradles were injection moulded from relevant resins and attached to the subassemblies. Overmoulded parts were then subjected to a JEDEC-A104B [JEDEC, 2000] thermal cycling test before the adhesion between the cradles and overmoulding polymers was examined. Although this support cradle approach was subsequently replaced with a contoured tooling design (see Chapter 5), the work conducted to understand adhesion between the cradle and overmoulding polymers nevertheless highlighted important features of the technology.

4.2. Substrate Support Structure

The stage 1 screening experiment in Chapter 3 employed substrate with support structures in its normal axis to reduce its distortions from adverse loading effect caused by an injection pressure difference. The support moulding designed for this experiment is shown in Figure 4-1. The structure had five supporting posts on each side of the circuit board and was attached with adhesive to the board to prevent slippage. Figure 4-2 shows an electronic specimen assembled for this experiment. Eight surface-mounted metal pins had previously been used to locate the electronic circuit within the mould cavity during the encapsulation process. In this moulding design, however, in addition to providing structural supports to the embedded subassembly, the support cradle was also designed to function as a mean of subassembly fixturing in the moulding cavity. This was achieved by locating an extension of each

supporting post into a recess in the tool wall, as illustrated in Figure 4-3. The polymer cradle attached to the circuit substrate was designed to function as warpage reducing supports as well as positioning mechanisms.
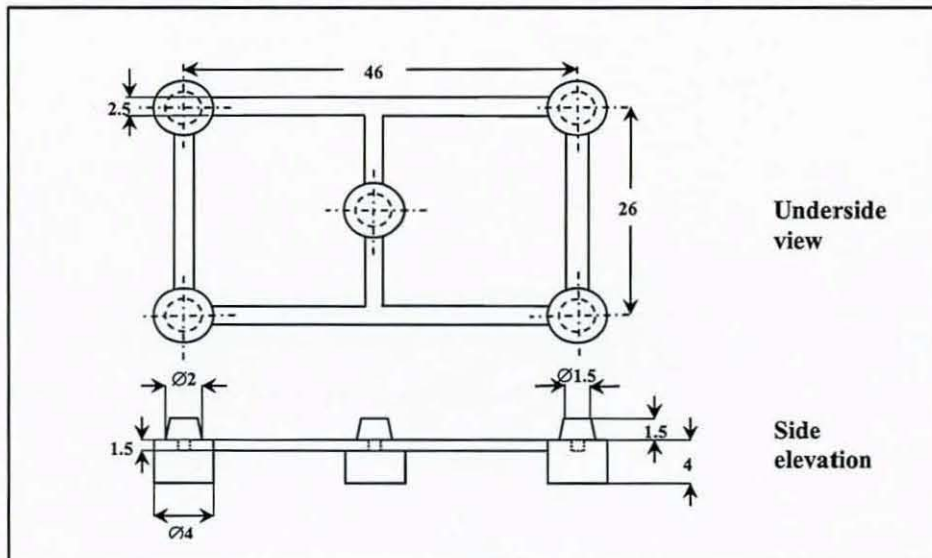
Figure 4-1 The design for the substrate support cradle
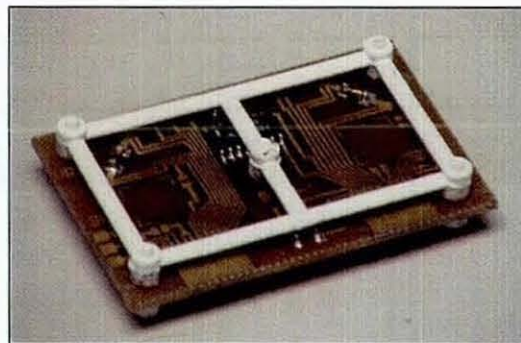
Figure 4-2 Electronic subassembly with attached support cradle
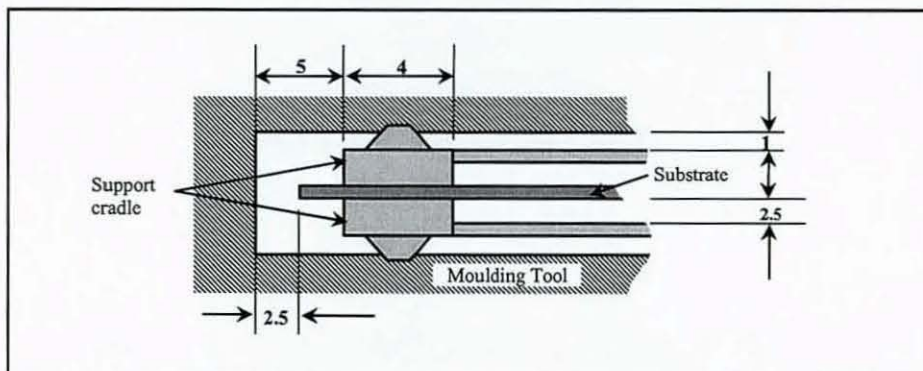
Figure 4-3 Positioning of supported substrate in the moulding cavity

4.3.   Experimental Design

Although initial overmoulding trials with the support structure showed satisfactory rectification to the warpage problem, the interface integrity between the overmoulding and support materials was compromised during the process. This led to leakage issues that would give rise to problems such as moisture ingress and ionic diffusion. The main objective of this experiment was to investigate the integrity of this polymer-polymer interface by exploring a range of suitable polymer combinations and various overmoulding settings, with the aim of identifying the materials most suitable for the proposed encapsulating process.

In this experiment, the support structures on both sides of the circuit substrate were equivalent to the preform from the first moulding shot, as suggested in the definition of the overmoulding technique. The subsequent shot of a second polymer around the electronic subassembly within the confined moulding cavity produces thermo-mechanical strains, thus inducing internal and external structural stresses. Factors such as CTE disparity, differential shrinkages and interface adhesion will therefore play important roles in the quality of the final article.

4.3.1. Materials Selection

Although the previous experiments had not included ABS, it was selected for these trials. ABS is an amorphous compound (in comparison to the semi-crystalline PBT) and although its resistance to solvents such as petrol is not very good and heat deflection temperature (HDT) not high, it is suitable for less arduous in-cab applications (e.g. dashboard instrumentations, door switches/sensors, airbag circuitry, etc.). The overmoulding polymer materials selected for this experiment were:

a) Crastin LW9130 from DuPont, a 30% glass-reinforced polybutylene terephthalate (GR-PBT) advocated from our previous experiment results, and

b) Novodur P2HGV from Bayer, a 16% glass-reinforced acrylonitrile-butadiene-stylene (GR-ABS).

For each of the GR overmoulds, support structures of the respective virgin/unfilled grade material and a polypropylene (PP) were tested. These were:

a) Valox 325F unfilled PBT from GE Plastics,

b) Novodur P2MC unfilled ABS from Bayer, and

c) Fiberfil, a chemically modified PP semi-crystalline homopolymer from DSM.

4.3.2. Experimental Procedure

Table 4-1 lists the injection parameters in this experiment. For each of the overmoulding materials, two injection pressures with two holding pressures were investigated. The moulding pressures were maintained for both overmoulding materials. The injection pressures were selected at a nominal value of 70bar and a maximum of 120bar. The holding pressures were set to 40 and 80bar, respectively. The mould temperature for overmoulding of both the glass-reinforced resins was maintained at a constant 80°C. The melt temperature for GR-PBT and GR-ABS was 250°C and 240°C respectively. Injection of the molten polymer was in the longitudinal direction of the substrate, corresponding to the "end-gate" design used in our previous experiment.

Trial no.	Overmoulding material	Support material	Injection pressure [bar]	Holding pressure [bar]
1	GR PBT	PBT	120	40
2	GR PBT	PBT	120	80
3	GR PBT	PBT	70	40
4	GR PBT	PBT	70	80
5	GR PBT	PP	120	40
6	GR PBT	PP	120	80
7	GR PBT	PP	70	40
8	GR PBT	PP	70	80
9	GR ABS	ABS	120	40
10	GR ABS	ABS	70	80
11	GR ABS	PP	120	40
12	GR ABS	PP	70	80

Table 4-1 Design of experiment (10 bar ≡ 1 MPa)

4.3.3. Results Analysing Mechanisms

Penetrant dye test (Mil. Std. 883 Test method 1034), where the overmoulded parts were impregnated in a dyed epoxy resin in vacuum and then cross sectioned, was employed as the failure analysis mechanism in this experiment. Any ingress of the dye into the module via material interface leakage would be visually detectable under UV light.

The encapsulated electronic product was designed with the objective to be operational in the harsh environments of automotive electronics, including extreme temperature fluctuations that may increase the likelihood of interface failures. Simulation of this condition was accounted for by incorporating the JEDEC-A104 test scheme to determine the ability of components to withstand mechanical stresses induced by alternating high and low temperature extremes

[JEDEC, 2000]. Half of the sample population in the experiment was subjected to a 200-cycle rapid dual-chamber -40°C to $+85^\circ$C temperature cycling (20 minutes dwell at each temperature and 8 seconds transfer time) prior to the dye-penetrant test. From a sample size of four units for each trial setting, two were then put through the thermal cycling.

4.4.   Results Discussion

After vacuum potting all the overmoulded specimens in the dye, these samples were then longitudinally cut by a metallurgical saw, to about 2-4mm away from the support pillars. These sectioned samples were then cleaned and polished to the desired plane using rotational grinding machines, through descending coarseness. Video micrography was used to inspect the samples under bright luminescent and UV lighting. The degrees of dye penetration in each case were analysed and systematically graded.

4.4.1. Dye Penetrant and Thermal Cycling Analyses

Figure 4-4(a) shows the images of a cross-sectioned support pillar from an as-moulded sample (not subjected to the thermal cycling) while Figure 4-4(b) shows those of a thermally cycled sample. Both samples are from Trial no.1 (GR PBT-PBT) in the DOE Table 4.1. As shown by the top and bottom pictures, the traces of the fluorescent dye along the leakage paths are more visible under the UV light. A comparison between the two cases of similar injection condition clearly reveals the difference in the interface integrity as a result of the thermal cycles. The effect of alternating extreme temperatures has degraded the adhesion at the materials' interface, magnifying the influence of materials properties incompatibility This is evident from increased dye penetration into the module via the weakened interface, in this instance by more than 50%.

The images in Figure 4-5 compare two samples from Trial no. 7 in the DOE, which overmoulded GR-PBT around a PP support structure. This combination of polymers exhibited the most serious degree of dye penetration into. A leakage penetration average of nearly 90% was observed in the as-moulded specimens, increasing to 95-100% in the thermal-cycled population. The best interface adhesion was shown by Trials no. 9 and 10, with GR-ABS overmoulded onto unfilled ABS. In both sets of pressure permutations, no trace of the penetrant dye was found in the cross-sectioned samples. Similar findings were observed with the samples that were subjected through the thermal cycling phase. Figure 4-6 shows the images of two of these samples.
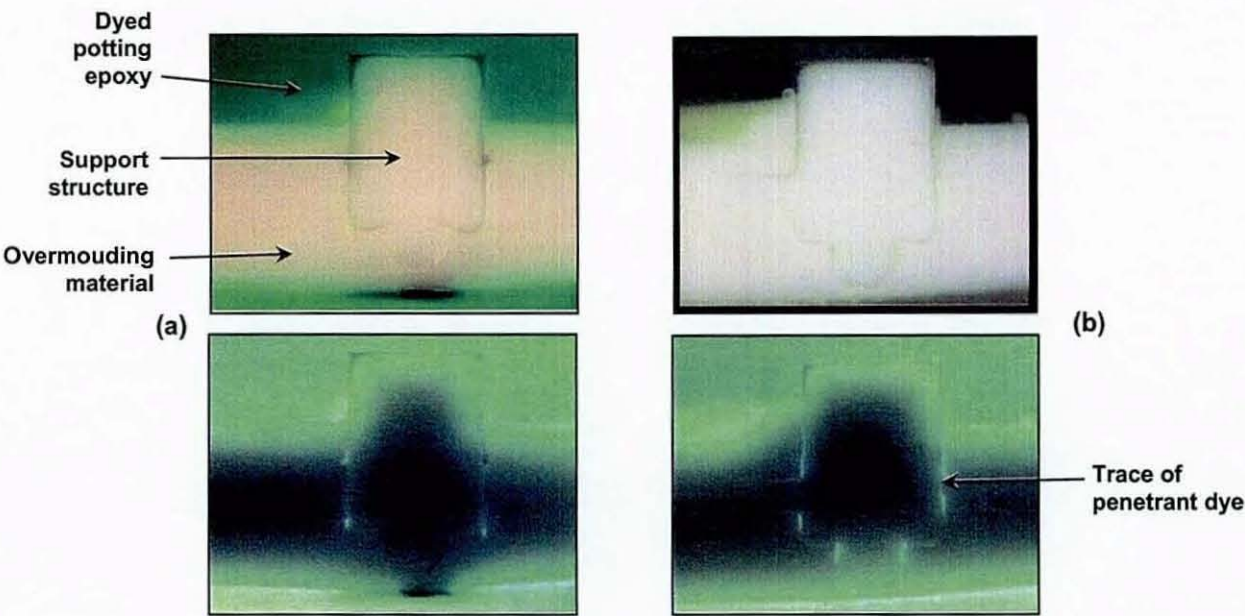
Figure 4-4 GR-PBT overmould and PBT support (a) without TC; (b) with TC
[Injection condition 1]
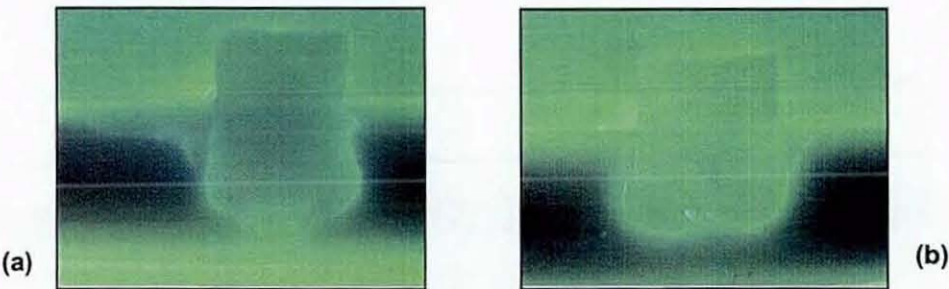
Figure 4-5 GR-PBT overmould and PP support (a) without TC; (b) with TC
[Injection condition 7]
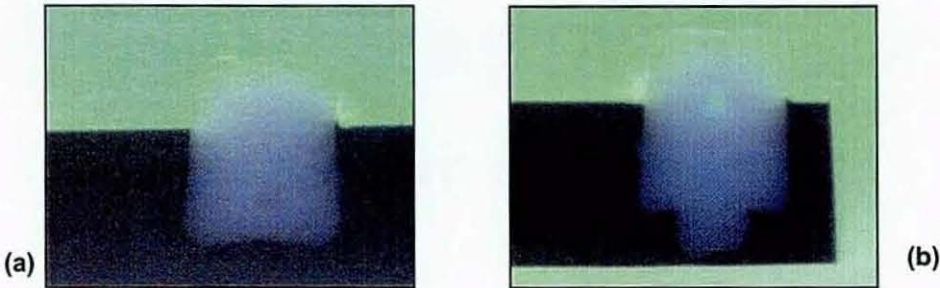
Figure 4-6 GR-ABS overmould and ABS support (a) without TC; (b) with TC
[Injection condition 9]

4.5. Overall Materials' Compatibility

The results from the dye penetration grading process is summarised into the bar chart shown in Figure 4-7. With exception to the GR ABS-ABS trials, it was apparent that the rapid twin-chamber temperature cycling process resulted in significant deterioration of the integrity at the material interfacial layer.

The adhesion of glass-filled overmould with its respective unfilled support cradles was overall significantly higher. In comparison to the other unfilled materials, the PP-moulded support structure has clearly exhibited lower degrees of adhesion to either of the overmoulding glass-reinforced polymers. For corresponding injection conditions, the GR PBT-PP trials have shown between 40-70% more dye penetration. A similar trend was evident in the GR ABS-PP cases, with the degradation increased to 60-80%. The dye penetration rates extended to almost complete intrusion of 85-100% after further erosion as a result of the temperature cycling. It was obvious that the PP material has failed to form satisfactory adhesion with the overmoulding polymers and would be unsuitable for this purpose.

By keeping the moulding pressures low, the GR PBT-PBT interface also showed satisfactory adhesion with only 20% leakage to the penetrant dye. However, a higher level of either injection pressure or holding pressure was found to almost double this leakage.

With zero traces of dye in both as-moulded and thermally cycled specimens under all moulding pressure conditions for the overmoulding of GR ABS onto unfilled-ABS support structure, this materials combination was found to have created the most robust interface. A near perfect bonding has been achieved at this inter-material boundary and a complete seal has formed along the weld-line at the periphery of the support structure.
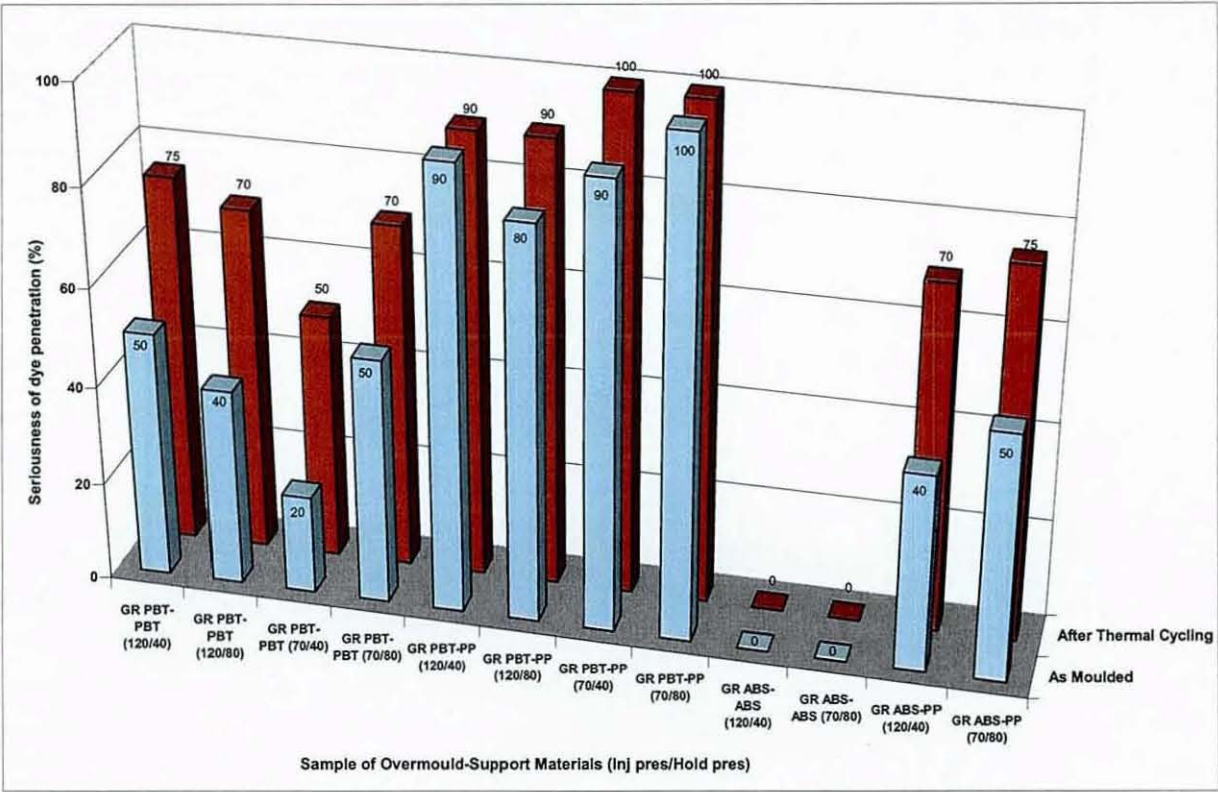
Figure 4-7 Grading of dye penetrations for all injection conditions

4.6.   Effect of CTE Difference

In order to study the influence of the CTE disparity on the adhesion quality at the interface of the GR overmould and the unfilled support structure, a comparison of the effective CTE difference of the two materials against the average dye penetrant leakage was made. Table 4-2 lists the properties of the materials used in the experiment and Figure 4-8 shows this comparison plot.

The CTE difference in each materials combination is: 100ppm/°C for GR PBT-PBT, 61.6ppm/°C for GR PBT-PP, 46ppm/°C for GR ABS-ABS and 14.4ppm/°C for GR ABS-PP respectively. The experiment, however, showed that the effect on the interface bonding as a result of the difference in CTE of the interfacing polymers had not prevailed as expected. It can be seen from Figure 4-8 that although more matching CTE values were obtained with the PP polymer as the support structure, the leakage to dye penetrant increased significantly for both glass-reinforced overmoulding polymers.

	Valox 325F	Crastin LW9130	Novodur P2MC	Novodur P2HGV	Fiberfill
Polymer type	Unfilled PBT	30% GR PBT	Unfilled ABS	16% GR ABS	Unfilled PP
Linear CTE ($\times 10^{-5}$ cm/cm/°C), parallel to flow	81.0	30.0	100.0	54.0	68.4

Table 4-2 CTE value of experimental materials
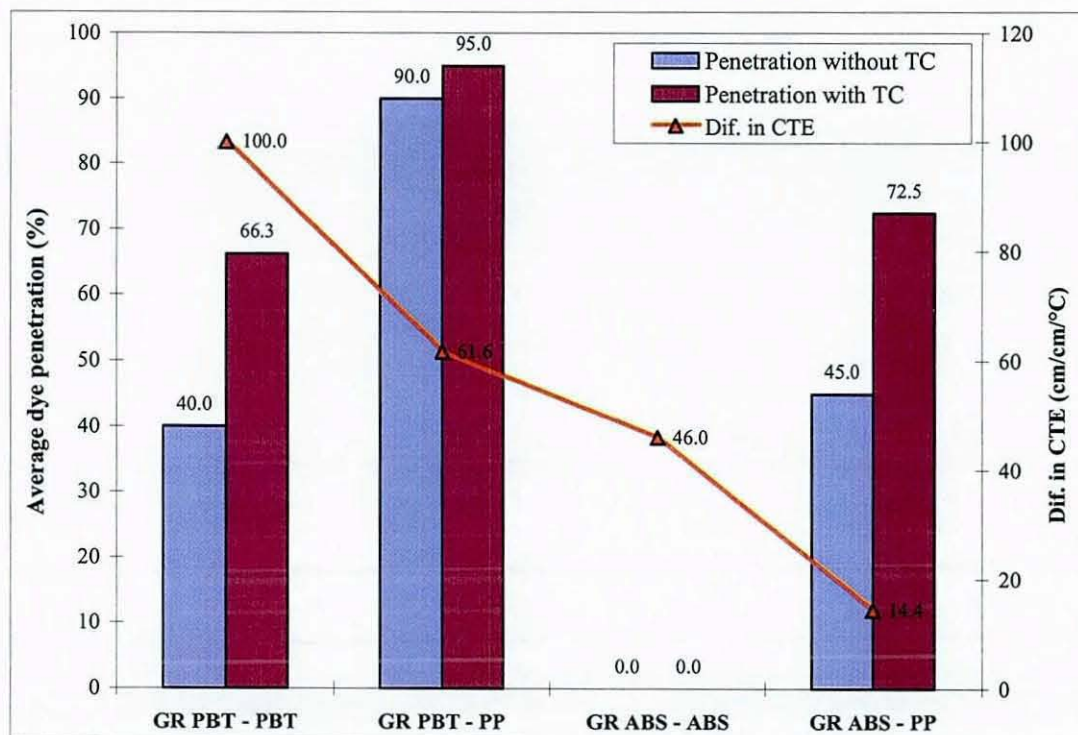
Figure 4-8 Comparison of CTE difference with average dye penetration for various materials interface

4.7. Effect of Polymer Morphology

The size and shapes of the molecules, together with their distribution patterns, play an important role in determining the properties and processibility of a plastic material. Some plastics are formed by aligning themselves into long chains of molecules while others are formed with complex branches or lateral structures. All these forms exist in three dimensions. Because of the geometry, or morphology, of these molecules, some can align closer together than others. Morphology can have influences on a plastic such as physical, mechanical, thermal and electrical properties.

In general, plastic molecules that can be packed closer together more easily form *crystalline* structures in which the molecules align themselves in some orderly pattern. This type of polymer tends to develop higher mechanical strength, such as resistance to creep, heat and stress cracking, in the direction of the molecules.

Amorphous polymers like ABS have molecules randomly oriented in different directions and undergo only small volumetric changes when melting or solidifying and hence have lower thermal shrinkage over semi-crystalline materials. This molecular structure also allows easier diffusion of the high temperature molecules across the polymer interface during the overmoulding to promote greater adhesion.

On the other hand, molecules of a semicrystalline plastic such as PBT align themselves in some orderly pattern during processing and develop higher strength in the direction of the molecules. These backbone molecular chains act as a deterring factor to the formation of good interface bonding because the self-diffusing molecules have to overcome high energy barriers to develop considerable interpenetration depth. Furthermore, because the molecules are more densely packed, semicrystalline polymers suffer from higher volumetric shrinkage during solidification. Because of this variation in molecular structures, semicrystalline polymers have higher shrinkage tendency than amorphous types [Rosato, 1995]. A brief comparison between these two types of plastic is presented Table 4-3.

Table 4-4 lists the linear mould shrinkage value for the materials investigated in this experiment. It is clear that the amorphous ABS resins have significantly lower shrinkage tendencies than the semi-crystalline grades. Comparing the GR grades, although containing only 16% of glass filler, GR ABS undergoes only about 1/3 shrinkage of that experienced by the 30% GR PBT. Similarly, the unfilled ABS undergoes only 1/2 and 1/10 shrinkage when compared to the unfilled PBT and PP, respectively.

Semicrystalline	Amorphous
Sharp melting temperature	Broad softening temperature range
Usually opaque	Usually transparent
High shrinkage	Low shrinkage
Fatigue/wear resistant	Poor fatigue/wear

Table 4-3 Distinctions between semicrystalline and amorphous

	Valox 325F	Crastin LW9130	Novodur P2MC	Novodur P2HGV	Fiberfill
Polymer	Unfilled PBT	30% GR PBT	Unfilled ABS	16% GR ABS	Unfilled PP
Shrikage (%)	0.90-1.80	0.25	0.45-0.65	0.15	1.30-2.00

Table 4-4 Shrinkage value of experimental materials

Figure 4-9 illustrates the comparisons of the degrees of dye penetration against the maximum difference in shrinkage values for each polymer-polymer combination. It is clear that there exists a relationship between the shrinkages and interface adhesion for unfilled resin overmoulded with its corresponding glass-filled variant. GR ABS-ABS had a maximum shrinkage difference of only 0.5% and resulted in 0% dye penetration, whilst GR PBT-PBT produced 66.3% penetration after thermal cycling for its 1.55% in shrinkage difference. In the cases of PP cradles, overmoulding with GR ABS produced lower penetration (72.5% after thermal cycling) than that with GR PBT (95% after thermal cycling) although the latter had a slightly smaller shrinkage difference, i.e. 1.85% for GR ABS against 1.75% for GR PBT.

This observation has been found to correlate with the results obtained from the experiment (see Figure 4-7). From this result of the shrinkage of the various polymers, it is evident that the morphologies, specifically the shrinkage properties of the plastics, have greater influence on adhesion at the interface of different polymers.
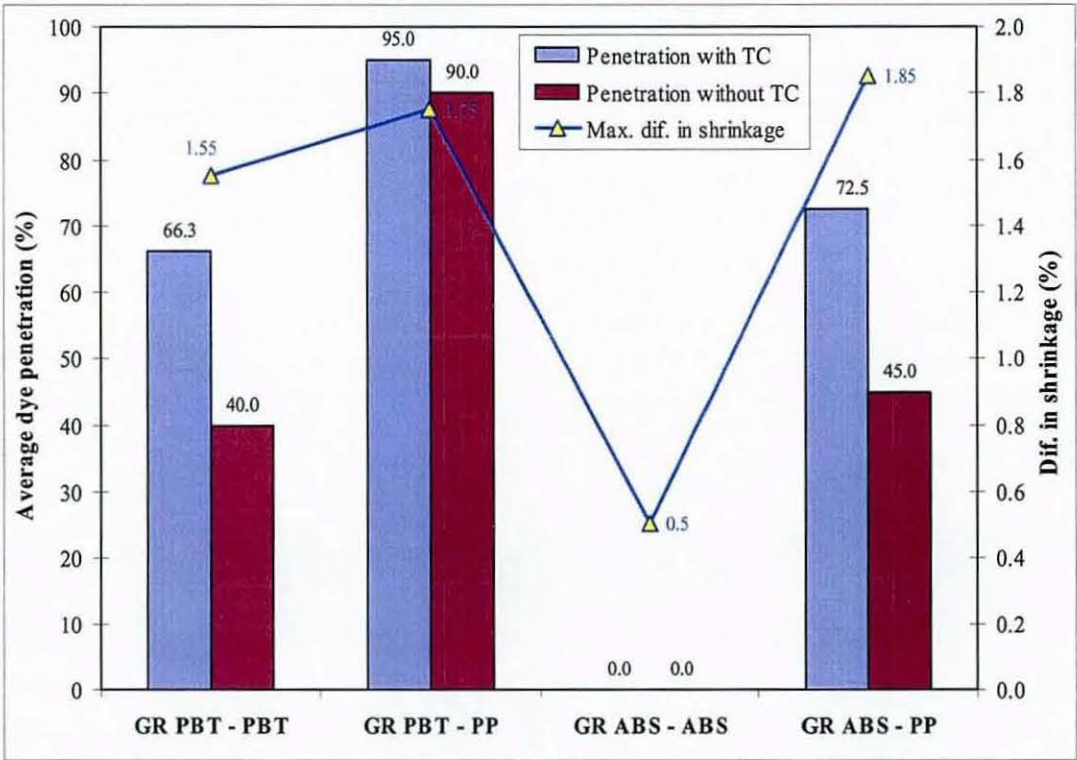
Figure 4-9 Comparison of shrinkage difference with average dye penetration for various
materials interface

4.8.   Statistical Optimisation

The results from the adhesion study were subsequently used in the DOE software Design
Expert, which has the optimisation capability to simultaneously evaluate all the factor levels
and searches for an optimised combination that simultaneously satisfy the requirements
placed on each of the responses and factors. A numerical optimisation approach with
minimum dye penetration as the desired goal was chosen for the study. A desirability function
was generated by the software and used to find a point that maximised the function,
characterised by the term *desirability* which ranged from zero to one (least to most desirable
respectively). The analysis produced perturbation plots of the parameter settings as a function
of desirability at the optimum response.

This exercise therefore statistically identified the most desirable overmoulding materials and
pressure conditions for the interfacial adhesion response. The selected permutations were
found to be in agreement with the actual experimental findings. These conditions were:

a)   *GR ABS- ABS*

Although the injection and holding pressures were found to be non-contributing

factors in the experiment, the statistical analysis software suggested a lower injection pressure and higher holding pressure as the best condition for this material interface. Figure 4-10 shows the result that was found with complete interface bonding.

b) *GR PBT-PBT*

In spite of the lower desirability of 50%, the most optimised condition suggested for this materials interface could only produce 80% adhesion at best, achieved with low injection and holding pressures. This is shown in Figure 4-11.

c) *GR ABS-PP*. As seen in Figure 4-12, the best condition for this selection of materials would still result in a 30% dye penetrant leakage. At the desirability of a low 25%, this combination of polymers would not be suitable for the proposed process.

d) *GR PBT-PP*

No solution of any leakage lower than 75% could be generated from the statistical analysis for the materials combination.
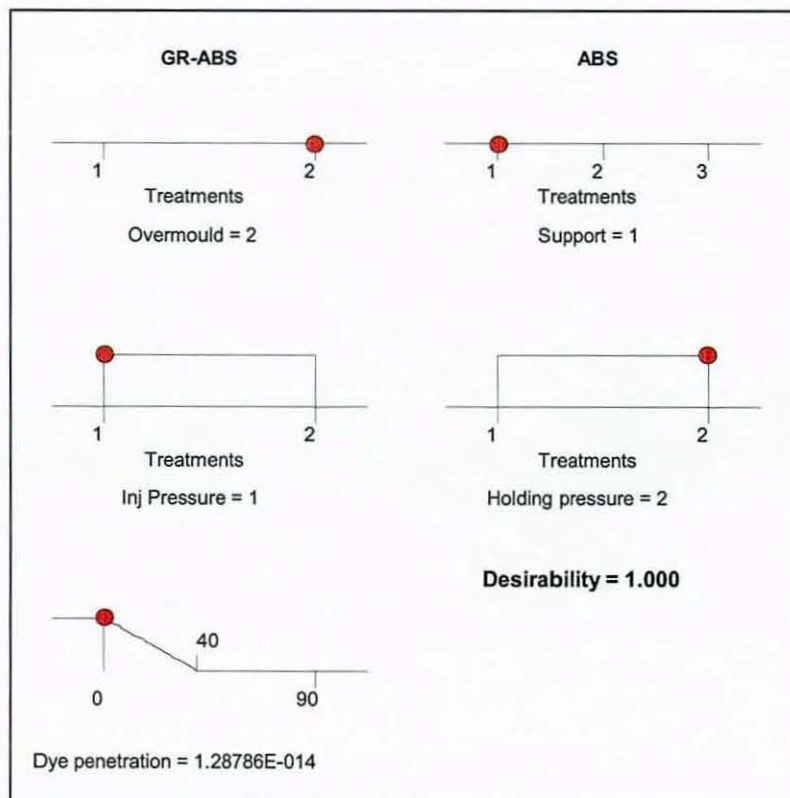
Figure 4-10 Statistical optimisation for GR ABS-ABS interface
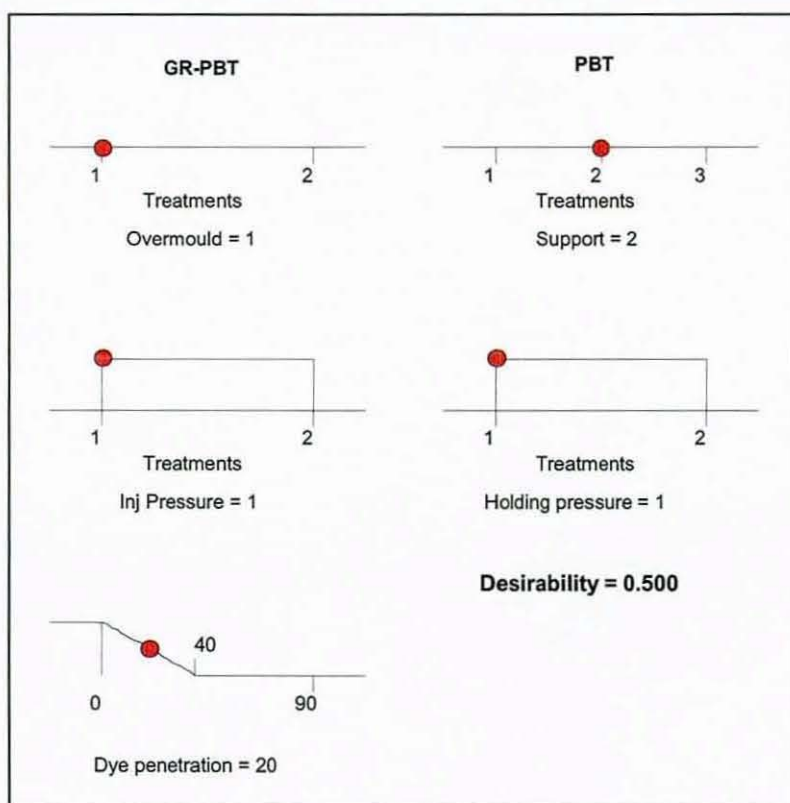
Figure 4-11 Statistical optimisation for GR PBT-PBT interface
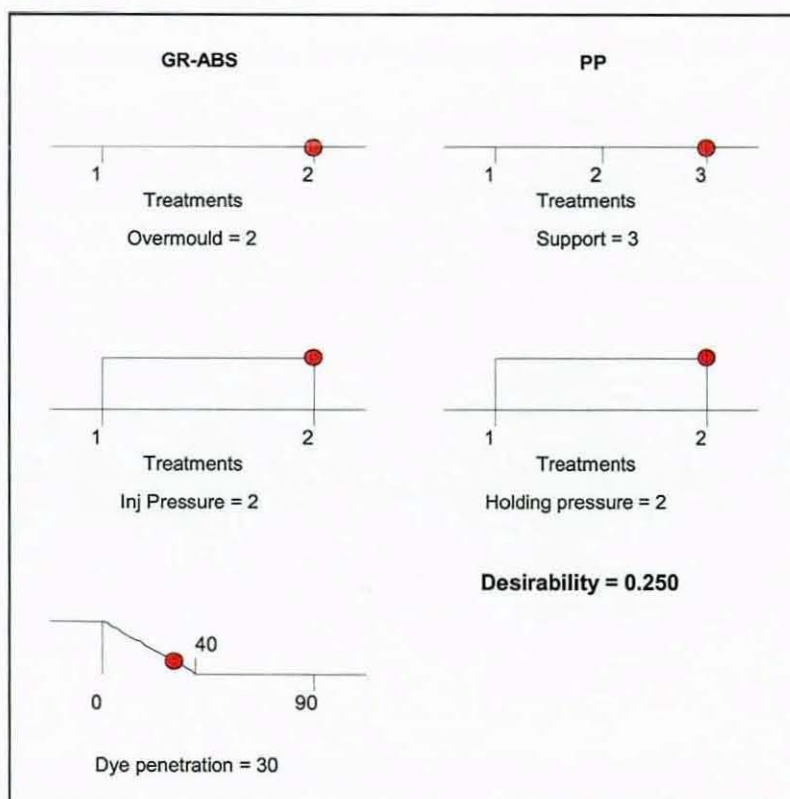
Figure 4-12 Statistical optimisation for GR ABS-PP interface

CHAPTER 5.   MOULDING TOOL RE-ENGINEERING FOR PROCESS IMPROVEMENT

5.1.   Introduction

In this chapter, a number of injection moulding issues unique to the proposed electronic encapsulating process are discussed. While the stand-off support cradle experiment in the previous chapter managed to reduce the deflection of the embedded substrate, the presence of these structures formed an obstruction to the flow front of the advancing polymer melt. As such, they became an impediment to achieving a balanced flow over both surfaces of the substrate and resulted in a differential cross-sectional stress, resulting in uneven thermal shrinkage that deformed the moulded plastic module. This stress would propagate through the encapsulant material during its cooling to instigate fatigue failure in the embedded electronics.

The presence of the support structure in a moulding cavity of uniform cross-sectional thickness also constricted the melt flow during the filling cycle. The result was the formation of weld-lines that reduced structural strength in the final plastic article. Furthermore, the restriction on the flow increased the likelihood of short-shots in the overmoulding cycle. A variety of moulding tool designs were experimentally exploited in an attempt to minimise the board deformation caused by the uneven flow front. Process models generated using CAE software were used as a verification tool to supplement the concept.

5.2.   FEA Flow Modelling

Extensive finite element modelling was undertaken elsewhere (TRW Automotive and Middlesex University) for verification as well as to derive design guidelines for the staged experiments. In addition to the structural thermo-mechanical models simulated using NISA FEA software (as discussed in Section 3.6) [De Cooper Jones, 1999], IDEAS-MoldFlow was used to analyse the dynamics of the overmoulding process and the warpage response of the subassembly [Schmidt, 1999]. Although the work was not carried out by the author, the results from these activities are reviewed in this chapter in order to form a complete insight into the engineering of a novel overmoulding tool for the proposed technology.

As a concept verification tool to the actual experimental investigations, the CFD models were built to explore alternative process envelopes and/or tooling designs to achieve uniformity of melt flow in the cavity during an overmoulding cycle. An additional objective was to look into alternative materials for reduced subassembly loads and shrinkage-warpage response. To this end, progress of the melt flow front at different stages in the mould cavity was simulated and provided useful understanding of the filling phase.

5.3.   Equi-thickness Moulding Tool

Figure 5-1 [Schmidt, 1999] depicts the model built for the embedded subassembly. The substrate used was of size $55\times35mm^2$ and thickness of 1.5mm with its support frame, showing only the surface-mounted IC as this represented the largest and most obstructive component. Note that the model shown has three flexible cables attached to the substrate, which was for the next design of the subassembly and will be discussed in more detail in the next chapter. Material used for this simulation was Zytel nylon-66, as experimented with in the previous trials. The melt temperature of the plastic was 295°C, with the temperature of the mould at 80°C.
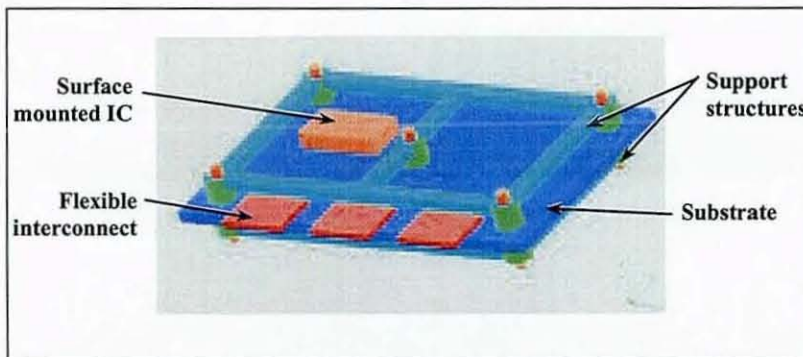
Figure 5-1 Model of the embedded subassembly [courtesy of Schmidt, 1999]

Figure 5-2 [Schmidt, 1999] shows the models constructed for an analysis of the conventional moulding design. The cavity had a fixed rectangular cross-sectional area that fitted evenly around the electronic circuit, as used in the experiments in Chapters 3 and 4. The height of the cavity was fixed at an offset of 2.0mm from the highest component on the substrate (in this case, the frame of support structure), giving the cavity a size of $60\times40\times10.5mm^3$, leaving a uniform gap of 2.5mm from the edges of the substrate (see Figure 4.4 for illustration). The injection of polymer melt was from the far-end of the cavity.

Figure 5-2(a) and (b) show the advance of the flow front in the cavity as a function of time. The theoretical filling time observed was 1.38 seconds, but the models indicate a lack of uniform filling in the last 2/3 of the cavity. A zone of low pressure formed beneath the PCB and behind the IC. A significant drop in temperature of about 24°C (295°C-271°C) during the filling cycle was observed. The non-uniform flow front created the so-called "racetrack effect", exhibiting a lead-lag of flow fronts above and below the subassembly.

Because of the presence of many sections with differing thickness, the bulk temperature of the module was not homogenous at the end of filling, as shown in Figure 5-2(c and d). As the result of racetrack effect and uneven temperature distribution, a residual stress was established within the module and induced the thermal shrinkage that led to warpage.

The formation of weld lines and air traps simulated in the flow models are shown in Figure 5-3. It can be seen that weld lines developed as result of the non-uniform melt flow. A weld or knit-line occurs whenever a polymer flow splits and recombines. In injection overmoulding, weld-lines result when the flow splits as it flows around an obstacle such as a pin in the mould cavity. This causes an inhomogeneity in the polymer's structure due to the disturbance in morphology [Kazmer and Roe, 1994]. Often the mechanical strength in areas where weld-lines occur is reduced as direct result of the localised change in the morphology of the polymer structure. Additionally, as the melt progresses through the cavity, it displaces the air in front of the flow. Even if adequate venting is provided, the two flow fronts must displace the air between them when they meet. Failure in complete displacement results in formation of air traps.
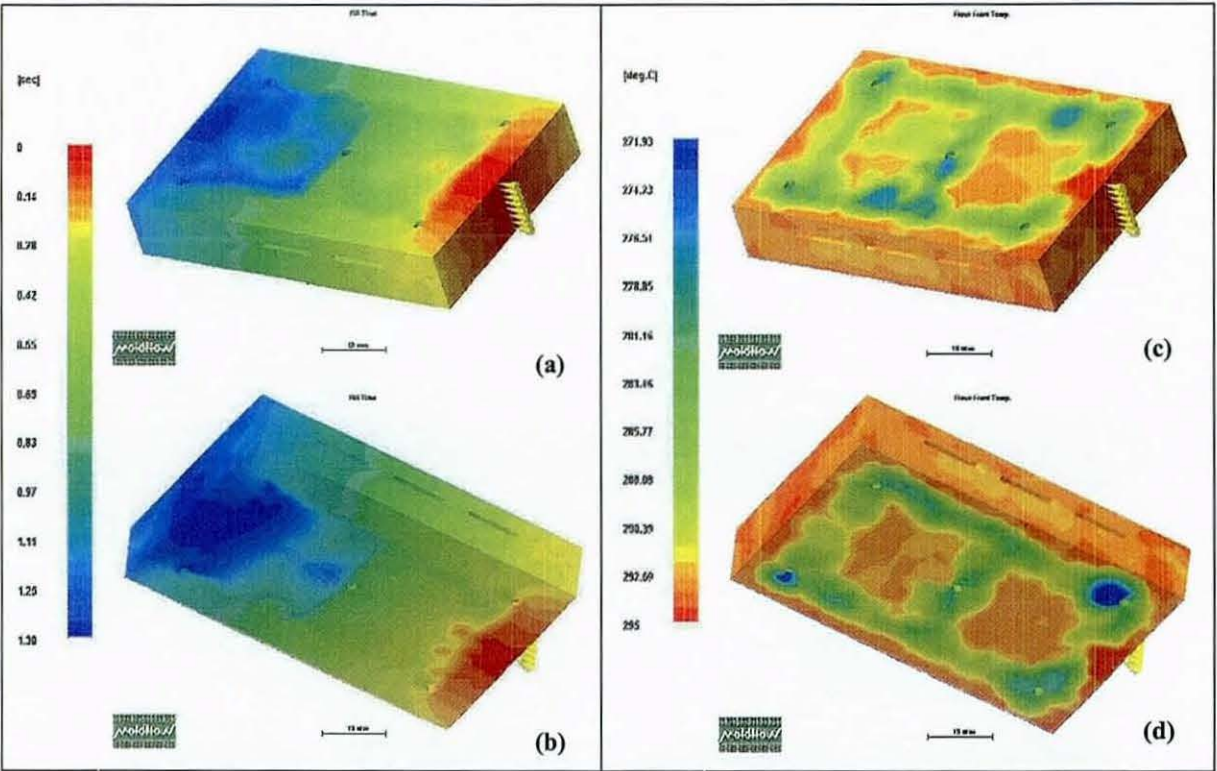
Figure 5-2 Flow models for equi-thickness rectangular moulding cavity: (a) and (b) fill time analysis, (c) and (d) flow front temperature [courtesy of Schmidt, 1999]
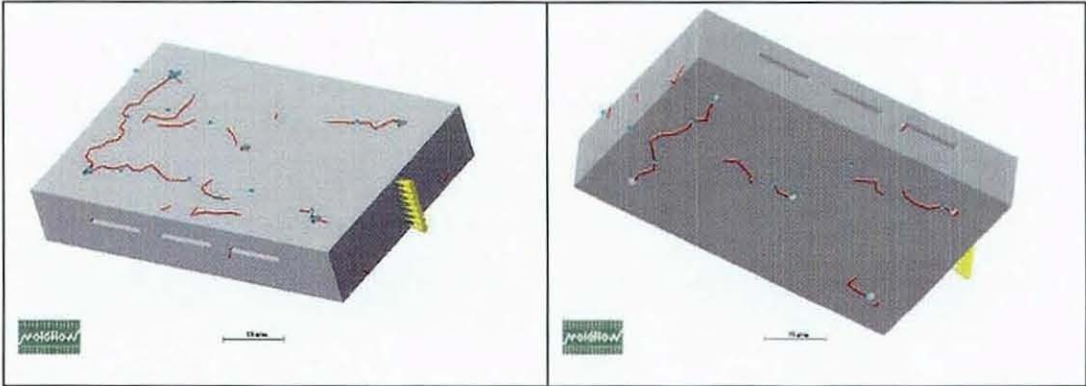
Figure 5-3 Weld lines and air traps at the end of injection cycle for equi-thickness rectangular moulding tool [courtesy of Schmidt, 1999]

5.4.   Topographical Moulding Tool

In an attempt to minimise the deformation from non-uniform flow fronts in the mould cavity, models simulating a "contoured" cavity showed substantial improvement. In this case, the tool surface was altered to follow the topography of the substrate and components on the electronic subassembly and so provide a consistent cross-sectional channel to reduce the lead-lag racetrack effect.

5.4.1.   FEA Models

The modelled cavity has a maximum thickness of 10.0mm. The surfaces of the tool were fixed at a distant of 2.5mm from the edges of the substrate. On the top and bottom of the subassembly, however, the tool was profiled to follow the topography of the various components at a constant distance of 2mm. The gap of 1mm between the tool and the support frame was maintained. Figure 5-4 shows the cross section drawing of this contoured tool. The injection gating position remained similar to the equi-thickness tool above. The structural model of the moulded part is showed in Figure 5-5 [Schmidt, 1999]. This is the simplified model using a subassembly with a representative 'gull-wing' IC and the two support structures, identical to the model discussed in section 5.3 above.
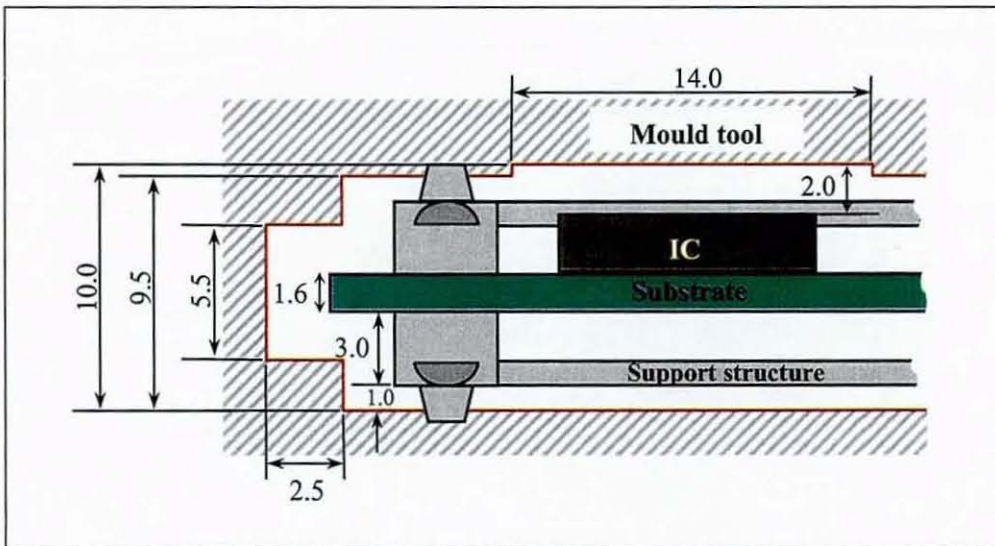
Figure 5-4 Cross-section drawing of the topographical tool

The fill time and flow front temperature simulation results are shown in Figure 5-6. The fill time analysis in Figure 5-6 (a) and (b) shows a uniform filling with no difference between the top and bottom surface of the substrate. The gaps of the support structure and the tool surface

were found to fill at the same time as the transversal location of the substrate. The flow was
nearly symmetrical along the longitudinal centre line of the PCB. The last point of fill was the
short-sided wall opposite the injection location. The model also showed a decrease in the
cavity filling time to only 0.68 seconds.

As seen in the models in Figure 5-6 (c) and (d), the flow front temperature along the substrate
was more uniform, if compared with the equi-thickness cavity. Moreover, the temperature
difference across the substrate was less than 5°C, with the coldest spots at the circular
surfaces of the support pillars. With a drop in temperature of only about 9°C (295°C-286°C)
during the filling cycle, the plastic was within its moulding window and the melt lines that
occur did not cause any crack that would lead to humidity ingress. A comparison between
Figure 5-7 and Figure 5-3 clearly shows that the melt/weld lines and air traps were
significantly reduced from those of the equi-thickness tool.

The variable topology re-design has given a more suitable hydro-dynamic path for the melt
flow fronts and, as a result, substantial improvements were indicated for the flow uniformity,
with little evidence of high temperature or pressure differentials and weld line effects.
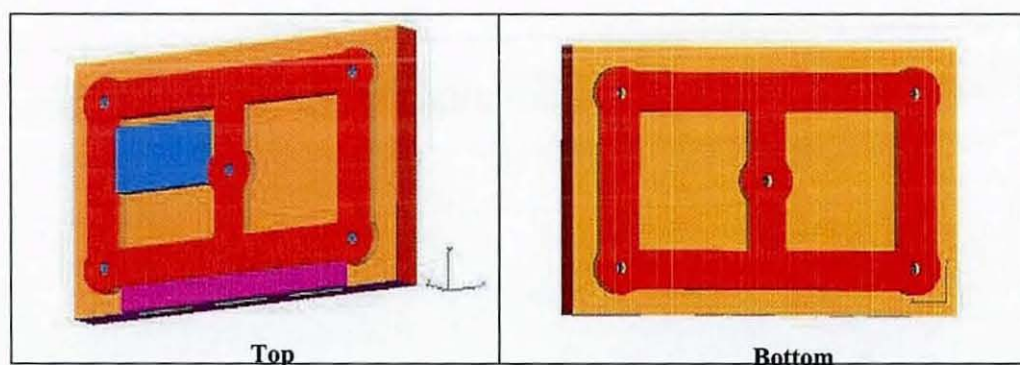
**Figure 5-5 Structural model of the plastic part moulded from topographical tool [courtesy of
Schmidt, 1999]**
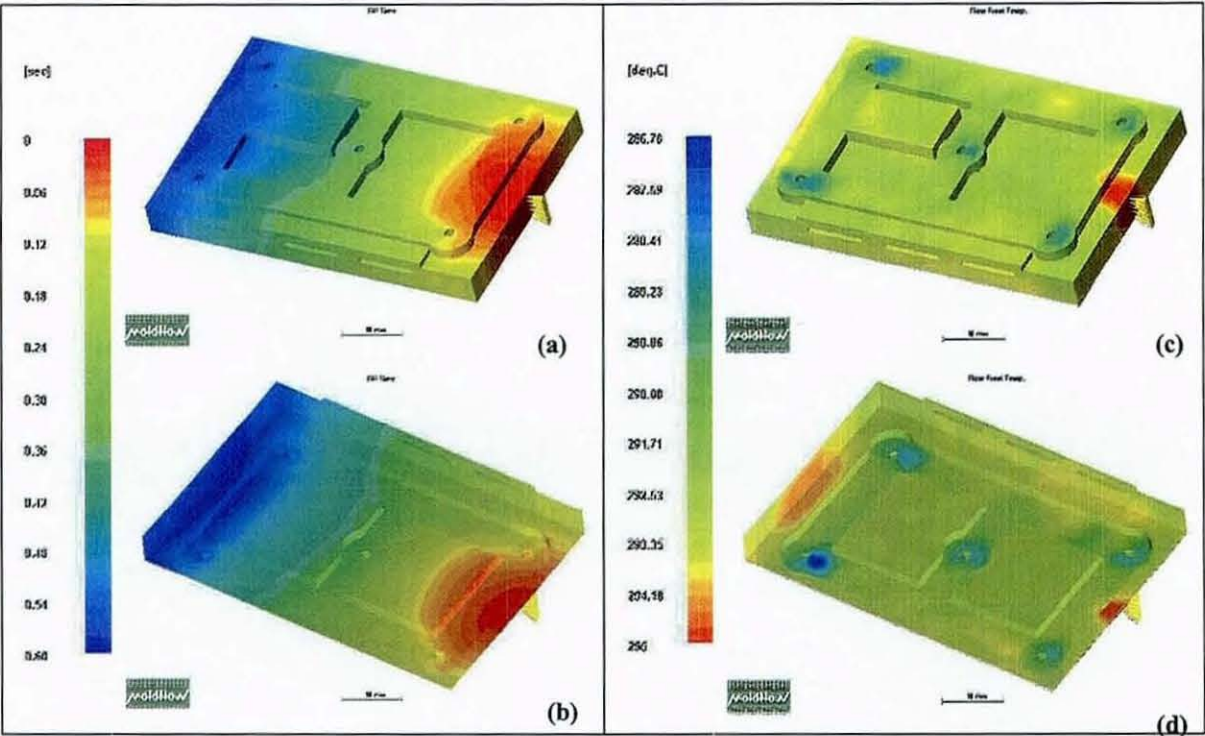
Figure 5-6 Flow models for the topographical moulding cavity: (a) and (b) fill time analysis, (c) and (d) flow front temperature [courtesy of Schmidt, 1999]
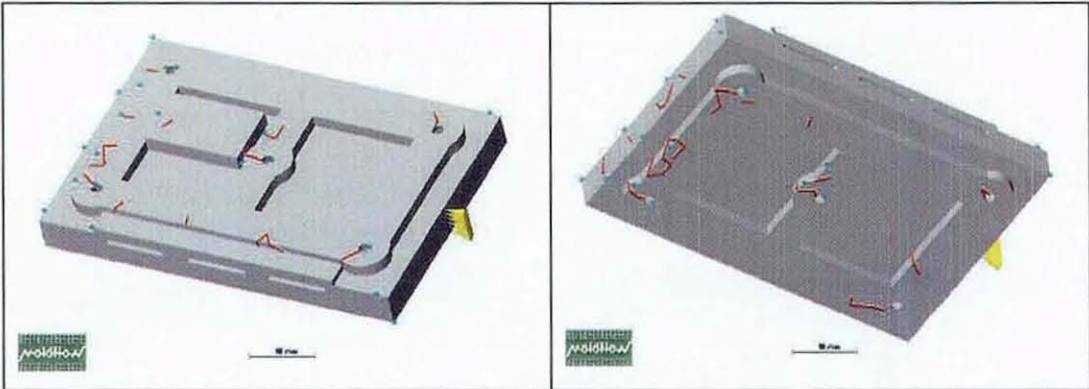
Figure 5-7 Weld lines and air traps at the end of injection cycle for topographical moulding tool [courtesy of Schmidt, 1999]

5.4.2.   Experimental Results

In the overmoulding trials using the topographically contoured tool, the embedded modules showed a high degree of conformity to the simulated results in terms of part warpage, weld-line/air trap formation and differential stress. However, a number of problems unpredicted by the flow models were encountered.

Firstly, the shearing force and thermal load exerted by the impinging plastic on the support frames were greater than the models had suggested. This caused the thinner sections of the frames to be swept to the surface of the tool. Figure 5-8 shows a GR-ABS overmoulded specimen with such a defect. Also, in many instances, the support frames were detached from the substrate, thus dislocating the subassembly during the filling stage.

In spite of the FEA models showing a reduction in the flow path constriction, the overmoulding trials did not show any such substantial improvement. This was partly because the simplified model did not take into consideration the gap of approximately 2mm between the substrate and support structure. It was observed that short-shots, due mainly to the presence of the supporting structures in the flow paths, were still not overcame. Figure 5-9 shows an overmoulded subassembly from the trials with serious short-shot failure. This incomplete filling was particularly evident in the moulding trials at lower injection pressures, which is one of the vital process parameters established from the Stage 1 experiment in Chapter 3.

Due to the experimental overmoulding showing unsatisfactory results, further work was undertaken to re-engineer the moulding tool design without the glued-on support structures
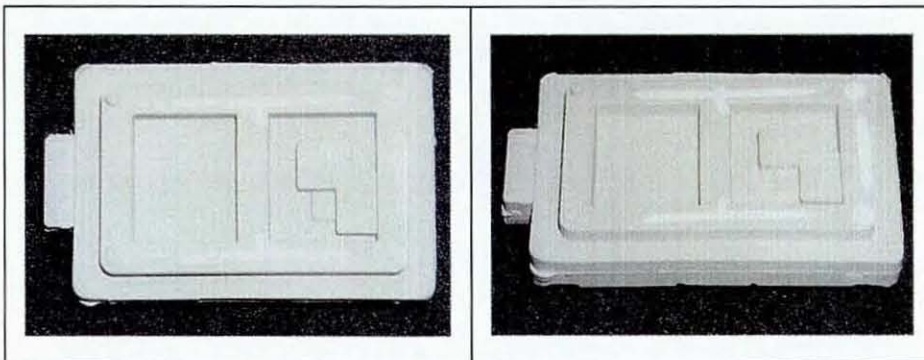
Figure 5-8 Flushing of the support frame to the surface by injection shearing force
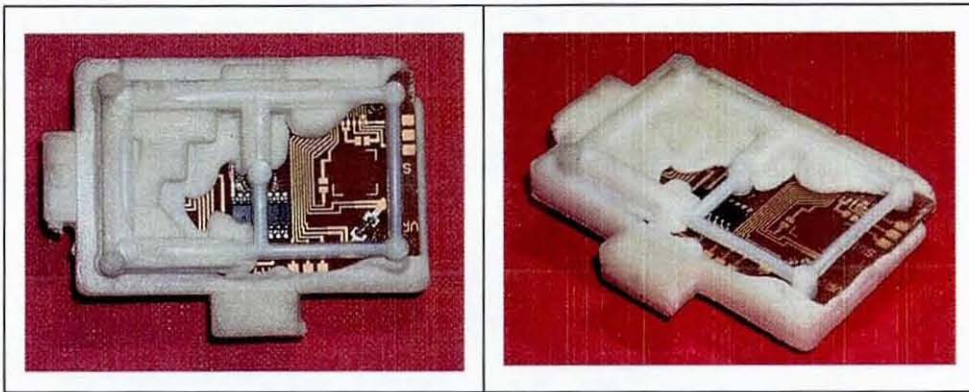
Figure 5-9 Overmoulded sample showing serious short-shot condition

5.5.   In-Mould Supported Topographical Tool

In this development, the support cradles were removed and fixed metal pins in the tool were added as means of substrate support and subassembly locator. As a preliminary stage to the actual design and machining the moulding tools, FEA models again simulated the melt flow fronts and pressure profile for the topographical cavity with in-mould supports.

5.5.1.   FEA Models

Figure 5-10 [De Cooper Jones, 1999] shows the result of the mould filling simulation. Comparisons can be deduced from contrasting Figure 5-10 with Figure 3-8 which shows the results for a non-supported conventional overmoulding tool from similar models. Figure 5-10 (a) and (b) show that the progress of the melt in the contoured cavity without the additional support frames was uniform throughout the filling cycle, with both the top- and bottom-half of the cavity filled at nearly the equal rate within half of the cycle time. Figure 5-10 (c) indicates that the bulk temperature of the moulded part as very homogenous at the end of the filling. The model also showed that, at 55% filling, the pressure differential within the cavity was nearly non-existent, as seen in Figure 5-10(d).
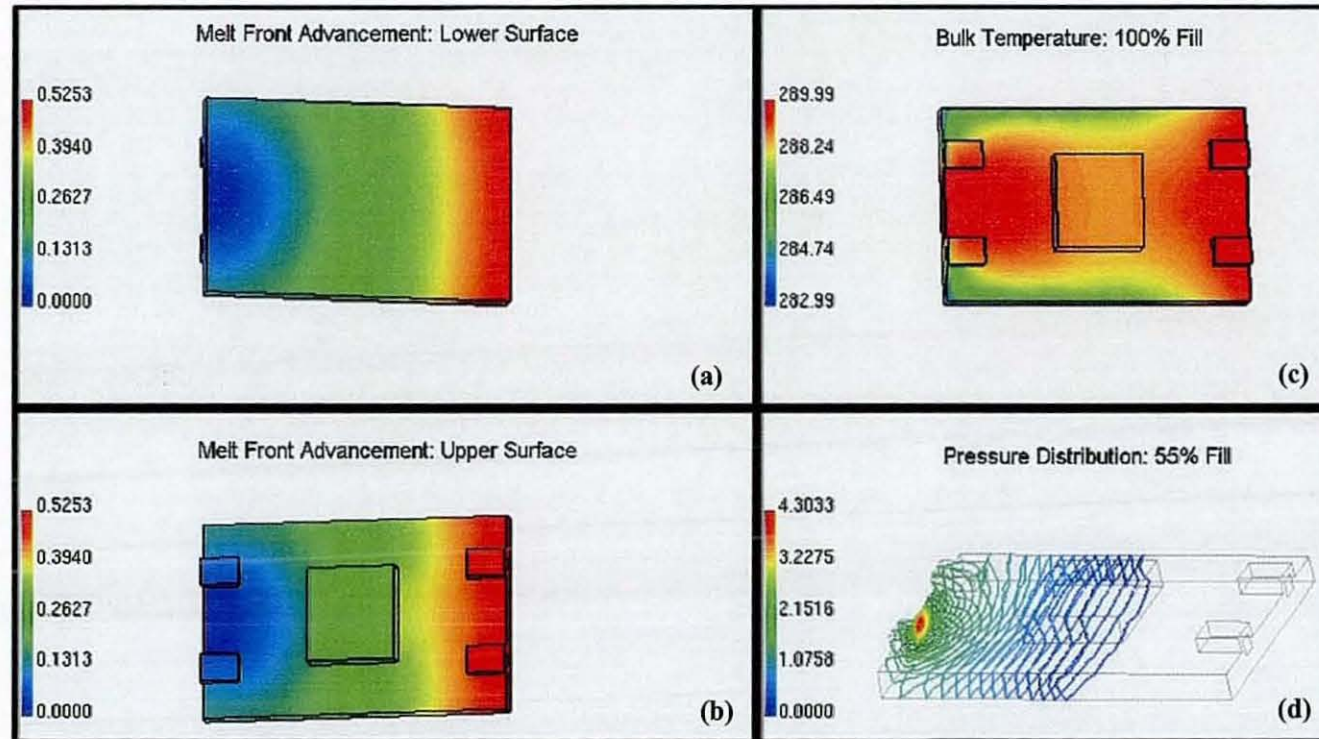
Figure 5-10 Mould filling simulations for in-mould supported topographical tool [courtesy of De Cooper Jones, 1999]

5.5.2.   *Tooling Design*

With the verification of the process enhancement from the flow models, the substrate support frames were removed. The means of supporting and locating the subassembly were instead provided by a combination of two sets of metal pins in the mould cavity. This revised design used four metal pins on each of half of the mould to rigidly retain the subassembly at its intended location in the cavity during the overmoulding cycle.

In the fixed-half of the mould, four 5mm-diameter pins with a right-angle stepped notch were inserted to retain the four corners of the substrate. These would prevent the substrate from any undesired lateral movement. The 2.5mm-deep cut-away indentations were at a 1mm offset margin from the centre of the pins, giving a holding capacity for substrates within 33±2mm wide and 53±2mm length size ranges. Figure 5-11 shows the schematic drawing of the insert for the fixed half of the revised tool. This insert would be fitted into a bulk steel mould attached to an injection moulding machine and hence inserts with different dimensions could be made to accommodate subassemblies of different sizes without creating new moulds.

The moving half of the tool had another means of support, which comprised of four 4mm dome-ended metal pins, as shown in the schematic drawing in Figure 5-12. These pins were aligned parallel with the step-notched supports in the fixed-half to restrain any movement in the direction of tool opening. The domed pins have an interference of 0.5mm with the board and, in order to avoid contact stress on the substrates, a compliant rubber disc was inserted behind each pin head so that the pin moves back, accounting for the board thickness. Changing the thickness of the rubber pads would vary the force exerted by the pins on the substrate. Additionally, removable shims behind the pins enabled position adjustment and gave flexibility for use with substrates of different thickness. Figure 5-13 illustrates the loading of a specimen subassembly into the moulding cavity, also showing the contoured section around the surface-mounted IC.
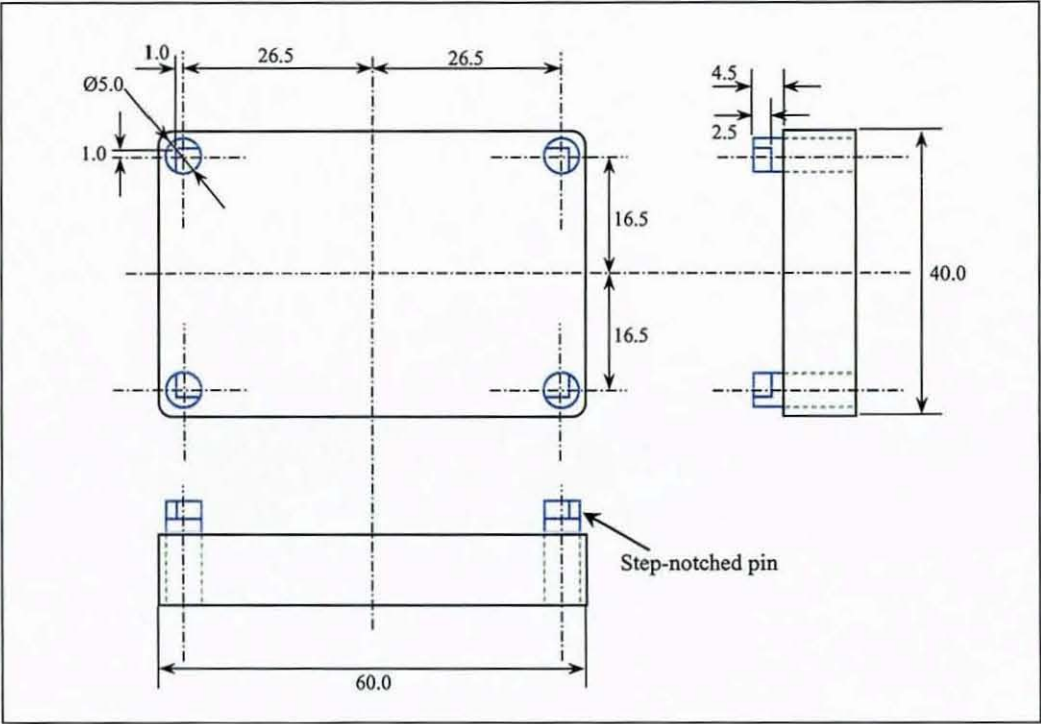
Figure 5-11 Fixed-half insert of the in-mould supported tool (with step-notched pins)
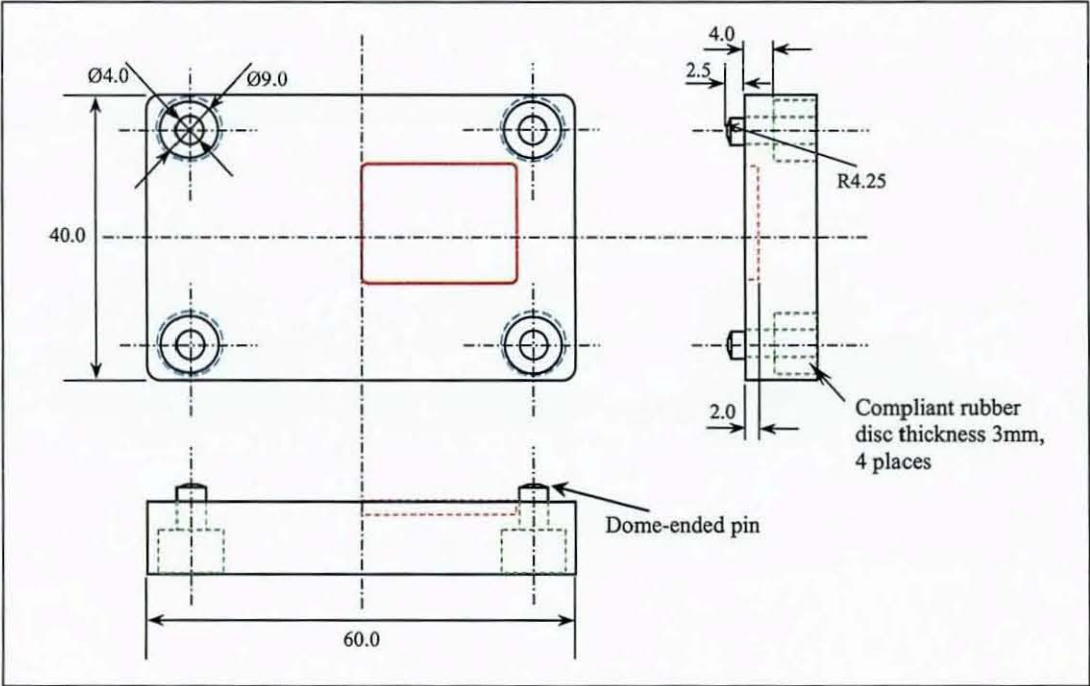
Figure 5-12 Moving-half insert of the in-mould supported tool (with dome-ended pins)
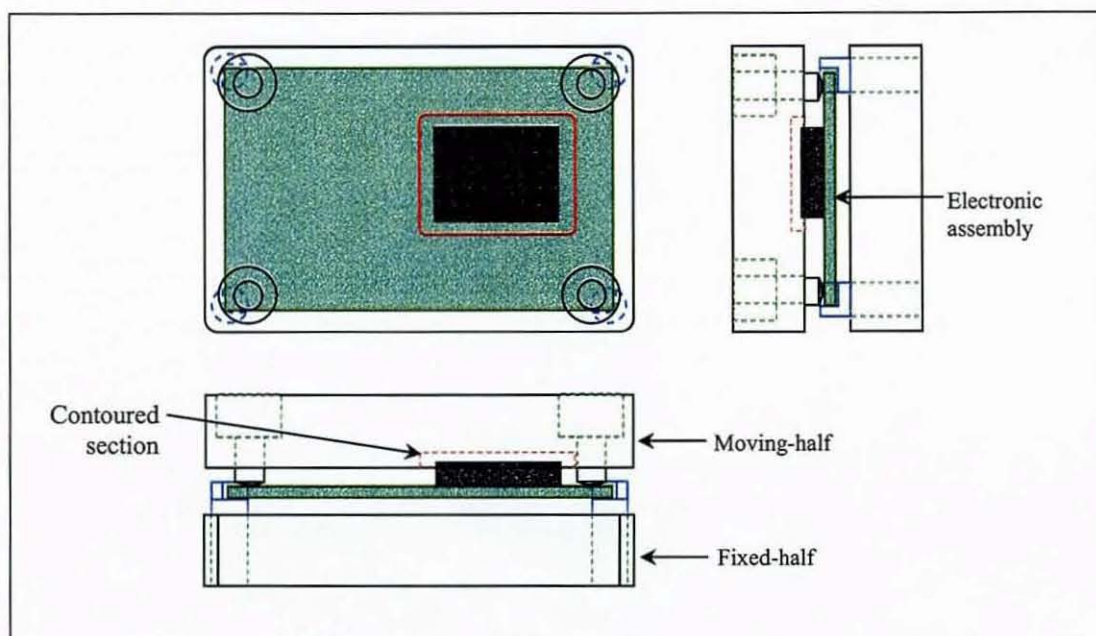
Figure 5-13 Subassembly loading within the in-mould supported topographical tool

5.5.3.   Experimental Overmoulding

Overmoulding trials with GR-PBT and GR-ABS were conducted using the in-mould supported tool design. A response surface method (RSM) DOE, using the software Design Expert [Stat-Ease, 1999], was performed on each polymer to assess the effects of the variation of injection parameters on the moulding quality. Reinforced grades of these polymers were used, as they were the established materials for the technology demonstrators to overmould BT substrate-based circuits, shown in Figure 5-14, which were designed for the real-time instrumentation experiments (see Chapter 6). The circuit consisted of a 16-pin IC, thermistors (VR1, VR2, A2 and A4), diode (A3), resistor pack (A1) and three sets of strain gauges rosettes (SG1 and SG2 on the front, SG3 on the back). As this set of trials was only aimed at validating the effectiveness of the in-mould supported tool, the electronic components only served as a topographical blueprint. Details of the electronic design and functionality of this circuit are discussed in Chapter 6.

Mould temperature, holding pressure, injection pressure and melt temperature were the factors (independent variables) used in these experiments, with three levels of each factor selected in order to reflect two extreme and intermediate moulding conditions within each material specification. Table 5-1 shows the full list of factor settings for both polymers, while Table

5-2 shows the complete DOE. The other process parameters were constant, with injection speed $v_{inj} = 200$mm/s, stroke distance $d_{stroke} = 70$mm, cooling time $t_{cool} = 50$s and holding time $t_{hold} = 70$s. The resultant modules overmoulded with GR-ABS and GR-PBT are shown in Figure 5-15 and Figure 5-16 respectively. In addition to the holes left by the support pins, the parts also had four small circular poles on the bottom surface from the part ejection mechanism that is not shown in the drawings of the mould design.
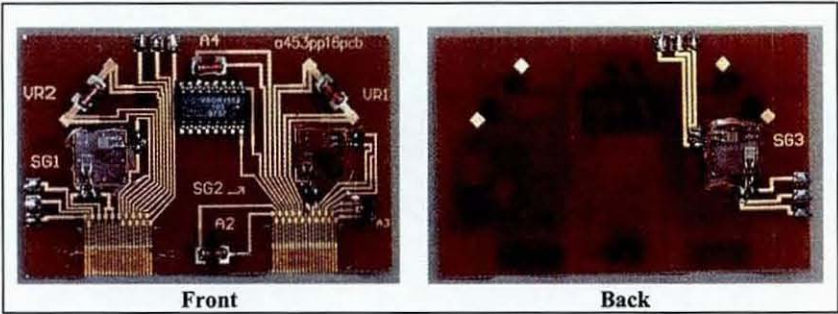
Figure 5-14 Electronic subassembly for overmoulding

Factor	GR-PBT			GR-ABS		
	Level 1	Level 2	Level 3	Level 1	Level 2	Level 3
Mould Temp., T_{mould} (°C)	20	60	90	20	50	80
Melt Temp., T_{melt} (°C)	230	250	270	249	255	270
Holding Pressure, P_{hold} (bar)	80	105	130	70	100	130
Injection Pressure, P_{inj} (bar)	80	105	130	70	100	130

Table 5-1 Factor levels in DOE for GR-PBT and GR-ABS polymers

Trial no.	Mould Temp., T_{mould} (°C)	Melt Temp., T_{melt} (°C)	Holding Pressure, P_{hold} (bar)	Injection Pressure, P_{inj} (bar)
1	1	1	1	1
2	3	1	3	1
3	3	1	1	3
4	1	1	3	3
5	1	3	1	1
6	3	3	3	1
7	3	3	1	3
8	1	3	3	3
9	3	2	3	3
10	3	2	1	1
11	1	2	3	1
12	1	2	1	3
13	2	3	2	3
14	3	3	2	2
15	2	3	3	2
16	2	3	1	1
17	2	1	3	1
18	3	1	1	2
19	1	1	2	3
20	1	3	2	1

Table 5-2 Layout of the 4-factor DOE

Front   Back
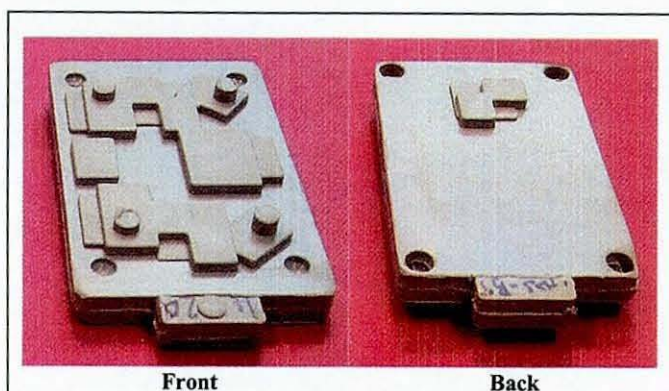
Figure 5-15 GR-ABS overmoulded sample with in-mould supported topographical tool

Front   Back
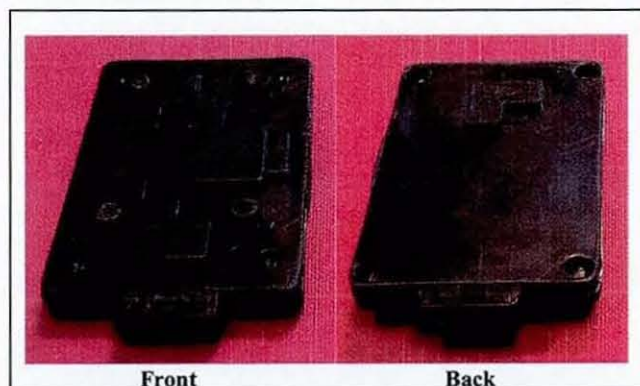
Figure 5-16 GR-PBT overmoulded sample with in-mould supported topographical tool

X-ray images of an overmoulded module are shown in Figure 5-17. From Figure 5-17(a), it can be seen that the embedded circuit was centrally aligned in the holding apparatus with all the electronic components remaining intact after injection moulding. Figure 5-17(b) is an x-ray image taken from the side of the module and shows there is no substantial longitudinal deflection to the substrate.

The module was subsequently potted and cross-sectioned along the A-A line and the result, as shown in Figure 5-18, validated the outcome predicted by the flow modelling, namely that improvement in the flow fronts and differential pressure would be attained. Also evident from Figure 5-18(b) is the integrity of the solder joints of the IC pins in the embedded circuit that showed no indication of solder melting due to the temperature of the polymer melt.

Measurements of the weight and longitudinal warpage of the GR-PBT and GR-ABS overmoulded parts were taken and plotted in Figure 5-19. The weight of specimens produced from each moulding polymer for all process conditions were found to be reasonably consistent, with GR-PBT specimens at a mean weight, $W\mu$ = 25.18g (standard deviation σ = 0.408g) and those of GR-ABS at $W\mu$ = 21.49g (σ = 0.379g). This showed that the injection settings used in the experiments, particularly injection and holding pressures, were effective in generating sufficient and uniform packing pressures to compensate for the apparent viscosity difference between the two materials. Inadequate packing pressures would result in short-shots, weak weld-lines and under-packed lighter parts. On the other hand, over-packing would increase mould pressure and produce a heavier part with stresses and defects such as flashing and mould sticking.
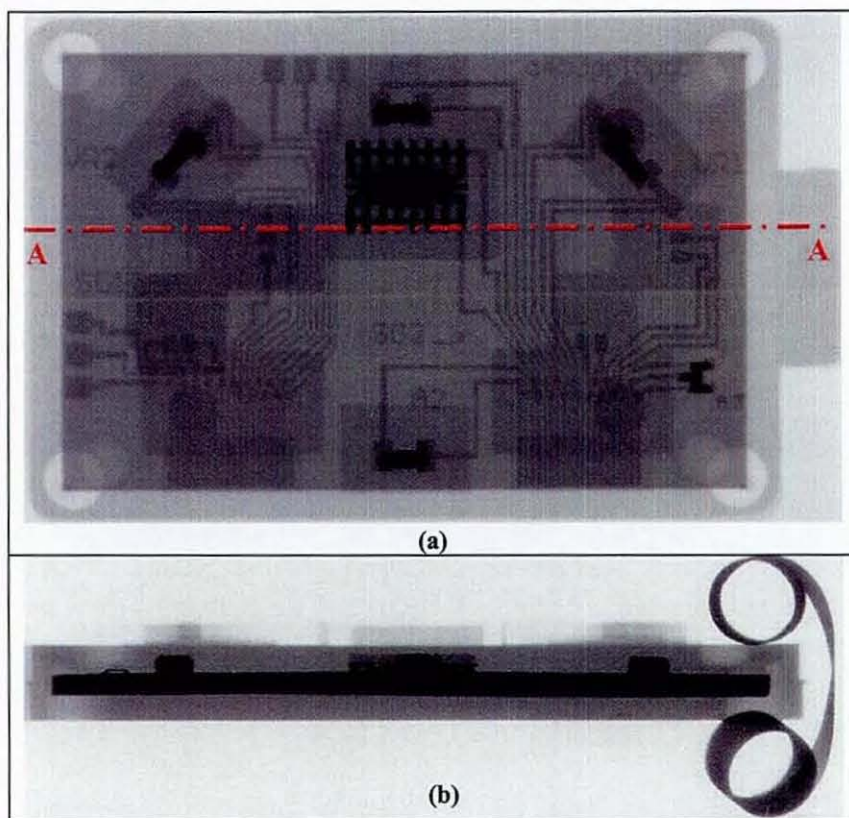
Figure 5-17 X-ray images of an GR-ABS overmoulded module
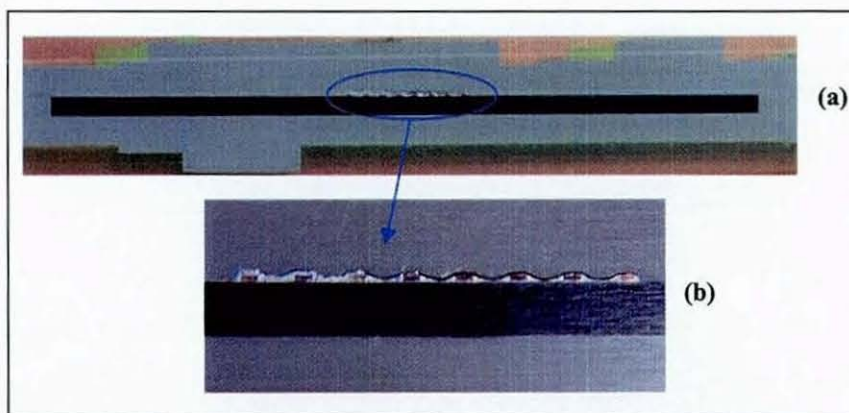
Figure 5-18 The A-A cross-sectioned sample of an GR-ABS overmoulded module

The revised mould produced substantial reductions in the longitudinal warpage of the overmoulded parts with measurements obtained in the ranges of 7.0-117.3μm for GR-ABS and 13.5-134.0μm for GR-PBT trials. Also, as evident in Figure 5-19, the two moulding materials showed a noticeable trend in the degrees of warpage under a number of similar

process conditions. This correlation becomes more apparent when the two sets of experiments are analysed statistically in the following section.

When these warpage measurements were compared with those obtained from matching overmoulding settings in the Stage 1 experiment (in which the subassembly was encapsulated in rectangular conventional mould without any substrate support mechanism), a very sizeable improvement was observed, such that in some cases over 90% reduction in warpage along the 60mm length was achieved. In order to obtain a comparison, the warpage deformation for four overmoulding trials with similar process conditions from these two sets of experiments are presented in Figure 5-20 below. A mean warpage of 400.0μm was found from Trial no. 14 in Table 3.3. Similar overmoulding conditions in this revised in-mould supported contoured tool produced a deformation of only 89.7μm (points 2 on graph). However, it must be noted that the significance of different injection gate position and holding pressure were disregarded in this comparison. The former was shown in Chapter 3 (section 3.3.5) to be statistically negligible in affecting the longitudinal warpage whilst the latter will be addressed in the next section.
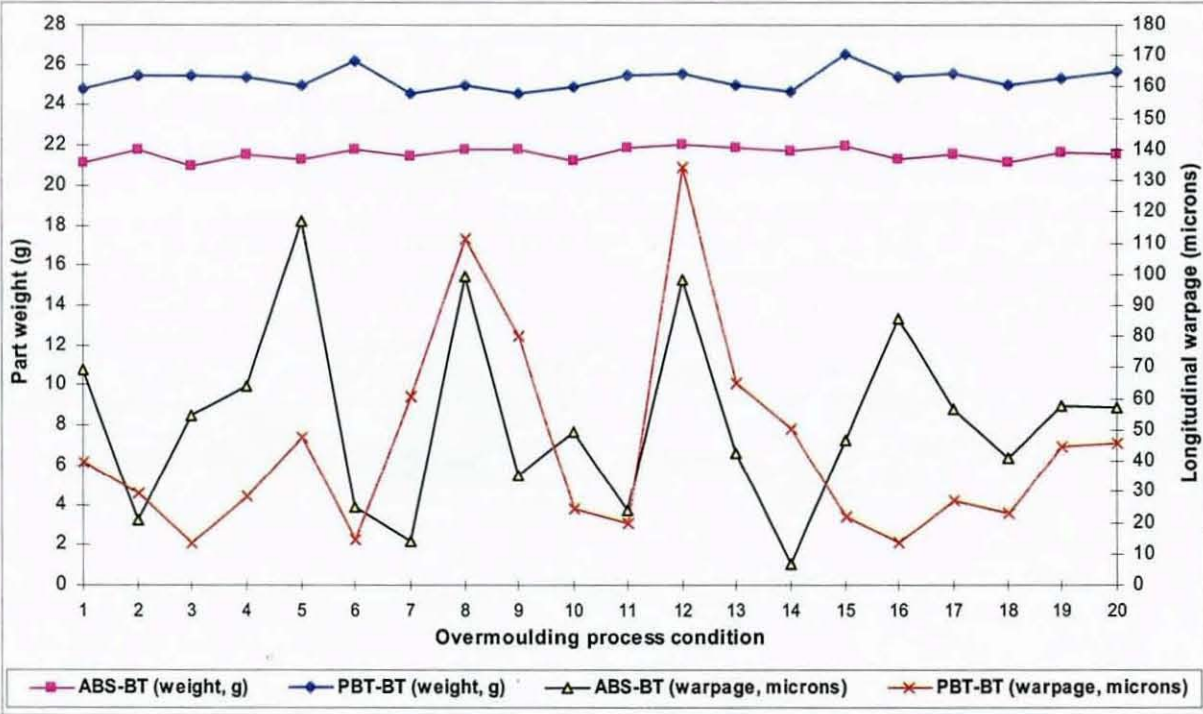
Figure 5-19 Weight and longitudinal warpage from in-mould supported topographical mould
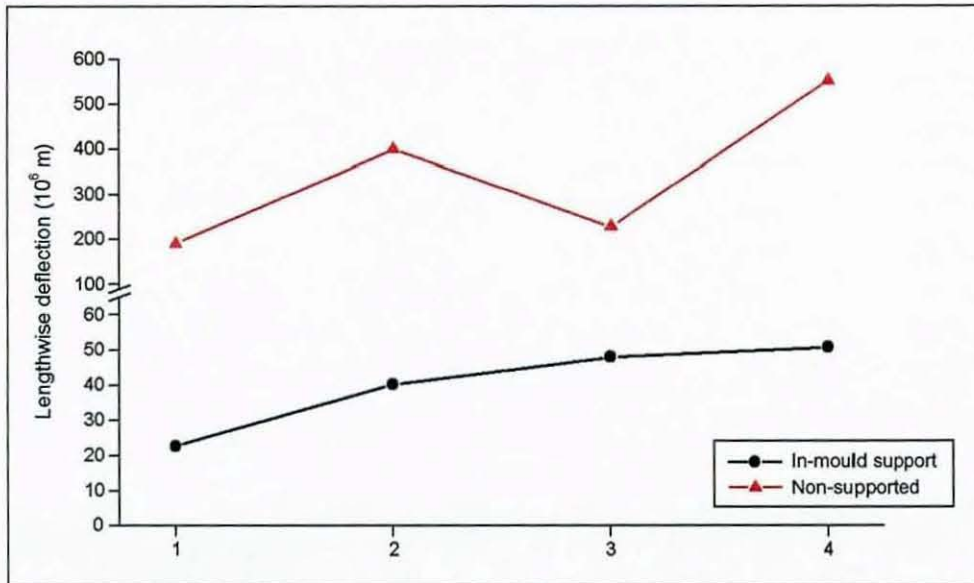
Figure 5-20 Comparison of deflections between non-supported (Stage 1) and in-mould supported topographical GR-PBT overmoulded samples

5.5.4.   Statistical Results

Whilst the initial exploration experiments discussed in Chapter 3 were analysed using the factorial DOE, which identified factors affecting the overmoulding process, the trials with the current in-mould supported contoured tool were carried out under a response surface method (RSM) DOE using the software Design Expert [Stat-Ease, 1999]. This was useful in finding the ideal process settings and hence achieving optimal overmoulding parameters. In statistical analysis of RSM design, the process parameters or factors, shown in Table 5-2, were quantified as continuous numerical variables. The objective was to find a desirable location in the design space that provided the lowest longitudinal deflection.

ANOVAs applied to the experimental results were extended to include the quadratic terms in order to improve the fitted response model. The factorial DOE in Chapter 3 was analysed up to 2-factor interactions (2FI) but the polynomial quadratic model applied in this chapter adds the squared terms. When the response models were increased to include the cubic terms, it was found that it became aliased, i.e. the process factors could neither be separated nor uniquely estimated by the model.

The significance of a variable in an ANOVA is expressed in terms of the sum of squares for a particular term as a percentage of the total sum of squares of all contributing factors in the

model, and this is known as %-Contribution. As such, the %-Contribution values represent the contribution of sources of variance by individual factors to the total model variance. To identify the significant process model, terms with "Prob > F" values of more than 0.05 were statistically classified as non-significant to the process model and hence eliminated from the ANOVA. This produced a reduced quadratic model with 95% confidence level. However, any linear terms contributing to significant higher terms (2FI or squared terms) would have to be kept in the ANOVA in order to support the model hierarchy.

5.5.4.1.   *GR- PBT*

Table 5-3 shows the reduced ANOVA for the quadratic model of the longitudinal warpage for GR-PBT overmoulding trials. The significant linear factors with their respective %-Contribution in this analysis were P_{inj} (25.64%), T_{mould} (9.70%) and T_{melt} (9.45%). P_{hold} was the only non-contributing linear term, but was included for the model hierarchical requirement. Significant 2FIs were $T_{melt}*P_{inj}$ (12.60%), $T_{mould}* P_{hold}$ (7.37%) and $T_{mould}* P_{hold}$ (3.50%). The only squared term significant in the model was $(T_{melt})^2$ which contributed 4.61%. Pure Error represents the amount of variation in the response in the replicated design points of the model, while Lack of Fit is the variation of the data around the fitted model. In this model, Pure Error and Lack of Fit contributed 18.07% and 8.26%, respectively, to the total variance. The "Model F-value" of 11.75 implied that the model was significant. The Design Expert model showed that there is only a 0.01% chance that a "Model F-Value" this large could occur due to noise. Also, the "Lack of Fit F-value" of 1.29 implies the "Lack of Fit" is not significant relative to the Pure Error. There is a 27.70% chance that a "Lack of Fit F-value" this large could occur due to noise. This showed that the model fitted satisfactorily to the empirical data.

The normal probability plot of studentised residuals in Figure 5-21 shows that the error residuals scattered in a normal distribution (in which case, the points will follow a straight line) and hence no mathematical transformation was required in the analysis. However, the "R^2 value" for the quadratic model was found to be relatively low at 0.6911, which was mainly due to the considerable Pure Error, and is reflected by the plot of actual response values versus the predicted response values shown in Figure 5-22. The "Predicted R^2 value" of 0.5057 was in reasonable agreement with the "Adjusted R^2 value" of 0.6323. (within 0.20 of each other), indicating that there was no problem with the data or the model.

Source	Sum of Squares	DF	Mean Square	F-Value	Prob > F	% Contribution
Model	41669.083	8	5208.635	11.7467	< 0.0001	
T_{mould}	6859.235	1	6859.235	15.4692	0.0003	9.70
T_{melt}	6687.066	1	6687.066	15.0810	0.0004	9.45
P_{hold}	570.721	1	570.721	1.2871	0.2630	0.81
P_{inj}	18139.027	1	18139.027	40.9079	< 0.0001	25.64
$(T_{melt})^2$	3259.976	1	3259.976	7.3520	0.0097	4.61
$T_{mould}* T_{melt}$	2472.291	1	2472.291	5.5756	0.0229	3.50
$T_{mould}* P_{hold}$	5214.672	1	5214.672	11.7604	0.0014	7.37
$T_{melt}* P_{inj}$	8909.415	1	8909.415	20.0929	< 0.0001	12.60
Lack of Fit	5840.582	11	530.962	1.2877	0.2770	8.26
Pure Error	12782.688	31	412.345			18.07

Table 5-3 ANOVA of longitudinal warpage for GR-PBT overmoulded samples
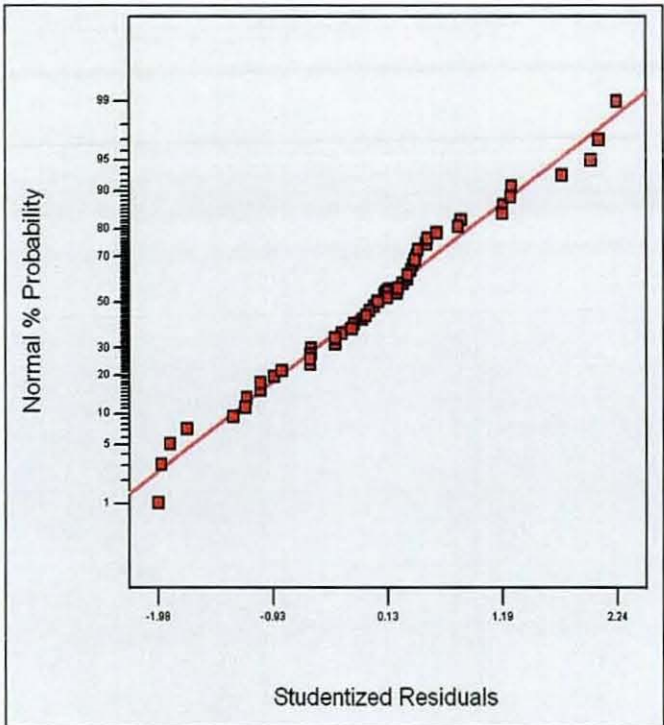
Figure 5-21 Normal plot of studentised residuals for GR-PBT quadratic model
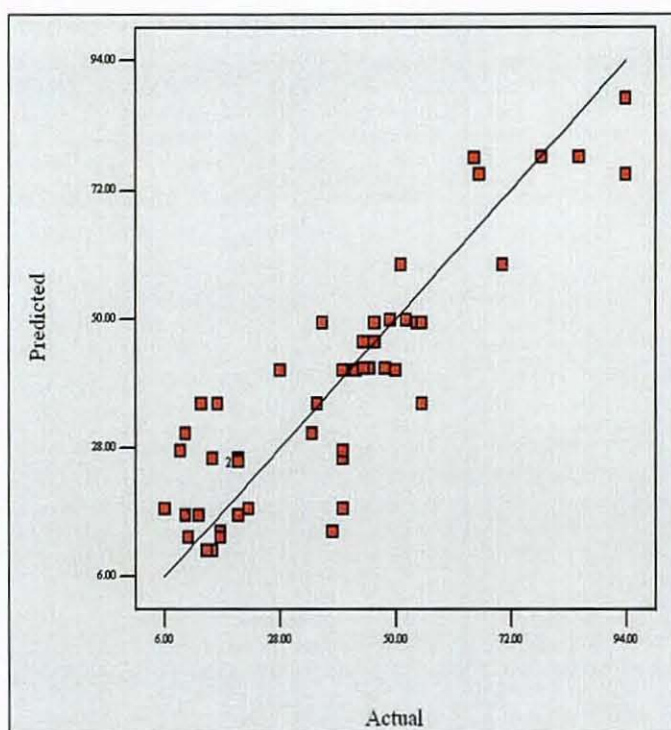
Figure 5-22 Predicted vs. actual responses plot for GR-PBT quadratic model

5.5.4.2.   GR-ABS

ANOVA results for the reduced quadratic model for the longitudinal deflection of the GR-ABS overmoulded subassemblies is shown in Table 5-4. From this analysis, linear factors significant to the model variance were identified as T_{mould} (23.28%), P_{inj} (22.94%) and T_{melt} (2.42%). Again P_{hold} was found to be non-significant and kept in the model to maintain its hierarchy. Although the collective contribution of significant 2FI and squared terms to the model was of considerable importance, individually they were found to have relatively minor effects by the ANOVA, i.e. the %-Contribution values of these significant terms were all <10%. The contributing 2FI terms were $T_{melt}*P_{hold}$ (7.83%), $T_{mould}*P_{inj}$ (6.97%) whilst the squared terms were $(T_{mould})^2$ (8.29%) and $(P_{inj})^2$ (3.65%). The significance of the Lack of Fit and Pure Error to the total model variance were 4.34% and 19.00% respectively.

From the standpoint of model integrity, the analysis produced a "Model F-value" of 20.90 and a "Lack of Fit F-value" of 0.85, thus implying that the model was significant and the Lack of Fit was not significant relative to the Pure Error. The normal probability plot of studentised residuals in Figure 5-23 shows that no mathematical transformation was required for the model. Additionally, the "R^2 value" of this model was 0.7628, providing satisfactory

goodness of response fitting in the plot of actual versus the predicted response values shown Figure 5-24. The "Predicted R^2 value" of 0.7263 and "Adjusted R^2 value" of 0.6745 again indicated there was no problem with the data or the model.

Source	Sum of Squares	DF	Mean Square	F-Value	Prob > F	% Contribution
Model	35507.340	8	4438.417	20.90241	< 0.0001	
T_{mould}	11016.667	1	11016.667	51.88222	< 0.0001	23.28
T_{melt}	1618.188	1	1618.188	7.620744	0.0080	3.42
P_{hold}	130.762	1	130.762	0.615817	0.4362	0.28
P_{inj}	10855.320	1	10855.320	51.12237	< 0.0001	22.94
$(T_{mould})^2$	3923.436	1	3923.436	18.47715	< 0.0001	8.29
$(P_{inj})^2$	1727.715	1	1727.715	8.136551	0.0062	3.65
$T_{mould}* P_{inj}$	3295.469	1	3295.469	15.51978	0.0002	6.97
$T_{melt}* P_{hold}$	3704.458	1	3704.458	17.44589	0.0001	7.83
Lack of Fit	2051.427	11	186.493	0.850502	0.5929	4.34
Pure Error	8990.250	41	219.274			19.00

Table 5-4 ANOVA of longitudinal warpage for GR-ABS overmoulded samples
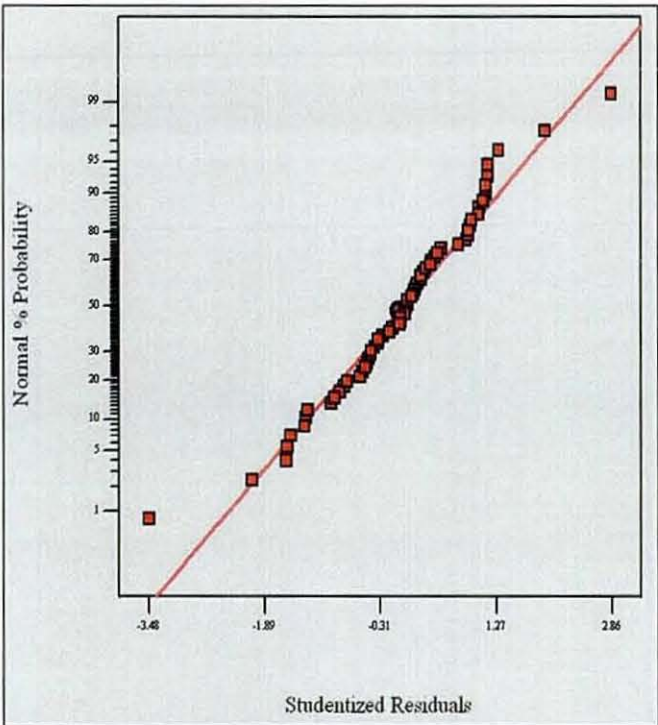
Figure 5-23 Normal plot of studentised residuals for GR-ABS quadratic model
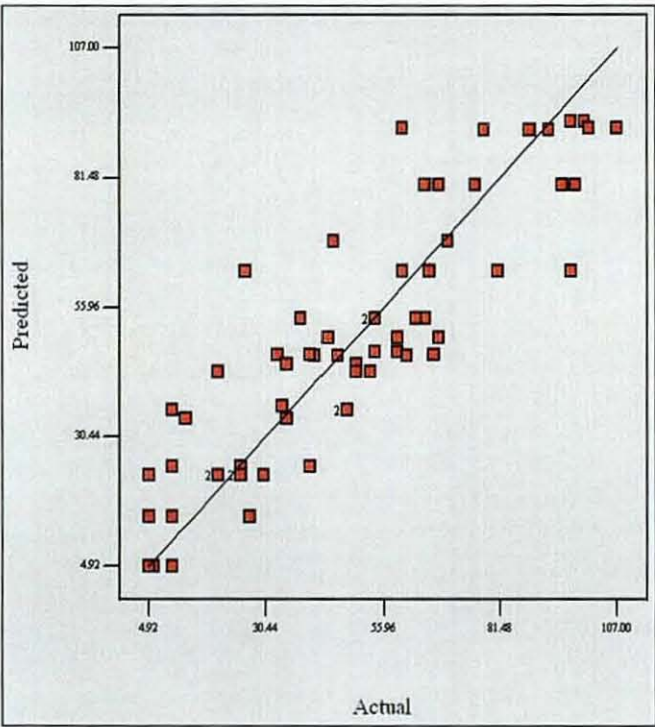
Figure 5-24 Predicted vs. actual responses plot for GR-ABS quadratic model

5.5.5.   *Parametric Optimisations*

The results from ANOVA analyses of the two overmoulding materials above have demonstrated considerable differences in the way injection parameters affected the process models from the standpoint of the part's longitudinal warpage. The deflection ANOVA has shown that the significant process variables for GR-PBT overmould were P_{inj} (25.64%), $T_{melt}*P_{inj}$ (12.60%), T_{mould} (9.70%) and T_{melt} (9.45%). However, this was slightly different for GR-ABS of which significant factors were T_{mould} (23.28%), P_{inj} (22.94%), $(T_{mould})^2$ (8.29%) and $T_{melt}*P_{hold}$ (7.83%). In order to further determine the process settings which would statistically predict the lowest resulting deformation, statistical process optimisations using longitudinal warpage as the design criterion were subsequently carried out.

The optimised parameters for GR-PBT overmoulding with predicted warpages of $\leq 20.0\mu m$ are listed in Table 5-5. Although RSM model provided a contour plot of continuous parameter values, the settings in this table were selected to reflect experimental setup. It can be seen here that P_{inj} showed little variation between 110-130bar to achieve this projection. On the other hand, T_{melt} was optimised to be either the low value of 230°C or the highest of 270°C. With exception to three settings associated with maximum P_{hold} of nearly 130bar (see rows 14, 16 and 18), T_{mould} varied between 73-90°C. As reflected in the ANOVA, P_{hold} had very little

effect on process and this can be evident in an almost similar reactions over its entire range investigated of 80-130bar. Although T_{melt} at its maximum of 270°C was predicted to produce lowest mechanical deformation, there was an overriding concern that the thermal degradation generated by this temperature may not be sustainable for the electronic components, solder joints and PCB. This must be taken into consideration for successful encapsulation.

With this in mind, it was obvious that, statistically, the best setting of T_{melt} was at 230°C and from a closer analysis of Table 5-5, it was found that settings 9, 11, 13, 15, 17 and 19 are possible optimised overmoulding conditions for GR-PBT. Settings 16 and 18 were not considered, due to very low T_{mould} values. The mean values of the parameters from selected settings were calculated to obtain the adjusted optimised process condition, as listed in Table 5-6, and were used as the guidelines for subsequent overmoulding with Crastin 30% GR-PBT.

Number	T_{mould} (°C)	T_{melt} (°C)	P_{hold} (bar)	P_{inj} (bar)	Predicted Deflection (µm)
1	88.27	269.86	106.56	112.65	0.10
2	88.34	265.53	88.88	110.16	0.60
3	85.39	269.46	106.75	111.53	1.10
4	89.98	268.45	90.41	115.62	1.10
5	78.91	269.81	103.34	110.61	1.80
6	89.92	269.98	114.27	112.61	1.80
7	82.96	270.00	125.74	110.00	4.10
8	78.18	270.00	121.78	110.00	4.60
9	80.00	230.00	80.44	110.00	9.00
10	90.00	269.97	125.48	115.98	11.60
11	80.00	230.00	80.00	123.82	12.60
12	90.00	270.00	130.00	115.66	12.80
13	80.45	230.00	80.00	110.00	13.70
14	20.00	230.00	128.26	123.65	14.40
15	90.00	230.00	80.00	129.13	14.90
16	42.82	230.00	130.00	111.56	16.40
17	73.14	230.00	80.01	110.00	17.50
18	28.35	270.00	129.84	110.00	17.50
19	56.08	230.08	130.00	110.11	19.70

Table 5-5 Optimisations of GR-PBT overmoulding conditions

	T_{mould} (°C)	T_{melt} (°C)	P_{hold} (bar)	P_{inj} (bar)	Predicted Deflection (μm)
Means Setting	79.95	230.00	88.41	115.51	14.65
S.D.	5.54	0.00	8.32	3.53	1.54

Table 5-6 Statistically optimised process conditions for GR-PBT

The results from the statistic optimisation for GR-ABS overmoulding are shown in Table 5-7 below. It can be noted that the predicted deflection values in these suggested settings were relatively higher than those of GR-PBT in Table 5-5 above. This suggested that although GR-ABS overmoulding produced lower maximum and minimum longitudinal warpages, as evident in Figure 5-19 above, its average values were, however, considerably higher than GR-PBT. This may be due to the morphological differences between semi-crystalline and amorphous materials as well as the percentage content of the glass filler. Recalling that T_{mould} and P_{inj} were the most significant variables from ANOVA, Table 5-7 shows that optimum settings for T_{mould} were either 20°C or 80°C, whilst P_{inj} varied between 60-90bar.

Similar to the GR-PBT overmoulding, the 20°C predicted for T_{mould} would be ineffective to heat up the inserted substrate to reduce the impact of thermal shock of the injected melt. Although T_{melt} was not identified by ANOVA as one of the main contributing parameters in generating serious part warpage, it was, nevertheless, very crucial from the electronic integrity standpoint and hence must be considered. The optimised values of T_{melt} for deflections of ≤25μm (rows 1-13) fell within the range of 240-270°C. In order to reduce any failure that may be induced by high thermal impact to the electronics or substrate, only the suggested settings with T_{melt} ≤260°C were taken into account to optimise the process, i.e. rows 7-11 and 13. The mean values for all the parameters are listed in Table 5-8 and this formed the process guidelines for Novodur 16% GR-ABS overmoulding.

Number	T_{mould} (°C)	T_{melt} (°C)	P_{hold} (bar)	P_{inj} (bar)	Predicted Deflection (μm)
1	80.00	270.00	104.79	90.00	1.09
2	79.99	269.97	111.45	90.00	1.92
3	80.00	269.98	96.12	90.00	2.39
4	80.00	269.98	115.31	90.00	3.06
5	80.00	266.24	114.17	90.00	6.86
6	80.00	270.00	115.68	73.86	7.74
7	80.00	259.93	112.63	90.00	7.86
8	79.99	240.00	104.87	73.06	10.57
9	80.00	243.30	105.31	72.00	11.37
10	80.00	256.21	106.00	83.39	14.85
11	80.00	255.01	97.55	90.00	21.03
12	20.00	269.98	124.41	89.96	22.23
13	80.00	240.00	94.78	81.83	24.08
14	20.00	270.00	128.68	77.16	26.14
15	20.00	263.07	124.47	70.00	31.65
16	20.00	265.00	125.43	71.42	32.23
17	20.00	262.46	127.34	60.19	34.09
18	20.00	264.73	123.18	70.09	35.37

Table 5-7 Optimisations of GR-ABS overmoulding conditions

	T_{mould} (°C)	T_{melt} (°C)	P_{hold} (bar)	P_{inj} (bar)	Predicted Deflection (μm)
Means Setting	80.00	249.91	103.52	81.71	14.96
S.D.	0.00	4.21	2.62	3.21	2.60

Table 5-8 Statistically optimised overmoulding conditions for GR-ABS

CHAPTER 6.   BOARD-LEVEL FUNCTIONAL SENSING OF OVERMOULDING

6.1.   Introduction

The previous chapter demonstrated the feasibility of the in-mould supported contoured tool design in counteracting against the thermomechanical deformations on the PCB-based electronic module during the overmoulding cycle. Having achieved this breakthrough in optimising the process variables, it was now critical to undertake a further investigation to understand the intricate consequences of this encapsulation process on the encapsulated electronic subassemblies. In order to gain an understanding of the mechanical and electronic responses of a subassembly to the thermomechanical strains imposed by the high-temperature, high-pressure melt flow in the moulding cavity, an in-line measurement for a variety of data *during* overmoulding process was necessary.

This chapter discusses the experiment conducted to investigate the *board level* interactions between the melt flow front and the subassembly components or substrate. A special instrumented SMT circuit was designed, in which various electrical and mechanical properties were monitored during the overmoulding cycles using the novel contoured tool. The real-time embedded electronic sensing system successfully provided an in-depth insight into the impacts of this process on the onboard components from the perspectives of performance and reliability.

6.2.   Objectives of Experiment

Thermoplastic injection overmoulding is a multi-variable process in which many variables interact to influence the quality of the moulded part. The preceding experiments have considered and analysed the interrelation of the key variables for the controlled implementation of the proposed electronic overmoulding technique. The characteristics of thermomechanical stress impingement on the embedded electronics by the dynamics of resin flow front have also been investigated and attested to by using structural and melt flow simulations. The results led to the design of a novel moulding tool that successfully minimised the deformations caused by the residual stress in the form of longitudinal

warpages. The reduction in this failure mechanism provided a breakthrough for the encapsulation process. However, it was obvious that further understanding of the stresses, strains and temperature excursions experienced by the electronics during this high-temperature high-pressure encapsulation cycle was vital to establish manufacturability and, more critically, the operating reliability and capability of the final integrated product. To this end, an experiment was undertaken to investigate the consequences of overmoulding process from the standpoint of the electronic functionality of the embedded circuitry.

With this in mind, the experiment discussed in this chapter was conducted to achieve the following objectives:

- To understand the physical stresses (force, stress, strain, temperature, pressure) experienced by the embedded electronics

- To experiment with different interconnection types (SMT, wire bonds, flexible I/O cable)

- To further appraise the injection settings proposed by the previous experiments.

6.3. Background of Experiment

An overmoulding scheme with an in-process measurement and monitoring system, consisting of two different types of electronic circuit designs was developed in this experiment. A regime of measurements of temperature profile, strains and electrical interconnectivity on the encapsulated subassembly was collected using a multi-channel real-time data acquisition apparatus.

6.3.1. On-board Temperature Sensing

Temperature is one of the key variables in the injection overmoulding. A thorough knowledge of the temperatures of the polymer melt in the machine and that of the actual heat reaching to the encapsulated electronics is vital to establish the sustainability of this process. The latter, the *effective component temperature*, is of considerable significance from the viewpoint of immediate survivability and longer-term reliability of the embedded subassembly.

Conventional temperature measurement techniques available in the industry are cement-on thermocouples, conventional thermocouples, optical pyrometers, ultrasonic probes, platinum resistance thermometer (PRT) probe, infrared (IR) probes with fibre optic sensor, refractive

index and temperature sensitive tracers [Chakravorty *et al*, 1997]. These systems are widely used for measuring the temperature of the plastic melt in various moulding processes. In general, accurate measurements of cavity temperature profiles for injection moulding can be difficult for the following reasons [Federico *et al*, 1991]:

- The temperature gradient across the thickness is large due to the polymer's low thermal conductivity. The measurements are thus very susceptible to position errors.

- The temperature is highly transient during the filling period, so a fast response system is desirable.

- In general, if sensors are positioned inside the mould cavity, they may disturb the polymer flow, resulting in measurement errors. This issue is, however, inconsequential to the proposed overmoulding process.

- If intrusive sensors are used, they have to be robust enough to withstand the repeated shear forces caused by the polymer flow. They also have to be in good thermal contact with the polymer.

However, there is a significant temperature distribution within the polymer melt so that a measurement along its flow path is not representative of the melt temperature reaching the embedded elements. The electronic components in this process were also coated with a glob-top material to absorb the thermomechanical stresses and hence reduce the effective temperature on the components.

It is clear that within the context of this experiment, the profiles of the effective temperature as experienced by the encapsulated subassembly were the focus of interest. *Board-level* temperature excursion experienced by components was measured by the surface-mounted thermistors and diodes, whilst at *chip-level* the effect was monitored by the on-chip diode temperature sensors on the wire-bonded PMOS4 Si test chip. The acquisition of actual surface temperatures for the components enabled the determination of the thermal impact sustained through the overmoulding cycle. This information could facilitate the selection of favourable circuitry components designed for overmoulding in similar environments. The details of these two specimen circuits are discussed in Sections 6.3 and 6.5 respectively.

6.3.1.1. Thermistors

Thermistors are *thermally sensitive resistors* whose sensing elements are fabricated from sintered semiconductor materials such as oxides of copper, nickel and titanium. They are

capable of generating relatively large changes in resistance with temperature. Due to their size advantage, thermistors permit point-sensing and rapid response to temperature variations. Other advantages are their high electrical resistance, which minimises lead-wire problems, and robustness which enables usage in harsh conditions. Current generation thermistors are fabricated from oxide systems such as manganese-nickel or manganese-nickel-cobalt and are stable, high sensitivity ($\Delta R/\Delta T$ up to 80Ω/°C) and can be accurate to $\pm$1% within specified operating temperatures [Dally *et al*, 1993]. Thermistors were incorporated into the process monitoring subassembly in order to obtain real-time information for the *board-level* temperatures during the overmoulding cycle.

6.3.2. On-board Strain Measurement

When a solid body is acted upon by a system of forces, which may be internal and/or external, it is subjected to stress. In essence, this means that forces are transmitted from one elemental particle to another within the body. How these forces are distributed on the external surfaces is of vital importance since the ability to withstand the action of the forces depends upon the force intensity prevailing at each point within the material. Since stress cannot be determined experimentally by direct measurement, strain on a surface is measured instead using strain gauges. In order to make use of the experimentally determined strains, transformation equations for plane strain are generated that are similar in form to the transformation equations for plane stress, where the orientations of the principal strains are identical to the orientations of the principal stresses for the chosen coordinate system.

6.3.2.1. Strain Gauges

The basic principle for a strain gauge can be illustrated in Figure 6-1. Within its elastic limit, when a strain gauge is stretched, it will become thinner and elongated, causing an increase of electrical resistance end-to-end. On the contrary, if the strip is compressed without buckling, it will broaden and shorten, resulting in a decrease of resistance. The new generation strain gauge foils are made from thin strips of metallic/alloy film (about 5μm in thickness) deposited on a nonconducting carrier film. Photoetching technology has enabled gauge fabrication in various lengths from 0.4 to 150mm with uniform gauge factor and in a variety of grid configurations, including single gauge, two-, three-, and four-element rosettes. These foil gauges have higher gauge factor and lower transverse response as well as good conformance to surfaces of various curvatures. Their relatively greater contact area at the grid ends reduces

shearing stress in the bonding layer, and consequently shows considerably little creep and hysteresis [Murray and Miller, 1992]. Due to extremely small footprint and lightweight, they have almost no loading effect on the test object. Therefore, together with significantly higher fatigue life, measurement precision and repeatability, foil gauges are widely used in both static and dynamic stresses measurement.

In the design of the embedded testpiece for this experiment, three rosettes comprising of two identical foil strain gauges of 2.5μm thick mounted at 90° to each other were used. These orthogonal gauges were bonded to the substrate in order to measure the surface strains in the longitudinal and transverse directions of the melt flow. Since the surface area (per unit length) of the foil is enormously greater than its cross-sectional area (for instance, the ratio is > 4000:1 for a 5.0μm foil), the filament is able to take up the necessary strain without excessive stress in itself.
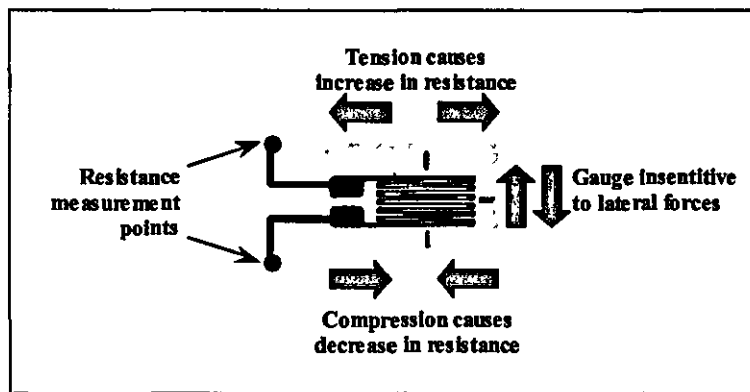
Figure 6-1 Reactions of a strain gauge

6.3.2.2. Signal Acquisition and Temperature Calibration

Typical unstressed strain gauge resistances range from 30Ω to 3kΩ. Given the limitations imposed by the elastic limits of the gauge material and of the test specimen, this resistance may change by only a fraction of a percent for the full force range of the gauge. Therefore, in order to use the strain gauge as an effective instrument, we must measure extremely small changes in resistance with high accuracy [Kuphaldt, 2002]. Also, an undesirable characteristic of strain gauge conductors is that of resistance change with changes in its ambient temperature. Such demanding precision requires a bridge measurement circuit with an ability to compensate for temperature drift for any high-temperature applications.

Conventionally, strain gauges are connected as an active arm in a quarter-bridge circuit, as shown in Figure 6-2, which uses a precision voltmeter in the centre of the bridge to accurately measure the voltage imbalance caused by any resistance change in the gauge. The rheostat arm R_2 is chosen at a value equal to the unstressed strain gauge resistance. The two ratio arms of the bridge (R_1 and R_3) are set equal to each other. The bridge will be symmetrically balanced with no force applied to the strain gauge and the voltmeter will indicate 0V. As the strain gauge is either compressed or stretched, its resistance will decrease or increase respectively, thus unbalancing the bridge and producing a voltage drop across the voltmeter.
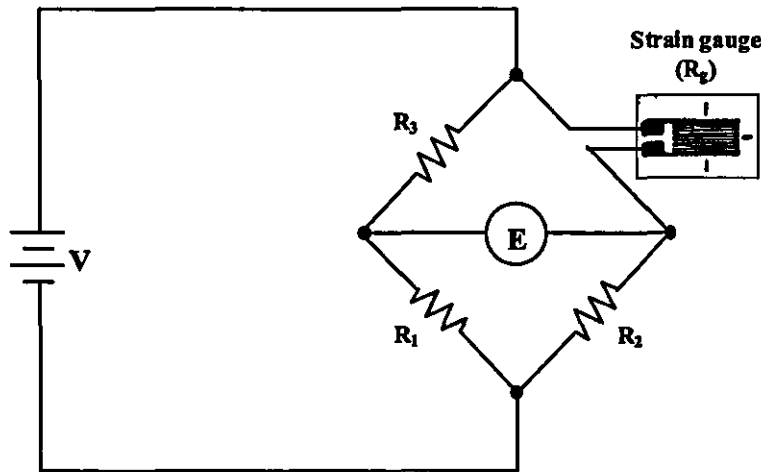
Figure 6-2 Quarter-bridge strain gauge circuit

The temperature drift problem can be overcome by adding a "dummy" strain gauge in the quarter-bridge. As depicted in Figure 6-3, resistors R_1 and R_3 are of equal resistance value, and the strain gauges are identical. Both gauges are bonded to the same test specimen, but only the *active* gauge is placed in a position and orientation exposed to physical strain. The unstressed *"dummy"* gauge is isolated from all mechanical stress and acts merely as a temperature compensation device. If the temperature changes, both gauge resistances will change by the same fraction, and the bridge's state of balance will remain unaffected. As such, only a differential resistance between the two strain gauges produced by physical force on the test specimen would cause unbalance of the bridge [Kuphaldt, 2002].
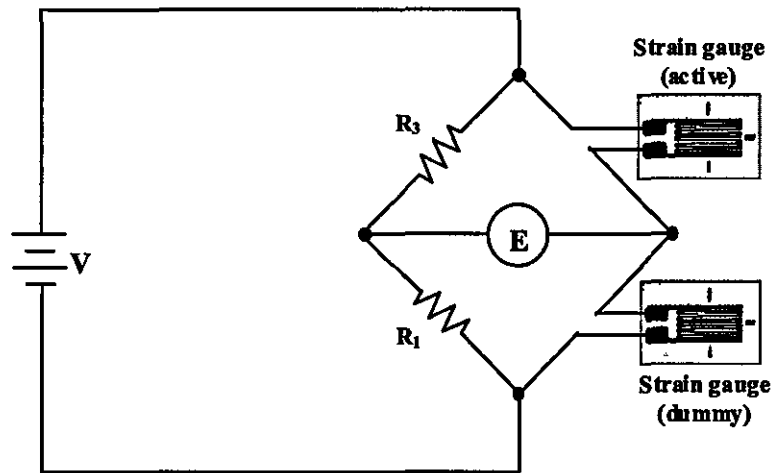
Figure 6-3 Quarter-bridge strain gauge circuit with temperature compensation

Temperature Calibration through Characterisation Programming

In the process monitoring of electronics polymer encapsulation, the melt has to solidify directly onto the strain gauges in order to account for the elements of strains sustained from both the thermal impact and mechanical forces imposed by the impinging melt on the surface of the substrate. Additionally, the gauge factor (GF) variation data as supplied by the manufacturer was only tested for steel hosting structure. This was particularly crucial as the laminated nature of the PCB substrate may produce more considerable nonlinear thermo-strains. It was hence unfeasible for a dummy gauge to be employed in the overmoulding process and an alternative method was achieved through characterisation programming technique.

In order to minimise the adverse temperature effect on the measurement accuracy of the strain gauges, a pre-characterisation calibration technique was adopted. A dummy BT substrate populated with strain gauge rosettes was heated in an oven up to 180°C and the thermal response picked up during this process was analysed. The characterisation curve obtained was then programmed into the data logger. In the actual overmoulding monitoring experiment, the temperature measured by the thermistors was incorporated as the reference offset data for the temperature drift compensation in the strain gauges. This approach dispensed with the need for a dummy gauge.

6.3.3. *Inference of Melt Pressure*

In essence, injection moulding is a statistical process because the performance of different injection velocity strategies influences the actual pressure profiles achieved on a cycle-to-cycle basis. Assuming that nozzle, runner and cavity geometries remain constant, the changes in raw material viscosity are reflected in hydraulic injection pressure and melt pressure at nozzle. The ideal relationship of these pressures is given Eqn. 2-2 as:

$$P_{noz} = \left(\frac{A_{piston}}{A_{screw}} \right) \times P_{inj}$$

(Eqn. 6-1)

where: P_{noz} = Nozzle melt pressure (bar or MPa)

P_{inj} = Hydraulic injection pressure (bar or MPa)

A_{piston} = Cross-sectional area of hydraulic piston or cylinder (m^2)

A_{screw} = Cross-sectional area of screw (m^2)

The ratio $\frac{A_{piston}}{A_{screw}}$ is referred to as the *screw intensification ratio* or *gain*, and can be defined as the ratio of the injection pressure to the pressure of the hydraulic fluid (line pressure) [Rosato *et al*, 2000]. It typically has a value of about 10. It may vary dynamically in operation due to [Speight and Hull, 1997]:

i) compressibility of the hydraulic oil caused by temperature changes;

ii) frictional effects between the screw and barrel; and

iii) the influence of polymer melt compressibility during the filling process.

In spite of the factors outlined above, it has been found from injection moulding control experiments that the derivation of the melt injection pressure from machine P_{inj} using (Eqn 6.1) gave a good correlation quantitatively and qualitatively. For instance, it has been found that the inference of P_{noz} from P_{inj} using screw intensification ratio gave the accuracies of – 0.95% to +0.01% and –0.27% to 1.66% during the primary injection and packing/holding phases, respectively [Speight and Hull, 1997]. Although this correlation should not be taken as using P_{inj} as the compromise to P_{noz} machine control, the measurement of the former is more preferable because it is simpler to construct [Johannaber, 1995]. Moreover, P_{inj} can be useful to evaluate many machine parameters, such as pressure settings, screw timings and monitoring of pressure changes. The pressure of the material and hydraulics in the machine barrel become similar as the mould is filled [Rosato *et al*, 2000].

The 30-tonne Engel injection moulding machine used in these experiments was not equipped with the facility to output a pressure-time curve per shot (see Appendix 2 for full machine specifications). However, values of the peak P_{inj} at switch-over were recorded. The specific P_{noz} at the screw was derived from the screw intensification gain, which was 7.6875. As each overmoulding process setting in the DOE was repeated with three runs, the average P_{inj} was used in the calculation of the P_{noz}. Hence, although sensing of material pressure at the nozzle can be done its usefulness is questionable. In this experiment, the melt injection pressure profiles are therefore determined using the screw intensification gain from the machine P_{inj} as discussed above.

6.4. Design of *"Board-level"* Process Monitoring Circuit

Figure 6-4 and Figure 6-5 show the schematic drawing and the final artefact constructed for the purpose of *board-level* real-time monitoring of the encapsulation process in this experiment. The properties of all the components as populated on the circuit are listed in Table 6-1. The circuit was assembled on a 35cm×55cm BT substrate, using surface mounting reflow soldering to reflect conventional technology. The signal interconnections from the subassembly were provided by two 20-way, 0.5mm pitch, 150mm long flat flexible cables (Sumitomo Electric, part no. SL20150BD8-BLP14M2896). These polyester-based flexes were constructed with polyimide reinforced terminations at each end. Standard 60/40 tin/lead solder, eutectic melting temperature of 183°C, was used in the mounting of the cables to the BT substrate via an area of 11mmx7mm bonding pads plated with 0.8μm electroless gold. Measurements showed the resistance from the start of a flex cable to the substrate termination was less than 300mΩ.

Component ID	Footprint	Type/value
SG1, SG2, SG3	7.2mm x 7.2mm	QFCA-1 Strain gauge
VR1, VR2, A2, A4	SOD-80	10kΩ NTC thermistor
A1	SO-16	(8 x 10kΩ) resistor IC package
A3	SOT-23	BAV99 dual silicon diode

Table 6-1 Components for the process monitoring circuit
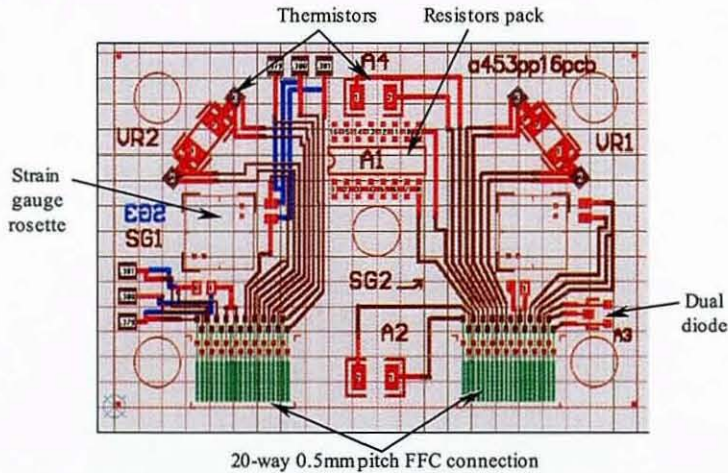
Figure 6-4 Schematic layout of the process monitoring circuit

(a) Top surface   (b) Bottom surface
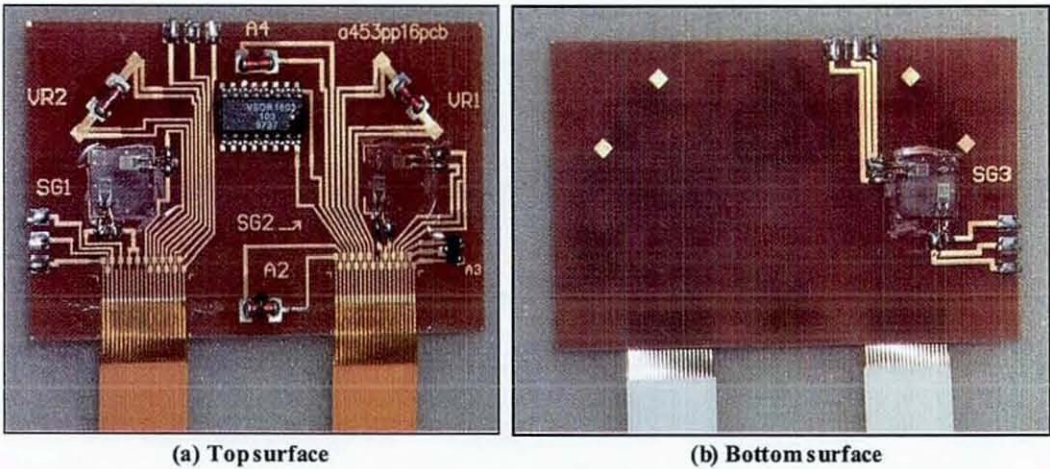
Figure 6-5 Fabricated process monitoring circuit (BT substrate, silicone glob-top)

6.4.1. Strain Gauge Rosettes (SG1/2/3)

SG1, SG2 and SG3 are two-element rosettes of two 1.0mm long by 1.3mm wide Cu-Ni strain gauge foils mounted at 90° to each other on the circuit substrate, occupying a footprint of $7.2 \times 7.2 \text{mm}^2$. This polyimide-laminated rosette is shown in Figure 6-6 below. Individually, each foil has a gauge resistance of 120Ω ($\pm$ 0.5%), nominal gauge factor of 2.10 ($\pm$ 0.1%) and linear CTE of $\pm 0.015\%/°C$ when tested on mild steel, as shown in Figure 6-7. These gauges have a maximum allowable strain level of $30,000\mu\text{m/m}$ (3%) with a nominal fatigue life of more than 10^5 reversals at $1,000\mu\text{m/m}$ within the operating temperature range of $-20°C$ to $+200°C$, hence making them applicable to both static and dynamic strains. Also, because both

surfaces of the foil are completely laminated, the gauge grids are entirely protected from external loading. Phenol-epoxy adhesive E110 was used to cement the rosettes to the substrate surface because it is the most suitable for polyimide backing gauges in high temperature applications, as recommended in the product data sheets.

The location of each strain gauge rosette was arranged such that SG1 and SG2 would measure the thermomechanical strains induced in the transverse (defined as X-axis) and longitudinal (defined as Y-axis) directions of the filling polymer melt on the top substrate surface, at the rear-end and front-end from the injection gate, respectively. The combination rosettes of SG1 and SG3 in an identical position on opposite surfaces would provide simultaneous measurement of differential strains caused by the bending moments as result of the thermomechanical stress from the melt. This layout can be seen in Figure 6-5.

As discussed in section 6.3.2.1 above, the thermal response of the strain gauges was pre-calibrated into the data logger in order to compensate for undesirable temperature drift. Without the need for a reference dummy gauge on the circuit, a 120Ω quarter-bridge signal-conditioning circuit, as shown in Figure 6-2 above, was used to process the acquired data. This setup provided six strain measurement outputs during the in-process data acquisition study.

The strain generated in the specimen is transmitted to the resistor (foil or wire) through the gauge base (backing), where expansion or contraction occurs. As a result, the resistor experiences a variation in resistance, which is proportional to the strain as indicated in the following equation:

$$\varepsilon = \frac{\Delta R/R}{GF}$$

(Eqn. 6-2)

where: ε = strain in the direction of gauge axis

GF = manufacturer-specified gauge factor

$\Delta R/R$ = unit change in measured resistance

Voltage drops across the strain gauges were the actual measured quantity in the process monitoring of the overmoulding with a supplied current of 1mA.

An amplifier was required to provide a buffered DC output voltage of selectable amplification to the data logging system. The gain used was 238, which for an excitation voltage of 2Vdc,

gave an output of 5Vdc for an anticipated full-scale deflection of 5000μm/m. Subsequently, the signal processing of the data was performed by the software of the PC-based data acquisition system, as outlined in Figure 6-8 below. The process started with the acquired voltage output from a strain gauge (V) divided by its current (I) to get the corresponding resistance (R). The latch constantly output the last received value (R_0) and when this is subtracted from its current value, the resistance change (ΔR) resulted from the strain was obtained. The unit resistance change $(\Delta R/R)$ was then divided by the gauge factor (GF) to produce the measured strain.
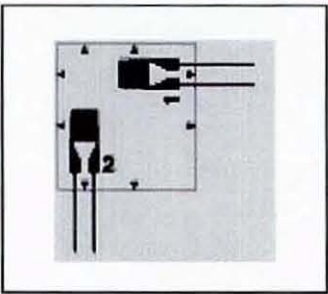
Figure 6-6 Polyimide-based 1mm Cu-Ni strain gauge rosette
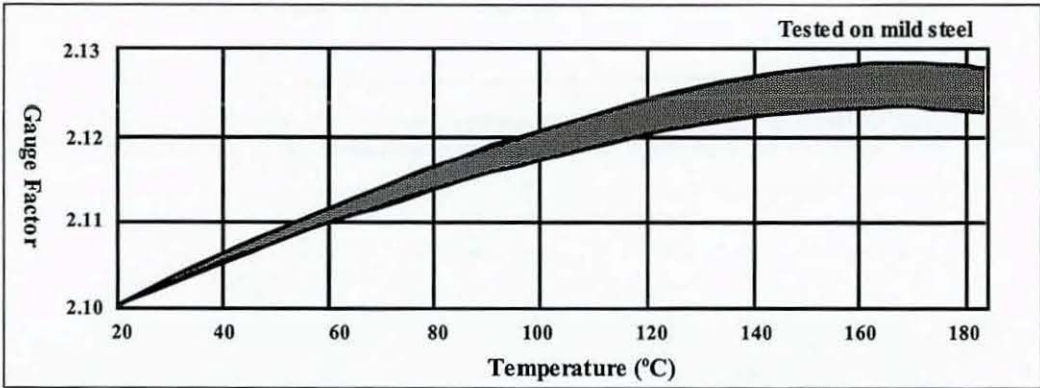
Figure 6-7 Gauge factor variation with temperature for the Cu-Ni strain gauge foil
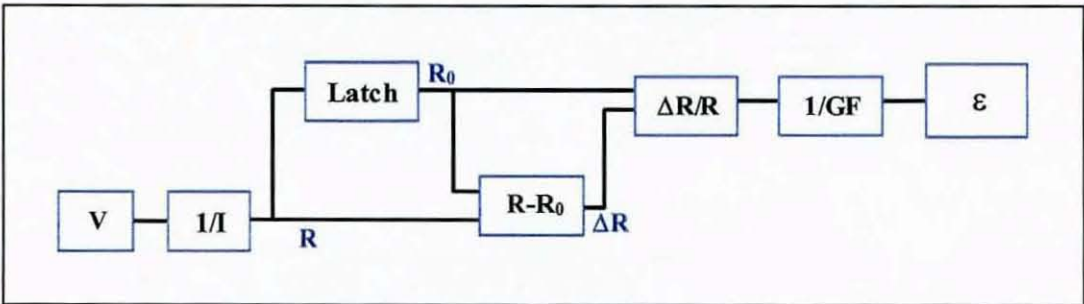
Figure 6-8 Software signal processing for strain gauges

6.4.2.   Thermistors (VR1/2 and A2/4)

A hermitically sealed glass-encapsulated thermistor is a cost effective solid-state sensor widely used in temperature measurement, due to its high sensitivity and rugged construction. VR1 and VR2 on the process board are SOD-80 surface mounted thermistors (Philips part no. 2322 633 53104) with an operating temperature range of $-40°C$ to $200°C$ and output resistance of $100k\Omega \pm 5\%$ (R_0) at $25°C$ (T_0). A2 and A4 are similar types of device, but were included due to the availability of substrate space and I/Os. The inclusion of these four thermistors not only allowed the measurement of board-level temperature distribution at various positions, but also provided a means of testing the integrity of solder interconnection as well as package thermal resistance assessments during and post overmoulding.

Semiconductor oxides are unlike metals in that they produce a decrease in resistance with temperature increment, known as a negative temperature coefficient (NTC). The standard resistance-temperature relationship for a thermistor can be expressed as:

$$ ln\left(\frac{R}{R_0}\right) = \beta\left(\frac{1}{\theta} - \frac{1}{\theta_0}\right) \quad \text{or} $$

$$ \frac{1}{\theta} = \frac{1}{\beta} ln\left(\frac{R}{R_0}\right) + \frac{1}{\theta_0} \tag{Eqn. 6-3} $$

where: R = the resistance of the thermistor at temperature θ

R_o = the resistance of the thermistor at temperature θ_0 (in this case, $10k\Omega$)

β = a material constant (in this case, 3977K)

θ = measured temperature in Kelvin

θ_o = the temperature in Kelvin at which R_o is rated (in this case, 298K)

β is the exponential factor, known as the "beta" value or sensitivity index of the thermistor material. Eqn 6.3 was subsequently programmed into the PC-based data acquisition system to obtain the measured values of θ (K), which was then converted into T (°C).

The sensitivity of a thermistor can also be calculated from [Dally *et al*, 1993]:

$$ S = \frac{\Delta R / R}{\Delta T} = -\frac{\beta}{\theta^2} \tag{Eqn. 6-4} $$

For the components used in this process monitoring circuit, $\beta = 3977$ K at $\theta = 278$ K. The sensitivity therefore equals −0.05/K, which is an order of magnitude more than that of other temperature sensors (for instance, sensitivities are typically +0.0035/K for a platinum resistance thermometer, 0.0025/K for gallium-arsenide diode sensors). This high sensitivity thus gives the SOD-80 thermistors an excellent response of $\Delta R / \Delta T = 500\Omega/K$.

Therefore, the major advantages of thermistors in this experiment can be attributed to their high sensitivity, high resistance and ruggedness. Because of its high sensitivity, the change in resistance due to temperature variation (ΔR) is much greater than the small resistance change in the lead-wires (ΔR_L) caused by the same temperature variation. Measurement errors resulting from temperature effects on the lead wires are therefore very small and can be neglected, even for relatively long wires [Dally *et al*, 1993]. Also, with its large output resistance relative to that of the lead-wires ($R \gg R_L$), any reduction in sensitivity of the device caused by its lead-wires bears little consequence to the overall system. A glass-encapsulated thermistor also offers extra thermomechanical robustness and higher stabilities, thus higher measurable and operating temperatures.

Self-heating of a thermistor can be a contributing factor to the sensing errors. The power dissipated ($p = i^2R$) will heat it above its ambient temperature and contribute to its output. In order to minimise this, the current flow through the thermistor should be limited to a value such that the temperature rise arising from the i^2R power dissipation is smaller than the precision to which the temperature is to be measured. In the case of the 10kΩ thermistors selected for this experiment, their dissipation constant was rated at 2.5mW/°C. Since a temperature measurement accuracy of 1°C was to be obtained, the power dissipated by the device should be limited to less than 2.5mW. This limitation set a maximum current i of:

$$i = \sqrt{p/R} = \sqrt{\frac{2.5 \times 10^{-3}}{10.0 \times 10^{3}}} = 500.0\mu A$$

The current i through the thermistors was therefore set to 400µA in this experiment to minimise the component heat dissipation drawback on the measured temperature. The high sensitivity of the device ensured that satisfactory response could be achieved even at this low current.

6.4.3. Resistor Pack (A1)

A1 is an SO-16 DIL gull-wing IC (Vishay Intertechnology, part no. VSOR-1603-103-9737) consisting of eight independent 10kΩ± 2% resistors, as depicted in Figure 6-9. The layout of the IC is such that it provides nominally equal resistors isolated from each other. The component rated operating temperature is –55°C to 125°C. In this experiment, these resistors allowed an assessment of the IC internal continuity as well as its solder joint integrity for a larger package during and post overmoulding. They could also act as a large area heat source with reasonably close temperature sensing in VR1 during the testing environment.

The eight equi-value resistors were connected in parallel to each other to form a resistance network, which was completely embedded by the polymer melt. A 430Ω resistor (R_{out}) was connected in series with this resistance network in the signal conditioning circuit external to the overmoulded article, as depicted in Figure 6-10. Variations of the resistance in any of the individual parallel resistors induced by thermomechanical effects during the overmoulding cycle would be reflected by the output voltage, V_{out}, across R_{out}. The net resistance of the parallel-connected resistor package, R_T, could be calculated as:

$$\frac{1}{R_T} = \frac{1}{R_1} + \frac{1}{R_2} + \cdots + \frac{1}{R_8} = \frac{8}{R} \qquad \text{as } R_1 = R_2 = \cdots = R_8 = R$$

$$\therefore R_T = \frac{R}{8} = \frac{10k\Omega}{8} = 1.25k\Omega$$

With $V_{in} = 5V$ and $R_{out} = 430\Omega$, the calculated unbiased output voltage was therefore:

$$V_{out} = \frac{430}{1250 + 430} \times 5.0 = 1.2798V$$
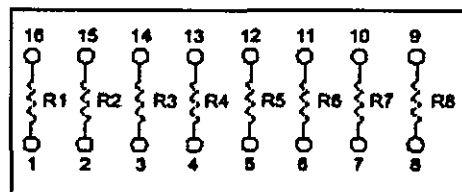
Figure 6-9 Internal connections of 10kΩ *A1* resistor IC package
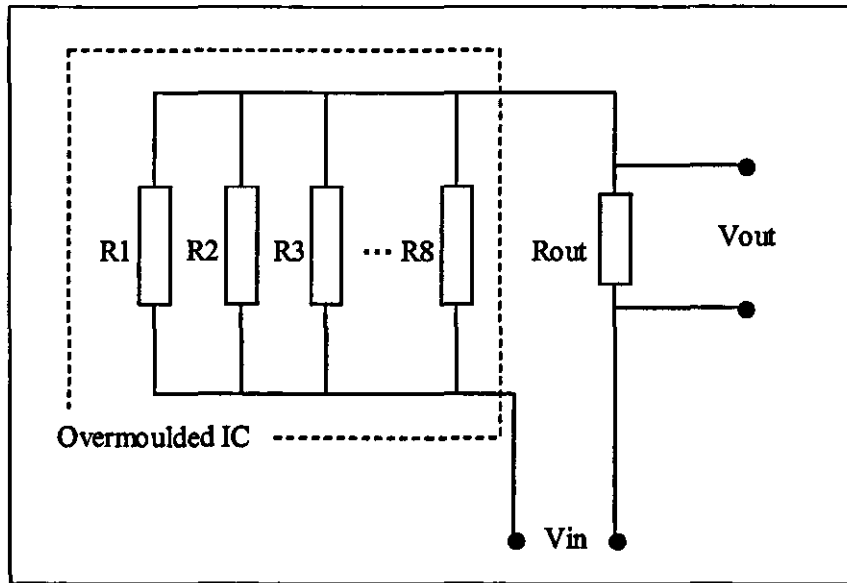
Figure 6-10 Signal I/O connections for *A1* resistor package

6.4.4.   Silicon Diode (A3)

A3 is an SOT-23 IC consisting of two N-type silicon diodes and is commonly used in high-speed switching applications. The rated operating temperature for this component is relatively low, in the range of –55°C to 150°C. The internal layout of the IC is depicted in Figure 6-11. The inclusion of the diode in the process monitoring subassembly not only provided an assessment of solder joint integrity, but also, by measuring the leakage current and forward voltage, correct functioning of the device could be monitored. *A3* could also act as a secondary temperature sensor to provide an additional indication of the thermal profile during the overmoulding.

The forward voltage drop for silicon diodes is nominally 0.7V at room temperature, but this varies inversely with the absolute temperature. As the ambient temperature increases, the voltage drop of the diode decreases proportionally. Ideal diode characteristics can be derived from the Shockley equation and expressed as:

$$I = I_s \left\{ exp\left(\frac{qV}{kT} \right) - 1 \right\}$$

where I_s = reverse saturation current, I = applied current, V = forward junction voltage, k = Boltzmann's constant (1.380×10^{-23} J/K), q = electron charge (1.602×10^{-19}C)

or $$V = \frac{kT}{q} ln\left(\frac{I}{I_s} + 1 \right)$$

In forward bias, I_s is assumed to be constant with temperature, the changes in voltage with temperature is:

$$\frac{dV}{dT} = ln\left(\frac{I}{I_s} + 1\right)$$

(Eqn. 6-5)

(Eqn. 6.5) thus defines that, if a constant current is supplied to a diode, the forward junction voltage can be measured to directly indicate its ambient temperature.
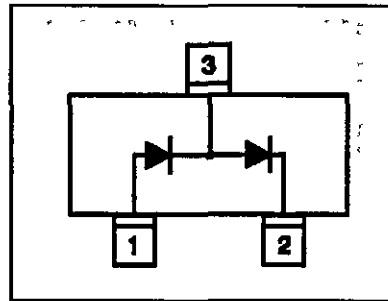
Figure 6-11 Internal schematic of *A3* dual-diode IC

6.4.5.   Flexible Connectors

In order to connect to the monitoring equipment, it was necessary to use two 20-way 0.5mm pitch flat flexible cables (FFCs) soldered to the board. The FFCs were made from polyester material with a polyimide strip protecting the conductors, where they joined the board. The flux used for the connector was a RMA (resin mildly activated). The connectors were also rather fragile and therefore Nomex (polyarylamide) tabs were bonded onto the board end of the FFC to reinforce them. The other end of each FFC was soldered to a small intermediate FR4 board onto which a socket had been mounted. For the soldered components on the board, a "no-clean flux" was used. However, as a precaution, this was cleaned using a vapour bath (Triklone-N).

6.5.   *"Board-Level"* Results and Analyses

6.5.1.   *Experimental Procedure*

The settings for these process monitoring experiments were defined based on the results
established from previous experiments. The overmoulding polymers selected were again 30%
glass-reinforced PBT (GR-PBT) (DuPont Crastin LW9130) and 16% glass-reinforced ABS
(GR-ABS) (Bayer Novodur P2HGV). The glob-top materials used were epoxy and silicone
(details in Chapters 3 and 4). For the board-level monitoring subassembly, only the solder
joints for the surface-mounted components were protected. The contoured moulding tool
designed was employed to minimise the thermomechanical stresses, as discussed in Chapter
5. The moulding conditions for each polymer were set per Table 6-2, as based on the
outcomes from previous experiments, while the materials properties are listed in Table 6-3.
The permutations for the polymer*glob-top in each of the board-level and chip-level
experiments and the number of trials repeated to maintain the confidence level were:

   i)   GR-ABS*Silicone (5 samples)

   ii)   GR-ABS*Epoxy (5 samples)

   iii) GR-PBT*Silicone (7 samples)

   iv)   GR-ABS*Epoxy (7 samples)

As shown in Figure 6-12, a subassembly was loaded in the fixed-half of the mould at its
corners by four step-notched pins. The FFCs were plugged into the DAQ connectors before
the moving-half of the mould closed with a set of four domed pins which applied pressure on
top surface of the substrate, holding the subassembly steady for the overmoulding process.
Figure 6-13 shows a sample of subassembly overmoulded with GR-ABS polymer. The results
from the measurements are discussed with details in the following sections.

Setting Polymer	T_{Melt} (°C)	T_{Mould} (°C)	v_{inj} (mm/s)	P_{Hold} (bar)	t_{hold} (s)	t_{cool} (s)	d_{SO} (mm)
GR-ABS	255	80	40	50	40	50	25
GR-PBT	230	60	40	50	40	50	25

Table 6-2 Overmoulding conditions for process monitoring experiments

Properties	GR-ABS	GR-PBT
IZOD notched impact strength, 23°C (kJ/m^2)	7	11
Vicat softening temperature (°C)	105	192
Melt volume-flow rate (cm^3/10min)	3 (at 220°C)	
Tensile modulus, 1mm/min (MPa)	5500	9500
Moulding shrinkages (%) Parallel	0.15 – 0.35	0.25
Across		0.65
LCTE (10^{-4}/°K) Parallel	0.4	0.3
Across	0.8	0.1
Density (g/cm^3)	1.16	1.51
Thermal conductivity (W/m-°K)	0.17	0.28
Melting point (°C)	105	213

Table 6-3 Material properties for the overmoulding polymers
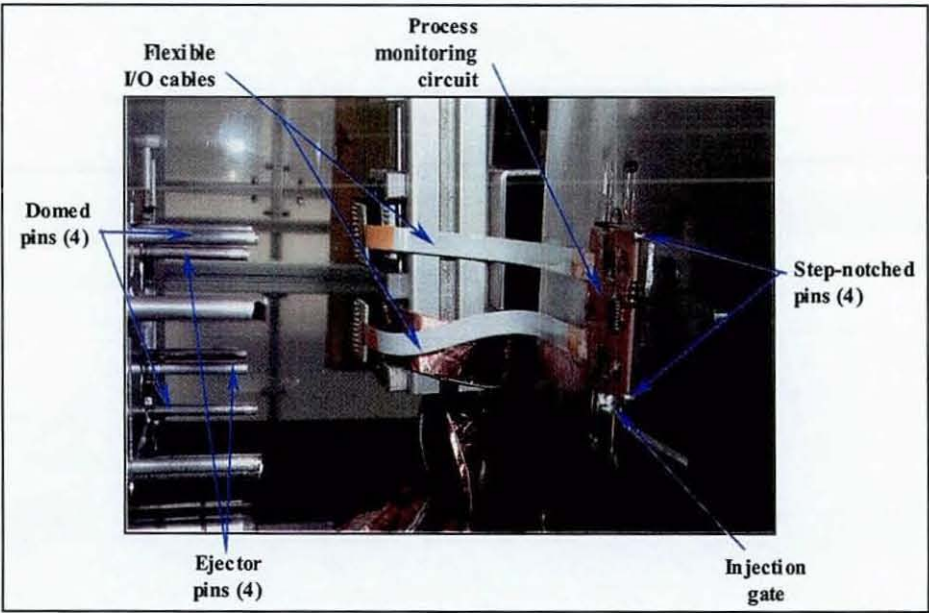
Figure 6-12 Loading of a subassembly into the overmoulding tool
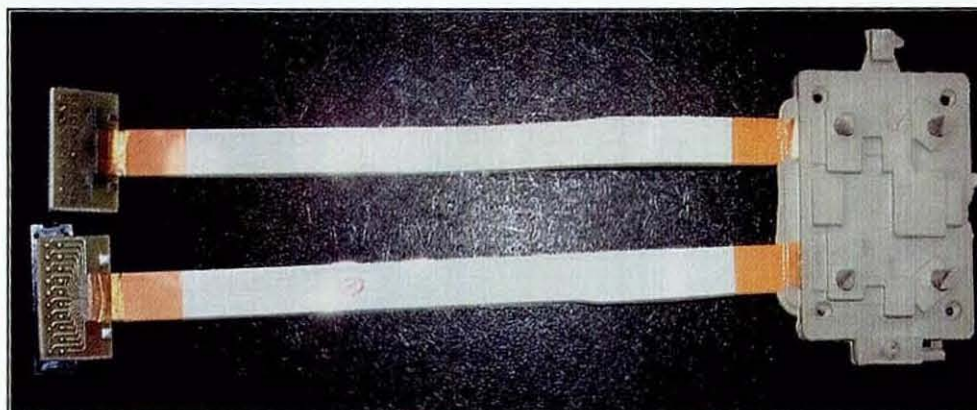
Figure 6-13 A GR-ABS overmoulded specimen

6.5.2.   Results Discussions

The injection profiles produced by the machine for both GR-ABS and GR-PBT were recorded and plotted in Figure 6-14. With both polymers programmed to be injected at the speed (v_{inj}) of 40mm/s and switch-over distance (d_{SO}) of 25mm, there was a noticeable difference in the hydraulic injection pressure (P_{inj}) that the screw had to produce to achieve that flow velocity. The machine had to produce significantly higher P_{inj} of about 135bar (13.5MPa) for GR-PBT to produce the specified melt velocity. Similar speed was achieved for GR-ABS at an injection pressure of only about 85bar (8.5MPa). This difference may be attributed to the PBT's significantly higher viscosity at its relatively low melt temperature as well as its semicrystalline molecular structure (causing a higher tendency to crystallise within the runner) than that of the amorphous structure of ABS. In general, the injection pressure during the dynamic filling phase is a function of:

    i)   the programmed injection speed;

    ii)   material viscosity at its melt temperature;

    iii) material crystallisation rate;

    iv) cavity flow resistance (geometry, wall thickness, flow length)

Factors (i) and (iv) were constant for both polymers, hence the P_{inj} was influenced mainly by the properties of the materials. From (Eqn. 6.1), with the screw intensification ratio for the Engel injection machine of 7.6875, the nozzle melt pressure (P_{noz}) of the polymers were calculated as 1037.8 bar (103.8MPa) for GR-PBT and 653.4 bar (65.3MPa) for GR-ABS. The melt filling phase took only about 1.2s for GR-PBT and 2.1s for GR-ABS to completely fill

the moulding cavity with dimensions of 35mm×55mm×22mm (not including the contour outlines). A holding pressure, P_{hold}, of 50bar was then applied for the following 40s. The part was subsequently cooled, with flowing water as coolant, in the tool for another 50s before it was ejected. Therefore, the total time from tool closing to part ejection was about 91.2s. The process cycle can be summarised in Table 6-4. However, the signal acquisitions for the various measurements were continued for up to a minimum period of 6.5 minutes. The results from these real-time monitoring studies are discussed in the subsequent sections.
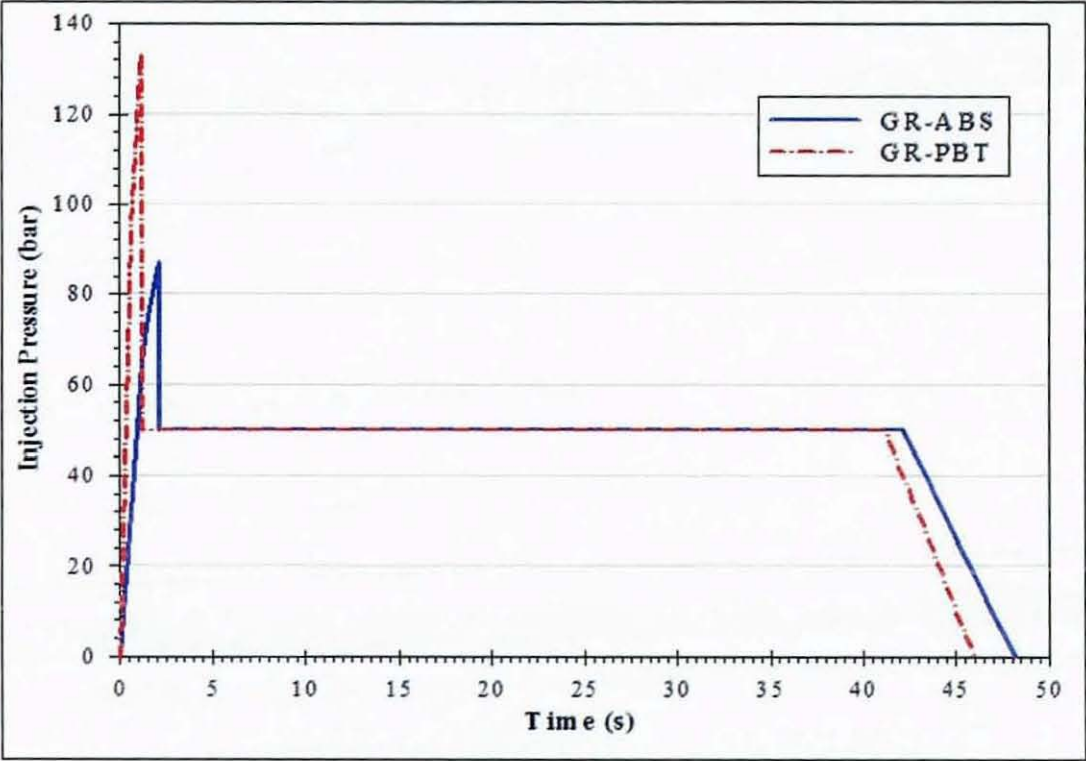
Figure 6-14 Injection profiles for board-level monitoring overmoulding process

Cycle phase	Time (s)	
	GR-ABS	**GR-PBT**
Melt filling	0 – 2.1	0 – 1.2
Holding	2.1 – 42.1	1.2 – 41.2
Cooling	42.1 – 92.1	41.2 – 91.2
Post ejection	> 91.2	> 91.2

Table 6-4 Overmoulding time phase

6.5.2.1. Temperature Measurement

<u>GR-ABS</u>

As mentioned above, GR-ABS was injected at a $T_{melt} = 255°$. From the measurement of board-level temperature using thermistors, it was found that the maximum detected temperature was consistently close to 180°C, which was always registered by VR1 – the component nearest to the injection gate. As expected, the temperature on the subassembly rose quickly during the melt filling phase, but only reaching the hottest point after 13-15s into the holding phase. When the average data was examined in the post-filling stages, it was found that thermistors VR1, VR2 and A4 cooled down at a rate of 1.35°C/s during the holding phase and then 0.68°C/s during cooling phase inside the mould. After ejection when the parts were allowed to cool down in an ambient room temperature condition, this cooling rate dropped to about 0.14°C/s and 0.11°C/s approximately150s and 250s from the instance of melt injection respectively. However, A2 was found to persistently exhibit faster cooling rate after the holding phase. It cooled more rapidly at 1.42°C/s during holding and 0.69°C/s during cooling phase, respectively. Nevertheless, it dropped back to 0.13°C/s after 150s and then at 0.11°C/s after 250s, thus approximating the rates of other thermistors. These changes in the heating/cooling rate can be observed clearly in Figure 6-15.

When the temperature profiles were examined within the overmoulding windows, as shown in Figure 6-16, the following were observed:
a) with the data acquisition trigger set to the tool closing signal generated by the moulding machine, the sensing lags were in sync with the melt flow, i.e. VR1 started to sense the flow after about 0.70s after melt injection, A2 and A4 lagged by 0.25s, and finally VR2 a further 0.20s later;
b) despite VR1 always experiencing the highest maximum temperature, the maximum temperatures measured by VR2, A2 and A4 did not show any fixed patterns. This could be due to the unpredictability of the melt flow around the various components in the cavity. Nevertheless, the profiles were of consistent patterns within a 15°C window.

The comparison between subassemblies with epoxy and silicone glob-top materials showed very similar results in term of the measured temperatures for the thermistors, as evident in Figure 6-15 and Figure 6-17. The maximum temperature recorded by VR1 in this case was 178°C. This showed that the thermal conductivity of the glob-top materials (0.63W/m-°C for epoxy and 0.26W/m-°C for silicone) did not cause much disparity on the measurement

efficacy, i.e. coating the solder joints of the thermistors with either material did not prevent
the measurement of the substrate surface temperature. This also substantiated that the
temperatures measured were the effective thermal profiles of the subassembly substrate level,
and not of the component junctions. Inspection of the other thermistors also showed that
cooling rates for corresponding components were also closely matched for both glob-tops.
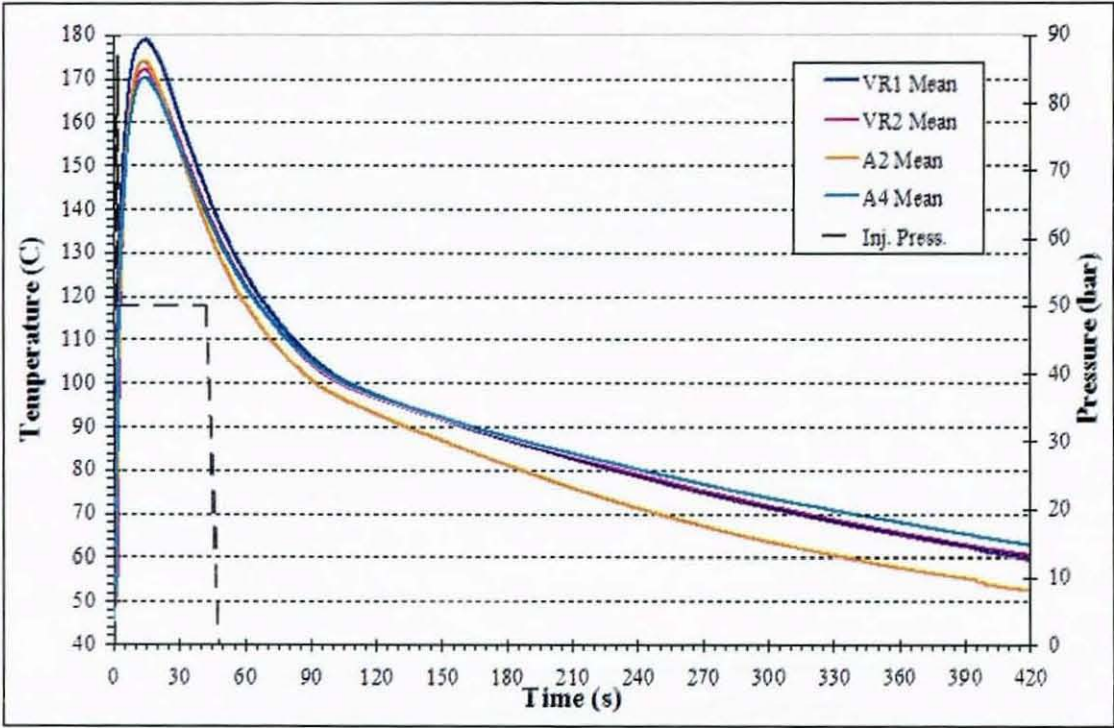
Figure 6-15 Board-level temperature profile (GR-ABS*Epoxy)
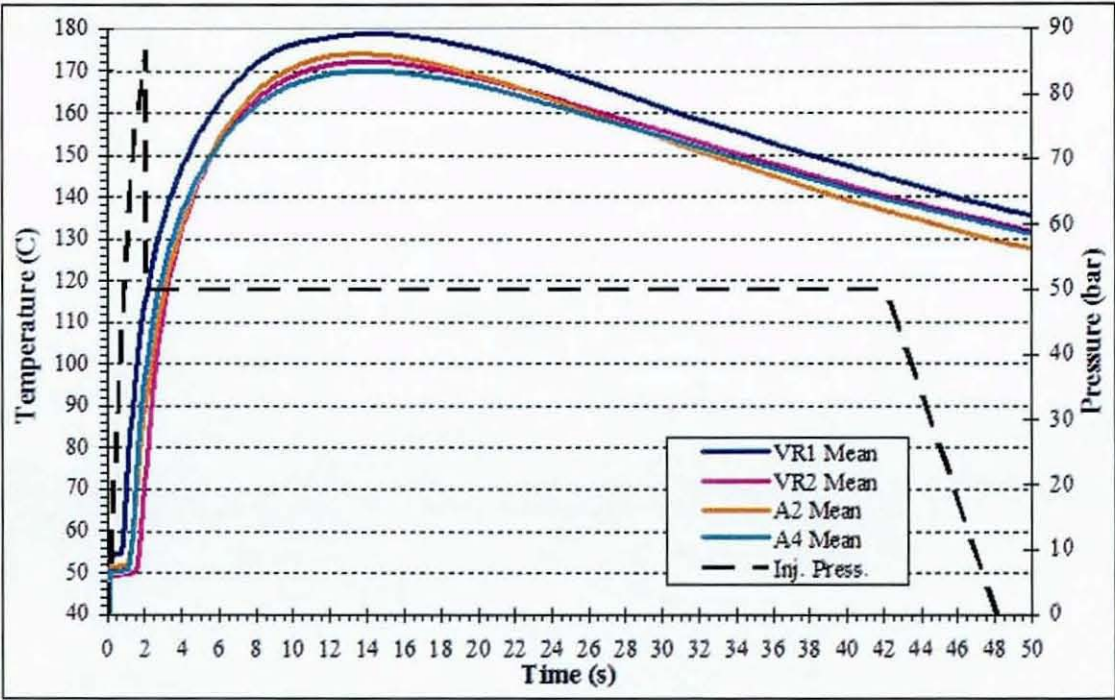
Figure 6-16 Board-level temperature profile during moulding phase (GR-ABS*Epoxy)
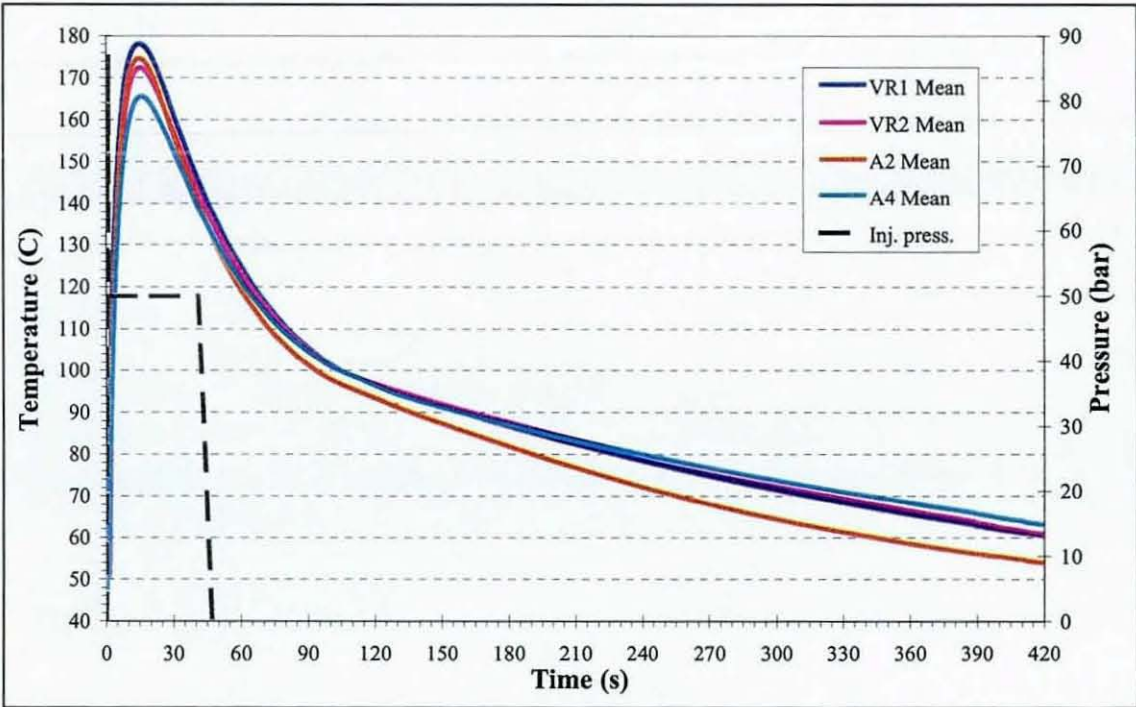
Figure 6-17 Board-level temperature profile (GR-ABS*Silicone)

GR-PBT

Due to its lower $T_{melt} = 230°C$, the subassembly overmoulded with GR-PBT as anticipated experienced lower board temperatures. The mean maximum temperature registered by VR1 was found to be about 168°C for GR-PBT*Epoxy and 164°C for GR-PBT*Silicone. Again, the maximum temperatures measured were varied among VR2, A2 and A4. The cooling rates during the holding and cooling phases were also comparable to those obtained with GR-ABS. Figure 6-18 and Figure 6-19 show the results from epoxy and silicone glob-top materials, respectively.

Thermistors VR1, VR2 and A4 cooled down at a rate of 1.55°C/s during the holding phase and then 0.58°C/s during cooling phase inside the mould. The post-ejection cooling rate dropped to about 0.07°C/s and 0.04°C/s approximately150s and 350s respectively. Similarly, A2 was found to have higher cooling rate inside the holding phase by a difference of about 0.07°C/s but again it dropped to be in line with other thermistor after ejection from the machine.
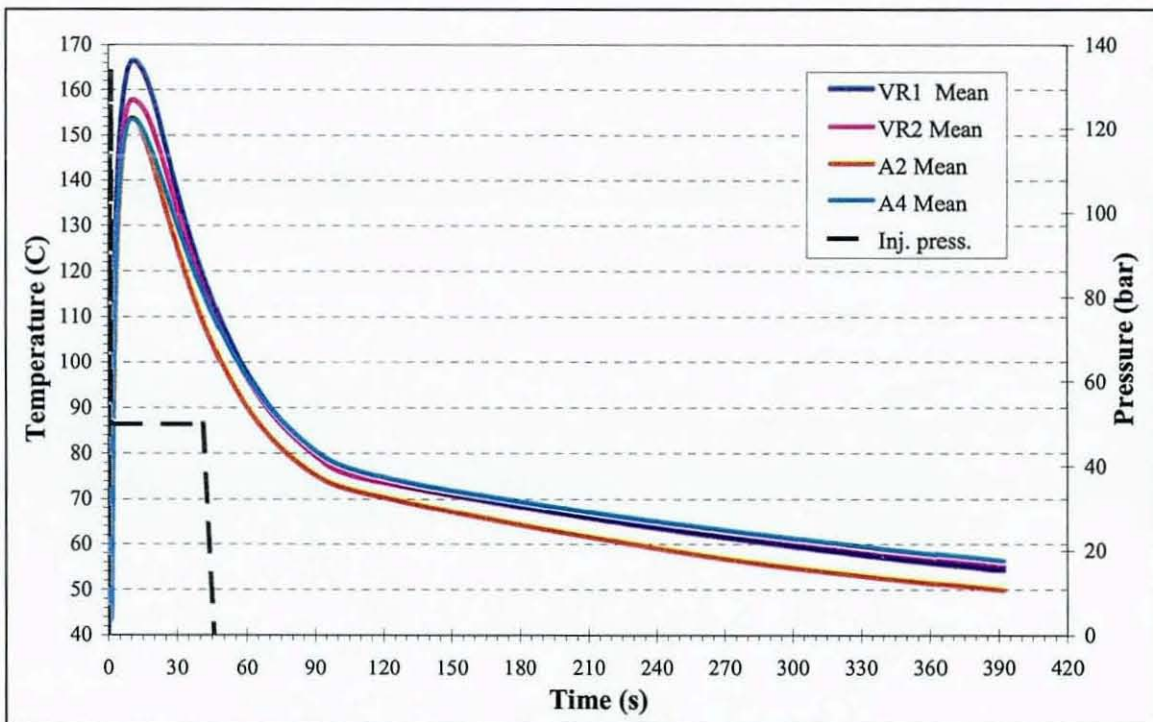
Figure 6-18 Board-level temperature profile (GR-PBT*Epoxy)
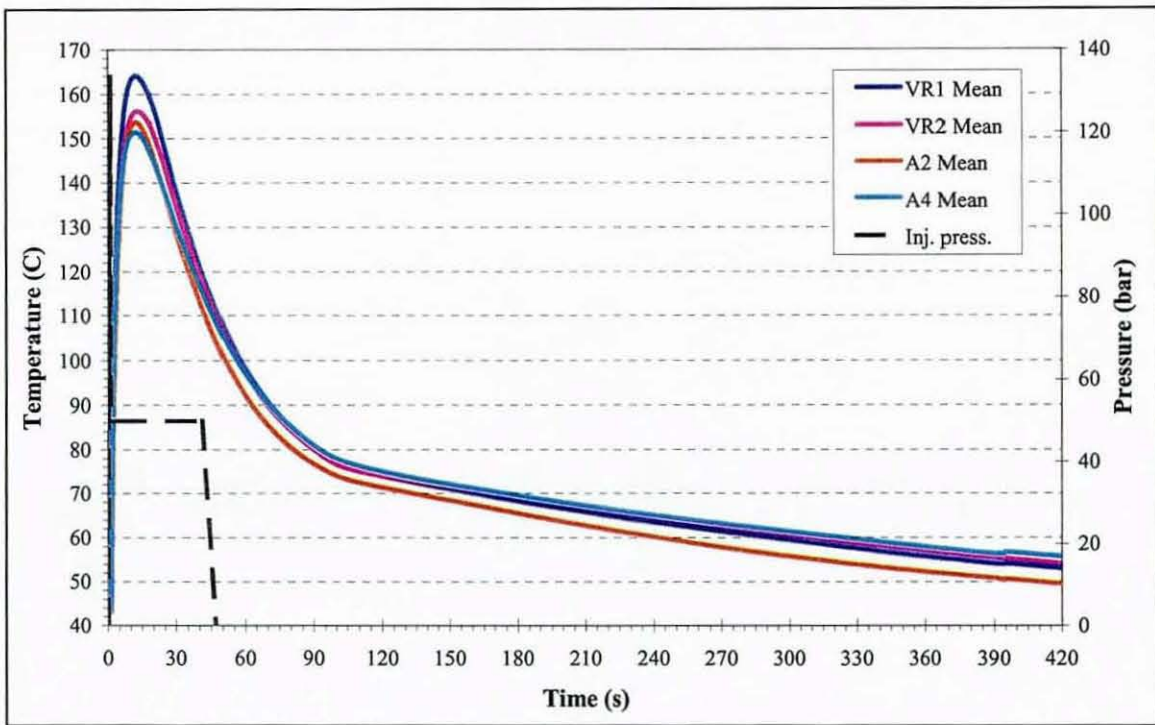
Figure 6-19 Board-level temperature profile (GR-PBT*Silicone)

The results from the temperature measurements of both overmoulding polymers have shown that the board temperature was substantially lower than the actual T_{melt}. The difference was about 75°C for ABS and 60°C for PBT. In the overall embedding of 24 subassemblies, only 5 out of the 96 thermistors monitored were found to have suffered adverse thermomechanical defect leading to malfunctions during the process, resulting in a component failure rate of 5.2% for the thermistors. When the effect of different glob-top materials was studied by comparing the results of VR1s (which recorded highest temperatures), it was found that the average temperature detected was about 2°C higher for epoxy than that of silicone for GR-PBT. This was because epoxy has a higher thermal conductivity of 0.63W/m-°C than silicone (0.26W/m-°C). However, this trend significantly diminished with GR-ABS overmould when a higher injection temperature was applied. These results can be seen in Figure 6-20 below. The results from the temperature monitoring therefore showed the following observations:

a) both the glob-top materials were able to provide the buffer against the thermal and pressure stresses for the solder joints (as no solder melting was found under x-ray inspection of overmoulded articles);

b) the thermomechanical stresses generated by the impinging polymer did not cause any
   alarming failure to the temperature-sensing components during and post overmoulding
   cycle, and,

c) the combination of glob-top layer and cooling rate of the melt in the mould was sufficient
   to significantly reduce the heat transferred to the components and solder joints.
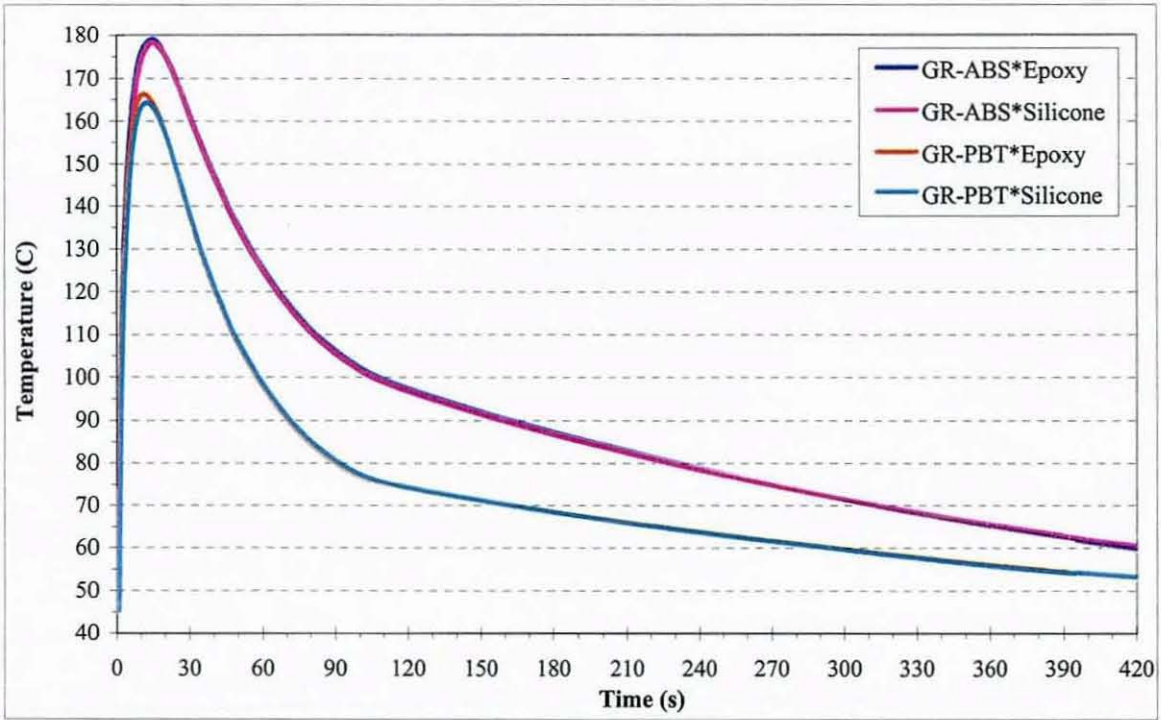
**Figure 6-20 Comparison of VR1 temperature data for "board-level" process monitoring in the
context of glob-top materials**

6.5.2.2. Strain Measurement

As the strain gauges on all subassemblies were not coated with the glob-top materials, direct
measurement of both thermal and pressure strains on the substrate was obtained from the
overmoulding experiments. With three orthogonal rosettes on each circuit at different
positions, the strains in the longitudinal direction (ε_y) and transverse direction (ε_x) to the melt
flow were monitored, as depicted in Figure 6-21. Shrinkage is considered positive when a
gauge undergoes a negative local strain. As the polymer solidified directly on the gauges
during overmoulding, the surface strain caused by both thermal and pressure effects would be
measured directly. However, through the characterisation programming for in-line
temperature calibration using the thermistor data (see sections 6.3.2.2 and 6.4.1 above), the

thermal drift was effectively isolated. The rosette SG2 was positioned immediately in front of the injection gate and SG1 was on the rear end of the circuit, while SG3 was on the bottom surface opposite to SG1.
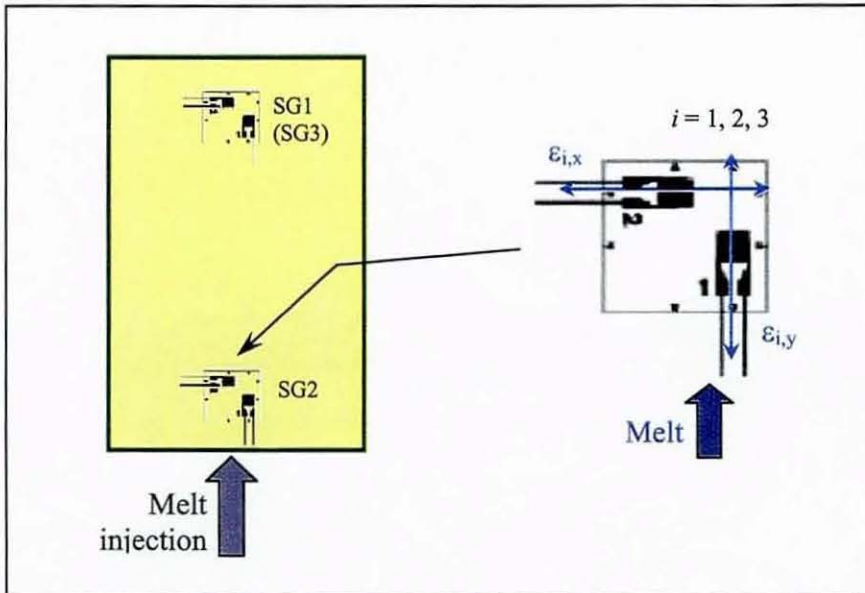
Figure 6-21 Strain directions in relative to melt flow (X – transverse, Y – longitudinal)

GR-ABS

The glass-filled ABS was injected within an injection time, $t_{inj} = 2.1$s at $T_{melt} = 255°C$ with the preset d_{SO} of 25mm and thus generating an approximately $P_{noz} = 65.3$MPa at the injection nozzle. Figure 6-22 shows the mean data of 11 overmoulded trials during the initial melt injection phase. It was found that SG1 underwent shrinkage in both X-Y directions while SG2 and SG3 experienced tensile strains. Within the first 2s, SG1 experienced a maximum $\varepsilon_{1,x} = -1400\mu$m/m (or 0.14% shrinkage) and $\varepsilon_{1,y} = -2450\mu$m/m (0.245%). In response to the bending moments of the substrate, SG3 showed strains of $\varepsilon_{3,x} = +2800\mu$m/m (0.28%) and $\varepsilon_{3,y} = +3750\mu$m/m (0.375%). The differences in the strains on the two surfaces may be attributed to the interfacial delamination of the BT laminate under the thermomechanical forces.

The SG2 rosette exhibited a more complex deformation profile during this period, in which it showed $\varepsilon_{2,x} = -1000\mu$m/m and $\varepsilon_{2,y} = -200\mu$m/m between 0.5-0.9s and then rapidly increased to $\varepsilon_{2,x} = +1900\mu$m/m and $\varepsilon_{3,y} = +3500\mu$m/m at time 1s. The strain gauges then showed considerable reductions after 1.2s (except for SG3-X, which only decreased after 1.4s) even though the injected melt pressure was increasing steadily to peak at 2.2s. It was also noted

that the gauges only started to register deformation after about 0.60s after melt injection. A similar delay was also observed with the temperature measurement by the thermistors and showed that the glob-top layer applied on the solder joints for the SMT components could have produced a signal acquisition delay of 0.10s. As predicted, ε_y was consistently higher than ε_x during filling, showing that the melt exerted greater thermomechanical shear in its direction of flow.

Immediately at the end of the injection phase, the strain gauges showed sharp falls from their respective peak strains reached during the melt injection cycle. This is clearly evident from the plot in Figure 6-23, which shows the strains measured over the injection phase. When the data are examined after the completion of the injection cycle to throughout the holding and cooling periods, as shown in Figure 6-24, it was found that the strains had reduced to within the range of $\pm1500\mu m/m$ ($\pm0.15\%$) for both directions. Significantly, SG2 was found to have dropped very rapidly close to zero strain in both the X and Y directions during this period. Another observation was that the symmetry along zero-strain axis for the pairs of SG1-X and SG3-Y as well as SG1-Y and SG3-X due to bending moments, which again suggested that interfacial delamination of the substrate may have arisen within the locality of the rosettes.

The magnitudes of all strains continued to fall exponentially after the removal of the 50 bar P_{hold}. It was found that SG2 gauges experienced the most rapid recovery to almost zero strain during the holding and cooling cycles. This may be largely due to its position at the near-end of the substrate close to the gate. This section of the mould was the last to be filled by the melt, thus meant that it was filled with relatively cooler polymer. Furthermore, the injection pressure was exerted for a slightly shorter time compared to SG1 and SG3. This may have led a better recovery capacity from the thermomechanical deformation for SG2.

Figure 6-25 shows the strain data for the complete process monitoring window of 390s for GR-ABS overmould. Note the sudden increase of magnitude in the strains at the instant of tool opening/part ejection at about time 92s. The release from the physical constraints of the mould walls gave rise to a sudden expansion envelope for the part. However, the strong adhesion formed by the solidification of polymer on the substrate in turn forced an instantaneous increase of planar tensile strains. This was more noticeable when the gauges in the transverse direction were studied. They were found to be undergoing compressive shrinkages (decreasing strains) due to polymer solidification cooling in the mould when the

ejection suddenly forced a change of magnitude into tensile expansion. Even though the longitudinal strain gauges were under tensile stress cooling in the tool, nevertheless they also showed a considerable rate of strain increment rate post ejection. It was also visible from Figure 6-25 that the post-ejection increment rates of both ε_x and ε_y were reasonably constant towards the residual strains of between +250-1000µm/m.

Figure 6-22 Average strain gauges data for GR-ABS during the *mould filling* phase

Figure 6-23 Average strain gauges data for GR-ABS during the *complete overmoulding* phase

Figure 6-24 Average strain gauges data for GR-ABS during the *holding* phase

Figure 6-25 Average strain gauges data for GR-ABS over the *complete monitoring* period

GR-PBT

The injection machine generated a $P_{noz} = 103.8$MPa at the same d_{SO} for the $T_{melt} = 230°C$ for GR-PBT resin. Due to the higher P_{noz}, it was found that t_{inj} was shorter at only about 1.2s in order to complete the filling phase. Therefore, in comparison with GR-ABS, GR-PBT was injected at a lower T_{melt} at a higher P_{noz} within a shorter t_{inj}. Also, other properties differences include the glass-filler content and polymeric nature, GR-PBT is a semicrystalline material with 30% filler content while GR-ABS is amorphous and consists of only 16% glass reinforcement. When the resultant data of SG-PBT overmoulded strain gauges were examined, slightly different patterns to those of SG-ABS were found.

Figure 6-26 shows the mean data obtained during GR-PBT melt filling cycle. An overview of the plots shows a comparable trend with the SG-ABS results in Figure 6-22 in terms of SG1 undergoing shrinkages in both X-Y directions while SG2 and SG3 experiencing tensile strains as these devices were encapsulated by the melt. SG1 experienced maximum $\varepsilon_{1,x} = -2500\mu m/m$ and $\varepsilon_{1,y} = -1600$ $\mu m/m$. However, SG2 and SG3 showed much higher deformation. Although SG2 rosette maintained the similar pattern of an initial shrinkage followed by an elongation, the strains were more prominent. Both $\varepsilon_{2,x}$ and $\varepsilon_{2,y}$ reached a maximum negative strain of - $2000\mu m/m$ at time 0.8s and then rose swiftly to $\varepsilon_{2,x} = +2800\mu m/m$ and $\varepsilon_{2,y} = +3100\mu m/m$ between 1.0-1.2s. SG3 peaked at $\varepsilon_{3,x} = +2300\mu m/m$ at 1.1s and $\varepsilon_{3,y} = +3700\mu m/m$ at 1.3s (which was outside the mould filling time window).

Table 6-5 summarises the maximum strains registered by the strain gauges during the filling cycle for both overmoulds. The results showed that both polymers exerted strains of relatively equal magnitude on SG1 and SG3. However, GR-PBT produced significantly higher transverse strains (ε_x) on SG2. It was therefore established that although GR-PBT was injected into the mould cavity at a higher P_{noz} at a lower T_{melt}, the overall maximum thermomechanical stresses produced were comparable to that of GR-ABS.

A characteristic distinction was found with the strain measured after the filling cycle between the two overmoulding polymers. From Figure 6-26, it can be seen that the behaviours of each individual gauge after reaching their respective peak deformations were dissimilar to GR-ABS (see Figure 6-22). In the overmoulding using GR-ABS, it was found that the substrate local deformations recovered to nearly the zero-strain axis almost immediately at the end of

the filling. This phenomenon was however not observed in the GR-PBT trials. With the exception of SG3-Y, all the strains gauges exhibited a sudden magnitude increase after the end of the melt fill, as evident in Figure 6-26. The longitudinal gauges data had particularly shown apparent but uniform instantaneous changes of directions at 1.2s, after which greater tensile strains were registered for $\varepsilon_{2,y}$ and $\varepsilon_{3,y}$, while $\varepsilon_{1,y}$ showed an increase in shrinkage. Although SG3 recorded a higher magnitude of strains in both directions, its pattern was nearly a mirror-image of SG1. After 1.5s, the directions of all the strains were found to undergo compressive stress with a decrement in the magnitudes and did not show a comparable recovery pattern seen in GR-ABS.

Peak Strain (μm/m) Overmould Polymer	GR-ABS	GR-PBT
$\varepsilon_{1,x}$	-1400	-1700
$\varepsilon_{1,y}$	-2450	-2500
$\varepsilon_{2,x}$	-1000	-2000
	+1900	+2800
$\varepsilon_{2,y}$	-200	-2000
	+3500	+3100
$\varepsilon_{3,x}$	+2800	+2300
$\varepsilon_{3,y}$	+3750	+3700

Table 6-5 Peak strains for GR-ABS and GR-PBT during the melt filling cycle

Figure 6-27 shows the strain measured over the subsequent holding period. It can be seen that the encapsulated substrates were under relatively high stresses. Between 9.0-11.0s, $\varepsilon_{1,y}$ reached a maximum shrinkage of -3100μm/m while $\varepsilon_{3,y}$ peaked at a maximum strain of +2200μm/m. On the other hand, $\varepsilon_{2,y}$ showed an unexpectedly high shrinkage of about -2100μm/m at 17s and then quickly fell to +500μm/m. For the transverse gauges, $\varepsilon_{2,x}$ exhibited a maximum shrinkage of only -200μm/m before recovering to the zero-strain axis, while $\varepsilon_{1,x}$ showed maximum shrinkage of +1100μm/m and gradually recovered to about +350μm/m. However, $\varepsilon_{3,x}$ was registered to peak at +2400μm/m and reduced to stay rather stable at +2000μm/m without recovery toward zero-strain.

When the strain data over the complete monitoring time of 390s were studied and plotted in Figure 6-28 below, the sudden increment of strains due to the effect of part releasing was again evident. $\varepsilon_{2,x}$ only showed very little increment as it was at an almost strain-free state. The residual strains leading to permanent deformations of the substrate surfaces were clearly greater for GR-PBT when compared to GR-ABS (see Figure 6-25). The highest residual strain was recorded by SG3 ($\varepsilon_{3,x} = +2500\mu m/m$; $\varepsilon_{3,y} = +1500\mu m/m$), thus indicating residual tension on the bottom surface of the substrate. However, SG2 showed a nearly complete recovery of strains to only $\varepsilon_{2,x} = -100\mu m/m$ and $\varepsilon_{2,y} = +200\mu m/m$; while SG1 also achieved relatively satisfactory low residual strains of $\varepsilon_{1,x} = -900\mu m/m$; $\varepsilon_{1,y} = -150\mu m/m$.
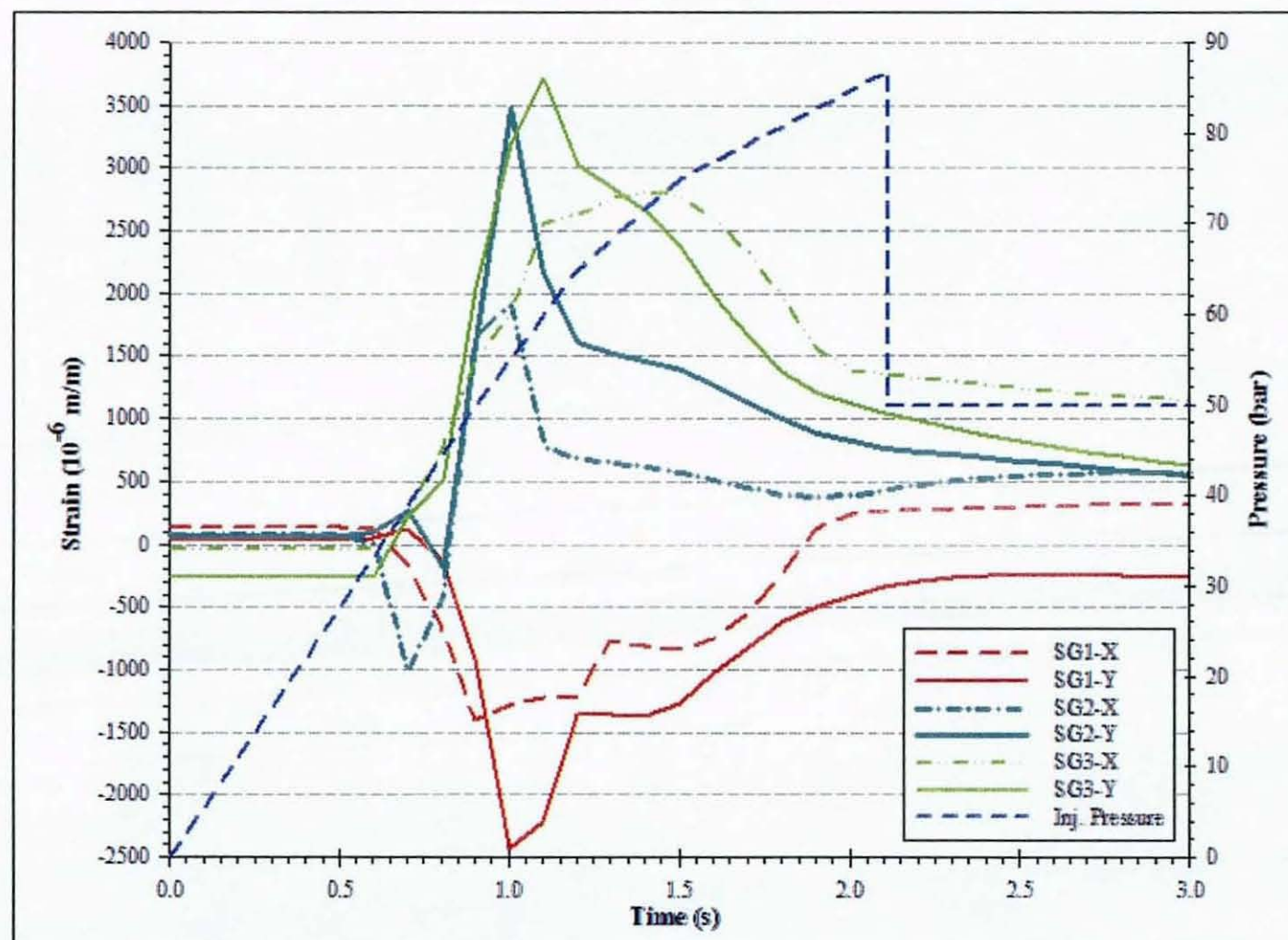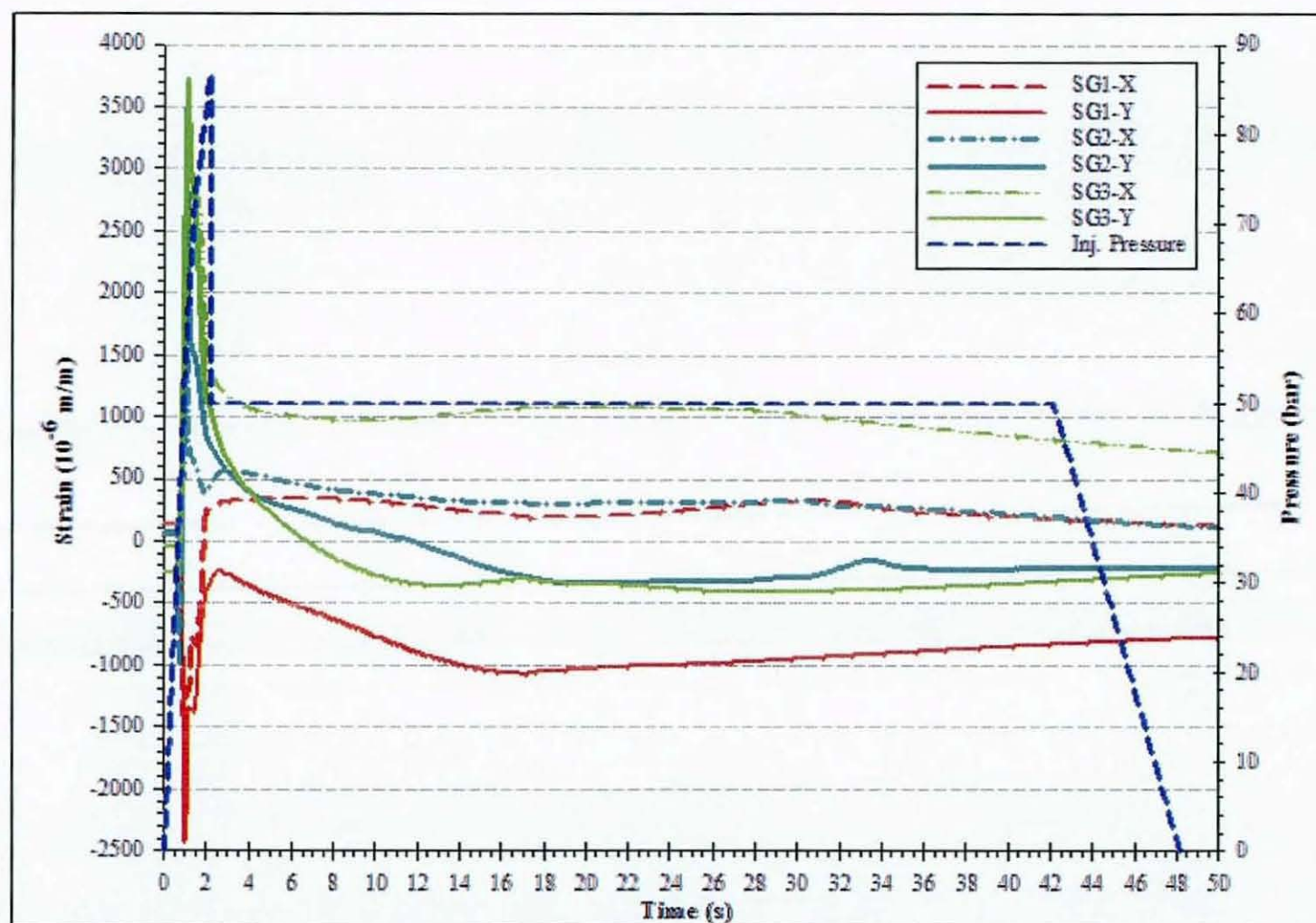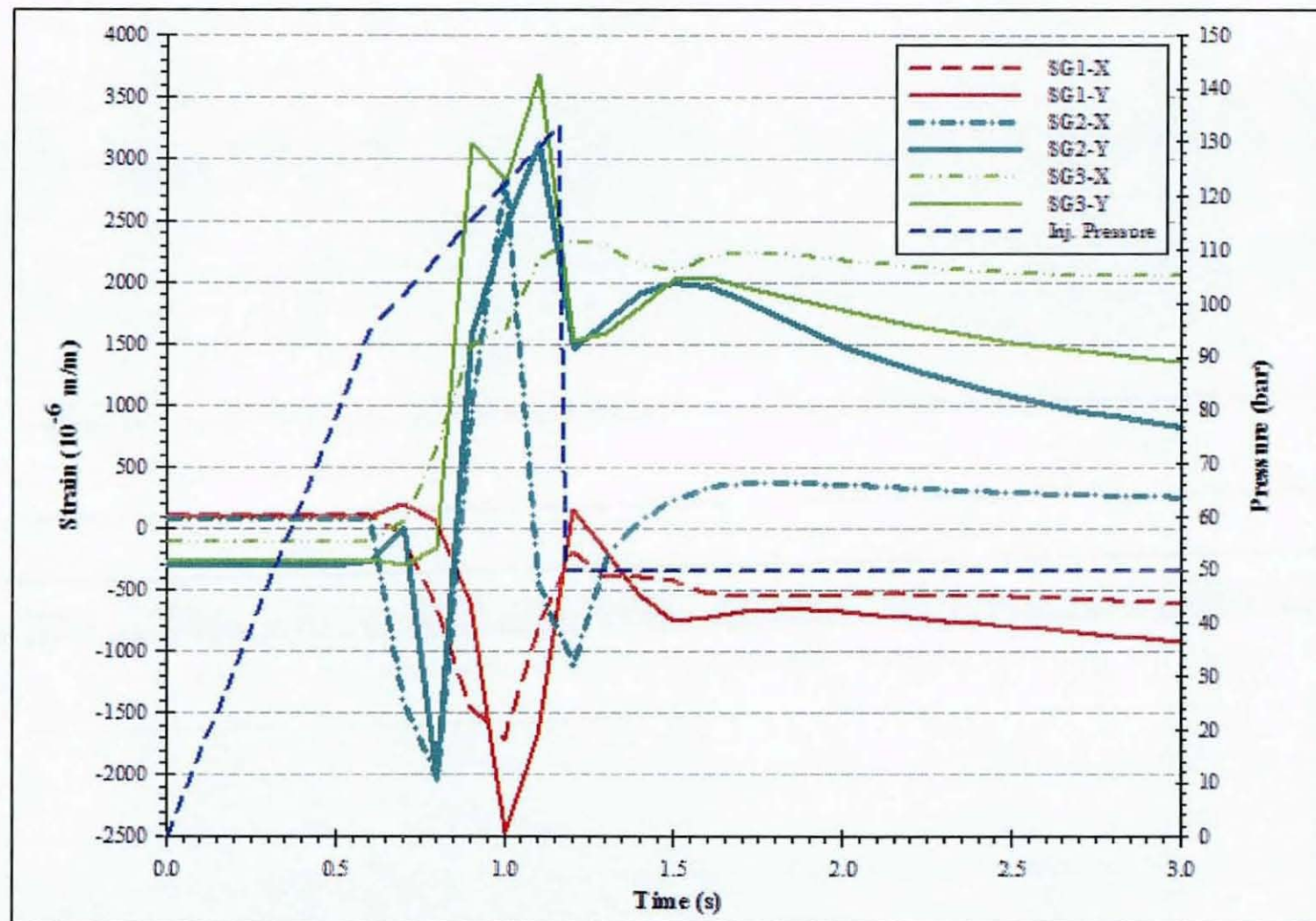
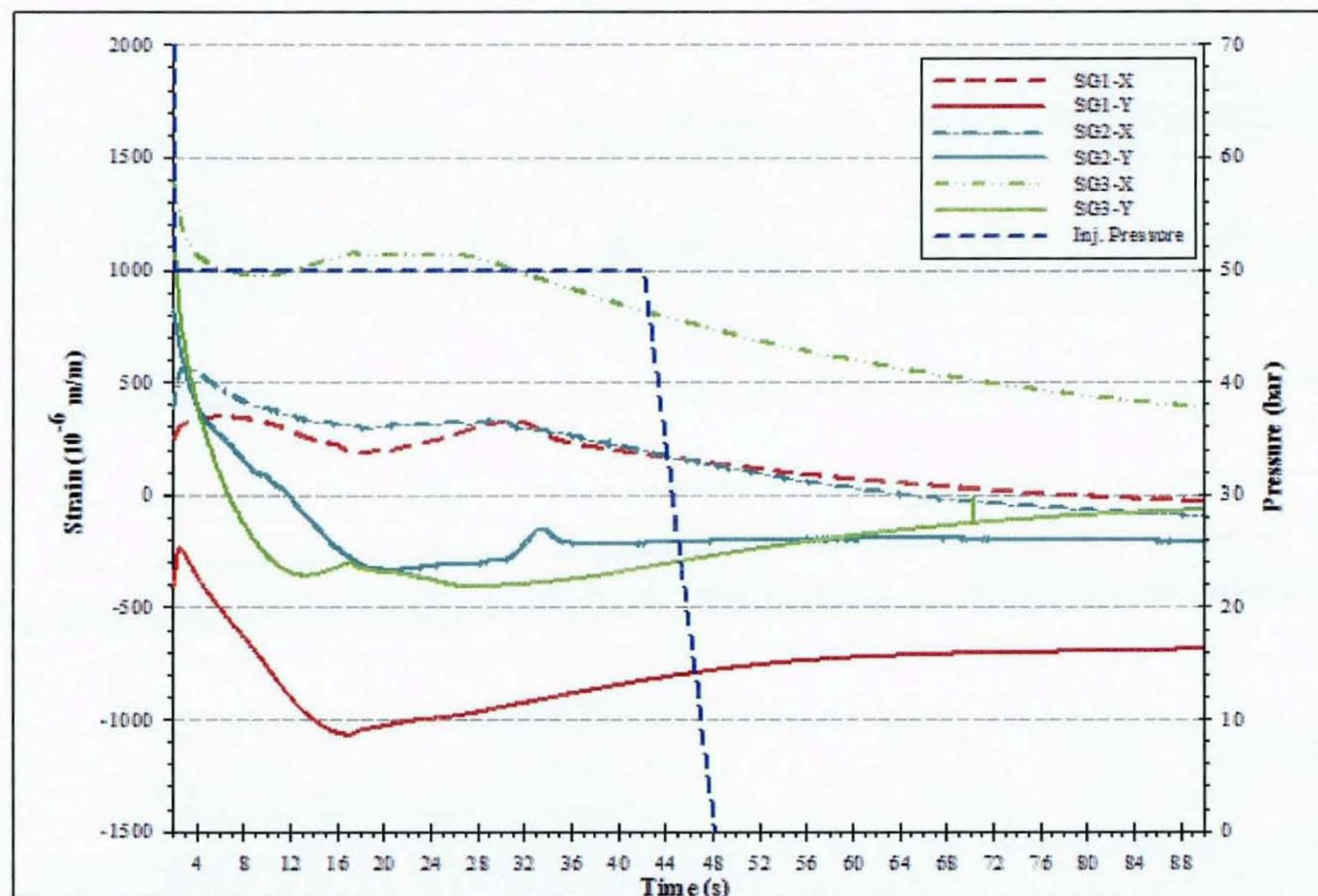**Figure 6-26 Average strain gauges data for GR-PBT during the *mould filling* phase**

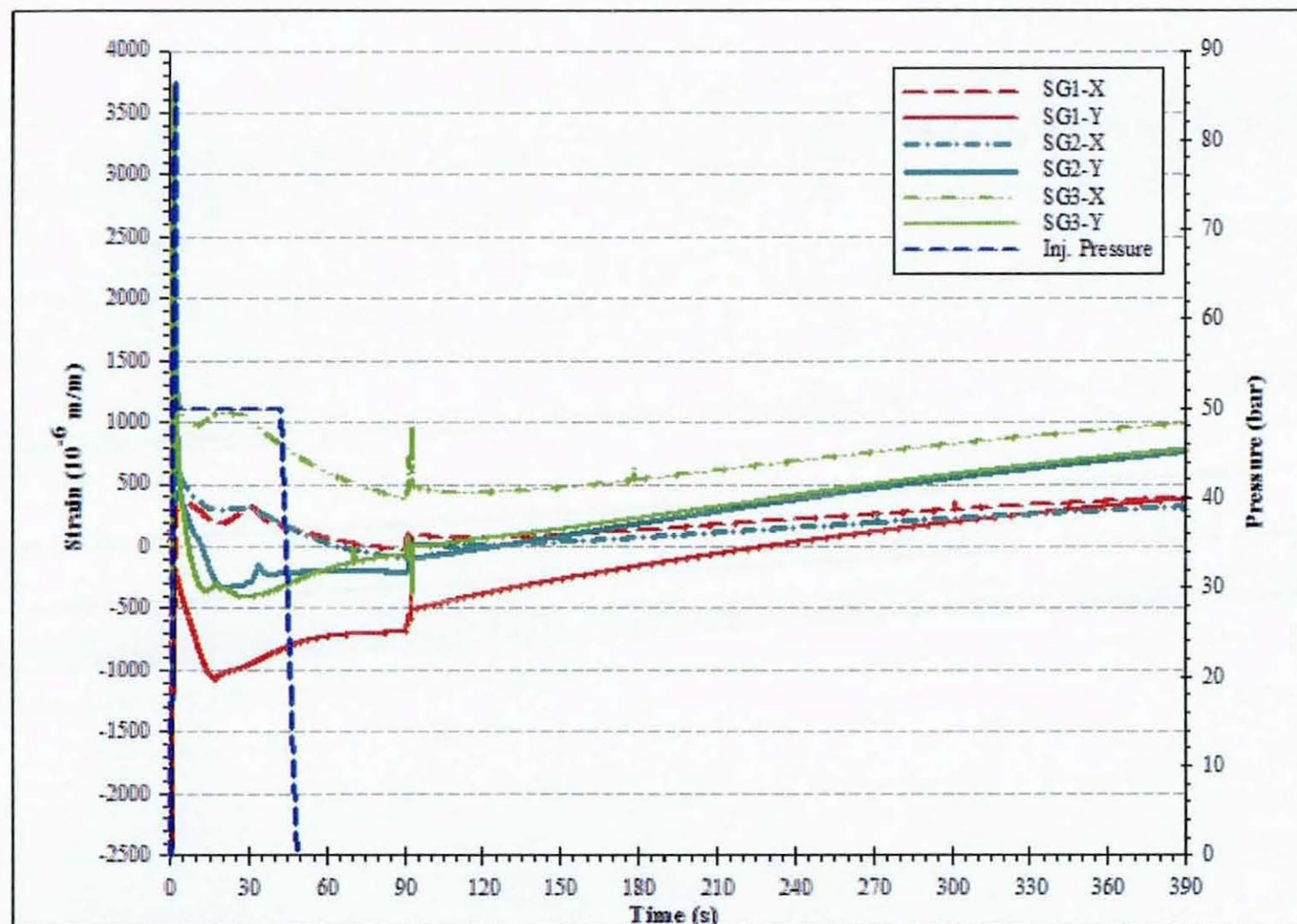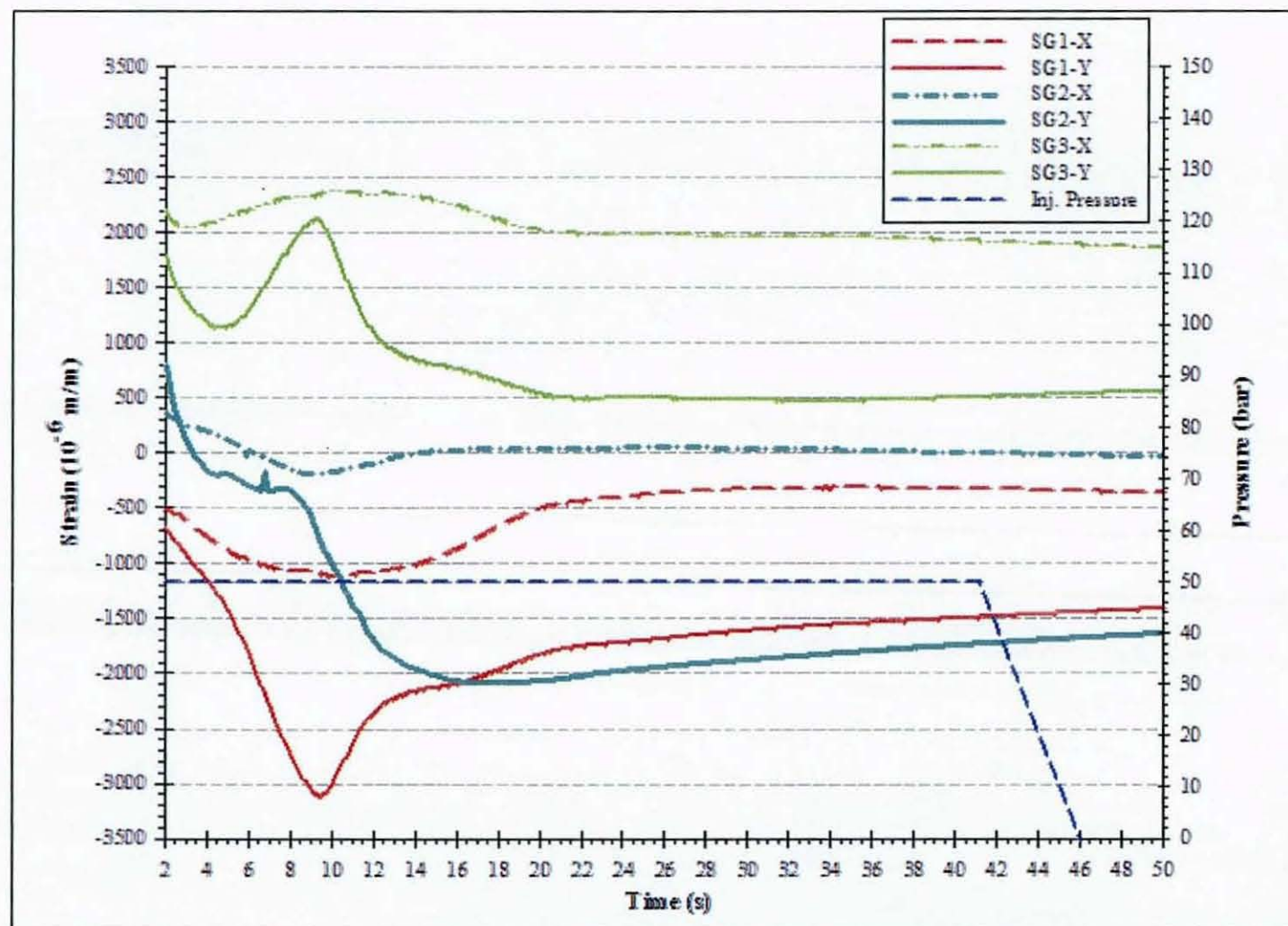**Figure 6-27 Average strain gauges data for GR-PBT during the *holding* phase**
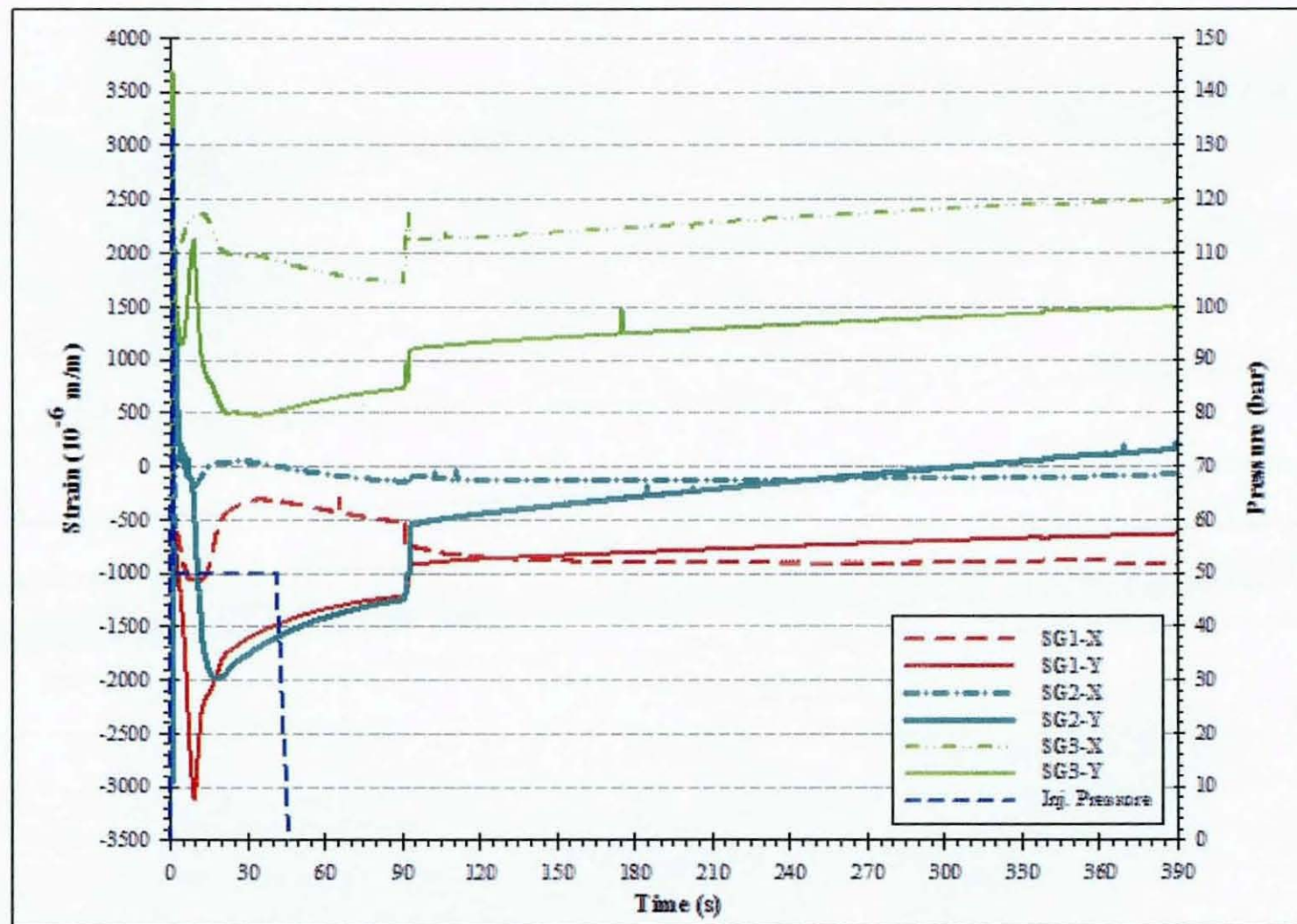
Figure 6-28 Average strain gauges data for GR-PBT over the *complete monitoring* period

Measurements of surface strains showed that the thermomechanical stresses developed during the process were of very complex patterns. The nature of the strains during the melt filling for both overmoulding polymers was of a similar pattern. Due to the shear forces of the polymer melt, strains longitudinal (ε_y) to the flow direction were much higher than the transverse component (ε_x), with corresponding differences ranging from 300-1600µm/m. It was also observed that, for all the rosettes, both transverse and longitudinal components simultaneously underwent deformations of same nature, i.e. both X and Y gauges detecting compressive (or tensile) strain at the same time.

The presence of very small unbalanced pressure distribution between the two surfaces of embedded PCB was apparent for both overmoulding polymers. The significant magnitude differences of incidentally-located component strains (such as $|\varepsilon_{3,x}|-|\varepsilon_{1,x}|$ etc.) also indicated that delamination had also occurred through the thickness of the laminate PCB at the end from the injection gate. Albeit different magnitudes, the strain profiles also showed an identical deformation pattern for both overmoulding polymers during the filling cycle which may signify the characteristic of melt flow, such that its injection pressure immediately after entering the mould cavity caused a considerable compression on the top surface of the PCB. The melt subsequently filled the cavity underneath the PCB when its packing pressure induced an upward force, hence causing a tensile elongation on the strain gauges. Furthermore, due to its higher solidification in the semicrystalline structure immediately at the end of melt injection, GR-PBT was found to impart higher packing stresses on the embedded substrates.

At ejection from the moulding cavity, it was observed that the release from the physical constraints of the mould walls gave rise to a sudden expansion envelope for the part. The strong adhesion formed by the solidification of polymer on the substrate, in turn, forced an instantaneous change from planar compressive strain into tensile strains for the transverse components, as well as noticeable increases in the longitudinal tensile strains.

The results from the strain measurement showed that, at the end of the whole overmoulding process, GR-ABS demonstrated a visibly more uniform recovery from surface thermomechanical strains. All the components strains measured were found to have recovered constantly to within residual strains of between the magnitudes of 250-1000µm/m. On the

other hand, the residual strains for GR-PBT were more inconsistent, with the magnitudes between 150-2500μm/m.

6.5.2.3. Electronic Integrity

Resistor IC (*A1*)

Section 6.4.3 has discussed the principle role of the *A1* resistor pack as a means of monitoring the internal connectivity of a standard IC package as well as the integrity of its solder joints. A nominal voltage of 5V was applied across the parallel network of 8-resitors and the voltage drop measured throughout the overmoulding process. The main focus was to detect any resistance changes resulting from thermomechanical stresses of the impinging melt. The mean data of all the overmoulding trials for all the candidate overmoulding and glob-top polymers are shown in Figure 6-29.

During the experiments, the actual input voltage fed from the data acquisition system was measured between 4.75-4.85V, thus giving an estimated output voltage range of 1.216-1.241V and this variation was reflected in the distribution of the results. Nevertheless, it was the changes in the voltage drop at the output of the IC that were of importance. In order to study the polymer thermomechanical effect, the results during the overmoulding period were studied in Figure 6-30 below. The initial output voltages were approximately 1.211V for GR-ABS*Epoxy, 1.213V for GR-ABS*Silicone, 1.219V for GR-PBT*Epoxy and 1.235V for GR-PBT*Silicone.

It was found that an increase in the output voltage occurred with the impinging of melt for all materials. The responses of the resistors to the high-temperature melt flow were almost identical for both of the overmoulding materials. However, the differences in the thermal conductivity of the glob-top coating are noticeable here: epoxy, with its higher thermal conductivity, produced more immediate and rapid increase in output voltages during mould filling, with GR-ABS*Epoxy and GR-PBT*Epoxy rising to 1.220V and 1.228V, respectively, simultaneously at about 0.35s. On the other hand, silicone showed a more gradual but greater rise of the voltage after the filling phase: GR-ABS*Silicone reaching 1.224V at about 23.5s and GR-PBT*Silicone reaching 1.243V at 16.5s.

As seen in Figure 6-29 above, all the data showed a steady decrease after reaching the respective maximum values. Table 6-6 summarises the overall results for the monitoring

period of 390s. The differences between the initial and final voltages for all overmoulding conditions were between 0.002–0.003V, thus giving the percentage voltage increase of 0.164–0.248%. From the perspective of the overall process success rate, it was found that during the overmoulding of 28 circuitry samples, only one unit of the IC (with ABS*silicone) was found to have encountered an adverse malfunction when its output voltage dropped to 0.2V during the melt filling phase.

	Output voltage at 0s (V_0)	Output voltage at 390s (V_1)	Voltage difference ($\Delta V = V_1 - V_0$)	% of ΔV
GR-ABS*Epoxy	1.211	1.214	0.003	0.248
GR-ABS*Silicone	1.213	1.216	0.003	0.247
GR-PBT*Epoxy	1.219	1.221	0.002	0.164
GR-PBT*Silicone	1.235	1.238	0.003	0.243

Table 6-6 Data analysis for the output voltage of the A1 resistor pack
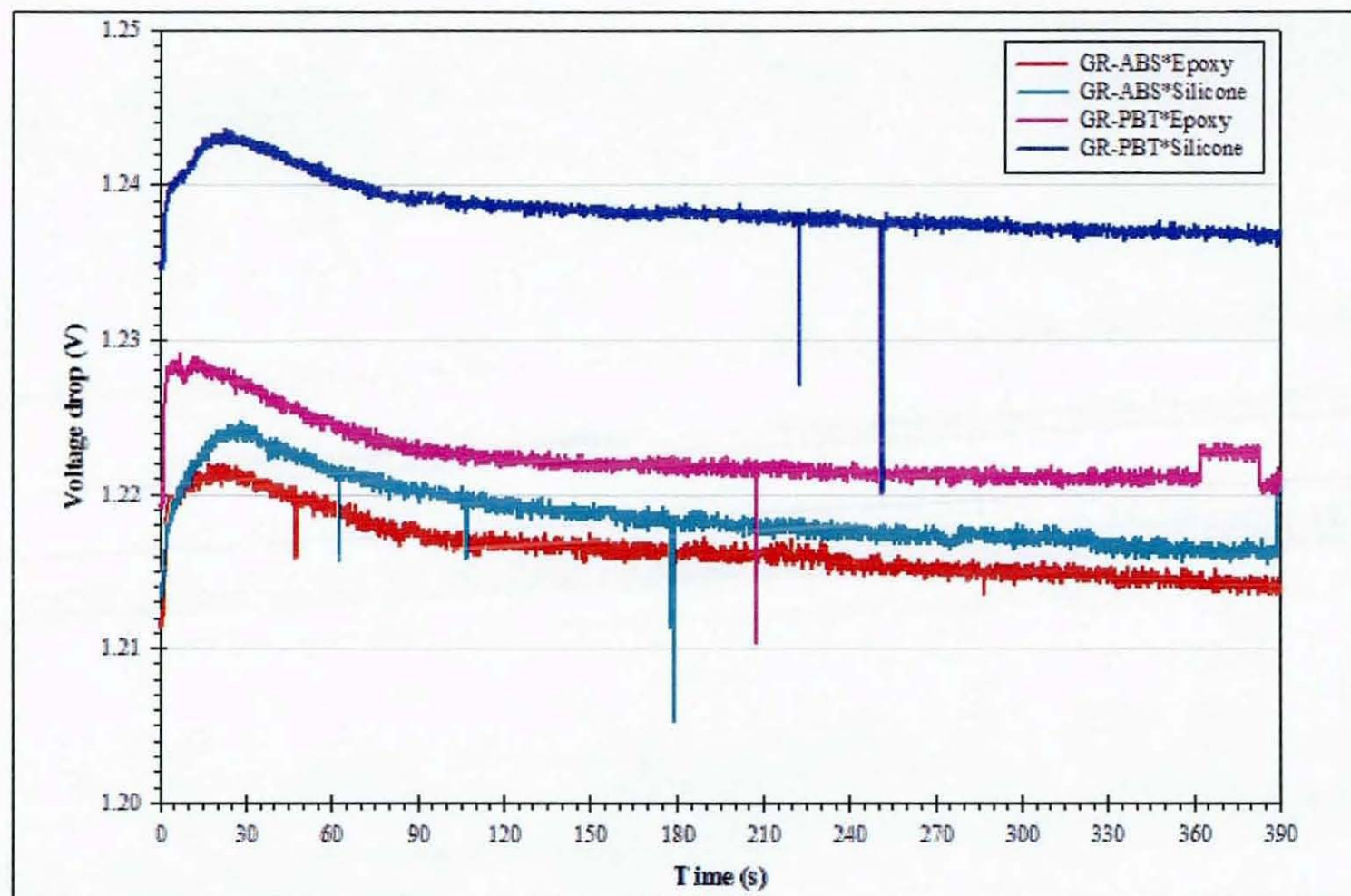
Figure 6-29 Voltage drops across resistor pack (A1) for all polymers and glob-tops
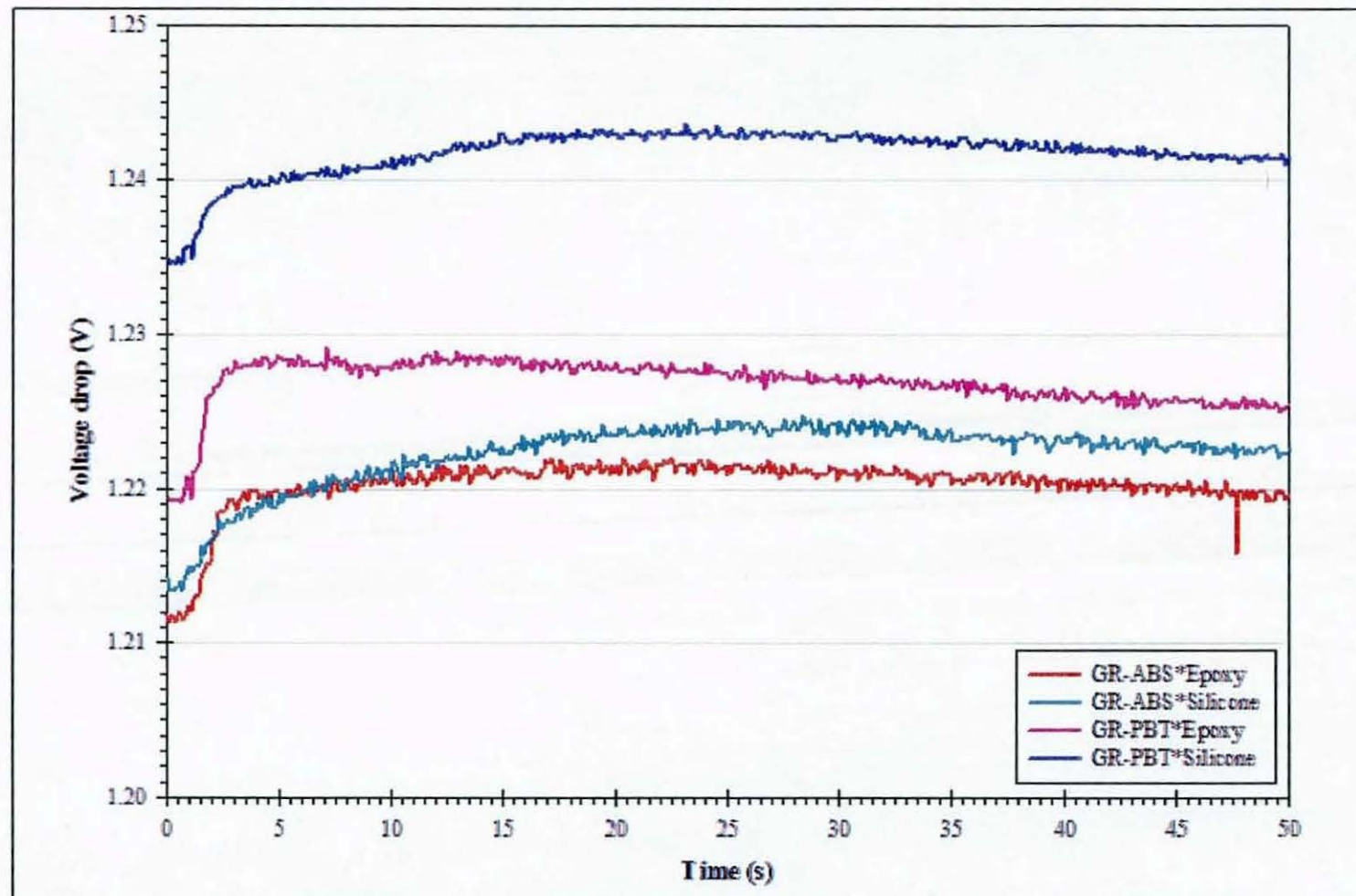
Figure 6-30 Voltage drops across resistor pack (A1) during the overmoulding phase

Silicon Diode (A3)

From the discussion in section 6.3.4, the silicone diode *A3* provided another real-time evaluation tool for the electronic integrity during the planned overmoulding process. The forward voltage of the diode on every specimen circuit was measured to monitor its response to the thermomechanical effects, as well as to detect any breakdown of internal interconnection. As the silicone diode is an NTC device, its forward voltage varies inversely proportional to its ambient temperature, i.e. the temperature of the encapsulating polymer in this process. It was noted that no A3 components among the 28 subassemblies showed any adverse functional deterioration throughout the overmoulding experiments.

Figure 6-31 shows the *A3* data for the entire overmoulding polymer*glob-top permutations during the filling and holding phases (first 50s). It is clear from initial comparisons that the results showed a good correlation to the temperature measurement results recorded by the thermistors (*VR1/2* and *A2/4*). The difference in mould temperature used for the two overmoulding polymers was reflected at the beginning of the data sets, where the output voltages of A3 were approximately 1.12V for GR-ABS ($T_{mould} = 80°C$) and 1.17V for GR-PBT ($T_{mould} = 60°C$). Consequently, the variation in the melt temperature was also evident in the results. Although the results from *VR1* demonstrated a small temperature difference of about 2°C between epoxy and silicone coatings for GR-ABS (see Figure 6.20 above), this was however not significantly noticed in A3 where the measured voltages showed similar result for both the materials.

When the output voltages from *A3* were studied in the complete process monitoring time of 390s, as seen in Figure 6-32, the results again continued to mirror those from the thermistors. As *A3* and *VR1* were positioned at almost the same distance from the injection gate in terms of the longitudinal direction of the flow, a direct correlation could be established. When the output voltages of *A3* were plotted against the temperature measurements of *A1*s individually for each overmould*glob-top combination, the results showed a consistent relationship between these two variables. As seen in the graphs in Figure 6-33 below, the output voltage of *A3* was linearly inversed to the temperature data of *VR1*. This finding has hence further validated the uniformity and accuracy of both sets of data obtained in the overmoulding process.
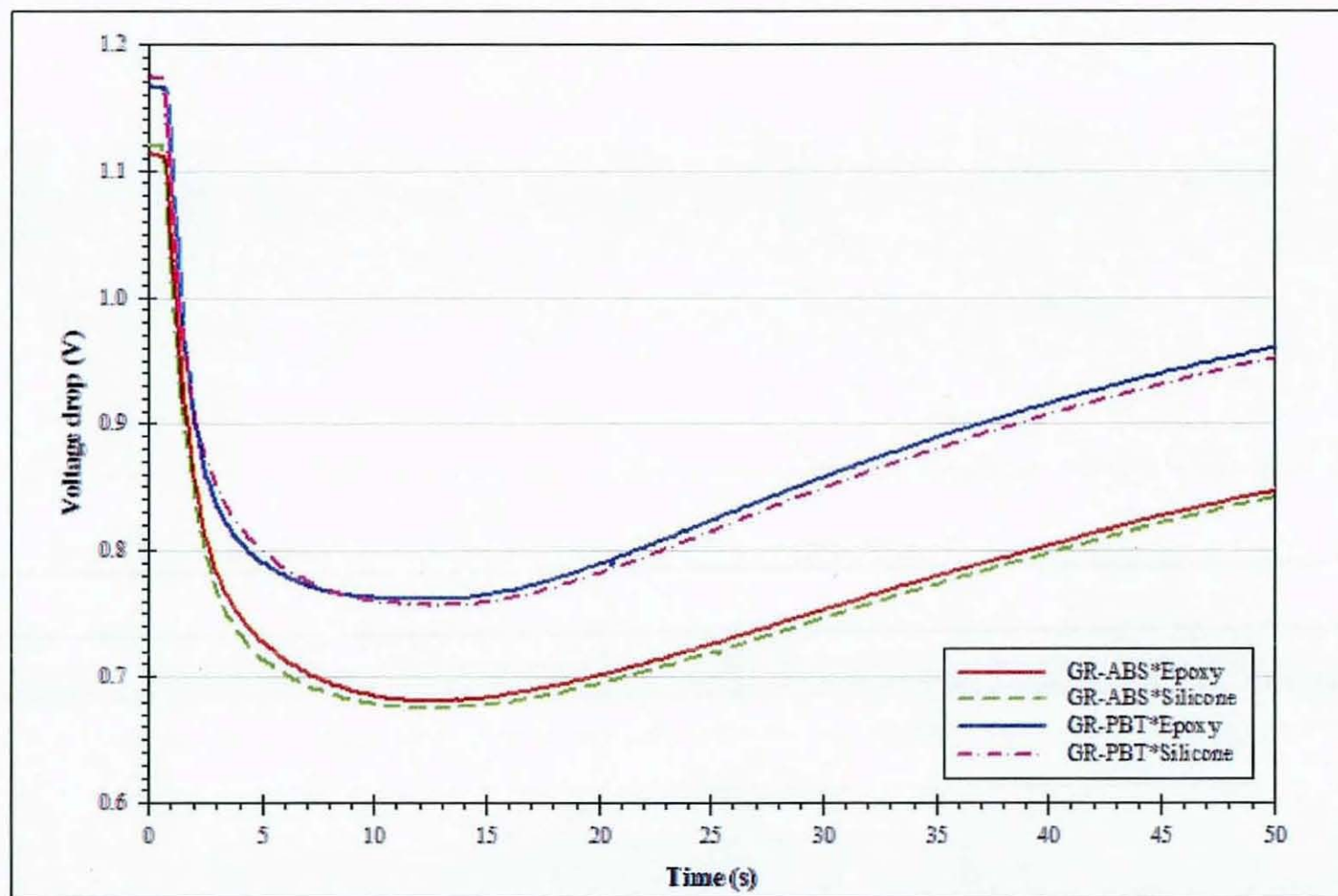
Figure 6-31 Voltage drops across silicon diode (A3) during the filling and holding phases
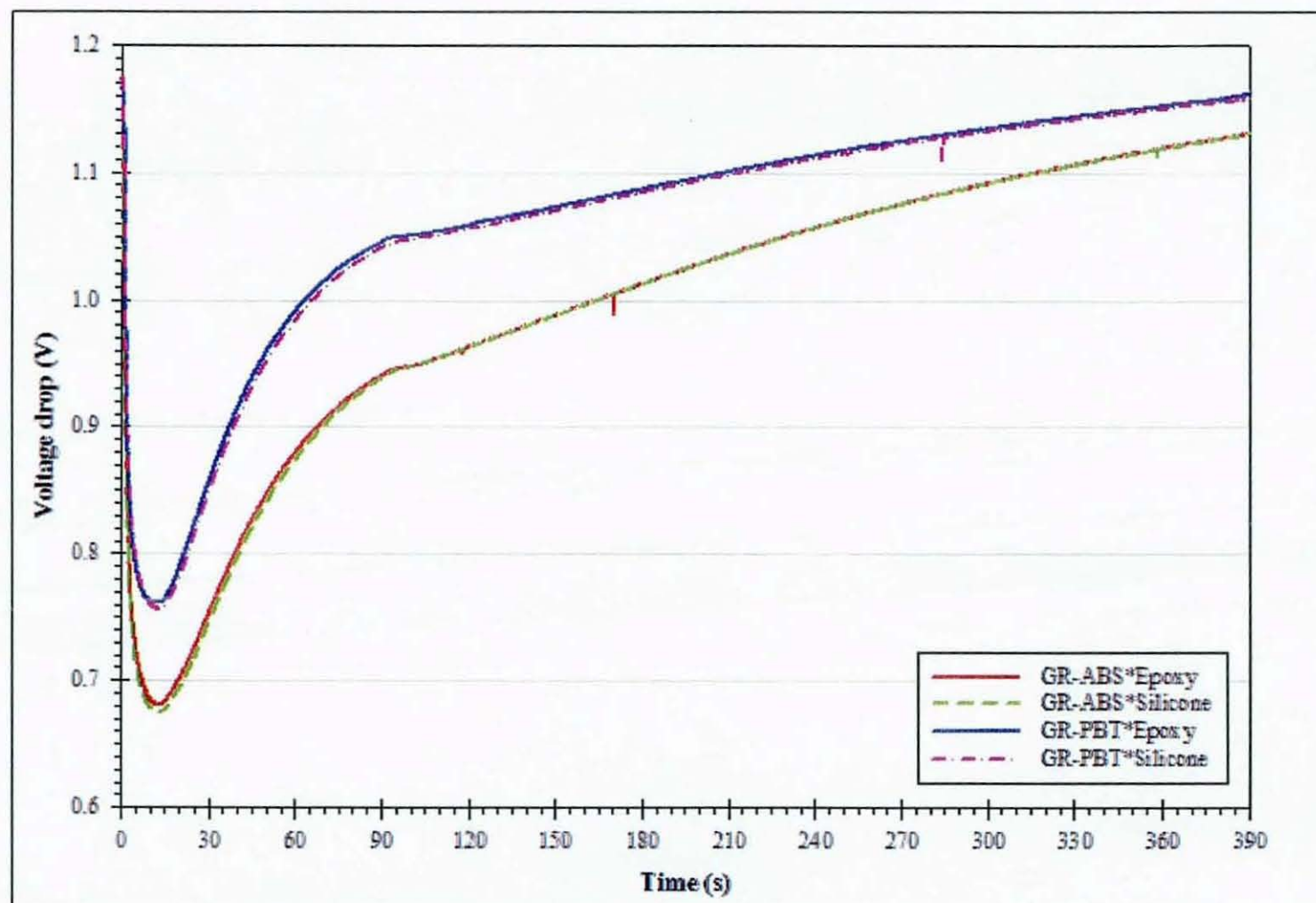
Figure 6-32 Voltage drops across silicon diode (A3) throughout the process monitoring period
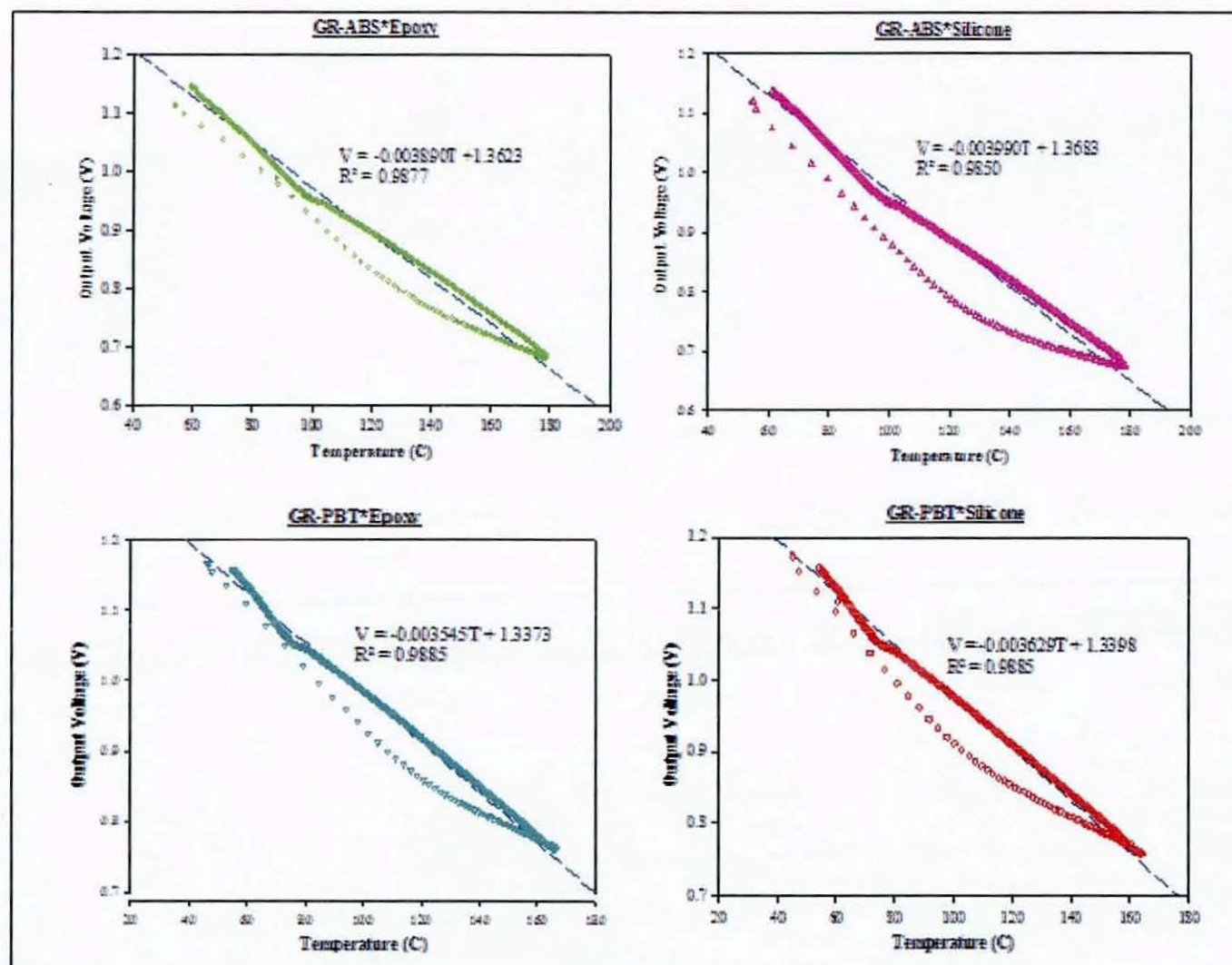
Figure 6-33 Correlation between A3 output voltage and VR1 temperature measurement

CHAPTER 7.   "CHIP-LEVEL" FUNCTIONAL OVERMOULDING

7.1.   Introduction

The preceding chapter discussed the experiment that provided real-time in-line process monitoring at the circuit board level during the overmoulding process, and presented results from the measurement of electronic integrity and mechanical strain. This has enabled the understanding of the thermomechanical stresses imposed by the overmoulding polymers on the subassembly's PCB substrate and electronic components. The use of the novel contoured tool was found to have successfully produced a noticeable improvement in balancing pressure distribution around the embedded PCB and hence minimising dimensional deformation.

The next measure was to explore the feasibility of encapsulating subassemblies with a wire-bonded silicon chip-on-board (COB) configuration, which would provide vital understanding of the thermomechanical impact of plastic overmoulding at the chip-level of the electronics. To this end, a special instrumented test subassembly comprising of a fully glob-topped wirebonded PMOS silicon test chip was developed and overmoulded using a set of contour tools. This offered a real-time measurement system to observe collated responses of the silicon chip to the overmoulding polymer. This chapter discusses the design of the test circuitry, its polymeric encapsulation process and the consequent measurements results.

7.2.   Design of "Chip-level" Process Monitoring Circuit

As with the board-level subassembly in Chapter 6, BT laminate was again used as the PCB base material for the subassembly. A single component (a COB test chip with $25\mu m$ wirebonds) was attached to the board and either epoxy or silicone used to glob-top the device. The PMOS4 test chip and its wire bonds were fully protected with the glob-top, as practised in standard COB assembly. The test chip was the PMOS4 design of dimensions 10mm×5mm, with a layout shown in Figure 7-1. It was acquired from the National Microelectronics Research Centre (Cork University, Ireland), which had previously designed and used it widely in tests for thermoset transfer moulding in IC packaging. The chip has a wide range of testing features, but only the following were used for the purposes of process monitoring:

a) *Silicon diodes* – two out of three available diodes were used to monitor temperature at the chip surface and as a means to check continuity. Diodes used were situated at the centre of the chip and at a corner.

b) *Piezoresistive strain gauges* – of six available strain gauge rosettes etched into the silicon, one (located on a corner) was connected for this work. Each rosette had an arm parallel to the long axis of the chip, one perpendicular and the third at 45 degrees. These devices were used to observe on-chip strains during moulding and subsequent environmental testing (using temperature compensation from the diodes) and also to measure continuity.

For a complete reference to the internal design of the PMOS4 test-chip, the manufacturer's datasheet is attached in Appendix 3. Three 20-way FFCs (0.5mm pitch) were employed to lead the tracks out of the moulding. The schematic layout of the test circuitry is shown in Figure 7-2 below. During the actual overmoulding cycle, measurements were only taken for the temperature diodes and one of the strain gauge rosettes, whilst the other features were retained for further operation monitoring during the environmental tests.

7.3. Temperature Calibrations

As with the board-level monitoring circuitry, the silicon test chip for the chip-level experiments was calibrated for thermal compensation. A similar calibration technique was employed for both strain gauge rosette and diode, in which a dummy BT substrate populated with the chip was heated up in an oven and its behaviour against temperature excursion determined. It was found that the responses of both components were linear with temperature; with the supply of 1Vdc at 100μA, the diode characterisation factor was $-1.27\text{mV/}°\text{C}$ and the aggregate strain value for the strain gauges was $4.33\mu\text{m.m}^{-1}.°\text{C}^{-1}$. According to the manufacturer's datasheet, the equivalent GF of the silicon gauges was 45 with excitation voltage of 1Vdc. This data was programmed into the DAQ system during the overmoulding experiments using a similar scheme to that of the board-level experiments.

7.4. Experimental Setup

The parameters for the overmoulding of the subassemblies were maintained similar to those of the board-level experiments, shown in Table 6.2. However, the moulding machine was found to have produced considerably lower injection pressure for these less populated subassemblies, as shown in Figure 7-3. The pressures recorded were approximately 82.5 bar

and 112.0 bar for GR-ABS and GR-PBT, respectively. Using Eqn. 6.1, the melt pressures at

the nozzle were therefore calculated to be 634.2 bar (GR-ABS) and 861.0 bar (GR-PBT).

When compared to the overmoulding of the board-level monitoring circuitry, these were

about 2.9% and 17.0% lower for GR-ABS and GR-PBT, respectively. A total of 36 samples

were overmoulded, which comprised of:

- GR-ABS*Silicone – 10
- GR-ABS*Epoxy – 8
- GR-PBT*Silicone – 8
- GR-PBT*Epoxy – 10

Figure 7-4 shows the subassemblies with the different glob-top materials. Unfortunately, the

silicone had a lower viscosity than the specification stated. This meant that at least two

applications were necessary to protect the wirebonds.
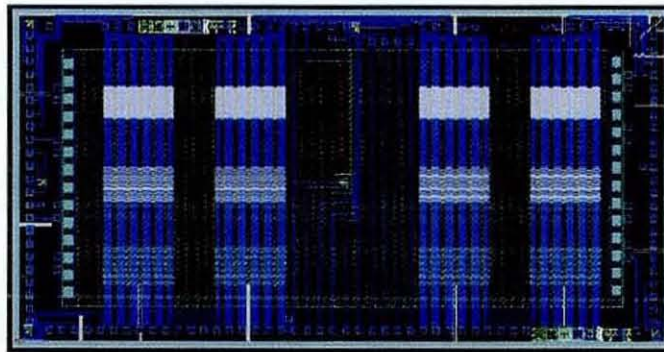
Figure 7-1 Layout of the PMOS4 package monitoring test chip (courtesy of NMRC, University College Cork)
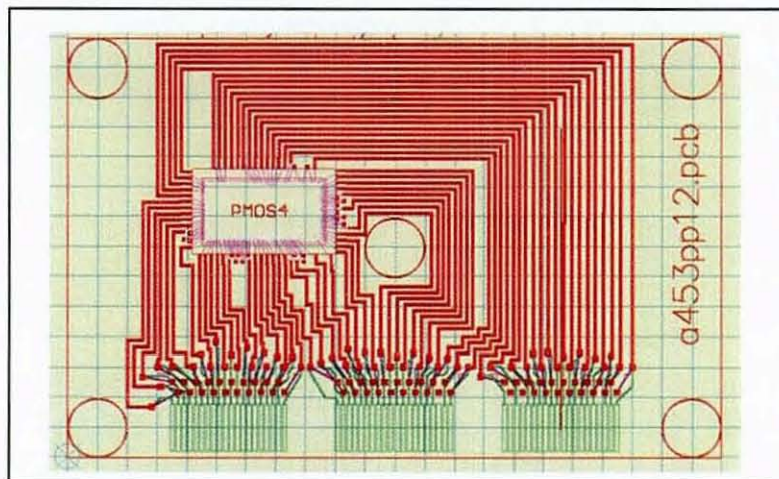
Figure 7-2 Schematic of the chip-level subassembly with the PMOS4 test chip
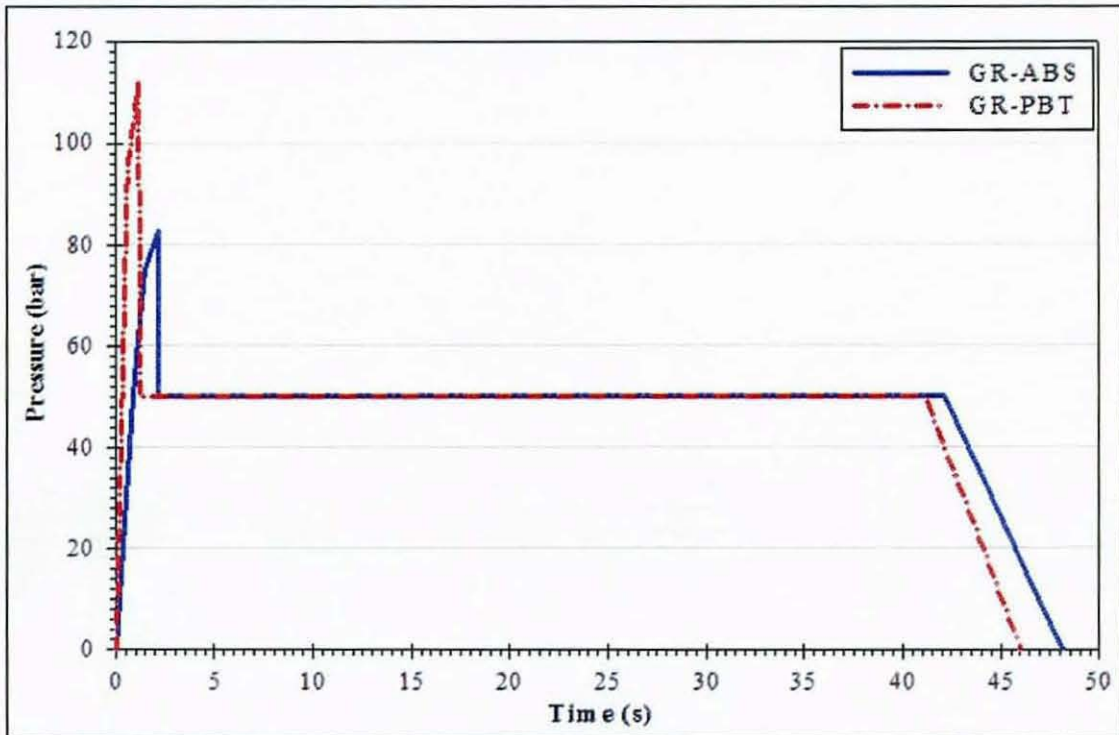
Figure 7-3 Injection profiles for chip-level monitoring
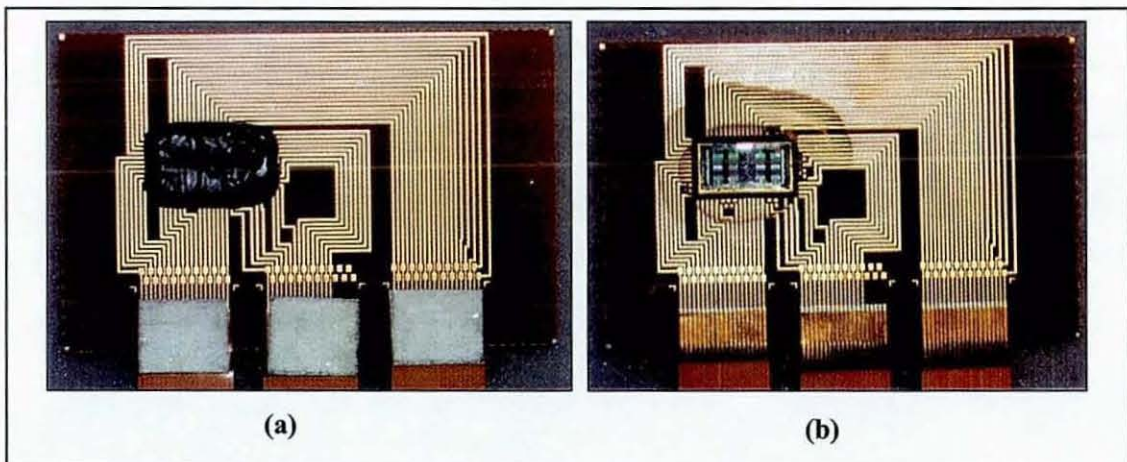
Figure 7-4 Chip-level monitoring circuit with different glob-top: (a) epoxy, (b) silicone

7.5.   Results and Discussions

Due to relatively low modulus of the silicone conformal coating, sweeping and short circuiting of the 25µm wirebonds during overmoulding cycle resulted in failures of test chips with this glob-top material. Consequently, no experimental results were available for such

samples from either GR-ABS or GR-PBT overmoulding. On the other hand, no such failure
was observed in the overmoulding of 18 samples with epoxy glob-top.

7.5.1.   Temperature Measurement

Figure 7-5 and Figure 7-6 show the results from the temperature measurement using the on-
chip silicon diodes for both overmoulding materials with epoxy glob-top. The maximum
temperatures for both cases were significantly lower than board-level measurements, where
GR-ABS and GR-PBT samples registered peaks of 180°C and 168°C, respectively (see
Section 7.5.2.1). In the overmoulding of test chips, it was found that temperatures at chip
level were substantially lower. For the GR-ABS overmould, the D2 and D3 diodes recorded
maximum temperatures of 138°C and 151°C respectively at 20s. In the case of GR-PBT
overmoulded samples, the maximum temperatures were 134°C and 142°C at 15s for D2 and
D3, respectively. When compared with results from Section 6.5.2.1, it was therefore clear that
the junction temperatures at the joints on the substrate were significantly higher than that on
the surface of the glob-topped test chip, i.e. differences of 26-29°C in terms of peak
temperatures. Table 7-1 summarises the results of the temperature measurement in this
experiment.

It was observed from the measured temperature profiles that the cooling rate during the
moulding and cooling phases (t = 0–90s) varied for the two overmoulding polymers. For GR-
ABS, which was injected at T_{melt} = 255°C and T_{mould} = 80°C, the average cooling rates were
found to be 0.60°C/s and 0.67°C/s for D2 and D3, respectively. GR-PBT was injected at T_{melt}
= 230°C and T_{mould} = 60°C, with resulting cooling rates for D2 and D3 of 0.73°C/s and
0.77°C/s. In terms of the absolute temperature difference during this period, GR-ABS samples
dropped 42°C (D2) and 47°C (D3), whilst GR-PBT samples experienced 55°C (D2) and 58°C
(D3). The faster heat dissipation for the GR-PBT overmoulded articles could be attributed to
the polymer's higher thermal conductivity of 0.28W/m-K (as compared to 0.17W/m-K for
GR-ABS) and the lower T_{mould} used in the moulding process.
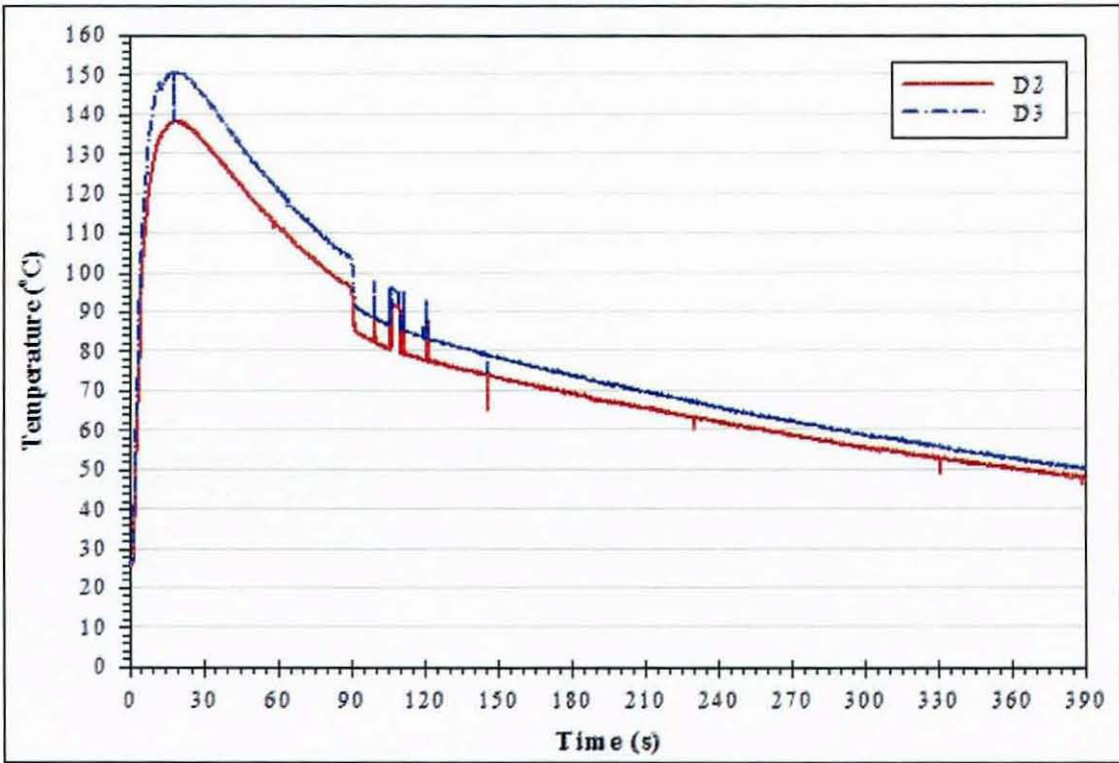
Figure 7-5 Chip-level temperature profile (GR-ABS*Epoxy)
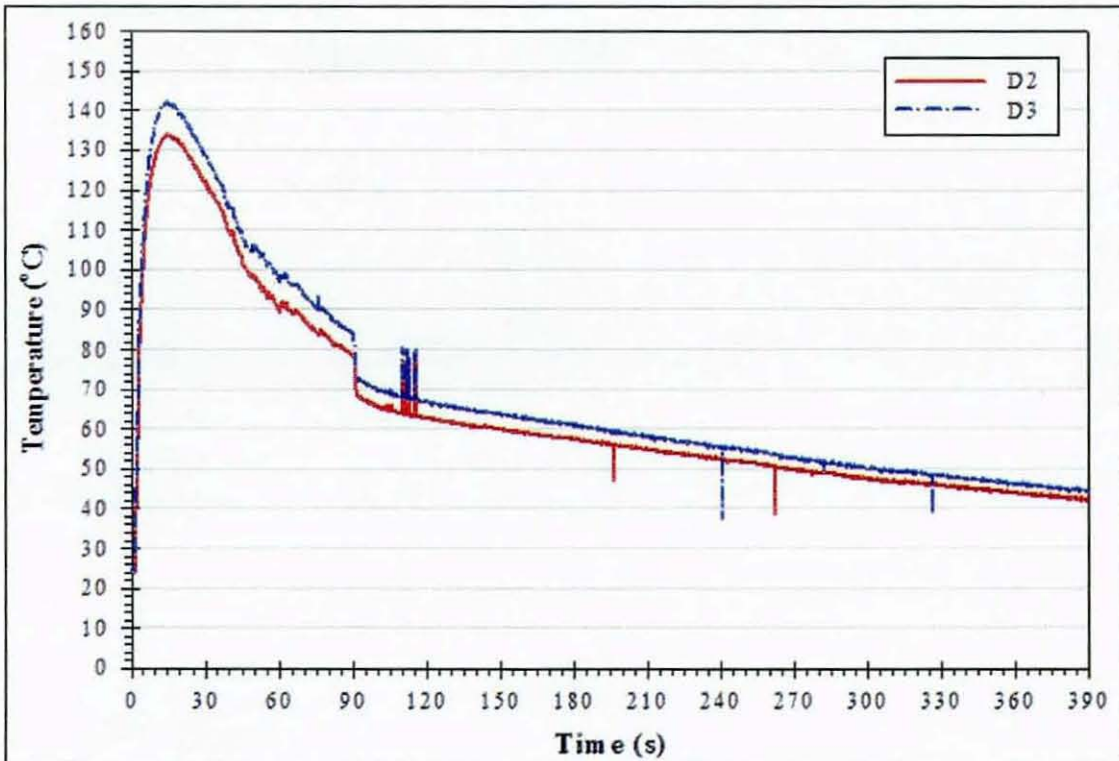
Figure 7-6 Chip-level temperature profile (GR-PBT*Epoxy)

Peak Temperature (°C) / Overmould Polymer	GR-ABS	GR-PBT
T_{melt}	255	230
T_{mould}	80	60
Diode D2	138	134
Diode D3	151	142

Table 7-1 Summary of temperature measurement for GR-ABS and GR-PBT

7.5.2. Strain Measurement

7.5.2.1. Strain Transformation

Only one of the piezoresistive strain gauge rosettes was used in this experiment and Figure 7-7 depicts the directional relationship of this 3-element orthogonal device with the overmoulding melt flow. With the availability of 3-directional strain data sets, it was possible for the principal biaxial strains (ε_1 and ε_2) exerted on the test chips to be calculated using equations [Dally et al., 1991][Murray et al., 1992]:

$$\varepsilon_A = \varepsilon_{xx} \cos^2 \theta_A + \varepsilon_{yy} \sin^2 \theta_A + \gamma_{xy} \sin \theta_A \cos \theta_A$$
$$\varepsilon_B = \varepsilon_{xx} \cos^2 \theta_B + \varepsilon_{yy} \sin^2 \theta_B + \gamma_{xy} \sin \theta_B \cos \theta_B \qquad \textbf{(Eqn. 7-1)}$$
$$\varepsilon_C = \varepsilon_{xx} \cos^2 \theta_C + \varepsilon_{yy} \sin^2 \theta_C + \gamma_{xy} \sin \theta_C \cos \theta_C$$
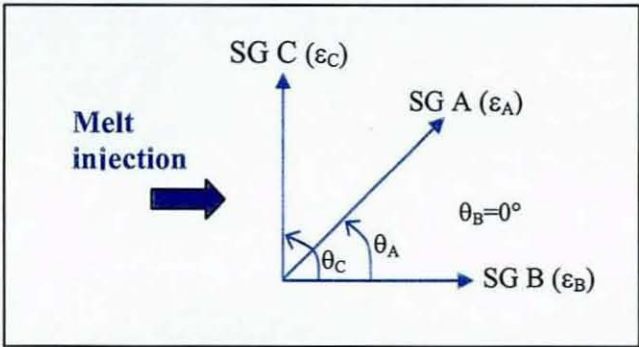
Figure 7-7 Orientation of strain rosette relative to melt flow direction

Solving Eqns. 7.1 simultaneously determined the Cartesian components of ε_{xx}, ε_{yy} and γ_{xy}. The principal strains ε_1, ε_2 and maximum shear strain in the plane γ_{max} were provided by equations:

$$\varepsilon_{1,2} = \frac{\varepsilon_{xx} + \varepsilon_{yy}}{2} \pm \sqrt{\left(\frac{\varepsilon_{xx} - \varepsilon_{yy}}{2}\right)^2 + \left(\frac{\gamma_{xy}}{2}\right)^2}$$

$$\tan 2\phi = \frac{\gamma_{xy}}{\varepsilon_{xx} - \varepsilon_{yy}} \quad\quad \text{(Eqn. 7-2)}$$

$$\left(\frac{\gamma}{2}\right)_{max} = \pm\sqrt{\left(\frac{\varepsilon_{xx} - \varepsilon_{yy}}{2}\right)^2 + \left(\frac{\gamma_{xy}}{2}\right)^2}$$

Where ϕ was the angle between the principal axis of ε_1 with the original x-axis. In this case, we measured strains ε_A, ε_B and ε_C with $\theta_A = 45°$, $\theta_B = 0°$, $\theta = 90°$ (Figure 7-7) and Eqns. 7.1 were reduced to:

$$\varepsilon_B = \varepsilon_{xx}$$
$$\varepsilon_A = \frac{1}{2}\left(\varepsilon_{xx} + \varepsilon_{yy} + \gamma_{xy}\right)$$
$$\varepsilon_C = \varepsilon_{yy} \quad\quad \text{(Eqn. 7-3)}$$
$$\gamma_{xy} = 2\varepsilon_A - \left(\varepsilon_B + \varepsilon_C\right)$$

And therefore the principal strains and angle were found from substituting Eqns 7.3 into Eqns. 7.2 to obtain:

$$\varepsilon_{1,2} = \frac{\varepsilon_B + \varepsilon_C}{2} \pm \sqrt{\left(\frac{\varepsilon_B - \varepsilon_C}{2}\right)^2 + \left(\frac{2\varepsilon_A - \varepsilon_B - \varepsilon_C}{2}\right)^2}$$

$$\tan 2\phi = \frac{2\varepsilon_A - \varepsilon_B - \varepsilon_C}{\varepsilon_B - \varepsilon_C} \quad\quad \text{(Eqn. 7-4)}$$

$$\left(\frac{\gamma}{2}\right)_{max} = \pm\sqrt{\left(\frac{\varepsilon_B - \varepsilon_C}{2}\right)^2 + \left(\frac{2\varepsilon_A - \varepsilon_B - \varepsilon_C}{2}\right)^2}$$

Eqns. 7.4 were used to transform the measured strains from the experiment into the corresponding principal components for analysis.

7.5.2.2. Results

The separate components of the strain measured from the rosette for GR-ABS*Epoxy are shown in Figure 7-8, demonstrating the effect of flow direction relative to the orientation of the individual gauges. As expected, the test chips experienced greatest strain parallel to the polymer flow and this was evident from the results of SG-B (max. ε_B = 4750μm/m). The deformation transverse to the flow, as registered by SG-C (max. ε_C = 4100μm/m), was the lowest. SG-A, at a 45° inclination off the melt flow, was slightly lower than SG-B with a maximum ε_A = 4600μm/m. All the maximum strain elements occurred at about 20s after the start of melt injection.

The principal strains were calculated using Eqns. 7.4, with the results displayed in Figure 7-9. It was found that ε_1 and ε_2 were very close to those values of ε_B and ε_C at 4800μm/m and 4000μm/m, respectively. The resulting γ_{max} was calculated to be 995μradians. The release of the subassembly at the opening of moulding tools at 90s caused a very significant decrease in γ_{max}. Analysis of the directions for the principal strains (see Figure 7-10) found that θ_1 and θ_2 remained almost constant at 10–20° and 190–200° respectively from 0–230s. A rapid increase in these principal angles then occurred for θ_1 and θ_2 to reach maxima of 45° and 225° at approximately 285s. Between 290–300s, there was a sudden reversal in the angles of ε_1 and ε_2, which were found to be acting in the directions of -45° and 135°, respectively. This corresponded to an overlapping of measured strains at about 1000μm/m, after which point the transverse strain ε_C became more dominant than the longitudinal element ε_B. By observing Figure 7-9 and Figure 7-10, it was seen that whilst the magnitudes of ε_1 and ε_2 only showed small noticeable changes during 290-300s, γ_{max} experienced an immediate increase to reflect the directional changes between the principal strains.

It was not possible to directly attribute the sudden change in the behaviour of strains acting on the test chip to the moulding conditions or tooling deign. However, from the material point of view, it could be triggered by the diminishing thermal effect during the solidification phase of overmoulding polymer melt, causing a relaxation in the longitudinal deformation. After this particular instant, the polymer would gradually undergo its intrinsic polymeric solidification and hence subject the embedded test chip to an equilibrium state for isotropic planar strains.
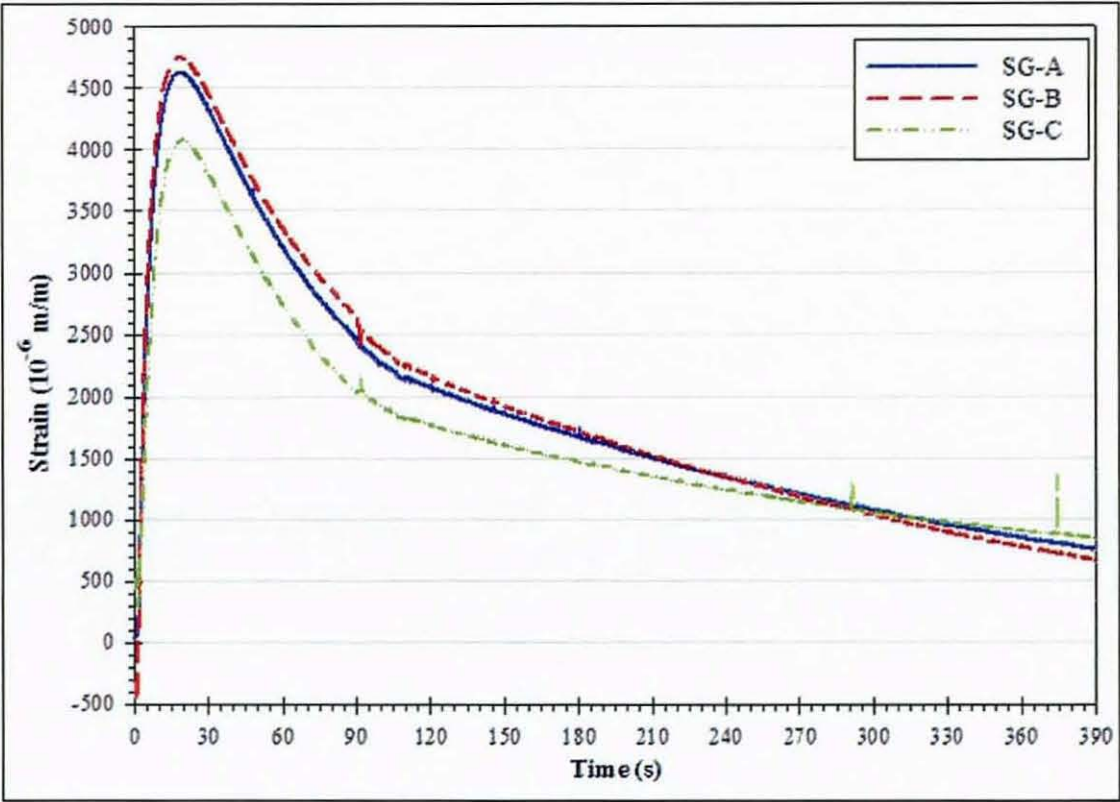
Figure 7-8 Measured strains for GR-ABS*Epoxy
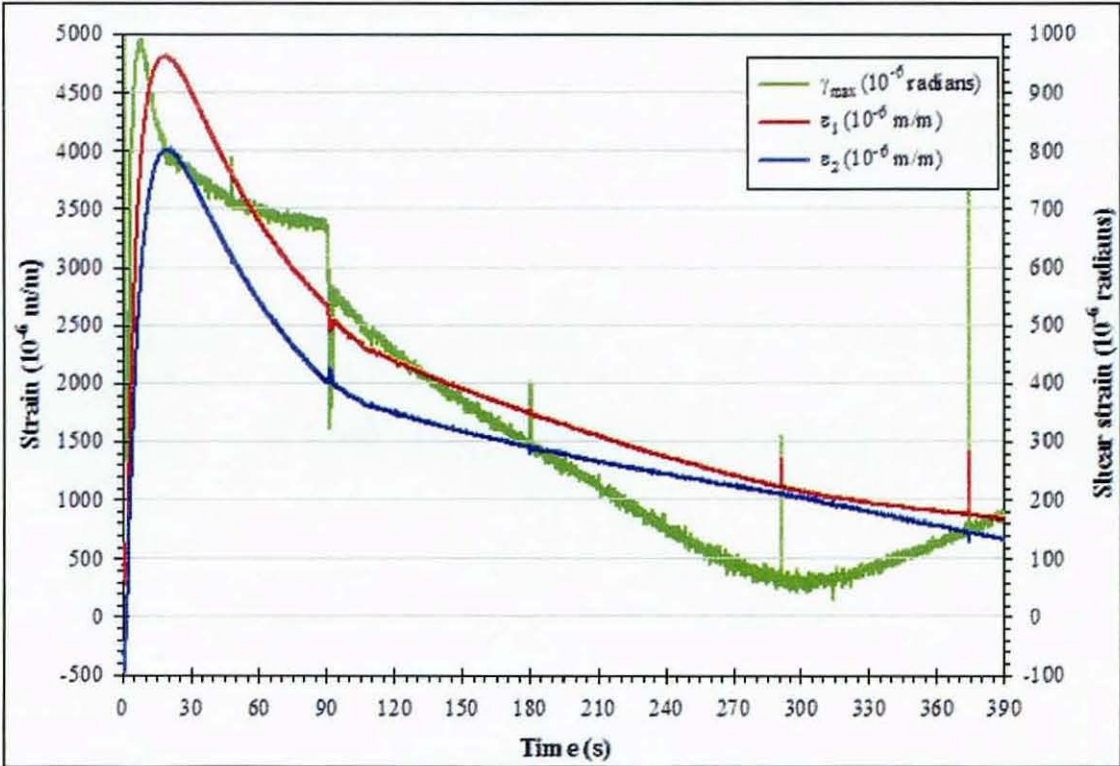
Figure 7-9 Magnitudes of principal strains and maximum shear strain for GR-ABS*Epoxy
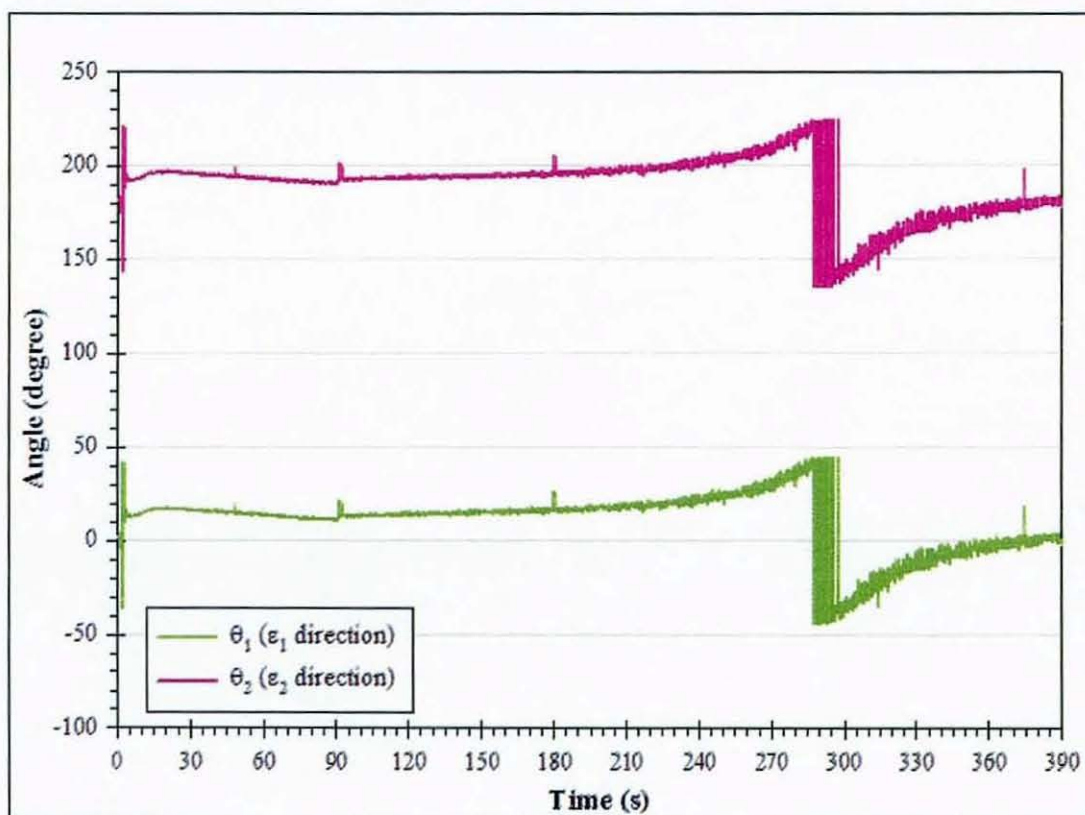
Figure 7-10 Directions of principal strains and shear strain for GR-ABS*Epoxy

The resultant orthogonal strains measured from the GR-PBT*Epoxy overmoulded samples
are shown in Figure 7-11. The relationship between melt flow direction and the mechanical
strains was again clearly observed. As expected, the highest strain was registered by SG-B
(max. ε_B = 4400µm/m) along the melt direction whilst the lowest was that of SG-C (max. ε_C =
3800µm/m). SG-A recorded a maximum strain of ε_A = 4250µm/m. In line with the shorter
injection cycle, the peak strains for GR-PBT were found at t = 15s, which was about 5s earlier
than GR-ABS.

The principal strains obtained from the transformation are shown in Figure 7-12. The
respective maximum values derived for these elements were ε_1 = 4400µm/m, ε_2 = 3700µm/m
and γ_{max} = 670µradians. The part release from the tools again generated noticeable effects. At
the ejection of the parts, γ_{max} showed an immediate decrement of about 60µradians, while
both principal angles θ_1 and θ_2 experienced a corresponding increment of 10°. These
observations are clearly evident in Figure 7-12 and Figure 7-13. When this was evaluated

against GR-ABS, it could be seen that γ_{max} decreased by 120µradians but there was no substantial changes in θ_1 and θ_2 (see Figure 7-9 and Figure 7-10 above).

Interestingly, the characteristics of the angles θ_1 and θ_2 for principal strains were found to be identical for both the overmoulding polymers. Similar to GR-ABS discussed above, θ_1 and θ_2 for GR-PBT remained almost constant at approximately 15° and 195° respectively, from 0–90s. As mentioned above, θ_1 and θ_2 underwent a sudden increment of 10° at part ejection (t = 90s) and maintained constant within ±5° deviation until about 250s, when they rose to 45° and 225° at approximately 295s. The instantaneous realignment for ε_1 and ε_2 were also observed with GR-PBT samples. This occurred over a longer period between 290–330s, causing θ_1 and θ_2 to drop to -45° and 135°, respectively. This change in the directions of principal strains ε_1 and ε_2 was consistent with the GR-ABS trials discussed above. It must also be noted that it is impossible to conclude that this characteristic of angular displacement for the principal strains is a common phenomenon in polymers other than GR-PBT and GR-ABS investigated in this experiment.

The overall results from the strain measurements in the experiments with the two overmoulding polymers have shown that GR-PBT generated significantly lower physical strains on the test chips than GR-ABS. Table 7-2 below makes a direct comparison of the measured strains between the two polymer variants. In terms of the measured components, it was found that GR-PBT produced strains in the magnitudes of 300–350µm/m lower than GR-ABS, thus resulting in a reduction of about 7.5%. For the principal components, the reduction was 8.3% for ε_1 and 7.5% for ε_2. The most substantial difference was observed in γ_{max} values, which showed a reduction of 32.7% (325µradians) for GR-PBT. Although the NMP was 103.8MPa for GR-PBT and 65.3MPa for GR-ABS (see Section 6.4.2), the scale of the difference in this factor was not explicitly reflected in the orthogonal strain components. One possible cause of this could be due to the lower longitudinal and transverse CTE values for GR-PBT.

Drawing from the results of the temperature and strain measurements discussed above, it was noted that GR-PBT polymer produced relatively lower thermomechanical exertion on the overmoulded silicon test chips. Also, epoxy glob-top was found to provide sufficient robustness for the wirebonds. The temperature measurement results further substantiate that

the effective temperature excursion at chip-level of the COB was at well below the injected melt temperature and hence sustainable to the silicon chip, BT substrate and epoxy glob-top.
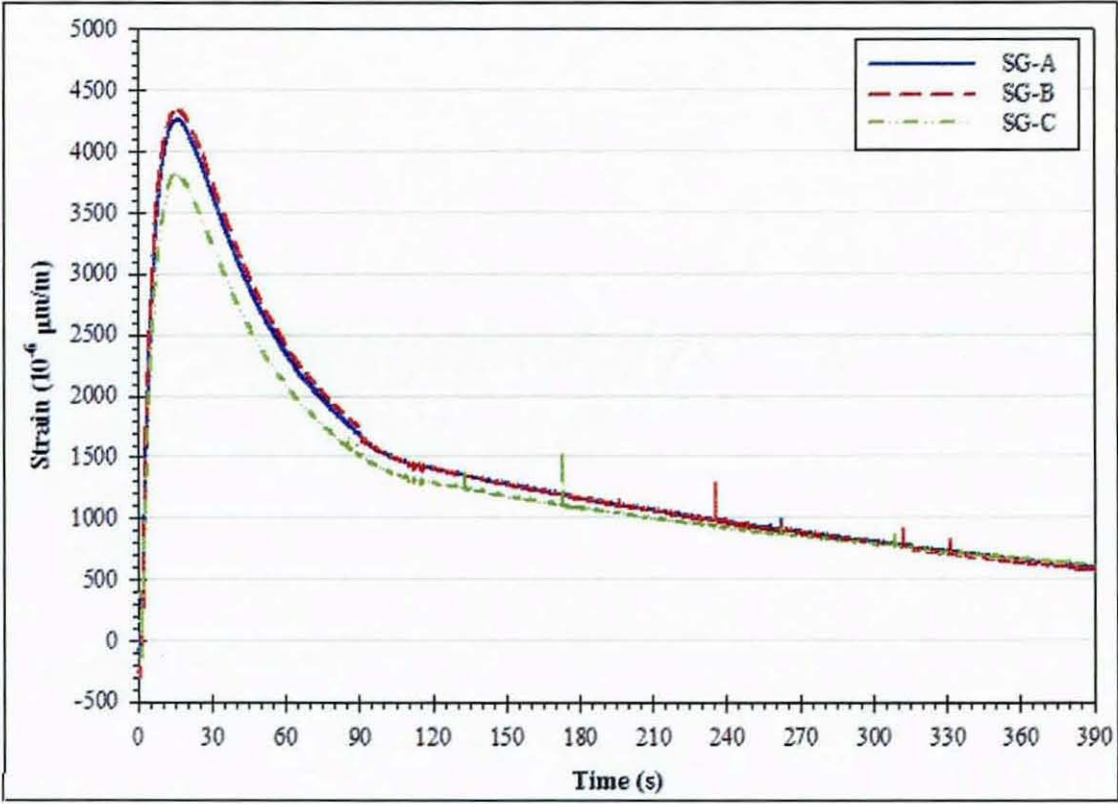
Figure 7-11 Measured strains for GR-PBT*Epoxy
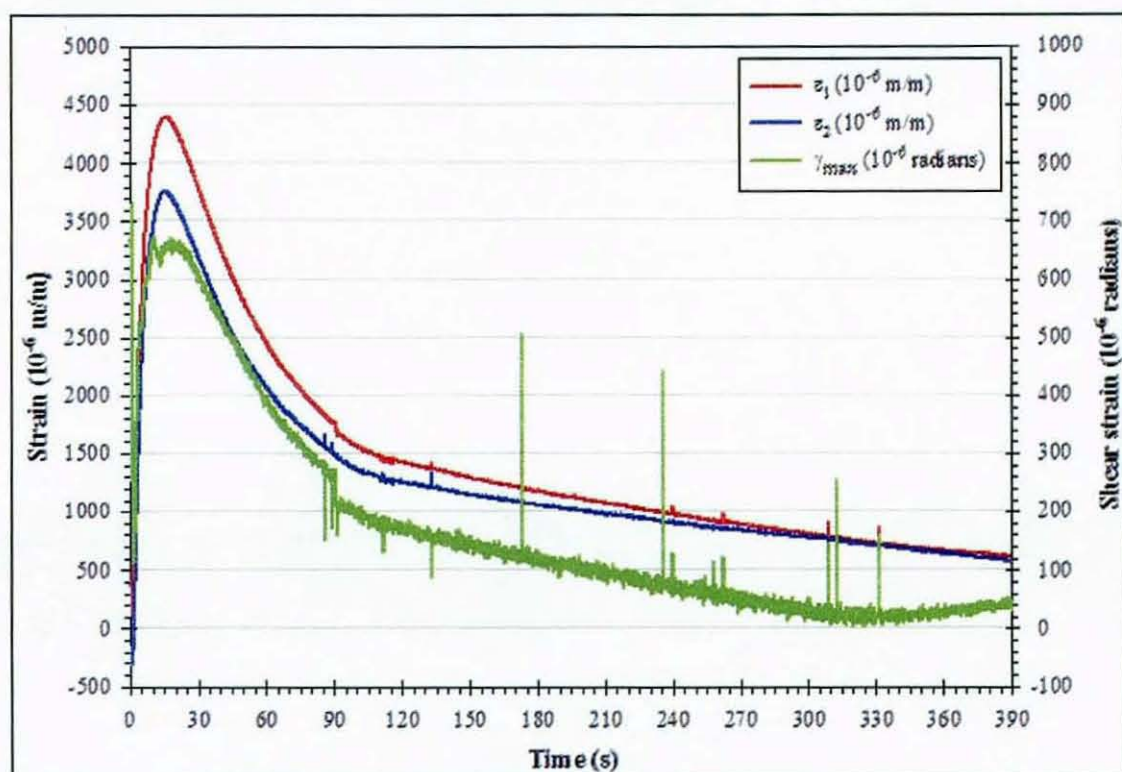
Figure 7-12 Principal strains and maximum shear strain for GR-PBT*Epoxy
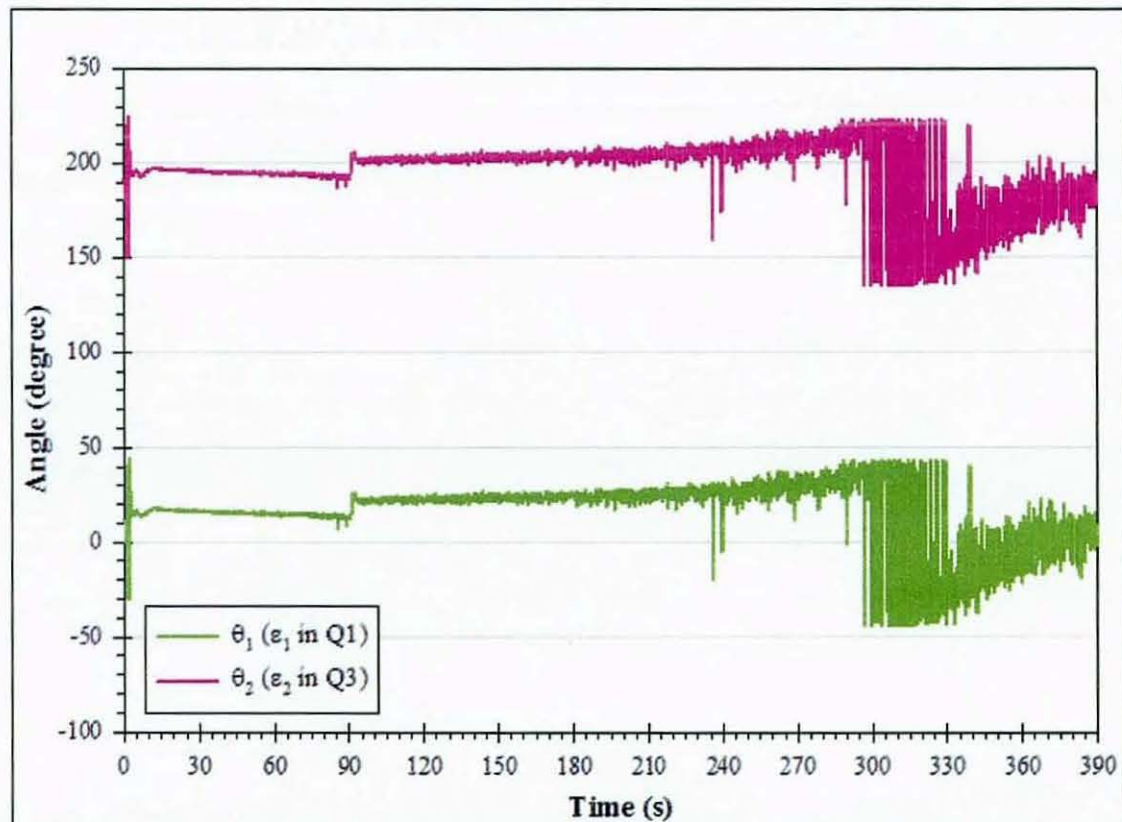
Figure 7-13 Directions of principal strains and shear strain for GR-PBT*Epoxy

Peak Strain / Overmould Polymer	GR-ABS	GR-PBT
ε_A (μm/m)	4600	4250
ε_B (μm/m)	4750	4400
ε_C (μm/m)	4100	3800
ε_1 (μm/m)*	4800	4400
ε_2 (μm/m)*	4000	3700
γ_{max} (μradians)*	995	670

Table 7-2 Comparison of the strain components for GR-ABS and GR-PBT overmoulds

(* - derived from strain transformation)

CHAPTER 8.   DISCUSSION AND CONCLUSIONS

In this chapter, the experimental results described in Chapters 3, 4, 5, 6 and 7 will be
evaluated and discussed further. Conclusions pertaining to the present research will be drawn
from these findings. Suggestions for future research in the area of polymeric encapsulation of
electronics will also be presented.

8.1.   Preliminary and Process Screening

The experiments discussed in Chapter 3 formed an effective screening exercise for the
variables and unknown factors involved in the process of electronic encapsulation with
conventional injection moulding technique.

The preliminary experiment examined the interactions of an overmoulding ABS polymer with
various circuitry substrates. The substrate deformation caused by the high pressure, high
temperature plastic melt highlighted the fundamental challenges to achieving successful
polymeric encapsulation of electronics using a conventional injection moulding process. The
results not only demonstrated the feasibility of the technology, but also provided guidelines
into critical process parameters and materials selection criteria. The experiment also indicated
that overmoulding of PE flexible substrates produced serious mechanical deformation and
more thorough studies would be required to develop a process with lower thermomechanical
force. Such work was beyond the time-scale of the current research, where the main focus was
on overmoulding rigid substrates.

The second experiment in Chapter 3 formed a follow-on screening investigation to explore
different injection parameters, tooling variations, polymers and electronic interconnections.
By using reduced factorial DOE and statistical data analysis techniques (ANOVA and
ANOM) to assess the mechanical failure modes, the results found that the moulding polymer
was the most influential variable, with 30% GR-PBT resin emerging as the most promising.
This confirmed the presence of glass fillers provided the dimensional stability to reduce the
longitudinal deflection. Analyses of solder joints defects and substrate distortions showed the
adverse results of using high melting temperature polymers and further demonstrated that the
combination of lower mould and melt temperatures under a low injection pressure provided
the best conditions. Thinner part thickness was also discovered to reduce part warpages. The

experiment also found that the 1.6mm BT laminate produced the lowest distortions than standard glass-epoxy laminated FR4 substrate. X-ray inspection of alumina substrate showed that its brittleness led to cracking under thermomechanical loads. Furthermore, the structural and flow models produced for the overmoulding process [De Cooper Jones, 1999] validated the substrate warpage caused by the unbalanced pressure distribution from an advancing melt flow.

These screening experiments not only identified the dominant process factors, but also successfully facilitated the elimination of trivial variables from subsequent investigations.

8.2.   Material Adhesion for Subassembly Supports

Chapter 4 investigated the design feasibility of incorporating a stand-off supporting cradle on an electronic subassembly in the moulding cavity to minimise physical distortions to the substrate. This technique located the circuit at the mid-plane of the mould to attain a balanced melt flow and support cradles of pre-moulded unfilled polymers were attached to both sides of the substrate to provide through-thickness support to withstand thermomechanical stresses from the melt impingement. The experiment determined the significance of process conditions and interfacial materials on the adhesion between glass-filled overmoulds and unfilled support structures.

The experiment validated that the supporting cradle provided significantly reduced substrate distortion as well as effectively offered the in-mould support and positioning for the subassembly. The experimental results showed a higher degree of adhesion for overmoulding of glass-filled polymer over its respective unfilled pre-moulded cradles, i.e. GR-PBT with PBT and GR-ABS with ABS. Apart from GR-ABS with ABS overmoulds. The thermal cycle considerably increased the dye penetration. Both the empirical and statistical results showed that GR-ABS with ABS as the most optimised combination with 100% adhesion for all moulding pressures. Analysis of the molecular structural disparity at adjoining polymers found that, in particular, the difference in polymeric shrinkage influenced the adhesion characteristics at their interface. The linear CTE difference between polymers was however not found to be of great significance to the interfacial adhesion in this study. Nevertheless, this factor could be critical throughout the operating lifetime of the products.

8.3.   Moulding Tool Re-engineering

The structural presence of the supporting cradle in the path of the melt flow was found to cause an unequal hydrodynamic resistance in an equi-thickness moulding cavity and the resultant changes in melt flow dynamics increased the occurrence of short-shot and weld line defects. The dynamic melt flow models [Schmidt, 1999] illustrated a lack of uniform filling in the last 2/3 of the cavity, causing "racetrack effects" and inhomogeneous bulk temperature distribution. As a result, residual stress within the plastic led to considerable thermal shrinkages and physical deformation. The formation of weld-lines and air traps also led to under-strength localised structural inconsistency. FEA modelling results reflected the defects observed in the experiments discussed in Chapters 3 and 4. Alternative moulding tool designs were therefore engineered to achieve a more effective overmoulding with minimum moulding defects and subassembly deformations.

In order to eliminate the non-uniform flow front in an equi-thickness cavity, the tool surface was contoured to profile the thickness topography of the embedded subassembly and its supporting cradles. Extensive FEA models [Schmidt, 1999] found that this topographical mould would provide consistent cross-sectional conduits for the melt flow, hence minimising the difference in hydrodynamic resistance to achieve improvements in flow uniformity, temperature and pressure differentials. However, results from the experimental study showed that the FEA models were unable to fully predict the overmoulding process with this topographical design. Firstly, the shearing force and thermal load exerted by the impinging polymer on the support cradles were greater than the models had suggested, and this caused the thinner sections of the frames to be swept to the surface of the tool. Also, the support frames were detached from the substrate in many instances, thus dislocating the subassembly from its origin during the filling stage. The improvements in the flow resistance suggested in the FEA models were not entirely evident in the overmoulding trials. Short-shots problems, due mainly to the presence of the supporting structures in the flow paths, was still observed, particularly at lower injection pressures. Nevertheless, physical deformations induced by residual thermomechanical stresses were significantly reduced in cases where complete overmoulding was achieved.

Subsequent tooling design led to the removal of the substrate supporting cradles, these replaced with two sets of in-mould metal pins within the cavity. Experiments with GR-ABS and GR-PBT polymers found this in-mould supported topographical tool effectively

eliminated the defects previously seen and produced components of consistent weight. The resultant improvement in the flow front uniformity and differential pressure reduction was able to considerably reduce the longitudinal warpage of the substrates, up to 90% for GR-PBT in certain cases. ANOVA results showed that the process variables which were significant to part deformations differed between semicrystalline and amorphous polymers. Finally, parametric optimisation analyses successfully produced a set of optimised conditions for both polymers as process guidelines in the experiments in Chapters 6 and 7.

8.4. Board-Level Functional Monitoring

Chapter 6 addressed stresses and temperature impacts on the encapsulated electronics during overmoulding process. Instrumented SMT circuitry allowed real-time monitoring of the overmoulding process cycle. The temperature measurements showed that the highest board surface temperatures were detected immediately in front of the injection gate. The detected board temperatures were about 65-75°C lower than the Tmelt, showing that the polymer melt was conducting its heat rapidly through the mould tool before reaching the embedded electronics. The maximum post-injection cooling rates of the melts were found to be relatively uniform for both GR-PBT and GR-ABS. The effect from the differences in thermal conductivity of the overmoulding polymers and glob-top materials was also evident in the results. In the embedding of 24 subassemblies, a component failure rate of 5.2% was successfully achieved. The following observations were established from the board-level temperature measurement results:

a) the thermomechanical stresses generated by the impinging polymer did not cause alarming failure to the temperature-sensing components during and post overmoulding cycle;

b) the combination of glob-top layer and cooling rate of the melt in the mould was sufficient to significantly reduce the effective heat transferred to the components and solder joints; and

c) both the silicone and epoxy glob-top materials were able to provide the buffer against the thermal and pressure stresses for the solder joints (as no solder melting was found under x-ray inspection of overmoulded articles).

The measurement of surface strains verified that the thermomechanical stresses developed during the process were of very complex patterns. The characteristics of the strains during the melt filling for both overmoulding polymers were of a similar pattern. The shear forces from

the polymer melt caused the strains longitudinal (εy) to the flow direction to be considerably higher than the transverse component (εx). It was also evident in all the rosettes, both transverse and longitudinal components simultaneously underwent deformations of same nature (compressive or tensile). Results also showed the presence of unbalanced pressure distribution and indicated possible substrate delamination. While both polymers exhibited nearly similar deformation characteristics at various phases of the overmoulding cycle, GR-PBT was found to impart greater packing pressure than the amorphous GR-ABS. This may be attributed to GR-PBT's higher solidification in its semicrystalline structure immediately at the end of melt injection. Over the whole overmoulding process, GR-ABS however showed a more steady recovery from surface strains.

The differential output voltage of a SO-16 10kΩ resistor network IC and the forward biased voltage of a SOT-23 silicon diode were employed to monitor the integrity of electronic interconnections during the overmoulding process. The results showed only 0.164–0.248% percentage increase from the nominal input voltage in all overmoulding conditions, exhibiting no significant sign of functional deterioration.

8.5.   Chip-Level Functional Monitoring

The experiment in Chapter 7 studied the thermomechanical effects of the overmoulding polymers on chip-level electronics by using a wire-bonded PMOS test chip with piezoresistive strain gauge rosette and temperature sensitive silicon diodes. It was evident that silicone glob-top, with its low modulus, was unable to withstand the shear forces from impinging melt flow. All the testchips with this coating failed under the process conditions and showed shorting of the wirebonds due to sweeping force and mechanical stresses.

The subassemblies with epoxy coated testchips provided information on the conditions experienced during the process cycle. The maximum temperature registered by the silicon diodes was found to be lower than that for board-level thermistors by about 26-29°C for both polymers. The maximum post-ejection cooling rates were found to be about 50% lower than those seen in board-level measurements. The test chips also experienced the greatest strain parallel to the polymer flow and lowest transverse to the flow. The results from both the overmoulding polymers showed that GR-PBT generated significantly lower surface and shear strains on the test chips than GR-ABS. The temperature and strain measurements established

that GR-PBT polymer produced relatively lower thermomechanical exertion on the test chips, and substantiated the temperature excursion at chip-level of the COB at well below the injected melt temperature and hence sustainable for the silicon chip, BT substrate and epoxy glob-top.

8.6.   Conclusions

Figure 8-1 summarises the overall research activities that have been discussed in this thesis. In order to present this direct electronic overmoulding technology for future implementations, a generic process guideline has been formulated from the collective findings from this thesis and is presented by the flowchart in Figure 8-2 to outline the possible design criteria for the essential process development stages. This research has successfully engineered the technology of polymeric encapsulation of PCB-based electronic subassemblies. Conventional injection moulding, tooling design and electronic manufacturing processes have been engineered to establish the core of the proposed technology. The use of conventional process elements maintains the low cost and manufacturability of the new technology.

Amongst the different plastic materials investigated were unfilled grades of nylon, acetal, PBT, ABS, and glass-filled nylon, PBT and ABS. The results obtained with these polymers have been presented in the main chapters of this thesis. The staged experiments focused mainly on the selection of electronic interconnections and substrates most suitable for this new process. Solder-based surface mount and direct wirebonding technologies were analysed on substrates of alumina ceramic, flexible polyester thick film and rigid laminates FR4 and BT. Furthermore, epoxy, silicone and polyurethane glob-top materials were tested in coating the solder joints and wirebonds. By exploring the different designs of moulding tools, a set of novel topographically contoured tools that offered in-mould fixture and support of the electronic subassembly was successfully created.

Factorial and response surface method (RSM) DOE methodologies have been applied to support the intensive experimental investigations and various failure analysis techniques were used to examine the resultant overmoulded parts. The results were also validated through structural and dynamic thermomechanical FEA simulations elsewhere [De Cooper Jones, 1999] [Schmidt, 1999] [Schmidt, 2000]. Statistical analyses, such as ANOVA and ANOM, and optimisation techniques were used to determine the optimum parameters for this novel process.
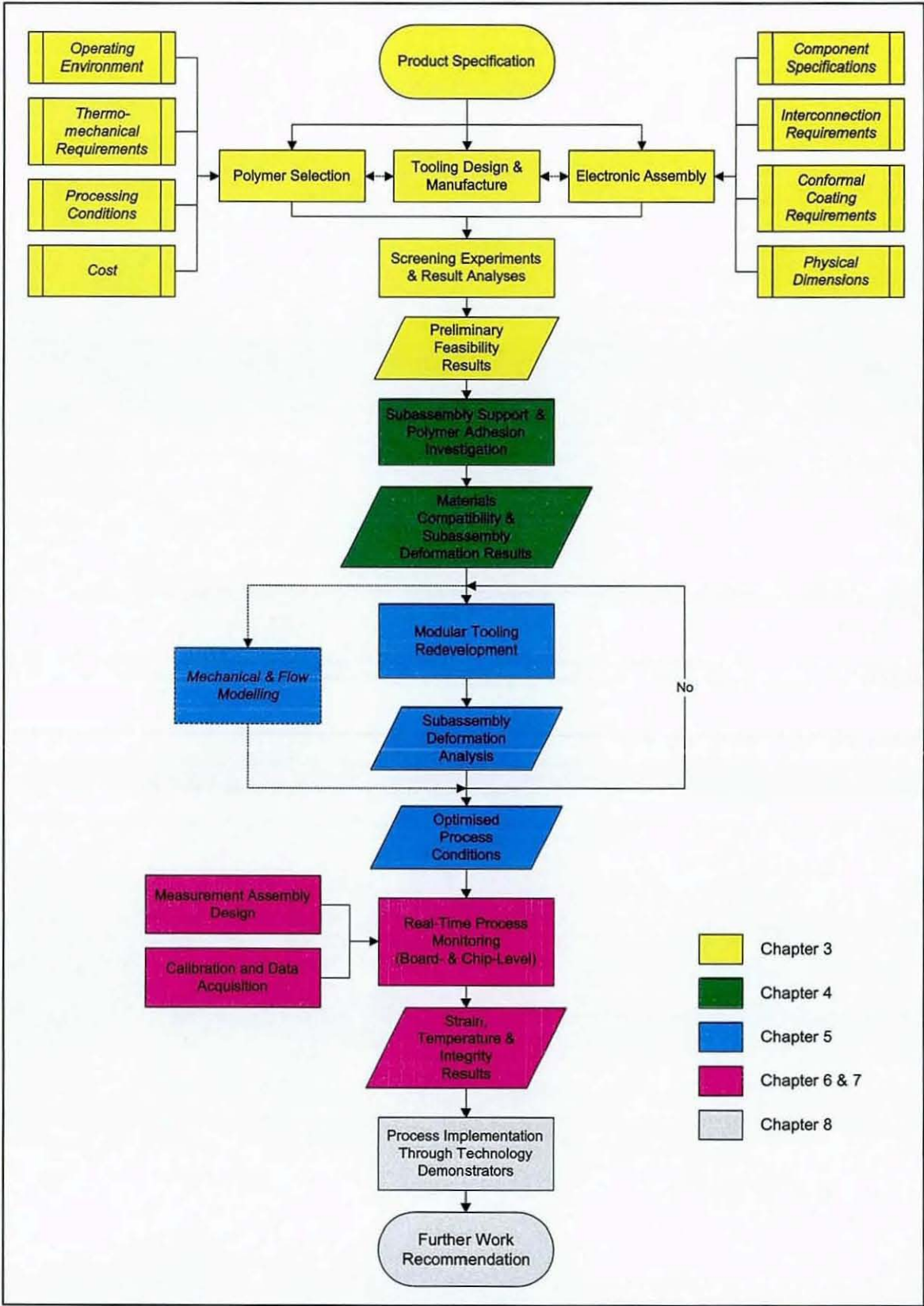
Figure 8-1 Research summary flowchart.
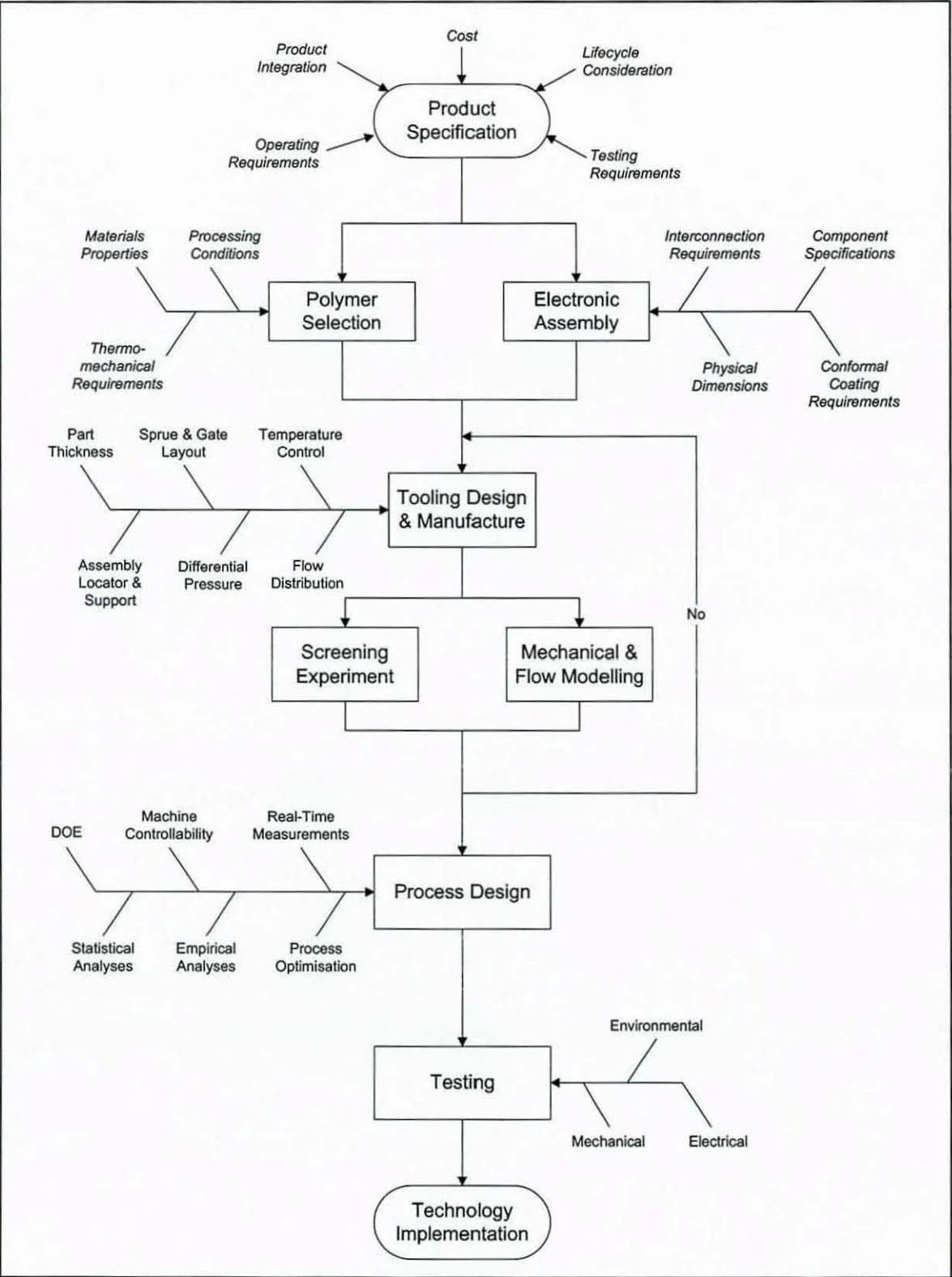
Figure 8-2 Overall process guideline for overmoulding of electronic assembly

8.7.   Technology Demonstrators

The results obtained from the real-time monitoring of two instrumented specimen subassemblies have revealed a valuable understanding of the proposed process and, together with the polymer-specific optimised parameter settings and novel in-mould supported contoured tooling, captured the process and design rules for the creation of two functional technology demonstrators for the automotive industry.

Figure 8-3 shows the first demonstrator developed, which was a circuit designed to convert a standard steering column switch pack to multiplex operation. The traditional design of the assembly is shown in Figure 8-3(a) where a circuit is mounted onto the steering housing and connected to other controllers via standard PTFE-insulated wires. The circuit is an in-car application and was selected to trial the principle of the encapsulation process delivered in this research. The modified subassembly was manufactured from a double-sided 4-layer BT board of 2mm thickness of dimensions 42mm×29mm. Its components comprised a QFP ASIC processor, various capacitors and resistors (the majority being 0402 size) and a wire-bonded 5V regulator chip (sealed with epoxy glob-top). Two 6-way FFCs were attached to the board, for connection to the column stalks. A further 10-way FFC provided power and CAN communication lines. Six pins were soldered to pads on the board. These plugged directly into corresponding sockets on the main moulding of the switch-pack.

The resulting GR-PBT overmoulded part is shown in Figure 8-3(b) and its new chassis mounting method depicted in Figure 8-3(c). As shown, the size of the overmoulded circuit was significantly reduced from its original design. This was achieved through higher integration of its electronic functionalities, component counts as well as FFCs. The reconfigurable geometry of the demonstrator also illustrated the potential to meet the concept of flexible design to produce ready-to-assemble electronic modules that offer advantages of shop-floor part handling and assembly, which, in turn, enables a leaner and lower cost manufacturing route in automotive industry.
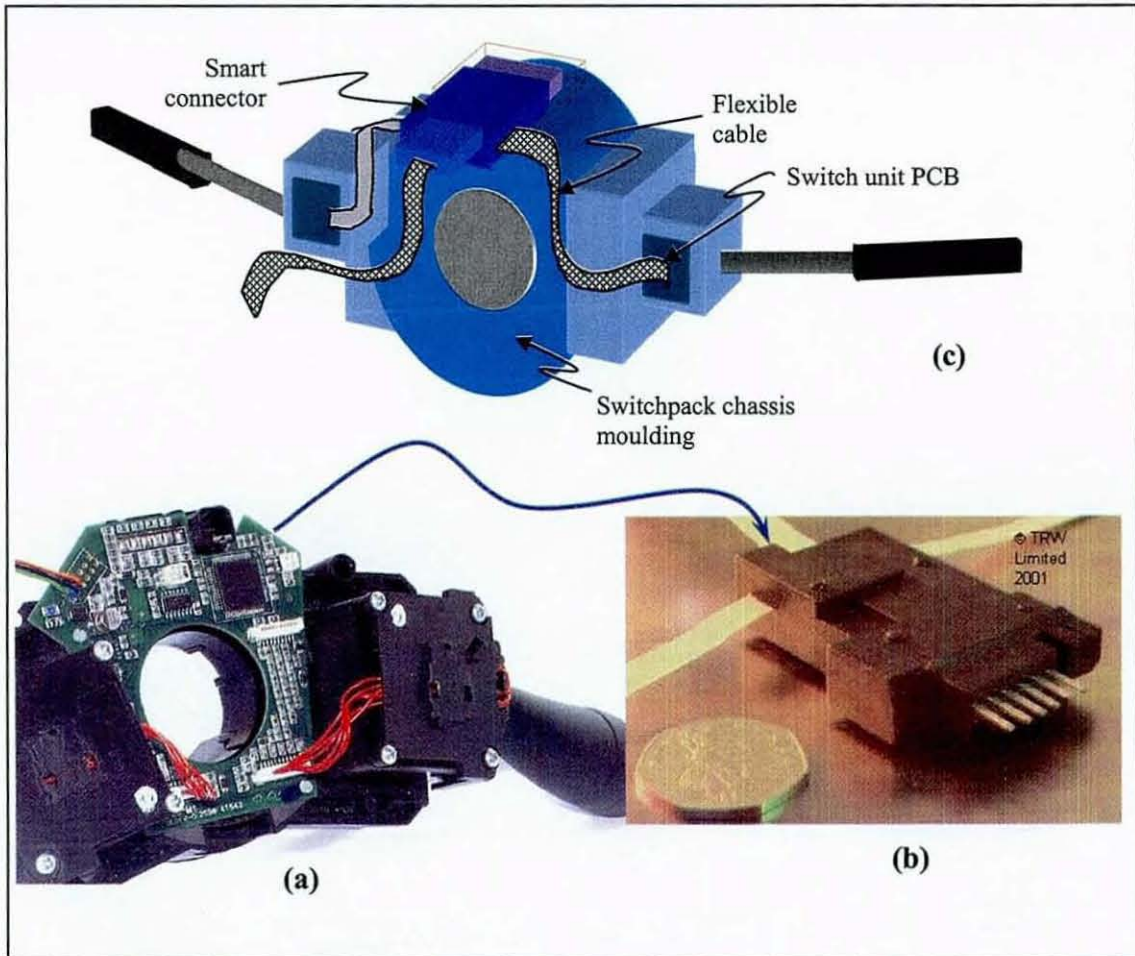
Figure 8-3 Technology Demonstrator 1: Steering column switchpack smart connector

The second technology demonstrator created was an electric parking brake (EPB) motor controller. This is a state-of-the-art conceptual design in the automotive industry as part of novel drive-by-wire technology, which is gradually being incorporated by many vehicle manufacturers. The system consists of an electronic control unit, which operates an electric stepper motor to exert the required clamping force on the brake discs of the vehicle wheels. This is an example application with sensing elements and a high switching current of up to 17A. The board had 108 components (both surfaces), including a processor, a CAN choke, a crystal, an electrolytic capacitor, a g-force sensor, MOSFETS, capacitors and resistors of various sizes, a Hall-effect sensor and a current sensor. Connections for power and CAN were via 6 through-hole pins mounted on the board. Similarly, two metal plates were provided for connection to the motor terminals.

The original unit is mounted within an external plastic housing which requires additional hermetic sealing in order to protect the electronic contents. This box is then assembled at the wheel bays and is subject to a harsh operating environment with exposure to demanding temperatures, vibration, dust and fluidic contaminations. As a result, the parts suffer from a severe mechanical and electrical failure rate. The advantages of embedding the electronic unit within polymeric overmoulding are mechanical and environmental protection for improved robustness and reliability. Figure 8-4(a) shows the circuit redesigned for the overmoulding process, which produced the final module shown in Figure 8-4(b). The overall assembled system can be seen in Figure 8-4(c).

The current research has, therefore, managed to engineer a manufacturing process that produces electronics sub-systems that are simultaneously packaged within the automotive structural thermoplastic components during the injection moulding process. It offers cost-effective integrated production technology for plastic automotive components with embedded electronics and power distribution. In addition to the two demonstrators generated from this work, other potential automotive applications are identified and illustrated in Figure 8-5. The innovative process and product integration achieved from this research in these applications offers a process with vast manufacturability potential for automotive suppliers to produce electromechanically-embedded, ready-to-assemble, component modules with superior robustness and, as such, may contribute to an increased incorporation of telematics for the improvements of vehicle safety and passenger comfort.
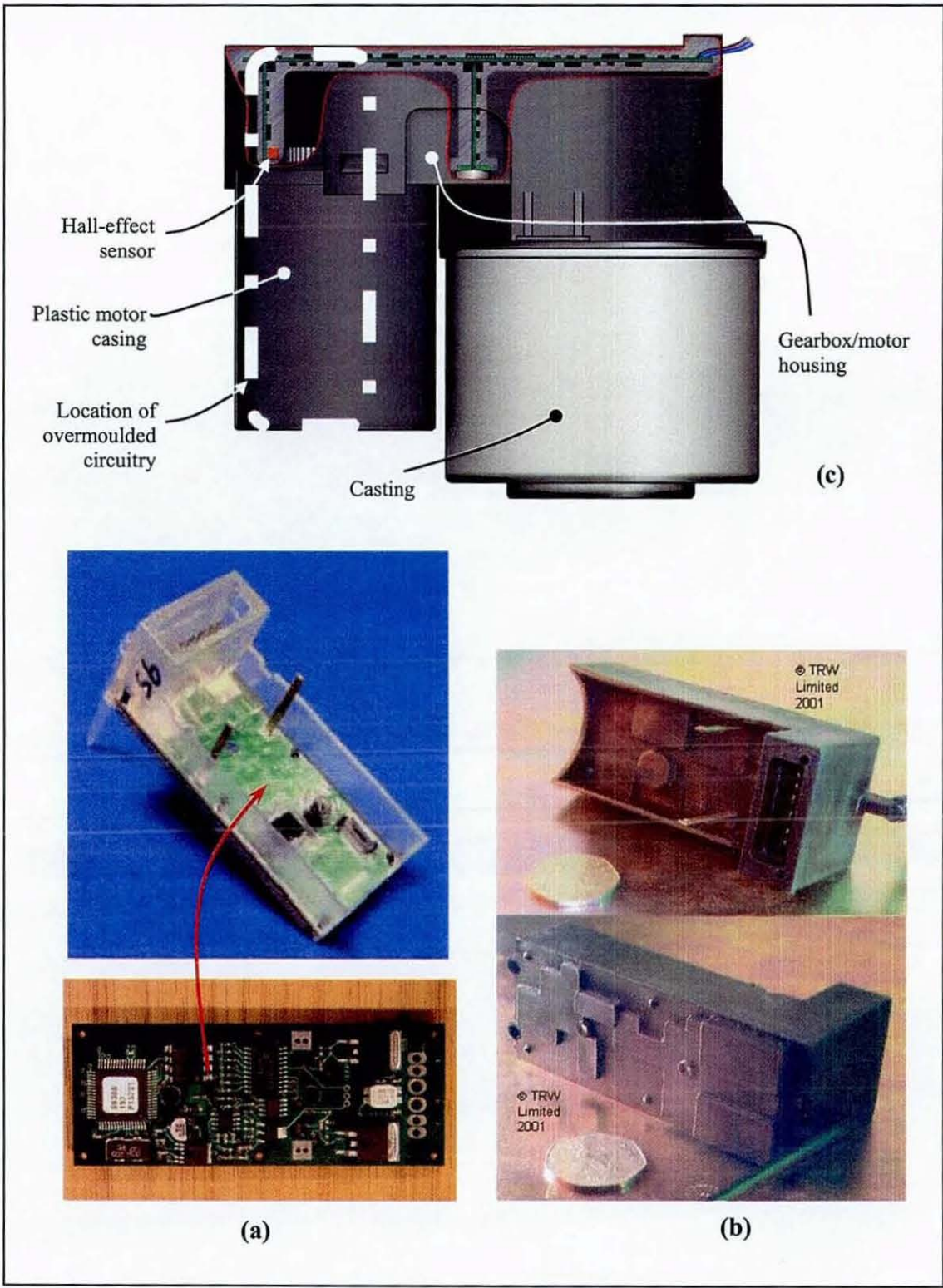
Figure 8-4 Technology Demonstrator 2: Electric parking brake controller
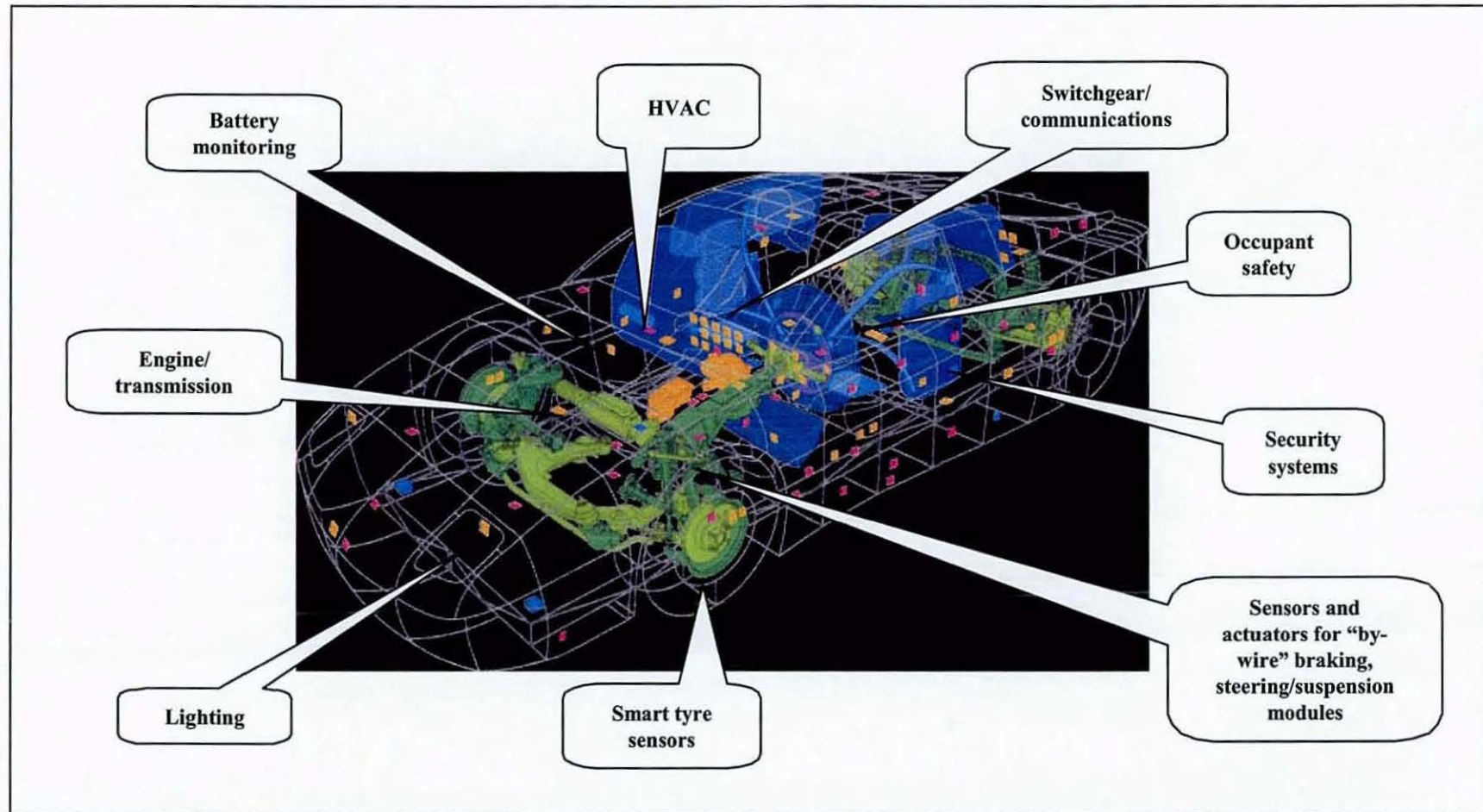
Figure 8-5 Possible future applications for overmoulding technology in vehicle electronic systems (courtesy of TRW Automotive)

8.8. Limitations and Recommendations for Further Work

This research has undertaken a number of extensive experimental studies to investigate various technological requirements fundamental to developing the process of simultaneously embedding electronics into thermoplastic components during injection moulding cycle. The results have demonstrated significant achievements in establishing the proposed technology. The findings obtained have also formed the foundation of knowledge necessary to carry out continuing work to further explore, exploit and refine this technology. The following sections recommend a number of viable routes to drive this research forward.

8.8.1. Thermomechanical Stress Reduction through Structural Foaming

Although it was observed that the high temperature from polymer melts did not cause unsustainable physical and functional failures to components and board warpages were successfully minimised through the process optimisation, it was evident from board- and chip-level strain measurements that the stress exerted on the PCB was substantial. This thermomechanical shock may compromise the structural integrity of the circuit board and can be detrimental to its operational reliability.

In order to further eliminate the physical and thermal stresses, future work may investigate the use of foamed polymers, which may be in the form of gas-assisted moulding or an additive chemical blowing agent (CBA). CBAs act as a source of gas by changing from their original physical state to gas during processing and are used to impart cellular structure to moulded plastics [Rosato et al, 2000]. However, gas-assisted foaming involves higher process complexity and therefore may incur extra manufacturing cost. One of the more established techniques of such process can be found in McClelland and Padsalgikar, 2003. The process may be undertaken by blending the polymer resin with a chemically matching foaming agent directly into the hopper and from there down through the barrel to the mould. Heat generated from the barrel causes a thermal decomposition of the materials and may be endothermic (primarily CO_2 producing agents) or exothermic (primarily N_2 producing agents). A polymeric emulsion, which is ideal for foam processing can be produced for compatible resin and CBA blends. This has a lubricating effect that not only reduces shear-heating forces, but also improves melt flow and consequently the polymer melt index [Reedy, 2000].

CO_2-based blowing agents are widely used because of low-pressure solubility and predictable post-mould foaming characteristic. The polymer-CBA blended resin is usually injected in a "short shot" (less than the volume of the mould cavity) and the gases released from the decomposition of CBA expand the polymer to fill the cavity. As the mould is not completely filled with polymer, the pressure is only generated by the foaming agent. Moreover, the cellular expansion fills any voids left from the cooling polymer and therefore complete cavity filling may be achieved without packing pressure. The foaming also lowers the viscosity of the injected resin and this offers the choice of reducing the processing temperature or utilising the improved melt flow at the same temperature. It has been reported that CO_2 CBA blended polymers can be injected at very low pressures of 7-12MPa and, in the case of PVC, reduces processing temperature by 50°C [Reedy, 2000].

However, there is an important disadvantage of foamed polymers, namely the reduced thermal conductivity due to the presence of air pores in the cellular structure. This effect has been previously studied by [Leach, 1992] and [Monkman, 2000], and a mathematic relationship approximating thermal conductivity (k) of the foamed material has been produced:

$$k \approx k_a + \frac{2}{3} k_s \frac{\rho}{\rho_s}$$

<div align="right">(Eqn. 8.1)</div>

where k_a is the thermal conductivity of air, k_s is the thermal conductivity of solid polymer, ρ is the density of the foamed polymer and ρ_s is the density of solid polymer. However, the use of foamed overmoulding polymers must be tested for breakdown resistance in high current applications. This may be in the form of surface insulation resistance (SIR) test according to IPC's TM-650 Electrochemical Migration Resistance Test [IPC, 2000].

8.8.2.   Increased Heat Transfer with Thermally Conductive Polymers

Almost all intrinsic and fibre-filled polymers are inherently thermal insulators with a thermal conductivity of approximately 0.2W/m-K, which is 2000 times less than copper and only about 10 times greater than most insulation materials or stagnant air. Therefore, heat transfer through overmoulding polymers may be a concern for thermal power dissipation during the operation of encapsulated electronics. This issue has not been addressed in the current research due to time constraints.

Further work may explore the incorporation of suitable thermally-conductive polymers (TCP) in the overmoulding process. Latest industry development has seen some new injection mouldable variants of TCP composites filled with boron nitride , aluminium nitride or alumina flakes that produce an increased thermal conductivity of up to 30W/m-K [McCullough, 2000] [Feng and Ellis, 2003] and may be suitable for this purpose. However, extensive studies must also be conducted to study the critical electrical insulation and dielectric properties of the TCP. These may include measurement of the surface insulation resistance (SIR) according to the IPC's TM-650 [IPC, 2000] or ASTM D-257-99 [ASTM, 1999] protocols, both tested under elevated temperature and humidity conditions. The electrical insulation property of the material is measured in terms of its electrical resistivity and must be typically in the range 10^{12}-10^{16} Ω-cm.

8.8.3.   Recyclable Polymeric Overmoulding

This research has successfully established a novel manufacturing technology for electronic embedded plastic components and two functional automotive demonstrators were created. However, with the introduction of the Directive on Waste Electrical and Electronic Equipment (WEEE) by the European Commission [European Council, 2003], the important of "design for environment" has become an increasingly critical factor in the electronic industry. This may give rise to the issue of extracting the embedded electronics from the overmoulding plastics at the end of their operating lifecycle. Future studies could study the implementation of recyclability for the current technology. It is clear that within the context of recycling polymeric electronic modules, one of the major challenges is the clean separation of original electronic subassemblies from the overmoulding polymer. When considering that the overmoulding polymers are injected at high temperatures and/or pressure and will have filled all the gaps between adjacent components and adhered to various surfaces on the PCB-based circuitry, a complete extraction of the components from standard plastic is almost impossible.

The use of biodegradable compostable polymeric materials may offer a possible route to overcome this problem. One of the materials that may be suitable for this application is pelletised water-soluble polyvinyl alcohol-based (PVOH) polymers, which are known for their capability to be "programmed" (or formulated) to dissolve at a pre-determined temperature (or within a temperature window) in the presence of moisture/water. PVOH-based polymers are gradually finding use in moulded and extruded products, but are not currently suitable for harsh automotive environments. PVOH by itself is not considered as a

thermoplastic because its melt temperature exceeds the degradation temperature for fully hydrolysed grades. However, this has now been overcome by the addition of plasticizers to control the processing melt temperature at about 200°C with adequate melt flow and improved heat stability. The unique capacity to biodegrade into CO_2, water and biomass, as well as to compost into non-toxic residues, is the crucial advantage of these polymers. Furthermore, currently available injection mouldable PVOH-based polymers have been shown to be similar to conventional polymers in both thermal characteristics and many mechanical parameters, such as flexural modulus, tensile and impact strengths. Also, as the PVOH can be processed at temperatures about 30-50°C lower than the glass-filled polymers, it will be critical in reducing the thermomechanical stresses that may lead to cracking of solder joints and component failures.

The solubility characteristics of PVOH polymers are governed by a complex set of criteria. The main polymer properties affecting the degree of solubility of PVOH polymers include the degree of hydrolysis, molecular weight, extent of any cross-linking, thermal history and degree of crystallisation. Commercial grades of PVOH are available in a range of molecular weights and degrees of hydrolysis. Therefore, experimental work may be undertaken to characterise properties of these materials which are fundamental to enable successful overmoulding process. However, in order to prevent dissolution of these polymers in the typically harsh automotive operating environments, a two-shot moulding technique may be used to apply a second overmoulding layer of a conventional engineering thermoplastic polymer, which could be a glass-reinforced grade for its higher dimensional stability. An economically practical or environmentally sound method of recovering these fully embedded electronic components from the water-soluble thermoplastic wastes may then be developed.

8.8.4. Thermomechanical Modelling

As evident from this work, the encapsulation process will provide a thermally insulating barrier around the electronics that will prevent the rapid dissipation of heat from the components, which will be further compounded by the high temperature operating environment, particularly for under-bonnet applications. For power devices, this could result in significant overheating and premature failure, together with heat damage to the polymer material.

Thermal models may be created to simulate the effects that encapsulation of electronics has on the in-service thermal performance and mechanical reliability of the electronic modules. While the foaming of polymers discussed in Section 8.8.1 may offer lower processing temperature and pressure, it does have the disadvantage of reducing the heat dissipation capacity. This shortcoming can be compensated through the addition of a thermally conductive filler, which is discussed in Section 8.8.2. However, the differences in the mechanical properties, such as the CTE, between this new foamed TCP and the embedded electronics may result in undesired propagation of stresses, leading to mechanical and functional failures. Thermal conduction and stress analyses by FE models may be employed to investigate the effects of heat transfer and thermomechanical properties of polymers with varying degrees of foaming and/or contents of conductive fillers, and further attempt to predict the developed stresses within the modules. This modelling initiative may also be utilised in the development of a suitable water-soluble TCP for the process to further embody the recyclability feature of the technology. Results from these models will create a set of design guidelines that will provide process specifications for an engineer to determine the required polymeric properties, electronic requirements for specific applications, and the subsequent in-service performance and reliability predictions.

8.8.5.   In-mould Retractable Supports

The current research has developed a novel set of overmoulding tooling in which the inserted rigid electronic subassembly was successfully fixed at the mid-plane of the cavity. This has ensured a balanced melt flow around the subassembly and hence minimised any differential pressure distribution that may lead to substrate warpage. Shear force from the impinging melt was utilised to fill the gaps offsetting the substrate and the locating pins and hence enabled completely sealing in the overmoulded modules. This design is, however, not fully practical for industrial manufacturing process and more development in this area may be necessary.

One of the possible techniques may be retractable supports in the form of hydraulic pins that are withdrawn as the molten polymer fills the mould cavity, before the melt freezes. This technique was first introduced for the encapsulation of golf ball cores by [Giza, 1992] and then refined by [Cupples, 2001]. A vertical clamp moulding machine may be preferred as it could use gravity to hold the insert subassembly in place. It is now also used in encapsulation of sensors and transformers, but an adaptation for overmoulding of rigid subassembly

consisting of delicate electronics will form another novel application for this technology [DuPont, 1997].

8.8.6. Environmental Testing

The technical benchmark and process guidelines of a novel electronic embedding technique have been established as part of this research. Two functional technology demonstrators were generated and have been shown to be fully operational in the test rigs. However, the long term performance and reliability of these parts were not entirely investigated within the time-frame of this research. The test pieces generated from the experiments in Chapters 6 and 7 may be used as test vehicles for this purpose by subjecting them to an appropriate test scheme based on the Automotive Engineering Council (AEC) [AEC, 2001] qualification procedure for electronic components. As a recommendation, they may be divided into three groups and subjected to a programme of environmental tests as listed in Table 8-1 below, which are intended to be representative of automotive components. The test regimes were modified according to the respective JEDEC (Joint Electron Device Engineering Council) standards to accommodate the proposed technology.

	Group 1	Group 2	Group 3
Test 1	High temp bake (based on JEDEC A103 [JEDEC, 1989]) **850 hours at 85°C**	Thermal cycle (based on JEDEC A104 [JEDEC, 2000]) **200 cycles of -40°C to +85°C**	Autoclave (based on JEDEC A102 [JEDEC, 1991]) **96 hours at 121°C and 100% RH**
Test 2	High temp operating life (based on JEDEC A108 [JEDEC, 1991]) **120 hours at 120°C**	Temperature humidity bias (based on JEDEC A101 [JEDEC, 1997]) **1000 hours at 85°C and 85% RH**	
Test 3	Thermal cycle (based on JEDEC A104 [JEDEC, 2000]) **1000 cycles of -40°C to +85°C**		

Table 8-1 Recommended environmental test programme for overmoulded automotive electronics

8.8.7. Future Exploitation

The primary automotive market potential for this electronic overmoulding technology is extremely large and growing, as the average car gets more sophisticated with the inclusion of more features such as anti-lock brakes, power steering, air-conditioning, parking sensors and safety systems. Future research may be undertaken to innovate the process in other electronic-related sectors. The EU's WEEE directive is designed to make recovery and recycling of electronic and electrical goods compulsory by 2004 [European Council, 2003]. This directive will make the proposed technology extremely attractive to many potential end users. Immediate applications where this proposed technology could be implemented are encapsulated electronics within mobile phones, Smartcard products, anti-fraud packaging for pharmaceuticals and drug delivery devices. Other examples of general potential areas are in domestic/household appliances (such as washing machines, fridge/freezers, security alarm systems, outdoor lights and equipments, etc.), consumer electronics (such as handheld computers, instrumentation devices, mobile phones, etc.), under-water exploration equipment and other applications with requirement for operation in more hazardous environments.

REFERENCES

American Society for Testing and Materials (ASTM), 1999, "D257-99 Standard Test Methods for DC Resistance or Conductance of Insulating Materials", ASTM International.

Association of Plastics Manufacturers in Europe (APME), Spring 2000, *"An Analysis of Plastics Consumption and Recovery in Western Europe 1998"*

Association of Plastics Manufacturers in Europe (APME), Spring 2001 (a), *"An Analysis of Plastics Consumption and Recovery in Western Europe 1999"*

Association of Plastics Manufacturers in Europe (APME), Spring 2001 (b), *"Plastics – Contributing to Economic Development: Adding Value Through Wealth Creation"*

Automotive Engineering Council (AEC), 2001, "Stress Test Qualification for Integrated Circuits", AEC-Q100-REV-E (January 31, 2001).

Bannatyne R.T., 2000, "Advanced Semiconductor Developments for Automotive Systems", SAE Technical Paper Series 2000-01-1550.

Bannatyne R.T., Warshawsky E.H., 1997, "The Changing World of Automotive Electronic Control Units", SAE Technical Paper Series 972638.

Bayer Plastics, 2004, "3D MID", Bayer MaterialScience AG, Germany.
http://plastics.bayer.de/AG/AE/technology/1012/50/index.jsp

Brancato R., 2000, "Millennium Prediction: A Package for All Occasions", Advanced Packaging. Vol. 9, no. 1, January 2000, pp 30-34. ISSN 1065-0555.

Brathwaite N., Huey K., 1997, "Advanced Electronic Packaging Techniques Enhance Function, Performance, and Portability", Medical Electronics Manufacturing,
http://www.devicelink com/mem/archive/97/10/009 html

Bryce D.M., 1996, "Plastic Injection Moulding – Manufacturing Process Fundamentals", Society of Manufacturing Engineers Publication, ISBN 0-78263-472-8.

Burk S., 2000, "Overmolding Circular Connectors in Cable Assemblies", Connector Specifier August 2000, http://cs.pennnet com/Articles/article_display.cfm?Section=Archives&ARTICLE_ID=80706 &Publication_ID=42

Burk S., 2001, "Overmolding of Embedded Electronics", Connector Specifier, April 2001.

Chakravorty S., Allen C.R.G., Brown C.S., 1997, "In-Line Temperature Measurement During Polymer Melt Flow", Polymer Testing, vol. 16, pp 455-460.

Cohn, C., Shih M.T., 2000, "Chapter 7- Packaging and Interconnection of Integrated Circuits, Electronic Packaging and Interconnection Handbook", edited by Harper C.A., McGraw-Hill Publication, ISBN 0-07-134745-3.

Creative Storage Systems, 2001, "Brakes", http://www.creativestorage.com/Products/Brakes.htm

Cupples V.J., 2001, "Golf Ball Mold Cavity with Subgates", US Patent 2001/0048180 A1.

Dally J.W., Riley W.F., 1991, "Experimental Stress Analysis", McGraw-Hill Education. ISBN 0-0701-5218-7.

Dally J.W., Riley W.F., McConnell K.G., 1993, "Instrumentation for Engineering Students – 2nd. edition", John Wiley & Sons Inc. ISBN 0-471-60004-0.

Day R., Latino F., 1988, "The Migration of Electronic Controls down to the Device Level Decentralises and Distributes Control Intelligence in Pneumatic Systems", SAE Technical Paper Series 981325.

De Cooper Jones M., 1999, "EMECMOLD Modelling Status Report 25/10/99", TRW Automotive.

De Cooper Jones M., 1999, "Preliminary CAE Simulation Studies on Resin Flow in Over-moulding of PCB Assemblies and Resulting Structural Implications 30/6/99", TRW Automotive.

DeVos G., Helton D., 1999, "Migrating of Powertrain Electronics to On-Engine and On-Transmission", SAE International Conference and Expo, 1999.

DKC Corporation, 2004, "Injection Moulding Operations" http://www.central-corp com/centeng/dkc htm

DuPont, 1997, "Electrical/Electronic Thermoplastic Encapsulation". http://ww dupont.com

DuPont, 1997, "Electrical/Electronic Thermoplastic Encapsulation", DuPont Engineering Polymers, 06/97, H-58633 (European version).

Electronic Industries Association (EIA), 1989, "JEDEC Standard A103: High Temperature Storage Life", JESD22-A103-A.

Electronic Industries Association (EIA), 1991, "JEDEC Standard A108: Bias Life", JESD22-A108-A.

Electronic Industries Association (EIA), 1991, "JEDEC Standard A102: Accelerated Moisture Resistance - Unbiased Autoclave", JESD22-A102-B.

Electronic Industries Association (EIA), 1997, "JEDEC Standard A101: Steady State Temperature Humidity Bias Life Test", EIA/JESD22-A101-B.

Electronic Industries Association (EIA), 2000, "JEDEC Standard A104: Temperature Cycling", JESD22-A104-B.

European Council, 2003, Directive 2002/96/EC of the European Parliament and of the Council of 27 January 2003 on Waste Electrical and Electronic Equipment (WEEE).

Federico M., Patterson W.I., Kamal M.R., 1997, "Cavity Temperature Profile Measurement During Injection Moulding", Proceedings from the SPE ANTEC'97 Conference, Toronto, Canada, pp 577-581.

Feldmann F., Barnd A., 1996, "SMD Assembly on to Moulded Interconnection Devices – Available Systems and Developments", Soldering and Surface Mounting Technology, vol. 8 no. 1, pp. 10-15, ISSN 0954-0911.

Feng J., Ellis T.W., 2003, "Thermal Management for Semiconductor Devices with Conductive Polymers", Synthetic Metals, 135-136 (2003), pp 155-156.

Frank R., Shukman H., 1998, "Electronics and the Digital Car of the Future - Automotive Electronics: The 1990's", pp 515-526. ISBN 0-7680-0399-7

Fried, J.R., 1995, *"Polymer Science and Technology."* Prentice Hall PTR publication, ISBN 0-13-685561-X

Gannamani R., Pecht M., 1996, "An Experimental Study of Popcorning in Plastic Encapsulated Microcircuits", IEEE Trans. on Components, Packaging and Manufacturing Technology, Part A, vol. 19, no. 2, June 1996.

Giza J., 1992, "Retractable Pin for An Injection Mold", US Patent 5,147,657.

Greene D.C., 2001, "Sensor Technology and Applications to a Real-Time Monitoring System", MEng dissertation, Dept. of Civil and Environmental Engineering, MIT.

Ham S., 2001, " Structural Plastics Fundamentals", PD3 Newsletter Archives, Issue 03-2001, http://www.pd3.org/Issue%2003_2001/StrucrualPlasticsFunda/structural_plastics_fundament als.htm

Hanrahan J., Griffith D.N., 2002, "Component Performance Advantages Realized Through Thermoplastic Encapsulation", http://www encaptech com/2002altconstrnv.pdf

Harkness E., 1995, "Automotive Electronics in Europe – Success in a Changing Market", ISBN 1-85334-418-4.

Harper C.A., 2000, "Electronic Packaging and Interconnection Handbook", McGraw-Hill Publication, ISBN 0-07-134745-3.

Harper C.A., 2000, "Modern Plastics Handbook", McGraw-Hill Publication, ISBN 0-07-026714-6.

Housden A., Gould J., 2002, "Moulded Interconnect Devices", PRIME Faraday Technology Watch, ISBN 1-84402-021-5.

Huang D.Y., Chen R.S., 1999, "Bonding Strength at Solid-Melt Interface for Polystyrene in a Sequential Two-Staged Injection Moulding Process", Journal of Polymer Engineering and Science, Nov 1999, vol. 39 no.11, pp 2159-2171.

Huang M.C., Tai C.C, 2001, "The Effective Factors in the Warpage Problem of an Injection-Molded Part with a Thin Shell Feature", Journal of Materials Processing Technology 110 (2001) 1-9.

Information Society Technologies (IFT), 2003, Research Networking – Glossary, http://www.cordis.lu/ist/rn/glossary.htm#t

IPC, 2000, "IPC-TM-650 - Electrochemical Migration Resistance Test".

JEDEC, 1989, "Test Method A103-A: High Temperature Storage Life", JESD22-A103-A.

JEDEC, 1991, "Test Method A102-B: Accelerated Moisture Resistance Test Unbiased Autoclave", JESD22-A102-B.

JEDEC, 1991, "Test Method A108-A: Bias Life", JESD22-A108-A.

JEDEC, 1997, "Test Method A101-B: Steady-State Temperature Humidity Bias Life Test", EIA/JESD22-A101-B.

JEDEC, 2000, "Test Method A104-B: Temperature Cycling", JESD22-A104-B.

Johannaber F., 1994, "Injection Moulding Machine – A User's Guide, 3rd. edition", Hanser Gardner Publications. ISBN 1-56990-169-4.

Kansala G., Raob P.N., Atreya S.K, 2001, "Study: Temperature And Residual Stress in an Injection Moulded Gear", Journal of Materials Processing Technology 108 (2001) pp. 328-337.

Kazmer D.O., Roe D.S., 1994, "Increasing Weld-line Strength Through Dynamic Control of Volumetric Shrinkage", Proceedings from SPE ANTEC'94, San Francisco, USA, pp 631-636.

Kiencke U., Kytölä T., Neumann K.J., 1996, "Architectural Trends in Automotive Electronics", A. Rev. Control, vol. 20, pp. 197-207, Intl. Fed. of Automatic Control.

Krimi S., 1998, "Alternative SMD Placement Systems for 3-D Circuit Boards", Proceedings from 3rd. Int. Cong. on MID, Erlangen, Germany.

Kuphaldt T.R., 2002, "Lessons in Electric Circuits, Volume 1 (DC)", http://www.ibiblio.org/obp/electricCircuits/DC/

Leach A.G., 1992, "The Thermal Conductivity of Foams. 1: Models for Heat Conduction", Journal of Physics (D): Applied Physics, 26, pp 733-739.

Lin T.Y., Tay A.A.O., 1997, "Dynamics of Moisture Diffusion, Hygrothermal Stresses and Delamination in Plastic Packages", EEP-Vol. 19-2, Advances in Electronic Packaging, ASME, pp 1429-1436.

Lu X., Lau S.K., 2001, "A Statistical Experimental Study of Injection Molding of Optical Lenses", Journal of Materials Processing Technology 113 (2001) 189-1095.

Manero F., Patterson W.I., Kamal M.R., "Cavity Temperature Profile Measurement During Injection Moulding", Proceedings from the SPE ANTEC'97 Conference, Toronto, Canada, pp 577-581.

Mapleston P., 2000, "3-D Interconnect Offers Sizeable Market Opportunity", Plastiscope, March 2000.

McClelland A.N., Padsalgikar A.D., 2003, "Gas Assisted Injection Moulding", US Patent 2003/0015815 A1.

McCullough K.A., 2000, "Thermally Conductive Composite Material", US Patent 6,048,919.

Monkman G.J., 2000, "Advances in Shape Memory Polymer Actuation", Mechatronics 10, pp 489-498.

Morgan G., 1997, "Fusible Coring - Practical For Forming One-Off Structures", Aircraft Engineering and Aerospace Technology, Volume 69 · Number 2 · 1997 · pp. 145–146, ISSN 0002-2667.

Morris A., 2003, "Plastic Injection Moulding – An Introduction", http://www.azom.com/details.asp?ArticleID=265#_Introduction

Muraki N., Matoba N., Takayuki H., Yoshikawa M., 2002, "Determination of Thermal Stress Distribution in a Model Electronic Device Encapsulated with Alumina Filled Epoxy Resin using Fluorescence Spectroscopy", Polymer 43 (2002) pp. 1277-1285.

Murray W.M., Miller W.R., 1992, "The Bonded Electrical Resistance Strain Gage", Oxford University Press. ISBN 0-19-507209-X.

Patterson J.F.B, 1992, "Advances in Thermoplastic Coil Encapsulation", Electrical Manufacturing, May/June 1992.

Pecht M.G., Nguyen L.T., Edward B.H., 1995, "Plastic-Encapsulated Microelectronics", Wiliey-Interscience Publication, ISBN 0-471-30625-8.

Reedy M.E., 2000, "How Chemical Foaming Agents Improve Performance and Productivity", Plastics Engineering, vol. 56(5), pp 47-50.

Rosato D.V Rosato D.V., Rosato M.G., 2000, "Injection Moulding Handbook, 3rd edition", Kluwer Academic Publisher. ISBN 0-7923-8619-1.

Rosato D.V., 1997, "Plastic Processing Data Handbook, 2nd edition", Chapman & Hall Publication, ISBN 0-412-80190-6.

Rosato D.V., et al. 1995, "Injection Moulding Handbook, 2nd edition", Chapman & Hall Publication, ISBN 0-412-99381-3.

Rubin I.I., 1972, "Injection Molding – Theory and Practice", Wiley-Interscience Publication, ISBN 0-471-74445-X

Rugenstein E., Füßer R., 2001, "Talking Point at K'2001 in Düsseldorf: Automation Technology for Plastics Machinery", http://www.messe-duesseldorf.de/k-online/en/70F2FB4E7D424716AF8609844C727B25_66654A5B013043CD87B98F489907D A86 htm

Schmidt O., 1999, "Mould Flow Analysis and Design Improvement of EMECMOLD Stage 2 Model 15/11/99", Middlesex University.

Schmidt O., 2000, "Interim Report for EMECMOLD Project 27/3/00", Middlesex University.

Speight R.G., Hull J.B., 1997, "Pressure Measurements for Injection Moulding", Proceedings from the SPE ANTEC'97 Conference, Toronto, Canada, pp 561-565.

Stevenson J.F., 1996, "Innovation in Polymer Processing Molding", Hanser Publishers. ISBN 3-446-17433-8.

Tat Ming Eng. Works Ltd., 2003, "How to Select a Plastic Injection Moulding Machine", http://www catalog.com hk/tatming/select/print html

Tummala R.R., Rymaszewski E.J., Klopfenstein A.G., 1997, "Microelectronics Packaging Handbook, Part I: Technology Drivers", Chapman & Hall Publication, ISBN 0-412-08431-7.

Tummala R.R., Rymaszewski E.J., Klopfenstein A.G., 1997, "Microelectronics Packaging Handbook, Part II: Semiconductor Packaging", Chapman & Hall Publication, ISBN 0-412-08441-4.

TWI, 1999, Technology File – Glob Top, http://www.twi.co.uk/j32k/unprotected/band_1/tfglobtp.html

U.S. Department of Defense, 2003, "Mil-Std-883: Test Method Standard for Microcircuits", http://www.dscc.dla.mil/Downloads/MilSpec/Docs/MIL-STD-883/std883inc.pdf

van der Sanden L., 1992, "Flow Length Versus Injection Pressure for PBT Engineering Plastics", AMP Journal of Technology Vol. 2 November, 1992.

Viswanadham P., Singh P., 1998, "Failure Modes and Mechanisms in Electronic Packages", Chapman and Hall Publication, ISBN 0-412-10591-8.

Ward D.K., Fields H.L., 2000, "A Vision of the Future of Automotive Electronics", SAE Technical Paper Series 2000-01-1358.

Willert, W.H.,1956, *"Injection Moulding Apparatus"*, US Patent 2,734,226

Wondrak W., Boos A., Constapel R., Wilde J., 1999, "Reliability Requirements for Microtechnologies in Automotive Applications", MicroEngineering '99.

Wong C.P., 2000, "Chapter 1- Materials for Electronic Packaging, Electronic Packaging and Interconnection Handbook", edited by Harper C.A., McGraw-Hill Publication, ISBN 0-07-134745-3.

Yanik J.A., 1998, "The Automobile: Unwanted Technology – The Later Years, Part II: The Downing of Automobile Electronics", Automotive Electronics: The 1990's. pp 213-233. ISBN 0-7680-0399-7.

Yee E., 2000, "Molded Interconnect Devices Reshape Electromechanical Design", Electronic Design, September 5, 2000, http://www.elecdesign.com/Articles/Print.cfm?ArticleID=4693

Yokoyama S., Iji M., 1995, "Recycling of Thermosetting Plastic Waste from Electronic Component Production Process", IEEE Conference on Electronics and Environments, pp 132-137.

Yokoyama S., Iji M., 1998, "Recycling System for Printed Wiring Boards with Mounted Parts", NEC Research and Development, vol. 39, no. 2, pp 111-115.

Zippman V., 1999, "Injection Molding of 3-D Molded Interconnect Devices, MID", Proceedings from the MIDIA MID'99 Symposium, Chicago, Illinois.

Zussman E., 1999, "SMD Placement on Three-Dimensional Circuit Boards", IEEE Trans. on Electronics Packaging Manufacturing, vol. 22, no. 2, pp. 147-150, ISSN 1521-334X.

APPENDIX 1. EXPERIMENTAL MATERIAL PROPERTIES

A.1.   Circuit Assembly

Materials / Properties	FR4	BT resin	Ceramic	Copper (track)	Solder	Die adhesive
Commercial grade	FR4-74 (glass fibre laminate)	BT-Epoxy G200	Rubalit 708S 96% Al_2O_3		Multicore Sn62RM89A A85	Loctite Chipbonder 3609 epoxy
Industry specification	MIL-P-13949GE UL-E41668	MIL-S-13949H UL-E37002			J-STD-006 EN 29453 Bellcore TR-NWT-000078	Siemens SN-59651 Bellcore TR-NWT-000078
Physical Properties						
Water absorption , %	0 12		0			
Flammability, s	25 [V-O] (UL 94)	[V-0]				
Surface roughness (R_a), μm			0 6 max.			
Mechanical Properties						
Young's modulus (E) [GPa]			340 (ASTM F417)	120 66		
Flexural strength, MPa	530 0 [lengthway] 425.5 [crosswise] (ASTM D229)	490 0 [lengthway] 390 0 [crosswise] (ASTM D229)	380			
Hardness (shore A)	115					
Shear strength, MPa	138 5			0 4		
Shear strain (γ)						
Peel strength, N/mm	1 95 (ML-P-13949)	1 23				30-80 N (Pull-off strength on FR4)
Peel strength after thermal stress, N/mm	1 90 (ML-P-13949)	1 23				
Thermal Properties						
T_g, °C		180	Very high (service temp ~1500°C)			73
Relative temp index (RTI), °C	130 (UL 746)					
CTE (α), ppm/°C	13-18 (x-y)	13(x), 15(y), 60(z) [RT-T_g]	7 3 [20 – 600°C] (ASTM C373)	17	21	145 (ASTM C696)
Thermal conductivity, K (W/m-°C)	0 3	0 36	24 (ASTM C408)	380 - 400	49	0 4 (ASTM C177)
Thermal stress (min 288°C), s		>1200 (E-2/105)				
Specific heat, J/kg °C			800	385 19		300
Electrical Properties						
Dielectric constant @ 1 MHz	4 55 (ML-P-13949)	4 1	9 8 ± 10% (ASTM C150)			3 2 (ASTM D150)
Electric strength, kV/mm		46	15 (ASTM D149)			
Dielectric breakdown, kV	58 (ASTM D149)					

Dissipation factor @1 MHz	0 0175 (ML-P-13949)	0 013	0 0003 (ASTM D150)			0 02 (ASTM D150)
Surface resistivity, Ω	5 x 10^{12} (IEC 249)	1 x 10^{11} (IEC 249)				2 x 10^{15} (ASTM D257)
Volume resistivity, Ω cm	3 x 10^{12} (IEC 249)	1 x 10^{13} (IEC 249)	10^{13} [20°C] 10^{12} [200°C] 10^{11} [400°C] (ASTM D257)	1.7 x 10^{-6} [22°C]	14.7 x 10^{-6} [22°C]	2 x 10^{15} (ASTM D257)

A.2.   Glob-top Materials

Materials Properties	Silicone	Epoxy		Polyurethane
Commercial grade	Elastosil RT601	Amicon 50300LT (polymeric substrate)	Amicon 50302HT (ceramic substrate)	Humiseal 2B74/95
Linear CTE (ppm/°C)	23 x 10^{-4}	25x 10^{-6}	35x 10^{-6}	N/A
Thermal conductivity (W/m-°C)	0 26	0 63	0 50	N/A
T$_g$ (°C)	N/A	140 min	130 min	N/A
Cure shrinkage (%)	0 82	0 2 – 0 5	0 2 – 0.5	0 8 – 0 9
Hardness	45	90 min	90 min	N/A
Density (g/cm^3)	1 02	1 71 – 1 75	1 65 – 1 69	1 05
Viscosity (Pa-s)	3 50 (low)	45-65	45 – 65	N/A
Curing profile	30min @ 150°C	30min @ 120°C	120min @ 150°C	24hrs @ 25°C

A.3.   Overmoulding Polymers

Material Property	Unfilled PBT	30% glass filled PBT	Unfilled Nylon 66	40% mineral filled Nylon 66	Acetal
Commercial grade	*GE Plastics Valox 325*	*DuPont Crastin LW9130 NC010*	*DuPont Zytel 103HSL NC010*	*DuPont Minlon 10B140*	*DuPont Delrin 900P NC010*
Physical Properties					
Density (ρ), g/cm^3	1 31 (ASTM D792)	1 51 (ISO 1183)	1 14 (ISO 1183)	1.50 [dam] (ISO 1183)	1 42 (ISO 1183 & ASTM D792)
Linear mould shrinkage, cm/cm	0 019	0 65 [normal] 1 0 [normal, annealed] 0 25 [parallel] 0 4 [parallel, annealed] (ISO 2577)	1 3 [flow] (ISO 2577)	1.2 [normal] 1.2 [parallel] [dam] (ISO 2577)	2 1 [flow], 2 0 [transverse] (ISO 2577)
Water absorption, %	0 08 (ASTM D570)	0 35 @50% RH (ISO 62)	8 5 @50% RH (ISO 62) 1 2 @saturation (ASTM D570)	5 @50% RH [dam] (ISO 62)	1.5 (ASTM D570) 1 4 @50% RH (ISO 62)
Humidity absorption, %		0 14 (ISO 62)	2 8 (ISO 62)	1 6 [dam] (ISO 62)	0 3 (ISO 62)
Mechanical Properties					
Tensile strength, MPa	52 (ASTM D638)				69 (ASTM D638)
Tensile modulus @1mm/min, GPa		9.5 (ISO 527-1/2)	1 25 [50% RH] 3.1 [dam] (ISO 527-1/2)	3.5 [50% RH] 5 8 [dam] (ISO 527-1/2)	3.2 (ISO 527-1/2)
Stress @ break, MPa		130 (ISO 527-1/2)		60 [50% RH] 89 [dam] (ISO 527-1/2)	
Elongation @ break, %	200 (ASTM D638)	2 6 (ISO 527-1/2)	>50 [50% RH] 40[dam] (ISO 527-1/2)	10 [50% RH] 3.7 [dam] (ISO 527-1/2)	30 (ISO 527-1/2)
Flexural strength, MPa		200 (ISO 178)	53 [50% RH] 85 [dam] (ISO 527-1/2)		

Flexural modulus, GPa	2 3 (ASTM D790)				3.0 (ISO 178)
Flexural yield strength, MPa	83 (ASTM D790)				97 (ASTM D790)
Impact strength, Izod, J/cm	0 5 (ASTM D256)				0 7 (ASTM D256)
Hardness, Rockwell					92 [M] 120 [R] (ISO 2039/2)
Thermal Properties					
Linear CTE, 20°C, μm/m-°C	130 [flow] 130 [transverse] (ASTM E831)	30 [flow], 100 [transverse] (ASTM E831)	100 [flow], 110 [transverse]	67 [flow][dam], 88 [transverse] [dam] (ASTM E831)	120 [flow] (ASTM E831)
Thermal conductivity W/m-°C	0.16	0.28 (DIN 51046)			0 4
Melting temperature, °C		213 (ISO 3146C)	263 (ISO 3146C)	260 [dam] (ISO 3146C)	178 (ISO 3146C)
Melt flow rate, g/min					250 (ISO 1133)
Deflection temp, °C	154 [@0 46MPa] (ASTM D648)	202 [@0 45MPa] (ISO 75-1/2)	200 [@0 45MPa] (ISO 75-1/2)	240 [dam] [@0 45MPa] (ISO 75-1/2)	165 [@0.45MPa] (ISO 75-1/2)
Deflection temp @1 8MPa, °C	54 (ASTM D648)	180 (ISO 75-1/2)	70 (ISO 75-1/2)	210 [dam] (ISO 75-1/2)	95 110 [annealed] (ISO 75-1/2)
Max service temp, Air, °C	54				
UL RTI, electrical, °C	120 (UL 746B)	140 (UL 746B)			
UL RTI, mechanical with impact, °C	120 (UL 746B)	140 (UL 746B)			
UL RTI, mechanical without impact, °C	140 (UL 746B)	140 (UL 746B)			
Flammability, UL94 (5=V0, 4=V1, 3=V2, 1-HB)	1 (UL94HB @0 8mm)	1 (UL94HB @0 8mm)	2 (UL94HB @0 7mm)		1 (UL94HB @1 6mm)
Processing temp, °C	252 [suggested injection temp 243-260°C]	240-260			210-220
Mould temp, °C	62 [suggested mould temp 48-76°C]	80			90
Drying temp, °C	250 [3-4 hrs]	110-130 [2-4 hrs]			
Electrical Properties					
Volume resistivity, Ω-cm	4x10^16 (ASTM D257)	>1x10^15 (IEC 93)	1x10^11 [50% RH] 1x10^15 [dam] (IEC 93)	1x10^12 [50% RH] (IEC 93)	1x10^15 (IEC 93)
Surface resistivity, Ω		>1x10^15 (IEC 93)	1x10^12 (IEC 93)	1x10^15 [50% RH] (IEC 93)	>1x10^15 (IEC 93)
Dielectric constant @1MHz	3 1 (ASTM D150)	3 5 (IEC 250)	4 0 [50% RH] 3 6 [dam] (IEC 250)	4 5 [50% RH] 3 9 [dam] (IEC 250)	3 6 (IEC 250)
Dissipation factor @1MHz	0 02 (ASTM D150)	0 0175 (IEC 250)	0 07 [50% RH] 0 02 [dam] (IEC 250)	0 055 [50% RH] 0 023 [dam] (IEC 250)	0 005 (IEC 250)
Electric strength, kV/mm		31 (IEC 243-1)	28 [50% RH] 31 [dam] (IEC 243-1)	40 [dam] (IEC 243-1)	32 (IEC 243-1)
CTI, V		400 (IEC 112)	525 [dam] (IEC 112)	575 [dam] (IEC 112)	600 (IEC 112)

APPENDIX 2. SPECIFICATION OF INJECTION MOULDING MACHINE

ENGEL Injection moulding machine   Instruction manual

3   MACHINE SURVEY

b020 001 00 153
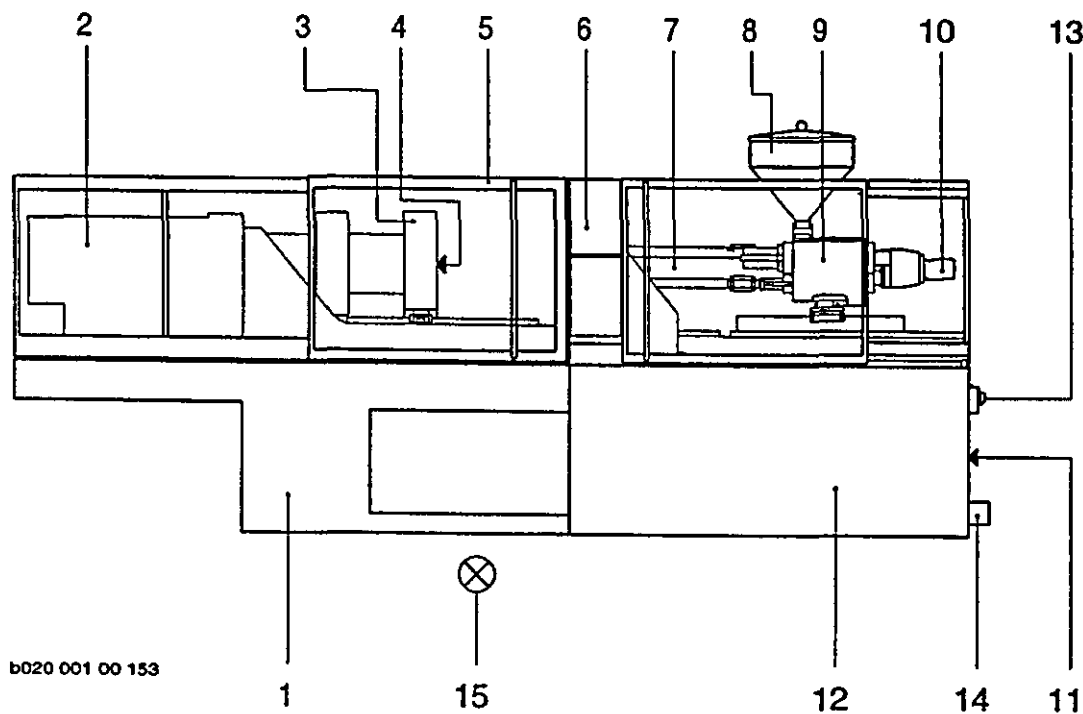
1	Machine frame	8	Material container
2	Clamping cylinder	9	Injection unit
3	Moving platen	10	Screw drive
4	Hydraulic ejector	11	Hydraulics
5	Moving cover	12	Electrics/Electronics
6	Microcomputer	13	Main switch
7	Plasticizing cylinder	14	Power supply
15	Place of work-operating personnel		

ENGEL SCHWERTBERG AUSTRIA	TECHNISCHE DATEN SPRITZGIESSMASCHINE ES 80/30 HL PERA TECHNOLOGY CENTRE, England	1999-07-29 TB-KMK/Kapplmüller

Internationale Größenbezeichnung [1]		80/30		
Maschinenbezeichnung		ES 80/30 HL		
Spritzeinheit				
Schneckendurchmesser	mm	18	22	25
Schneckenlänge Standard	L/D	22,5	18,7	16,4
Plastifizierleistung Standard [2,3,4]	g/sec	3,5	6	8
Schneckenlänge Barriere	L/D	-	-	-
Plastifizierleistung Barriere [4,5]	g/sec	-	-	-
Dosierweg	mm	100	100	100
Schneckendrehzahl	r/min	20-450	20-360	20-360
Einspritzstrom [6]	cm^3/sec	52	78	100
Max. Hubvolumen	cm^3	25	38	49
Spez. Spritzdruck	bar	2200	1590	1230
Spez. Spritzdruck erhöht	bar	2200	2060	1600
Düsenweg	mm	200	200	200
Düsenanpreßkraft	kN	28	28	28
Heizleistung [7]	kW	5,3	5,3	5,3
Anzahl der Heizzonen inkl. Düse [7]		4	4	4
Schließeinheit				
Schließkraft	kN	300		
Öffnungsweg	mm	350		
Auswerferkraft	kN	40		
Auswerferweg	mm	100		
Werkzeugeinbauhöhe min.	mm	180		
Plattenabstand max.	mm	530		
Werkzeugaufspannplatten				
- Gesamtgröße	mm	550 x 330		
- vergrößerte Aufspannplatten	mm	550 x 430		
Ausfallschachtbreite	mm	360		
Trockenlauf (Euromap 6) ∞ Hub	sec ∞ mm	1,3 ∞ 150		
Antrieb				
Pumpenantriebsleistung	kW	7,5		
Ölfüllung	l	115		
Gewicht				
Netto gesamt (ohne Öl)	kg	2900		
Abmessung				
LängexBreitexHöhe (Standardmaschine)	m	3,30x1,20x1,80		

1 Arbeitsvermögen Spritzeinheit-Schließkraft in MP
2 Werte für Polystyrol (MVR 200/5=10cm^3/10min) bis Spritzeinheit 2550 nach EWN
3 Werte für HDPE (MVR190/5=13cm^3/10min) mit PE-Schnecke ab Spritzeinheit 3550 nach EWN
4 Werte für PP (MVR230/2,16=12cm^3/10min) bei TM-Maschinen
5 Werte für HDPE (MVR190/5=13cm^3/10min) nach EWN
6 Theoretische Werte
7 für Standardschneckenlänge

Z.Nr.: 0713 022 01 034
A.Nr.: 10 719/22

ENGEL

Internationale Größenbezeichnung		International size designation
SPRITZEINHEIT		INJECTION UNIT
Schneckendurchmesser	mm	Screw diameter
Dosierweg	mm	Metering stroke
Schneckendrehzahl	min-1	Screw speed
Plastifizierstrom	g/sec	Plasticizing rate
Einspritzstrom	cm3/sec	Injection rate
Maximales Hubvolumen	cm3	Maximum stroke volume
Spezifischer Spritzdruck	bar	Specific injection pressure
Spezifischer Spritzdruck erhöht	bar	Specific inj pressure increased
Düsenweg	mm	Nozzle stroke
Düsenanpreßkraft	kN	Nozzle contact pressure
Heizleistung	kW	Heating capacity
Anzahl der Heizzonen		Number of heating zones
SCHLIESSEINHEIT		CLAMPING UNIT
Schließkraft	kN	Clamping force
Öffnungsweg	mm	Opening stroke
Auswerferkraft	kN	Ejector force
Auswerferweg	mm	Ejector stroke
Plattenabstand maximal	mm	Platen distance maximum
Werkzeugeinbauhöhe minimal	mm	Mould height minimum
Aufspannplatten		Mould fixing platens
- Gesamtgröße	mm	- Total size
- Vergrößerte Aufspannplatte	mm	- Enlarged mould fixing platen
Trockenlauf	sec	Dry cycle time
ANTRIEB		DRIVE
Pumpenantriebsleistung	kW	Pump drive power
Ölfüllung		Oil filling:
- Hauptölbehälter	l	- Main oil tank
- Nachsaugbehälter	l	- Post-suction tank

ENGEL

Version:

GEWICHT		WEIGHT
Netto	kg	net
Schließeinheit-Netto	kg	Clamping unit-net
Schließeinheit-Netto (vergrößerte Aufspannplatten)	kg	Clamping unit-net (enlarged mould fixing platens)
Spritzeinheit-Netto	kg	Injection unit-net

/pehb/techn.dat/formul.1.E - 06/1998

SPRITZDRUCKDIAGRAMM
INJECTION PRESSURE DIAGRAM
DIAGRAMME PRESSION D'INJECTION
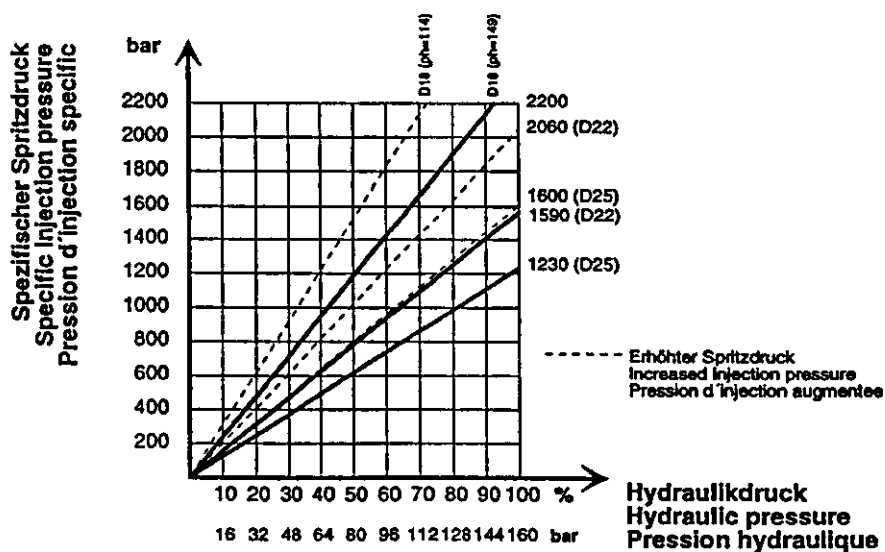
0713 720 04 214

APPENDIX 3. PMOS4 TEST CHIP DATASHEET

PMOS4 Package Performance Monitoring Test Chip

National Microelectronics Research Centre

University College Cork

Lee Maltings

Prospect Row

Cork

6th Nov. 1998

C.1. Test Chip Summary

The PMOS4 test chip, shown in schematic form in figure 1, is a general-purpose package performance monitoring test chip which contains test structures to evaluate the following IC package performance parameters:

- environmental reliability in terms of corrosion of on-chip metallisation.
- thermo-mechanical reliability in terms of:
  - stress induced resistance changes in silicon-based diffused resistors.
  - stress induced metal shift in on-chip metallisation.
- thermal resistance between the chip surface and some external reference temperature on the IC package, circuit board or the ambient air.

PMOS4 is a 10mm x 5mm test chip containing the following:
- 1 passivated corrosion monitor, covering approximately half of the die.
- 1 heater resistor, covering 85% of the die.
- 3 temperature sensing diodes, located at the centre, corner and edge of the die.
- 6 * 3-leg strain gauge, P-doped diffused resistors.
- Daisy chain wire bond structures.
- Metal shift patterns.

Before discussing the test chip in more detail, it is worth considering the main criteria or guidelines, which were considered in its design. These are summarised here and should form a baseline for any similar future designs :-

- It should be possible to simulate a range of functional chip sizes both currently on the market and under consideration for implementation in future designs. This was considered as essential for maximum utilisation of the test chips by both manufacturing and Research & Development sites, where a range of functional die sizes are under consideration at any one time. The advantage of this strategy was that test chip design cycles could be significantly reduced since only a single interconnect layer was required to customise a given test chip size.

- Thermal characterisation is performed using on-chip heater resistors used to supply large power to the chip, combined with p-n junction diodes used for on-chip temperature measurement. The heat sources were designed to meet power density requirements for current and future applications where power densities in the range 25 to 100W/cm square are projected for future high speed computing.

• The thermal test structures (heaters) were required to meet or at least be comparable to existing SEMI test chip guidelines, i.e. the heater element should cover at least 85% of the die surface.

• A number of temperature sensors were required on the chip to measure maximum chip surface temperature, average chip surface temperature and to obtain a temperature profile across the die surface.

• Resistance to harsh environmental conditions is measured using triple-track corrosion monitors. By suitably biasing the meanders - centre track grounded and the outer two tracks biased positive and negative - the occurrence of electro-chemical corrosion of the aluminium can be monitored. This form of corrosion results in an increase in leakage current between the tracks and an increase in track resistance.

• On chip stress measurements are made using diffused resistor strain gauges. Since silicon is a piezoresistive material, the resistors are sensitive to stress changes on the surface of the die. The requirements were as follows :-

- The full stress content (all six unique stress components) on the surface of the die should be measured if possible.
- The measured stress components should be inherently temperature compensated to eliminate thermal errors (the resistors are sensitive to temperature as well as stress).
- The gauges should occupy as small an area as possible, yet have a resistivity high enough for the resistance changes to be measurable
- The resistors should preferably be manufactured at medium doping levels (10^{16}-10^{19} cm^{-3}). The piezoresistive coefficients are larger at low doping levels ($<10^{16}$ cm^{-3}) which makes the resistors more sensitive to stress, however they become more temperature dependant. The opposite occurs at high doping levels ($<10^{20}$ cm^{-3}) where the temperature dependence of the coefficients practically disappears, but the coefficients decrease in value, making the gauge less sensitive to stress. By using a medium doping concentration the piezoresistive coefficients are sufficiently large without being overly temperature sensitive.

• Wire bond reliability is tested using daisy chain bond pad structures. These are a series of bond pads shorted together. A change in resistance indicates the growth of an intermetallic layer between the pad and the wire bond, while a complete bond failure results in an open circuit These daisy chains can also be used to check the reliability of flip chip solder bump connections.

C.2. Test Structure Specifications

Thermal Testing Procedure

The PMOS4 contains one single P-diffusion heater resistor, which covers approximately 85% of the die surface. Three diode temperature sensors are available on the chip, one in the centre and one each in opposite corners of the die, which allows for an assessment of the temperature variation across the chip. The temperature sensitive parameter (TSP) of the diode is the forward voltage drop under a constant current.

1.1/ Calibration and thermal testing.

Force measuring current (typically 10uA, 100uA or 1mA) through diode and measure Vf at different temperatures. Vf v temperature for the diodes is approximately 1.6 to 2.2mV/°C.

1.2/ Thermal Resistance Measurement

To prevent electrical interference between the diode and the heater the biasing of the device must be carefully setup. Configure circuit as shown below, ensure no common ground point between the heater measurement circuit and the diode measurement loop. The diode excitation current should be 'sourced' into the anode of the diode rather than 'sinked' from the cathode. This is necessary due to the common substrate between the heater and the diode.
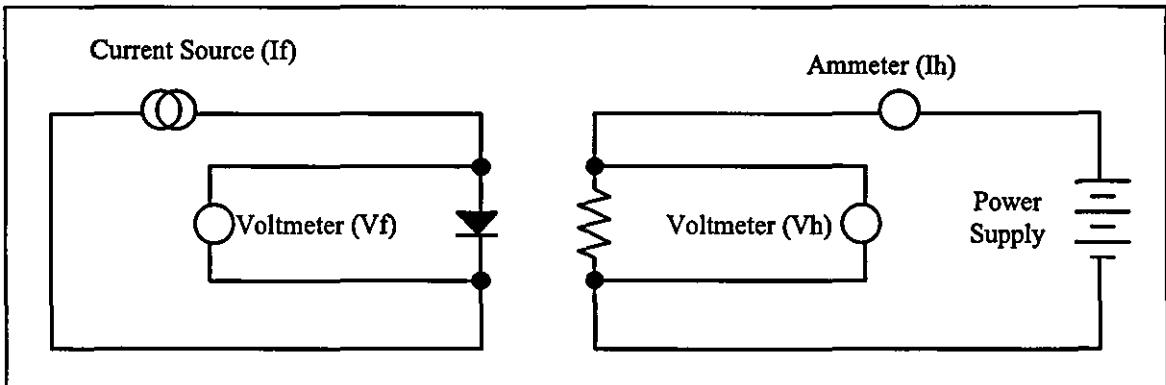
MAX bias for Heater is 40V, this corresponds to approximately 6W per PMOS4 (5 x 10mm) chip, in a 10 X 10mm configuration, 12W will be achievable.

Corrosion Monitors

The main function of the triple track metal meanders is corrosion detection. There are two individual corrosion monitors on the die. The line width and line pitches are both 10 microns each respectively, with a thickness of 1 micron. Metal1 "runners" are incorporated

into the structures at right angles to the metal tracks to simulate the topography of an actual IC.

On-chip metal corrosion is measured by grounding the centre track while biasing the outer tracks positively and negatively. The occurrence of both anodic and cathodic corrosion is then detected by an increase in leakage currents between the tracks or by an increase in track resistance.

The metal track meanders can also be used as a surface conductivity monitor in conjunction with the temperature sensing diodes. By cooling the package and measuring the leakage current between the tracks, a large increase in leakage current is observed when the dew point is reached. This is due to the condensation of moisture on the chip surface as the dew point is reached, which can be measured using the diodes. Knowing the dew point and ambient temperature means that the relative humidity can be calculated easily even within hermetically sealed packages.

MAX bias for the corrosion monitors is ±20V. Bias voltages greater than this can cause destructive breakdown of the oxide beneath the material.

Strain Gauges

Piezoresistance is that property of a material, which causes a change in electrical resistance under applied mechanical stress. Single crystal silicon is one material, which has this property and has been widely used in the manufacture of miniature strain gauges. Suitable resistors may be fabricated by diffusing impurities into the silicon surface.

The resistance change is coupled to applied stress levels by a six by six matrix of piezoresistive coefficients. The carrier type, concentration and the temperature are required to quantify these coefficients from measured results in the literature if available. Silicon is characterised by six fundamental piezoresistive coefficients, three each for N-type and P-type dopants. These coefficients are usually denoted by π_{11}, π_{12} and π_{44}.

Once the piezocoefficients are known, formulae for resistance variations are used, taking account of wafer type and orientation, to calculate die surface stresses. The stress-induced resistivity change is dependant on the direction of current flow with regard to the crystal lattice. Thus it is vital to know the orientation of the crystallogrphic axes with respect to the silicon surface.

The PMOS4 test chip contains P-doped strain gauge resistor rosettes with typical resistance values of 1.3kΩ. Each rosette consists of three resistors which enables the calculation of the two in-plane direct stresses, σ_x and σ_y, as well as the in-plane shear stress

τ_{xy}. There are six such rosettes distributed across the surface of the die as illustrated in figure 1.

In a typical application, for example measuring the stress induced on the surface of the die due to the plastic encapsulation process, the procedure is as follows :-

- The resistors are measured in wafer form (stress free state), noting the ambient measurement temperature. If possible the ambient temperature should be controlled to an accuracy of 0.1°C.
- The resistors are re-measured after packaging. Note the measurement temperature. Again the measurements should be performed in a controlled environment at the same temperature as the wafer level measurements, if at all possible. If this can be achieved, thermal errors are almost completely eliminated.
- If the wafer level measurements were carried out at a different temperature to the packaged IC measurements, temperature compensation must be performed as follows :-

$$R_i = R_i (1 + \alpha_T [T_f - T_i])$$

where α_T is the TCR of the strain gauge resistors, R_i is the initial wafer level measurement, T_i is the wafer level measurement temperature and T_f is the final measurement temperature. α_T has been measured as 0.1%/°C.

- The final values are subtracted from the initial temperature compensated values to give the measured resistance change due to the applied stress. These values can then be used to give the stress values.

C.3.   Wirebond Details

The following tables give the wire bond details for each of the structures on the PMOS4 test chip.

Corrosion Monitors:

A sketch of the corrosion monitor is shown below. The corrosion monitor consists of a triple aluminium track, which can be biased to accelerate corrosion between tracks. The triple tracks can be measured at interval points between terminals A and F.
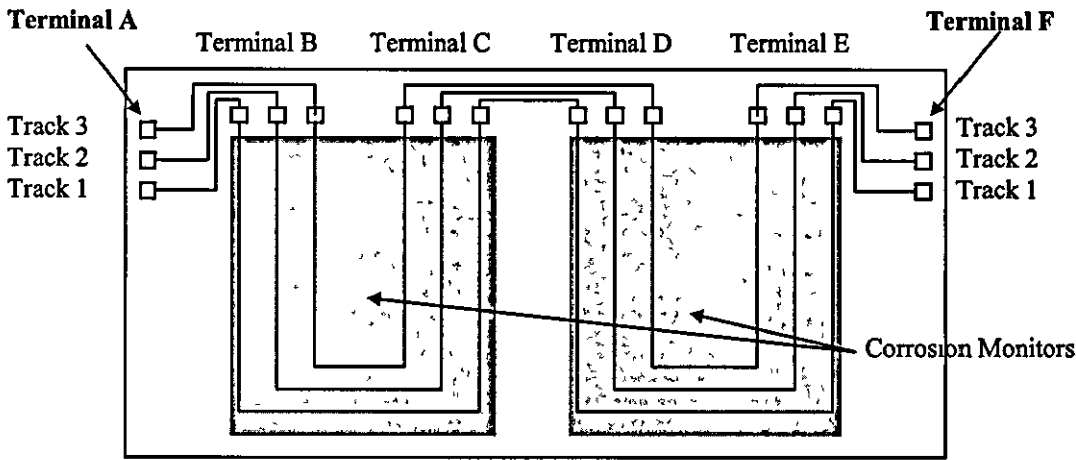
Location of Corrorsion Monitoring Pads on PMOS4 test chip

Corrosion Monitor Pad Connections				
Meander Track	Terminal , Pad Number			
	A	Pad #	F	Pad #
Track 1	CMA1	(109)	CMB1	(35)
Track 2	CMA2	(110)	CMB2	(34)
Track 3	CMA3	(111	CMB3	(33)

Corrosion Monitor Internal Pads								
Meander Track	Terminal , Pad Number							
	B	Pad #	C	Pad #	D	Pad #	E	Pad #
Track 1	CMC1	(2)	CMD1	(8)	CME1	(19)	CMF1	(28)
Track 2	CMC2	(3)	CMD2	(7)	CME2	(20)	CMF2	(27)
Track 3	CMC3	(4)	CMD3	(6)	CME3	(21)	CMF3	(26)

Heaters:

A sketch of the heater location is shown here. On the PMOS4 the heater is implemented as a single resistor with an approximate value of 300Ω. A number of connections are provided as illustrated in the diagram below. This is to allow a higher current carrying capacity for larger heat dissipation.
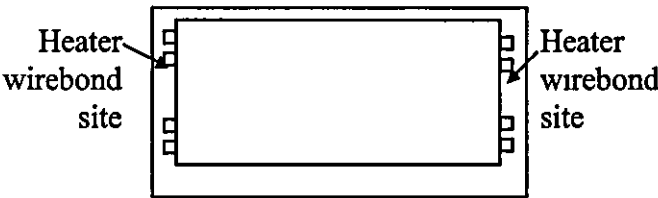
Heater WireBond Locations on PMOS4

There are also pads for 4-wire connection to the heater on the periphery of the die:

	Terminal 1	Terminal 2

Device	Label	#	Label	#
Heater	HTA1	(102)	HTB1	(31)
	HTA2	(108)	HTB2	(55)

Diodes:

A sketch of the diode locations is shown here. On the PMOS4 die there are three diodes available as sketched.
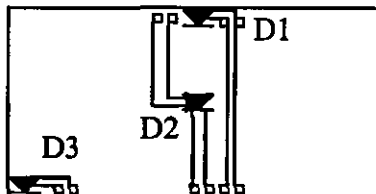
Diodes location on PMOS4

	Anode		Cathode	
Device	Label	#	Label	#
Diode D1	D1A1	(17)	D1C1	(18)
	D1A2	(66)	D1C2	(65)
Diode D2	D2A1	(71)	D2C1	(70)
	D2A2	(9)	D2C2	(10)
Diode D3	D3A1	(90)	D3C1	(89)

Strain gauges:

There are six strain gauge rosette each consisting of three P-doped resistors. One end of each resistor is shorted together (centre pads) so that four pads are required to measure all of the resistors in an individual rosette.

Strain Sensor 1 to 6	Terminal A Pad No	Terminal B Pad No
Resistor 1A	14	17 or 66
Resistor 1B	15 or 68	17 or 66
Resistor 1C	16 or 67	17 or 66
Resistor 2A	52	53
Resistor 2B	54	53
Resistor 2C	51	53
Resistor 3A	73	71
Resistor 3B	74	71
Resistor 3C	72	71
Resistor 4A	92	90
Resistor 4B	93	90
Resistor 4C	91	90
Resistor 5A	105	107
Resistor 5B	106	107
Resistor 5C	104	107
Resistor 6A	115	113
Resistor 6B	114	113
Resistor 6C	116	113

Daisy Chain (Wire Bond Reliability Structures)

	Terminal A	Terminal B
Daisy Chain No.	Pad No	Pad No.
1	11	12
2	22	23
3	24	25
4	29	30
5	36	37
6	38	39
7	40	41
8	43	44
9	45	46
10	47	48
11	49	50
12	56	57
13	58	59
14	60	61
15	62	63
16	76	77
17	78	79
18	80	81
19	82	83
20	84	85
21	86	87
22	94	95
23	96	97
24	98	99
25	100	101

Substrate Contacts: Pad 13, Pad 42, Pad 75 & Pad 103.

Number of Pads Required to Measure Each Test Structure

- Strain gauges : four pads per strain gauge, 24 pads for all six strain gauges

- Heaters and Diodes : heater requires two pads minimum, preferably four pads for four-wire Kelvin resistance measurement. Each of the three diodes requires two pads. This gives a total of 10 pads for thermal characterisation

- Corrosion Monitors : requires six pads to measure the corrosion monitor from terminals A to F. This can be split into two monitors by the use of terminals B and C. This requires 12 pads in total.

- Daisy Chains : there are 25 daisy chain links on the PMOS4, each link requires 2 pads.

C.4. Bond Pad Co-ordinates

The following table gives the pad co-ordinates for the 116 I/O pads on the PMOS4 test chip. The co-ordinates are referenced from the left-hand top corner of pad number 1 as illustrated below.

(0,0)

PMOS4 Test Chip
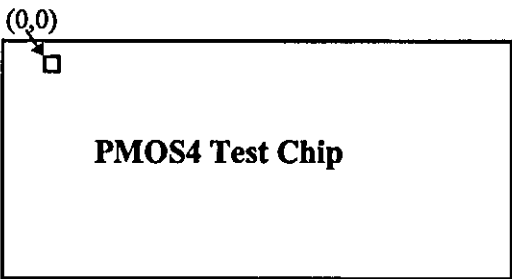
PAD	X	Y	PAD	X	Y
1	0	0	59	6800	4672
2	865	0	60	6600	4672
3	1065	0	61	6400	4672
4	1265	0	62	6200	4672
5	2993	0	63	6000	4672
6	3193	0	64	5800	4672
7	3393	0	65	5600	4672
8	3593	0	66	5400	4672
9	3793	0	67	5200	4672
10	3993	0	68	5000	4672
11	4193	0	69	4800	4672
12	4393	0	70	4600	4672
13	4593	0	71	4400	4672
14	4793	199	72	4200	4672
15	4993	199	73	4000	4672
16	5193	199	74	3800	4672
17	5393	199	75	3600	4672
18	5593	199	76	3400	4672
19	5793	0	77	3200	4672
20	5993	0	78	3000	4672
21	6193	0	79	2800	4672
22	6393	0	80	2600	4672
23	6593	0	81	2400	4672
24	7685	0	82	2200	4672
25	7885	0	83	2000	4672
26	8085	0	84	1800	4672
27	8285	0	85	1600	4672
28	8485	0	86	1400	4672
29	8685	0	87	1200	4672
30	8885	0	88	1000	4672
31	9085	0	89	800	4672
32	9371	143	90	600	4672
33	9371	343	91	400	4672
34	9371	543	92	200	4672
35	9371	743	93	0	4672
36	9371	943	94	-305	4541
37	9371	1143	95	-305	4341
38	9371	1343	96	-305	4141
39	9371	1543	97	-305	3941

| 40	9371	1743	98	-305	3741
41	9371	1943	99	-305	3541
42	9371	2143	100	-305	3341
43	9371	2343	101	-305	3141
44	9371	2543	102	-305	2941
45	9371	2743	103	-305	2741
46	9371	2943	104	-305	2541
47	9371	3143	105	-305	2341
48	9371	3343	106	-305	2141
49	9371	3543	107	-305	1941
50	9371	3743	108	-305	1741
51	9371	3943	109	-305	1541
52	9371	4143	110	-305	1341
53	9371	4343	111	-305	1141
54	9371	4543	112	-305	941
55	9100	4672	113	-305	741
56	7400	4672	114	-305	541
57	7200	4672	115	-305	341
58	7000	4672	116	-305	141

The co-ordinates for the internal Heater pads locations are given in the table below, again referenced to the top left corner of pad number 1.

PAD	X	Y	PAD	X	Y
1	122	940	9	8972	742
2	122	1140	10	8972	942
3	122	1740	11	8972	1542
4	122	1940	12	8972	1742
5	122	2740	13	8972	2742
6	122	2940	14	8972	2942
7	122	3540	15	8972	3342
8	122	3740	16	8972	3542

C.5.   Wafer and Die Specifications

Wafer Diameter: 4 inch
Wafer Thickness: 525 ± 25 microns
Metallisation: Aluminium / 1% silicon
Passivation: Silicon Nitride
Die Size: 10,000 microns X 5,000 microns
Die Pitch: 10,100 microns X 5,100 microns
Scribe Channel Width: 100 microns
Number of periphery I/O: 116
I/O Pad Size: 100 microns square
I/O Pad Pitch: 200 microns
Passivation Window Opening over I/O Pads: 90 microns

C.6. PMOS4 Layout
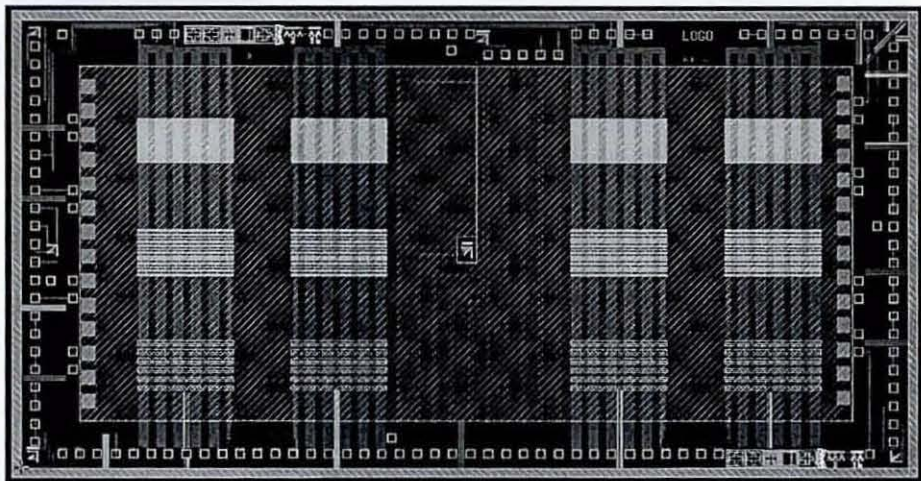
C.7. PMOS4 Multi-up Format

The PMOS4 can be used in multi-up as a 10mm X 10mm or 5mm X 20mm die, simply by dicing 2 single die side by side. The 10mm X 10mm version is shown below. The pad co-ordinates can be easily obtained using the die step size, 10,100microns by 5,100 microns.
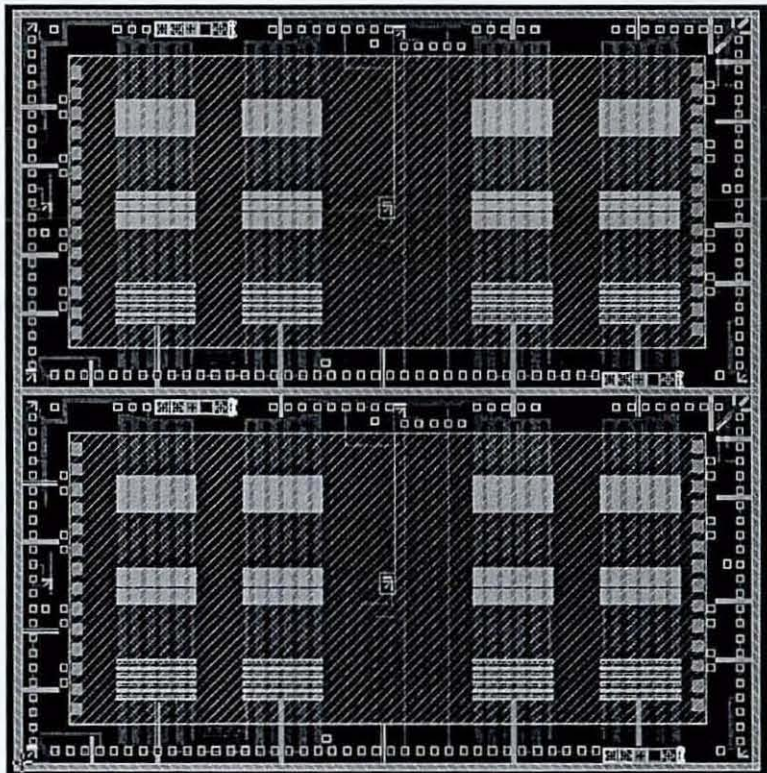
NMRC PMOS4 Test Chip

Prepared By:	Ger McCarthy	Date:	March 11, 1997
Drawing	PMOS4	Rev	1

APPENDIX 4. LIST OF PUBLICATIONS

1. **Teh N.J., Palmer P.J, Conway P.P.,** "Low-cost Embedding of Electronics within Injection Moulded Polymers." Proceedings from the 16th. NCMR, London, UK. Sep 2000. pp 375-379.

2. **Teh N.J., Conway P.P., Palmer P.J., Prosser S., Kioul A.,** "Embedding of Electronics within Thermoplastic Polymers using Injection Moulding Technique." Proceedings from the 26th. IEMT Symposium, Santa Clara, CA., 2000, pp 10-18.

3. **Teh N.J., Conway P.P, Palmer P.J.,** "Statistical Optimisation of Thermoplastic Injection Moulding Process for the Encapsulation of Electronic Subassembly", Journal of Electronics Manufacturing, vol. 10, no. 3 (2000), 2001, pp 171-179.

4. **Teh, N.J.** "Materials Adhesion Investigation in Thermoplastic Overmoulding Process of Electronic Subassembly." Dept. of Manufacturing Engineering, Loughborough University, UK. 2001.

5. **N.J. Teh, M.D. Jones, D. Bevan, I.C. Cleathero, A. Kioul, O. Schmidt, P.P. Conway, S. Prosser, P.J. Palmer.,** "Re-Engineering of Thermoplastic Injection Moulding Process for Electronics Encapsulation In Automotive Applications", 5th International Conference on Electronics Materials and Packaging (EMAP), November 17-20, 2003, Singapore.